Bubbly Flow Physics for Applications in Aerated Hydroturbines and Underwater Transport

A DISSERTATION

SUBMITTED TO THE FACULTY OF

UNIVERSITY OF MINNESOTA

BY

Ashish Karn

IN PARTIAL FULFILLMENT OF THE REQUIREMENTS

FOR THE DEGREE OF

DOCTOR OF PHILOSOPHY

Advisors: Jiarong Hong and Roger E A Arndt

May 2016

Acknowledgements

As I am concluding this dissertation, it is but natural to reminisce the chronology of events that have led me here, in the first place. My deepest acknowledgment of gratitude thus, for my beloved teacher who gave me the inspiration to pursue a doctoral degree. Because of his inspiration and support, these years in the grad school were the most enriching years of my life.

I would like to express my profuse appreciation and thankfulness to my advisors Dr. Jiarong Hong and Dr. Roger Arndt for letting me join their groups. I could not have completed this thesis without their help at every step, and I felt fortunate to have them as advisors at every step of my PhD. I am thankful to them for patiently listening to all of my puerile ideas and showing immense faith in me throughout. I would like to thank Dr. Hong particularly for teaching me how to never give up and become responsible towards my commitments. He has trained me at every step of my graduate career in every single skill that I needed to be successful as a graduate student. I would also like to thank Dr. Peter H. McMurry for his support in helping me pursue a graduate career at the U.

I am deeply thankful to all my colleagues at the University of Minnesota: Ellison Kawakami, Garrett Monson, Chris Ellis and Chris Milliren for their guidance during the first few years of my research. I would also like to thank my group members including Rohan De, Roger Borgeson, Siyao Shao, David Sorenson, Brett Rosiejka, John Turner, Lei Cao for helping me out in carrying out experiments at the water tunnel, at different stages of my research. My thanks also to Mostafa, Kevin, Teja, Santosh for their invaluable comments and assistance during the group meetings. A deep note of thanks to my beloved friends Sanyam Mehta, Ayush Singhal, Shashank Goyal, Saket Gupta, Ankit Mahajan, Raghav Karumur, Gokul Hariharan, Srijan Agarwal, Ankur Khare, Brijesh Kumar, Pulkit Agarwal, Gyanender Singh and others for their valuable friendship and brotherly association which made grad school a memorable and cherishable experience for me.

I would like to thank my committee members: Prof. Ellen Longmire, Dr. Lian Shen and Dr. Cari Dutcher for their insightful comments during my PhD. Thanks also goes to Dr. John S Gulliver for his support and valuable collaboration. Many thanks to the staff members at SAFL, particularly Ben Erickson, Erik Steen and Jim Tucker for their prompt and responsive support. I would also like to acknowledge the funding support received from Graduate School under Doctoral Dissertation Fellowship, which was instrumental in my graduate research and getting this dissertation completed in time.

Last but not the least, I would like to thank my parents and family members for all the sacrifices they have done in letting me pursue my doctoral degree at the U.

Abstract

Bubbly flows occur in a wide variety of situations and are frequently employed in industry and other engineering applications. The current work deals with two such examples of bubbly flows: speed enhancement and controllability of next-generation high–speed underwater vehicles for naval defense applications and environment-friendly power generation through aerating hydroturbines. A complete understanding of the bubbly flow physics is imperative to leverage it for these different applications. These investigations into bubbly flow physics are accomplished by studying the fundamental fluid dynamics of bubbles at different size scales. A large bubble is used to envelop an underwater vehicle causing tremendous reduction in flow resistance while the small bubbles are employed for aeration applications in a hydroturbine. Our experiments have provided critical insights into the design and development of operational strategies and models for these novel technologies. For the dispersed bubbly flow regime, bubble size characteristics in the wake of a ventilated turbine blade is measured using shadow imaging and a newly developed image processing approach. Simultaneous mass transfer measurements in the wake have shown an interrelationship with the bubble size and high speed imaging of the bubbles reveal the physical mechanisms of bubble breakup and coalescence and its effect upon the bubble sizes in the wake. In the supercavity bubble regime, systematic studies are carried out to investigate the supercavity closure mechanisms in detail, and a unified theory is proposed to predict different closure modes. Further insights are provided into the interrelationship between supercavity closure, ventilation demand and gas entrainment behaviors of supercavity. The effect of ocean waves on the stability of supercavity bubbles and its closure are also investigated by replicating the ocean waves in the high speed water tunnel. Specifically, a novel aspect of the current research pertains to the visualization and quantification of the internal flows inside supercavity bubbles and drops.

Table of Contents

List of Tables

List of Figures

Chapter 1 Introduction

This thesis focuses on the experimental investigations of multiphase flows (particularly, cavitation and bubbly flows) for applications in aeration through ventilated hydroturbines and drag reduction of underwater vehicles through supercavitation approaches. Although these two potential next-generation technologies are vastly disparate, the current thesis brings it together by studying it from a fundamental perspective of bubbly flows, or broadly, multiphase flows.

1.1. Multiphase flows

The term *multiphase flows* can be used to describe any fluid flow that consists of more than one phase or component. Thus, according to the state of different phases, multiphase flows can be classified as gas-solid flows, liquid-solid flows, gas-particle flows, vapor-liquid flows, gas-liquid (/bubbly) flows and so on. The current work

primarily deals with flow situations having two phases, also called ‘two-phase flows’. Such two-phase flows can be classified into two parts, based on their topology: ‘dispersed flows’ and ‘separated flows’. Dispersed flows consist of a number of finite-sized drops or bubbles distributed in a connected volume of continuous phase (viz. bubbly flows, droplet flows). On the other hand, separated flows are identified by two continuous streams of different fluids separated by interfaces (Brennen 2005).

Two-phase flows are encountered in numerous situations. They are present in our everyday life (cosmetics, food, medical diagnosis, etc.) and are ubiquitous in the environment in the form of rain, fog, snow, mist, mud slides, sediment transport, debris flows etc. Numerous applications make the use of gas-liquid systems a crucial point for their proper operation. For example, some industries that currently require the use of two-phase flows are: the aerospace industry, process industry, nuclear industry, oil industry, metallurgical industry, biological, pharmaceutical and medical industry. More explicit applications are the heat-exchangers, cleaning devices, propulsion systems, energy transport and conversion systems, oxygenation, diesel engines, refrigeration, mixing devices and environmental systems (Kleinstreuer 2003, Brennen 2005, Clift et al. 2005, Ishii and Hibiki 2006). It is worth noting that nearly every processing technology must deal with multiphase flow in some form or the other, viz. cavitating pumps and turbines, electrophotographic processes, papermaking etc. (Brennen 2005). The current work covers aspects of both dispersed flows (bubbly flows, vaporous cavitation) and separated flows (ventilated and vaporous supercavitation), and are described in greater detail in the following sections.

1.2. Cavitation and Supercavitation

Cavitation occurs in a variety of hydrodynamic applications. These applications include, but are not limited to, hydraulic pumps and motors, hydrofoils, propellers and spillways. For many applications, cavitation has negative effects. Many manufacturers take great efforts to reduce or eliminate cavitation. Cavitation can alter the performance of a hydraulic system (reduction in lift and increase in drag for a hydrofoil, decrease in turbomachinery efficiency, reduced capacity to evacuate water in spillways, unwanted noise, etc.). However, cavitation has been advantageously employed in certain other applications, such as the homogenization of milk, cleaning of surfaces by cavitating jets and drag reduction by means of supercavitation. Depending on the application, cavitation provides different issues that the designer must address. The application of drag reduction by means of supercavitation is another example where the phenomenon of cavitation has been used to an advantage. Although the concept itself is simple enough, its application is challenging due the highly complex physics involved.

1.2.1. Fundamentals of Cavitation

Cavitation can be defined as the breakdown of a liquid medium under very low pressures. Visually, cavitation can be observed in the formation of vaporous bubbles, or cavities in a liquid. In this sense, cavitation is very similar to the boiling of water. For boiling, the breakdown of the liquid medium occurs as a result of an increase in temperature at nearly constant pressure. The difference with cavitation is that the breakdown of the liquid medium results from a decrease in pressure at nearly constant

temperature. This is illustrated in Figure 1.1. This decrease in pressure typically occurs in a high-speed flow, or because of the presence of a sharp object in a flow.

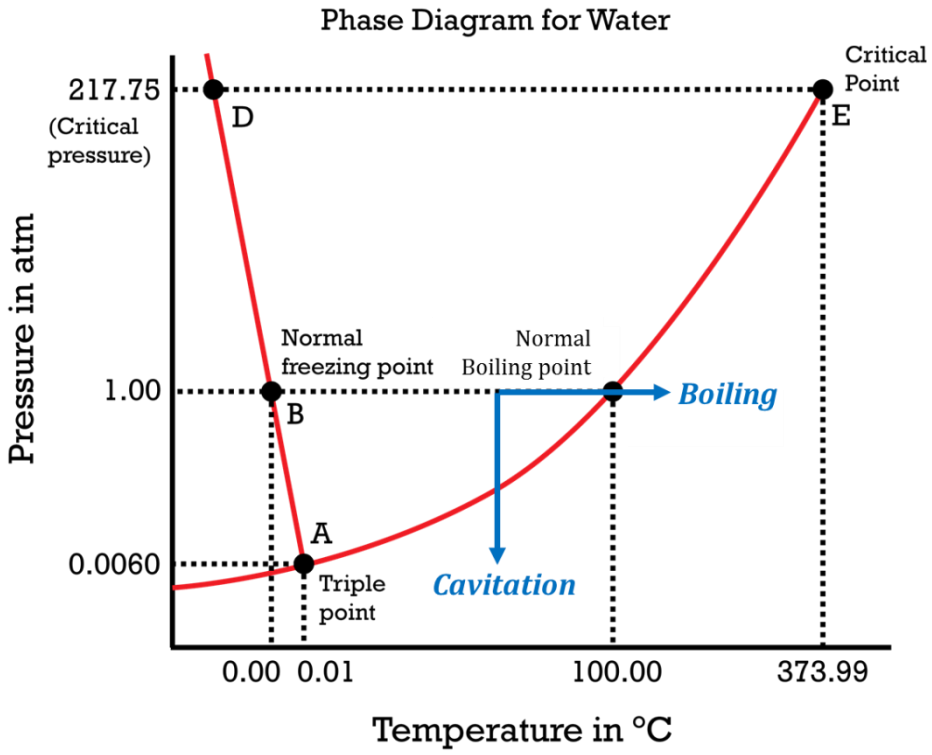

Figure 1.1: Difference between cavitation and boiling

The fundamental parameter used to describe cavitation is the cavitation number

$$\sigma_v = \frac{P_\infty - P_v}{0.5\rho {U_\infty}^2} \tag{1.1}$$

where P_∞ is the static freestream pressure, P_v is the vapor pressure of water, ρ is the density of the liquid, and U_∞ is the freestream velocity. The cavitation number corresponding to the initial formation of vaporous bubbles (inception cavitation number) in an initially single phase flow is defined as

$$\sigma_i = -C_{P,min} \tag{1.2}$$

where $C_{P,min}$ is the minimum pressure coefficient, which is normally negative. The minimum pressure coefficient is expressed as

$$C_{P,min} = \frac{P_m - P_\infty}{0.5\rho U_\infty{}^2} \tag{1.3}$$

where P_m is the minimum pressure. For a liquid it can be assumed that the minimum pressure, P_m, is equal to the vapor pressure of the liquid, P_v. One way to decrease the cavitation number is by decreasing the pressure difference seen in the numerator (only feasible in closed-circuit water tunnels). A second way is to increase the freestream velocity. Initially with a cavitation number greater than the incipient value, $\sigma > \sigma_i$, no cavitation effects are present. As the cavitation number drops below the incipient value, $\sigma < \sigma_i$, transient isolated bubbles become apparent. Continuing to lower the cavitation number to values much lower than the incipient value, $\sigma << \sigma_i$, leads to the development of attached cavities (3D flows) or sheet cavities (2D flows). Attached cavities are seen at the leading edge of a body, while sheet cavities are seen on the low-pressure side of blades and foils. When the cavitation number drops far below the incipient value, $\sigma <<< \sigma_i$, supercavitation and cavitating vortices are formed. Supercavitation can be seen as a vapor-filled cavity encompassing a body underwater or as vortices seen at the tips of 3-D wings or propeller blades.

1.2.2. Supercavitation: A limiting case of cavitation

Figure 1.2 illustrates the process of decreasing ambient pressure beginning from an initially non-cavitating liquid phase flow to a supercavitating flow for a body with sharp-edged disc in front. As the figure shows, from an initial pressure of P_1, as the

pressure drops to P_2, the formation of vapor bubbles is observed indicating that σ has dropped below σ_i. Upon further reduction in pressure, these vapor bubbles grow in number and size, and further coalesce leading to a partial cavity which covers a part of the body. This stage is called 'developed cavitation'. With further reduction in pressure, σ continues to decrease till an incipient value, usually below 0.1, a large, attached cavity can be obtained which encompasses the entire body.

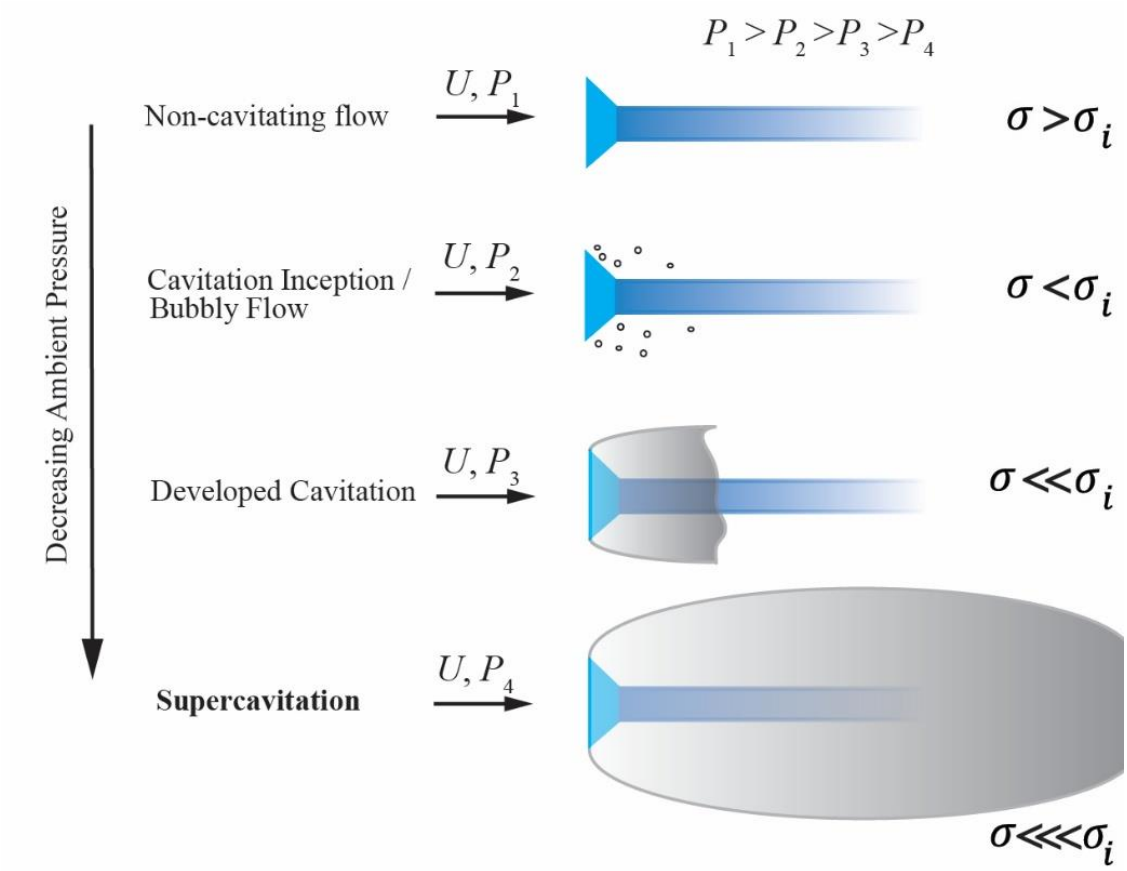

Figure 1.2: The transition of a liquid phase flow to supercavitation by the gradual reduction of ambient pressure

When such a ‘supercavity’ is formed, the drag of the body surrounded by the cavity is greatly reduced. This is due to the reduction in skin friction drag, which depends on the viscosity of the fluid the body is traveling through. Skin friction drag is much lower for the interaction between a liquid and a vapor than between a liquid and a solid. The generation of such ‘natural supercavities’ are accomplished through a reduction in local freestream pressure (possible only in closed-circuit water tunnels) or by accelerating the body to an extremely high velocity underwater.

For a natural supercavity, the required cavitation number, usually less than 0.1, requires a speed in excess of 46 meters per second (>90 knots) at a depth one meter. The required velocity increases with depth (Wosnik et al., 2003). From an initially non-cavitating flow, the high speeds required for an underwater vehicle to form a natural supercavity are extremely difficult to achieve. However, a gas supercavity (or an artificial supercavity) can be alternatively achieved much more easily, as described in the next section.

1.2.3. Supercavitation: A limiting case of bubbly flow

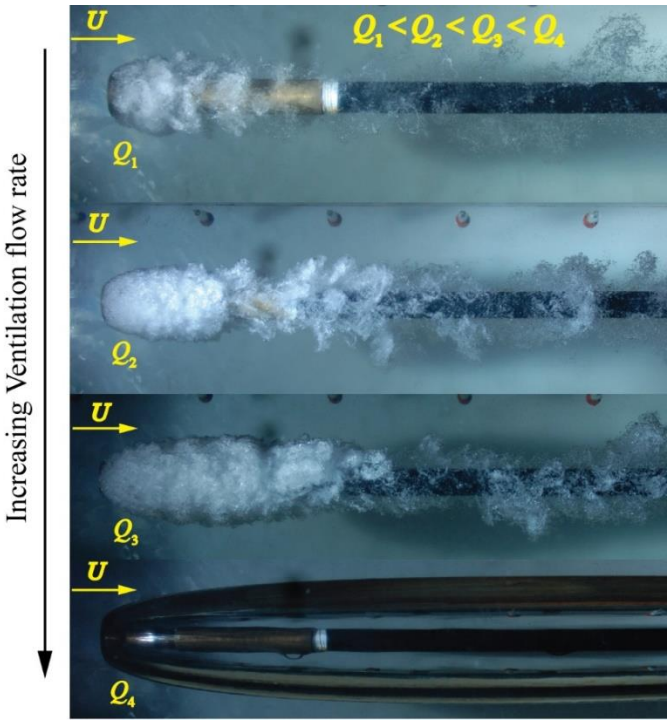

Figure 1.3: Supercavitation as a limiting case of a high-speed bubbly flow

Figure 1.3 demonstrates the concept of attainment of a supercavity beginning from a bubbly flow at the low speeds. In this approach, also termed as 'artificial supercavitation', a non-condensable gas is injected at the rear of the sharp-edge disk cavitator. As gas bubbles enter the flow, these break into individual bubbles resulting in a bubbly flow around the body. However, as the ventilation flow rate of gas is increased, more number of bubbles conglomerate together, resulting in coalescence and a foamy cavity. This foamy cavity gradually transitions into a clear supercavity above a ventilation flow rate threshold. This approach was first suggested by Epshtein in 1944-45

(Epshtein 1975). The pressure of the injected air into the cavity is then used in place of the vapor pressure of the liquid when determining the cavitation number according to

$$\sigma_C = \frac{P_\infty - P_C}{0.5\rho {U_\infty}^2} \tag{1.4}$$

where P_C is the pressure of the air inside the cavity. This is referred to as the ventilated, or artificial, cavitation number. Note that it was pointed out before that the supercavitation can be achieved at small σ (viz. $\sigma < 0.1$) and it was mentioned that the small vales of σ can be attained by two ways, either by reducing P_∞ or by attaining high speeds (i.e. U_∞). However, artificial supercavitation allows us to 'artificially' increase P_C by means of gas injection ($P_C = P_v$ always for a natural supercavity), and consequently attain a low σ. This enables us to attain artificial supercavities even at low U_∞. Natural and artificial cavities are identical at the same cavitation number given that the Froude, Reynolds, and Weber numbers are equal, though this is not often the case (Schiebe and Wetzel 1964, Birkhoff 2012).

1.3. Research Motivation: Underwater ventilated flows

Underwater ventilation refers to the entrainment of an air stream inside water, conventionally employed in a number of applications ranging from aeration in common household aquariums to wastewater treatment, ship hull drag reduction etc. Ventilation technology is involved in a broad range of engineering applications. The current research focusses on two very novel applications of underwater ventilated flows: supercavitation for improved performance of underwater vehicles and bubbly flows for turbine aeration. Both these applications employ bubbles at different size scales: supercavitation regime

deals with bubbles at large size range, whereas small size bubbles are of concern in the bubbly flow regime.

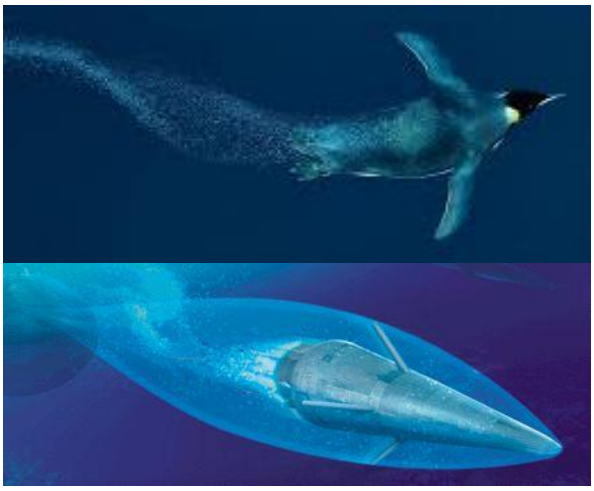

Figure 1.4: Comparison of the underwater motion of a penguin and a supercavitating vehicle. (Source of top and bottom figures: http://ngm.nationalgeographic.com/; http://orbitalvector.com/)

The efficacy of the bubbles in drag reduction can be best illustrated through the fascinating underwater motion of penguins as shown in Figure 1.4. The typical speed of a penguin underwater ranges from 1 – 3 meters/sec. However, when chased by a predator, a penguin can triple its speed in short bursts to escape or launch itself out of water at speeds as high as 9 meters/sec. It performs this neat trick by fluffing its feathers to use air to generate a buffer between their bodies and the water around them. The air entrained in the feathers (during diving) is broken into small microbubbles and covers the majority of the penguin's body, thus allowing the penguin to cruise effortlessly inside an air cavity of bubbles. This is so because the friction drag experienced by a body inside water is significantly higher than the drag experienced in air (compare the ease in moving your hand in and outside water!). Evidently, this is a major bottleneck in the attainment of high

speeds by underwater vehicles as compared to their aerial counterparts (For instance, the speed of a typical commercial airplane is 200 – 300 meters/sec while peak speed of a submarine stands at a mere 13 meters/sec). It is clear then that similar to penguins, the swift movement of vehicles underwater necessitates a large air cavity (also called a 'supercavity') which can envelop the entire vehicle. This is typically done by blowing some non-condensable gas like air or rocket exhaust at the front part of the vehicle body as shown in Figure 1.5**.** This technology, called 'ventilated supercavitation' is of immense promise for naval applications and underwater travel (For more insight, please refer to our research featured in the *WIRED* magazine in 2014).

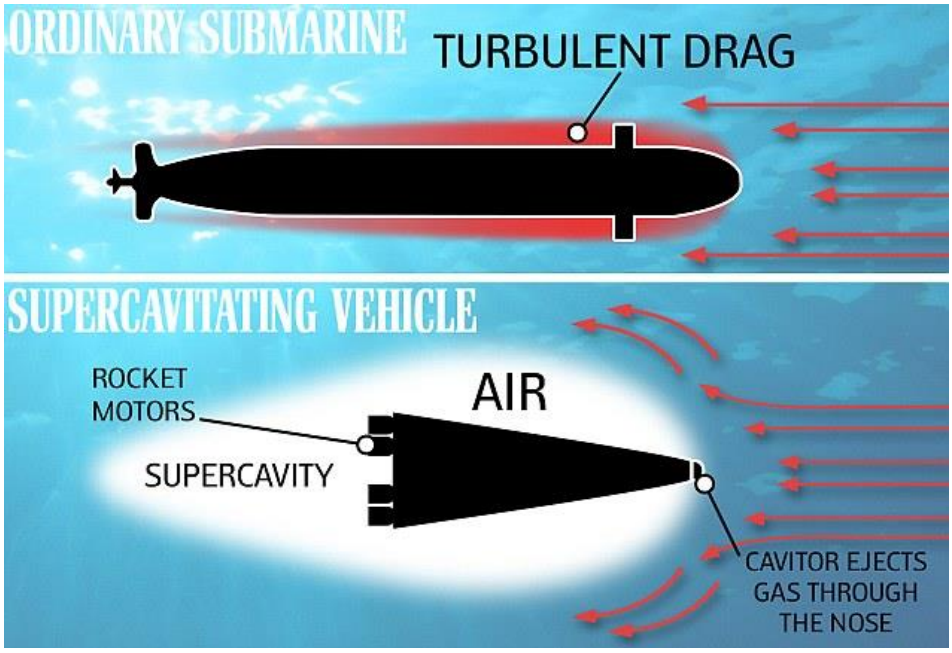

Figure 1.5: Comparison of a conventional underwater vehicle and a supercavitating underwater vehicle (adapted from www.smh.com.au/technology)

However, there are several challenges involved in taking this technology from a concept to reality. The first challenge relates to the prediction of ventilation demand

required to establish a supercavity under different flow conditions. This is crucial since it determines the amount of gas to be carried on-board. The second challenge pertains to the determination of ventilation demand to sustain a supercavity under different sea-states, particularly unsteady state conditions caused due to wave train on the sea surface. The vehicle might encounter unsteadiness at various phases of operation and under variable environments. Such unsteady phenomena can increase the ventilation demand and cause wetting of the body, resulting in increased drag, cavity breakup or even damage to the vehicle. These need to be avoided through a series of control strategies under various flow environments (e.g. vehicle rising or dipping under the ocean, vehicle riding under the effect of surface waves etc.). Such optimal control strategies are governed by distinct factors such as energy efficiency, maneuverability or noise reduction (a supercavity formation suppresses underwater noise caused by the vehicle). Finally, the most important and intricate challenge is vehicle control and maneuverability. Here, total ventilation demand is not the only parameter of interest, but it is of great significance to understand how the ventilation gas distributes itself inside the cavity. This knowledge can enable us to steer the vehicle safely or to further reduce the ventilation demand for maintaining a supercavity, provided the ventilation gas is entrained at some 'strategic' sites of the vehicle. To locate such 'selective' ventilation sites requires an in-depth understanding of the flow and pressure distribution within a cavity under various unsteady conditions. The proposed research envisages a study of the flow inside a cavity in sync with the unsteady cavity pressure measurements to fully characterize such processes and suggest control strategies for the operation of the underwater vehicles. This

is accomplished by studying a supercavity under three distinct regimes: (i) Clear supercavity and its internal flow physics. (ii) Supercavity closure, and (iii) Bubbly wake. Therefore, the first goal of this thesis is to characterize the ventilation demand of a supercavity by studying these three regimes separately and suggest possible control mechanisms for maneuvering the vehicle.

Moving over to the bubble formation and physics at small size scale, my doctoral research also investigates bubbly flow which is relevant for applications in next-generation aerated hydroturbines. Aeration in hydroturbines is of great concern and interest because the water discharged by hydropower facilities is of increasing concern due to its effect on downstream water quality. This decreased water quality arises from two different mechanisms: increased dissolved gases such as nitrogen over high spillways and greatly diminished oxygen content in the water discharged from hydroturbines to the downstream environment. The impoundments necessary for creating the hydraulic head to operate conventional hydroturbines can degrade water quality. The residence time of water within these reservoirs is long and processes such as respiration by aquatic plant and animal life, biodegradation of organic materials in the sediments, oxygen-consuming chemical reactions, etc. can decrease the DO levels, especially at greater depths (i.e. the hypolimnion) within the reservoir. Thermal stratification due to solar heating enhances conditions for low DO in the hypolimnion. Such a system, being hydrodynamically stable, inhibits mixing between layers and isolates the bottom water from atmospheric oxygen. Only surface waters are replenished with oxygen through gas transfer processes resulting from wave action. As shown in Figure 1.6, Hydropower projects often have

hydroturbine intakes located in the hypolimnion where DO levels may drop to anoxic conditions. Hypolimnetic anoxia in turn leads to trace metals, nutrients, and hydrogen sulfide being released from sediments and a drop in the pH of the water endangering fish and other aquatic life in downstream rivers. US Environmental Protection Agency has set minimum standards for dissolved oxygen content in the downstream water.

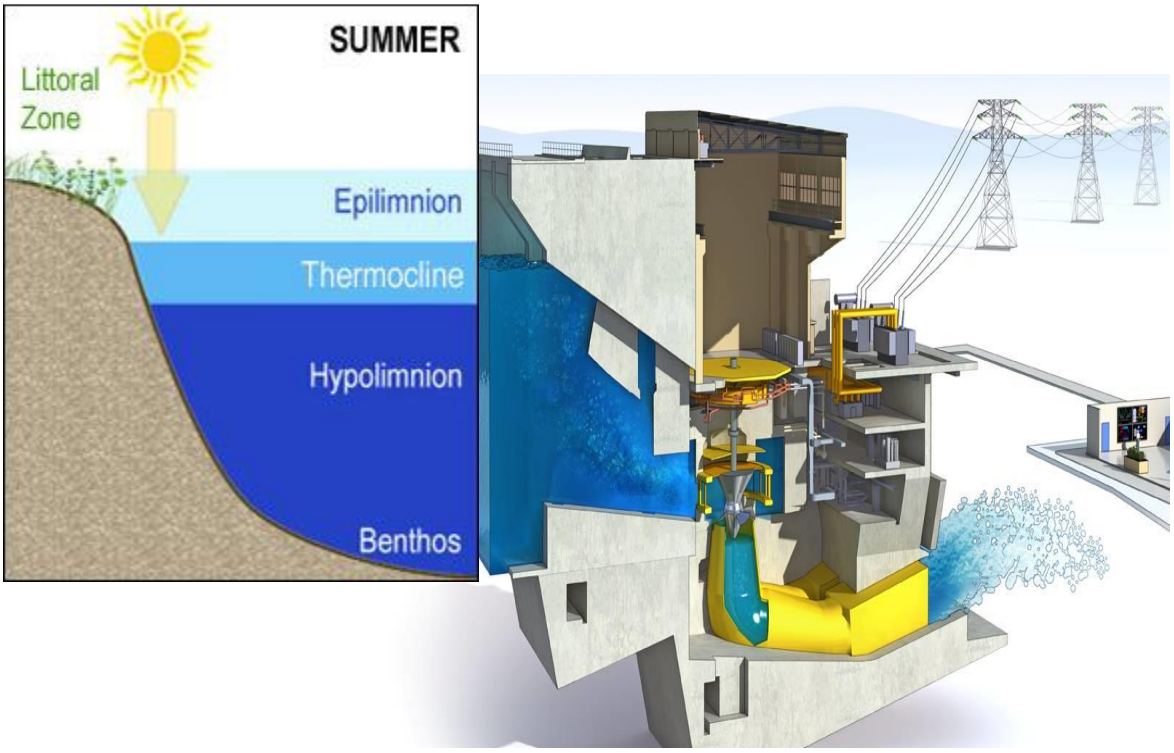

Figure 1.6: Schematic of a hydropower facility along with a schematic showing the stratification caused in the impoundment of water in the summer months

Relatively limited research has been undertaken on optimizing the performance of auto venting systems. Broadly, there are three important factors influencing the performance of an AVT: the quantity of entrained air, the bubble sizes resulting from competing breakup and coalescence processes, and the rate of oxygen transfer from the

bubbles. In the current thesis, these different factors have been investigated in detail, beginning with the development of required measurement and post-processing techniques.

1.4. Thesis Outline

As described in the previous sections, the thesis is divided into two distinct parts (Part A and B), based on the bubble size-regime and its corresponding applications. In the Part - A of the thesis (Chap. 2 – Chap. 5), small-bubble size regime is covered with a focus on aeration applications. Part - B of the dissertation deals with the large bubble size regime for drag reduction of underwater vehicles (Chap. 6 – Chap.9).

In chapter 2, a robust image measurement technique is proposed to measure the bubble size distribution in dense bubbly flows. The proposed technique was implemented to obtain bubble information within a wide size range of 120 μm – 4 mm from the images acquired in ventilation experiments for highly turbulent bubbly flows. The image analysis technique was first validated using synthetic bubble images. A further validation was performed by comparing volumetric airflow rates derived according to the bubble size information obtained using the proposed technique with those measured from a mass flow controller (Karn et al. 2015a).

Chapter 3 provides aeration statistics and capabilities for the NACA0015 ventilated hydrofoil through a series of ventilation experiments in the SAFL High speed water tunnel. Of particular interest are the bubble size distribution, bubble velocity field, void fraction profiles, bubble spread in the wake, number of bubbles and wake width.

Further, a variation in these parameters of the bubbly wake is studied with respect to the Reynolds number, air entrainment coefficient, the hydrofoil orientation and air injection configuration. Finally, a simple numerical formulation is proposed for the bubble sizes in the hydrofoil wake (Karn et al. 2015b).

Next, in chapter 4, we focus our attention on the bubble size evolution in the hydrofoil wake. The mean bubble statistics is measured at different liquid velocities and air entrainment rates, and then the variation in mean bubble statistics is studied at different downstream locations in the wake. The bubble size distributions at different downstream locations have revealed the presence of distinct coalescence-dominant and breakup-dominant regimes. Analytical expressions are derived for the prediction of maximum stable diameter and Sauter mean diameter of bubbles, in the breakup and coalescence regimes, respectively. The observations from high speed imaging provide support for the measurements of bubble statistics, and physical insights into different mechanisms of bubble breakup and coalescence in turbulent wake (Karn et al. 2016a).

Chapter 5 investigates the performance of a water tunnel test-bed for CFD simulations of an auto-venting hydroturbine through the use of a ventilated hydrofoil and simultaneous bubble size and oxygen transfer measurements in the bubbly wake. Bubble-water oxygen transfer is measured by the disturbed equilibrium technique and a one-dimensional gas transfer model is proposed (Karn et al. 2015c).

Part-B of the dissertation concerns with the large bubble size (supercavity) regime. The primary focus of this part of the dissertation is upon the supercavity closure mechanisms, its dependence upon the flow unsteadiness and its relationships with the

ventilation demand. Chapter 6 covers an extremely comprehensive study on supercavity closure mechanisms. Supercavity closure is investigated with an objective to understand the physical mechanisms determining closure formation and transition between different closure modes and to reconcile the observations from prior studies under various flow settings. Subsequently, a physical framework governing the variation of different closure modes is proposed, and is used to explain mode transition upon the change of flow conditions including the blockage effect. This framework is further extended to shed light on the occurrence of closure modes for ventilated supercavitation experiments across different types of flow facilities, the natural supercavity closure and the pulsating supercavity reported in the literature. Finally, combining with a recent numerical study, our research discusses the role of the internal flow physics on the observed features during supercavity formation and closure mode transition, paving the way for future investigations in this direction (Karn et al. 2016b).

Chapter 7 reports the dependence of supercavity closures upon the flow unsteadiness. Our experiments have shown that incoming flow unsteadiness does not only affect supercavity shape but also leads to a change in supercavity closure, irrespective of the presence of a body inside the supercavity. Synchronized high-speed imaging and pressure measurements have ascertained the dependence of supercavity closure on instantaneous cavitation number under unsteady flow conditions. Further, control-volume analysis at the closure shows the intricate relation among the cavitation number, pressure difference occurring at the supercavity closure and the obtained closure mechanisms (Karn et al. 2015e).

Chapter 8 begins with the relationship of supercavity closure with the ventilation demand and hysteresis as pointed out in Chapter 6 and further discusses some interesting gas entrainment behaviors in the formation and collapse of a ventilated supercavity under steady and unsteady flow conditions. Our experiments show that the gas entrainment required to establish a supercavity are much greater than the minimum gas entrainment required to sustain it, and these gas entrainment values depend on Froude (*Fr*) number, cavitator size and the flow unsteadiness. Moreover, the introduction of unsteady gusts causes a slight monotonic increase in the formation and collapse gas entrainment requirements. Our study points out the crucial factors to be considered in the estimation of gas storage requirements for a ventilated supercavitating vehicle (Karn et al. 2016c).

Lastly, in chapter 9, some ongoing work upon the hypothesis presented in the last chapters regarding the role of internal flow physics on the supercavity formation and closure mode transitions is discussed briefly. This chapter discusses the strategies for novel experiments that can provide some insights into the supercavity internal motions and ways to characterize it. Numerous techniques were employed at the SAFL water tunnel to study these internal motions and these have been discussed very briefly. Finally, a need for an image reconstruction approach was realized to reconstruct particle images for Particle Image Velocimetry measurements for such internal motions. Such a reconstruction technique was developed for drops impacting a surface. It is hoped that the integration of the image reconstruction approach along with the flow visualization technique will provide for a robust measurement technique for the characterization of

internal flow structures of a supercavity. Finally, some recommendations for future research are outlined.

Part A: Small Dispersed Bubble Flow Regime

Chapter 2. Development of an Integrative Image Measurement Technique for Dense Bubbly Flows

The measurements of bubble size distribution are ubiquitous in many industrial applications in chemical engineering. The conventional methods using image analysis to measure bubble size are limited in their robustness and applicability in highly turbulent bubbly flows. These flows usually impose significant challenges for image processing such as a wide range of bubble size distribution, spatial and temporal inhomogeneity of image background including in-focus and out-of-focus bubbles, as well as the excessive presence of bubble clusters. This article introduces a multi-level image analysis approach to detect a wide size range of bubbles and resolve bubble clusters from images obtained in a turbulent bubbly wake of a ventilated hydrofoil. The proposed approach was implemented to derive bubble size and air ventilation rate from the synthetic images and the experiments, respectively. The results show a great promise in its applicability for online monitoring of bubbly flows in a number of industrial applications.

2.1. Bubbly flows and characterization techniques

Bubbly flows occur frequently in natural systems and are also used for different applications in petroleum, energy-producing and chemical industries. Some of the common applications involve bubble columns which are used as reactors in a variety of chemical and biochemical processes, e.g. the Fischer-Tropsch process for hydrocarbon synthesis, hydrogenation of unsaturated oil, coal liquefaction, fermentation, waste water treatment etc. (Smith et al. 1996, Lau et al. 2013). Bubbly flows are also ubiquitously found in flotation cells (Sadr-kazemi and Cilliers 1997), aeration studies (Roesler and Lefebvre 1989) and spargers (Geary and Rice 1991) etc. In many of such processes, the accurate prediction of pressure drop and wall heat transfer is necessary, both of which are strongly dependent upon the concentration, spatial distribution and morphology of the bubbles (Kamp et al. 2001). Similarly, in many liquid-gas systems, gases are dispersed in liquids to obtain large interfacial area available for chemical reactions, heat and mass transfer processes. The rate of such processes is characterized by bubble surface area flux which is closely associated with the bubble size distribution (Junker 2006).

Different techniques have been employed to measure bubble size distributions. Broadly, it can be divided into two categories – intrusive and non-intrusive techniques. Both these methods have been extensively reported in the literature – some of the intrusive methods employ capillary suction probes (Laakkonen et al. 2005), conductivity probes (Liu and Bankoff 1993), optical fiber probes (Saberi et al. 1995) and wire-mesh sensors (Prasser 2008), etc. The non-intrusive methods include interferometric particle imaging (Glover et al. 1995), laser Doppler velocimetry (Mudde et al. 1998), extinction

and scattering activity measurement (Zaidi 1998), phase Doppler anemometry (Laakkonen et al. 2005) and other particle-imaging techniques (Tayali and Bates 1990, Adrian 1991, Grant 1997) etc. In general, non-intrusive methods are preferred over intrusive methods which disturb the local flow fields because of the placement of the probes.

Digital image analysis offers many advantages in terms of flexibility, relative insensitivity to the optical properties of the dispersed phase, easier optics alignment as compared to laser-diffraction methods, as well as the capability of providing the velocity and size information of the dispersed phase simultaneously. Thus, it is very convenient and time efficient for online monitoring and analysis of a large number of images. However, to implement this technique for real-time analysis of the bubbly flow images from different engineering applications pose multifarious challenges. These challenges include, for instance, the computational speed for real-time image processing, the ability to cope with the poor quality of images caused by varying intensity characteristics of the background and out-of-focus objects, and the robustness of the technique especially in its capability to resolve overlapped clusters in the high void-fraction flows.

The optical image analysis have been used recently for quantifying the bubble size distribution (e.g. Honkanen et al. 2010, Ferreira et al. 2012, Do Amaral et al. 2013, Kracht et al. 2013, Lau et al. 2013). Generally, due to the excessive coalescence and break-up of bubbles, most of the proposed techniques for bubble image processing produce considerable errors when applied to flows with high superficial gas and liquid velocities. These errors are closely related to the challenge of extracting accurate bubble

information from large clusters due to the coalescence of bubbles. A brief review of these techniques will be presented in section 2.3. Overall, these techniques are still limited in their robustness to resolve large bubble clusters particularly under highly unsteady flows with large void fractions of bubbles. Another limitation of the reported techniques is related to their ability to deal with a wide range of bubble size distribution. In addition, algorithms with significant improvements in computational speed are needed for fast processing of a large number of images and online monitoring of bubble concentration and distribution.

Thus, in the present study, we introduce an integrative image measurement technique to analyze high void fraction bubbly flows with a wide dynamic size range of bubble size. The development of this technique is driven by our recent study on the bubbly wake flows of aerated hydrofoils. This research is focused on developing a test-bed through conducting physical water-tunnel experiments to quantify the dissolved oxygen transfer across bubbles under various flow conditions. The experiments result in a large quantity of varying quality of bubble images with significant clustering due to highly unsteady and complex flows and coalescence of bubbles. These images make it unfeasible to implement prior measurement techniques to achieve fast and accurate image analysis.

2.2. Description of Experimental Setup

The experiments were conducted in the high-speed water tunnel at Saint Anthony Falls Laboratory (SAFL) of the University of Minnesota, which is shown in Figure 2.1. The tunnel has a horizontal test section of 1 m (Length) × 0.19 m (Width) × 0.19 m

(Height) with three sides having plexiglass wall for optical access. The tunnel is designed for cavitation and air ventilation studies and is capable of operating with velocity in excess of 20 m/s. A special design feature of the tunnel provides for fast removal of large quantities of air bubbles generated during cavitation and ventilation experiments, allowing us to conduct bubbly flow experiments for extended periods of time with little effect on test section conditions.

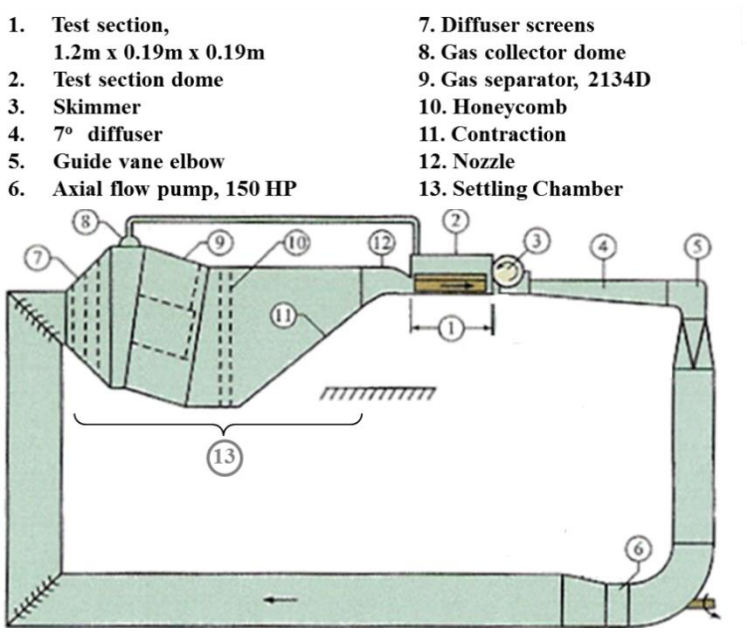

Figure 2.1: Schematic of the SAFL Water tunnel facility

During the experiments, a NACA0015 hydrofoil was installed in the test section with angle of attack (α) of 0°, 4° and 8°. The hydrofoil was 190 mm in span and 81 mm in chord. As shown in Figure 2.2, a narrow spanwise slot allows air to be injected into the flow over the hydrofoil. The full width of the injection slot is used for measurements of oxygen uptake. This results in a dense spanwise bubbly wake. However, in order to make bubble measurements, ventilation was limited to a narrow 9.6 mm slot at the center of the

span. This configuration ensured that bubbles remain mostly within a narrow distance away from the center. Considerable thought was given to obtain a reasonable representative sample of the bubble population that exists when the full span is ventilated. Under this scheme, 45 different experiments were conducted at different water speeds, ventilation gas flow, angles of attack of hydrofoil and the bubbly wake images were obtained at three different axial locations, i.e. 109, 243 and 377 mm from the hydrofoil center. 90,000 bubble images were captured using the SIV technique.

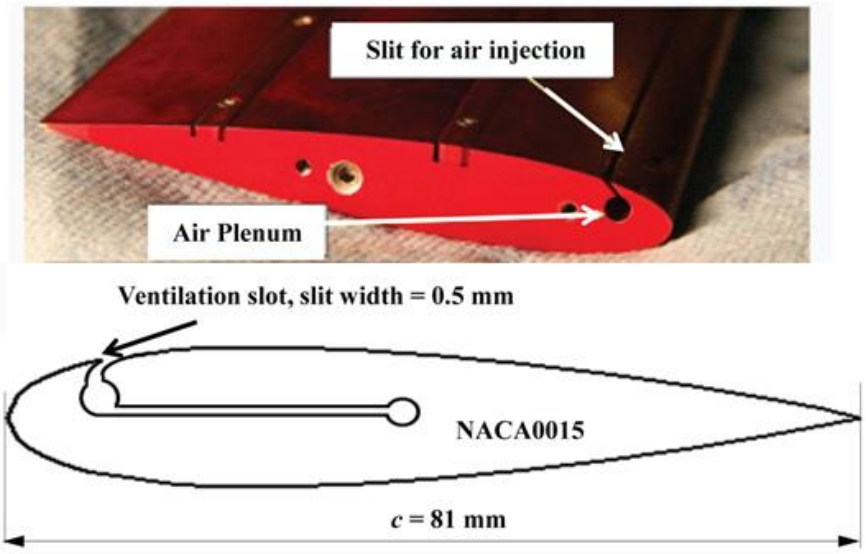

Figure 2.2: Details of the ventilated foil

Shadow Image Velocimetry technique (SIV) is most suited for analysis of bubbly flows. It employs direct in-line volume illumination using low power sources such as LED and an optical setup to produce a narrow depth-of-field for 2D plane imaging (Goss et al., 2007, Broder and Sommerfeld 2007). Figure 2.3 shows a schematic of the experimental setup. A custom-made pulsed LED light source from Innovative Scientific Solutions Inc. was used to illuminate the flow. The pulsed LED array has flash rates up to

10 kHz with a 5 μs pulse width and rise and fall times ~200 ns. To ensure uniform back-lighting in the images, a light shaping diffuser is placed between the light source and the flow, which eliminates noise generated by non-uniform lighting. A 1k × 1k pixel Photron APX-RS camera (capable of 3000 frames/second at full resolution) with a 60 mm lens was used to obtain images.

In the SIV technique, two LED light pulses separated by a short time are synchronized with camera exposure in order to obtain two consecutive images (or, double frames). The first pulse is fired at the end of the first exposure and the next at the beginning of the following exposure. In our experiments, the time duration between two pulses was kept 100-230 μs depending on free stream velocity. Using the obtained image pairs, the instantaneous velocity field of the bubbles was obtained using commercially available Particle Image Velocimetry (PIV) software (DaVis 7.2 from LaVision). The image pairs were captured at a frame rate of 25 image-pairs per second and the exposure time for individual images was kept 15 μs to prevent any blurring in the images. A data set consisted of 1000 image-pairs taken over 40 seconds. The field of view of the captured images was approximately 60 mm x 60 mm. The imaging system was calibrated prior to the beginning of the test program using a 2.5 mm x 2.5 mm grid located at the water filled test section centerline. The calibrated images produced by the test program and used in the analysis described here had a constant (square) pixel dimension of 0.059 mm. As mentioned, this pixel dimension was determined by a grid placed at the test section centerline. The bubble plume exited the foil with a spanwise depth equal to the non-masked slot length of 9.6 mm and spread to at most twice this depth at the

downstream measurement location. This uncertainty of spanwise bubble location translated to a length scale (and calculated velocity) uncertainty of 1.6% near the foil and 3.2% at the downstream measurement location. The image depth of field was determined to be approximately 15 mm. The bubble sizes were in the range of 2 to 68 pixels, which corresponded to a bubble radius of 0.06 to 2 mm.

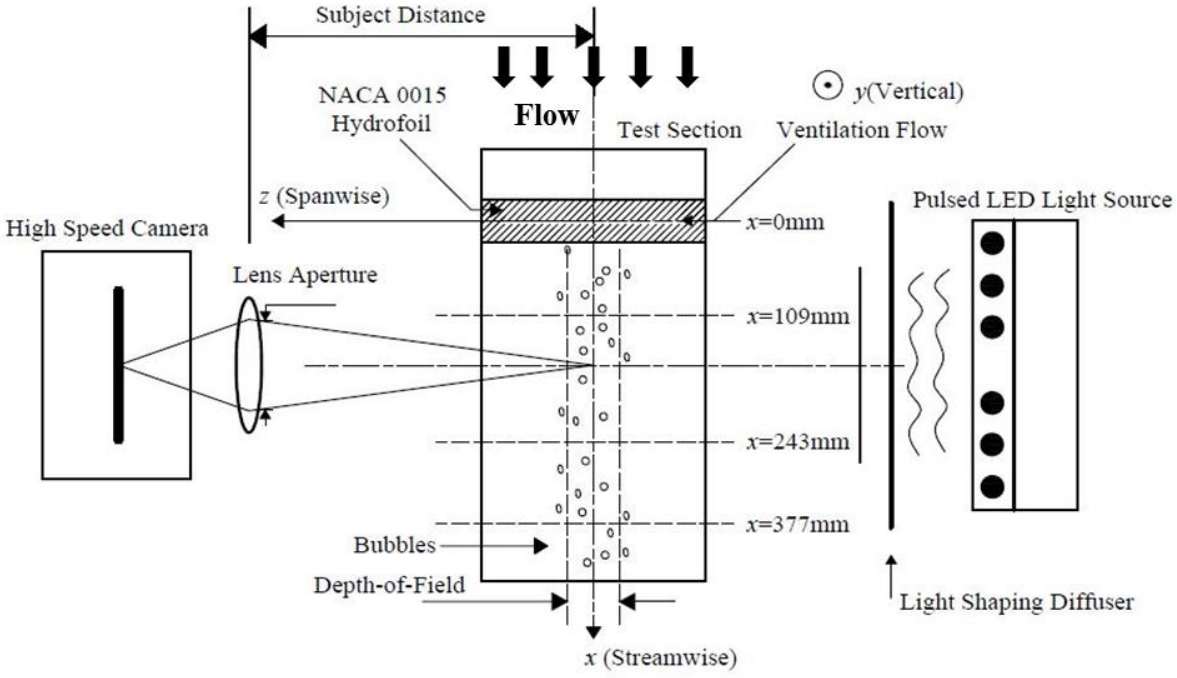

Figure 2.3: Schematic of the experimental setup for shadow imaging of bubbly flows in an aerated hydrofoil wake.

2.3. Overview of the image-processing task

Figure 2.4 presents a sample of the original bubble images obtained from our measurements to illustrate a number of challenges involved in the analysis of our images. These challenges include: (1) the spatial and temporal non-uniformities of the image

background; (2) a wide range of bubble size distribution; (3) the co-existence of in-focus and out of focus bubbles; and (4) the large bubble clusters.

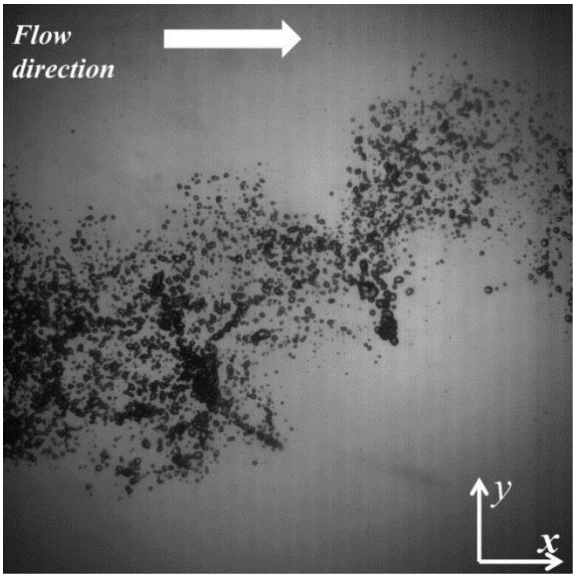

Figure 2.4: A sample of an original bubbly wake image from our experiments

This spatial non-uniformity, shown as a relatively brighter central disk in Figure 2.4, is generated by the non-uniform spatial profile of the LED illumination. The temporal non-uniformity in the background is contributed by the fluctuations of LED illumination, and more significantly, by the fluctuating void fraction of bubbles associated with highly unsteady turbulent flows in the field of view. In our experiments, the high ventilation rate and high Reynolds number turbulent flow enhance the bubble break-up and coalescence, which leads to a large dynamic range of bubbles including micro-bubbles to large clusters of several bubbles. In addition, the complexity and three dimensionality of turbulent flows result in a substantial amount of out-of-focus bubbles.

In our case, the conventional methods reported in the literature to deal with these challenges proved to be inadequate. Usually, a background subtraction can be employed

to compensate for the temporal non-uniformity. However, since the background illumination intensity varies both with location and time, the background subtraction can lead to substantial loss of bubble information. Similarly, the spatial non-uniformity caused by the uneven illumination poses a problem for image filtering using either a global, local thresholding or a combination of both. Specifically, for image-filtering using a local thresholding based on block-processing with a suitable filter function, different filter functions have been used in the literature for the determination of threshold value (e.g. Otsu 1979, Sahoo et al., 1997, Sahoo and Arora 2004). In the current research, these different filter functions were tried on a variety of images, but were found to be unsatisfactory. It was observed that huge variations in the local void fraction in different images rules out the possibility of a single threshold value for every image or even for small local regions in the image.

These drastic differences in the local void fraction can be attributed to the presence of dense bubble clusters. Usually, bubble clusters are very difficult to deal with and require specific approaches for analysis. Sometimes, these clusters are ignored in the analysis by constraint conditions such as sphericity (Bailey et al. 2005) or concavity index (Mena et al. 2005). From a classical image analysis point of view, it is assumed that bubble clusters occur as a non-selective process and ignoring these clusters would not bias the measurement. However, recently Kracht et al. (2013) showed through a stochastic approach that even if the bubble clusters are non-selective, large bubbles are more likely to be present as clusters. Thus, ignoring these clusters in the measurement would bias the estimations. To consider the size of such bubble clusters, some authors

have proposed to approximate the overlapping bubbles through an object recognition approach which fits an ellipsoidal shape to the object areas (Pla 1996, Honkanen et al. 2005). Some other reports have focused upon segmenting these clusters by implementing watershed algorithm (Bonifazi et al. 1999, Lin et al. 2008, Zhou et al. 2010, Zhang et al. 2011, Lau et al. 2013). However, a substantial over-segmentation was observed in many cases upon using watershed transform. Such over-segmentation is usually avoided by suppressing the shallow minima using H-minima transform (Gonzalez and Woods 2004). However, the different variability in the image makes the exact definition of "shallow" minima difficult. In addition, the application of watershed transform requires a pre-processing step to overcome the problems of over-segmentation, which can eliminate small size bubbles in a bubbly flow with a large dynamic range of bubble size. The small size bubbles, because of their large surface area to volume ratio are extremely crucial in our experiments because of their significant contribution to the oxygen transfer as compared to the large size bubbles. Also, there are a large number of small bubbles in the flow field and thus these can't be ignored.

Finally, it was concluded that to effectively extract the bubble information over a wide size range, to overcome the different non-uniformities in the images and to deal with both in-focus and out-of-focus bubbles, a robust and integrative algorithm is needed.

2.4. Proposed image-processing approach

2.4.1. Summary of the algorithm

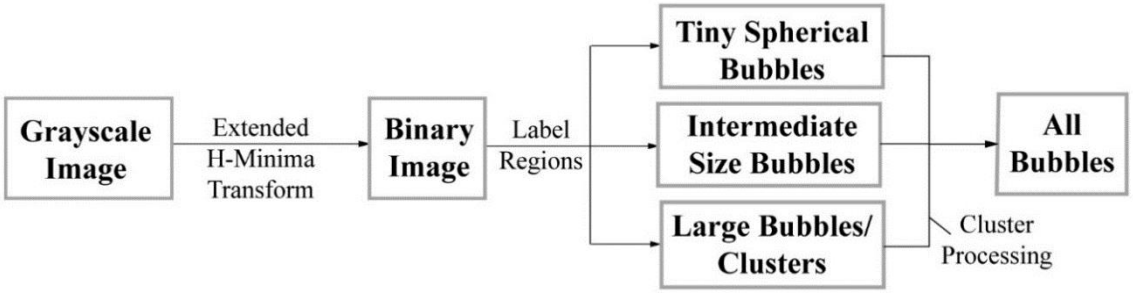

Figure 2.5: Basic outline of the image-processing technique

The proposed approach assumes bubbles are generic ellipsoids and thus the bubble properties such as centroid location, size and shape can be extracted from the projected area of a bubble. Figure 2.5 above shows the basic outline of the image analysis procedure. As shown in the figure, the image analysis consists of three major steps: (1) Image binarization: the original grayscale images are converted into binary images using extended H-Minima transform with a suitable parameter (details presented in Section 2.4.2); (2) Bubble categorization: all the bubble regions are labelled and characterized by their position and a series of metrics including area, centroid, major and minor radius and circularity factor. Based on the area of each region, the bubbles are divided into tiny spherical bubbles, intermediate-size bubbles and large bubbles/clusters. (3) Bubble information extraction: Owing to the different sizes and characteristics of bubbles in the images, a single universal approach cannot be used to extract the size information of all the bubbles. Thus, a multilevel segmentation approach is suggested to extract the maximum possible information from the images. A customized approach referred to as

‘Cluster Processing’ (see Section 2.4.3 for details) was developed using advanced morphological operations and a watershed transform to extract individual bubbles from bubble clusters.

2.4.2. Extended H-Minima Transform

H-minima transform of a grayscale image suppresses all minima in the image whose depth is less than a particular value (Soille 2003). Here, the depth of a minimum refers to the difference in grayscale intensity value of background and the bubble. A unique feature of this technique is that thresholds are applied to the depths of minima and not the grayscale intensity value in itself. Extended H-minima transform is the regional minima of the H-minima transform, where a regional minima is defined as connected components of pixels (8-connected) with a constant intensity value whose external boundary pixels all have a higher value. Thus, the extended H-minima transform of a grayscale image produces a binary image with ‘0’ representing the background and ‘1’ representing the bubble region. It is important to note that the extended H-Minima transform of an in-focus bubble produces a hole in the bubble region owing to the central bright portion in the bubble. Since extended H-minima transform computes the regional minima and does not require a fixed pre-defined global threshold for the grayscale intensity value for conversion of grayscale image to binary image, it is more robust to the variability in the image caused by fluctuations in background illumination intensity and also because of uneven illumination in the background. Also, the binarization process is not extremely sensitive to the depth-of-minima threshold.

2.4.3. Cluster Processing

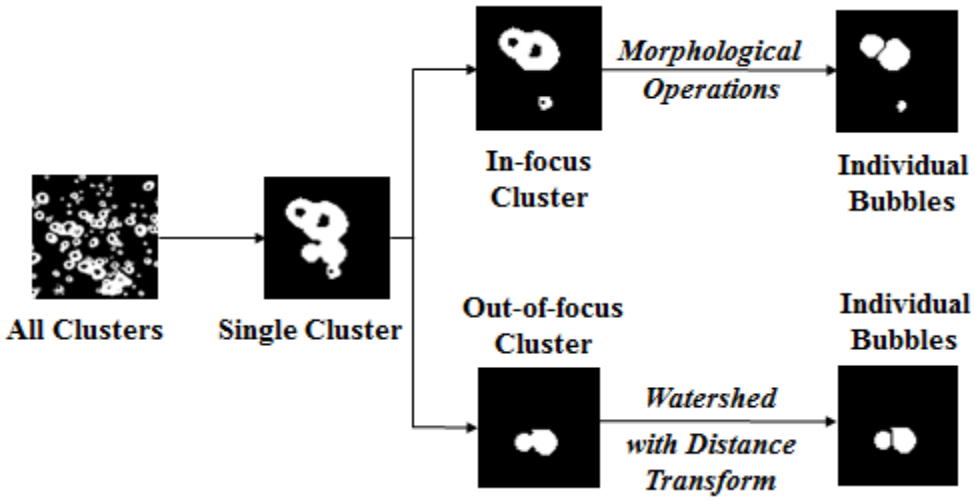

Figure 2.6: A detailed outline of steps in the 'cluster-processing' technique for a hybrid cluster

Figure 2.6 illustrates our approach to extract individual bubble information from bubble clusters. A bubble cluster might contain both in-focus and out-of-focus portions. As shown in Figure 2.6, the in-focus and out-of-focus portions of a bubble can be distinguished by a central dark hole, which is generated from the central bright portion in the original grayscale images of in-focus bubbles (see Figure 2.4). However, for the out-of-focus bubbles, only the bubble boundaries can be traced. It is important to note that the narrow ventilation slot in our experiments ensures that bubbles stay near the depth-of-field of our measurements as discussed in Section 2.2. Based on the characteristic features of in-focus bubbles, a bubble cluster is divided into the in-focus and the out-of-focus portions and different techniques are employed to segment each portion into individual bubbles. Specifically, first, a set of morphological operations are applied to a bubble cluster (shown in Figure 2.6) containing both in-focus and out-of-focus portions.

These morphological operations resolve only the in-focus bubbles and the out-of-focus bubbles are eliminated in the process. Subsequently, the out-of-focus portion is obtained by subtracting in-focus separated individual bubbles from the original bubble cluster and resolved separately into individual bubbles.

Figure 2.7 describes the set of morphological operations that were employed to resolve an in-focus cluster into separate bubbles. First, a single cluster is selected with a bounding box around its centroid. Portions of the other contiguous clusters that fall into this bounding box are eliminated based on an area threshold (Figure 2.7a). The skeletonization of the chosen cluster reduces the foreground regions in the cluster to a skeletal remnant that preserves the shape and connectivity of the original region (Figure 2.7b). This is followed by a morphological 'shrink' operation, which is iteratively performed on the cluster till a point when there is no further change in the skeleton. A shrink operation combined in succession with an area-opening operation removes all the foreground pixels and retains the pixels around the hole. Next, a flood-filling operation was carried out and a complement was taken to obtain a cluster where the boundaries of bubbles are not visible (Figure 2.7c). The bubble skeleton is then superimposed to obtain the separated bubbles (Figure 2.7d). Subsequently, a complement and thicken operation was done to offset the effect of iterative shrink operation and finally obtain the separated individual bubbles (Figure 2.7e, 2.7f). The structuring element size for the 'thicken' operation was chosen in a way so as to ensure that the sum of all separated individual bubble areas equals the total filled area of cluster. Note that, due to inherent nature of the proposed technique there may be an error of a pixel in resolving the boundary between

two different bubbles. Thus, to obtain the actual size of the bubbles, a boundary correction has to be added after the measurements of the bubble size from Figure 2.7f.

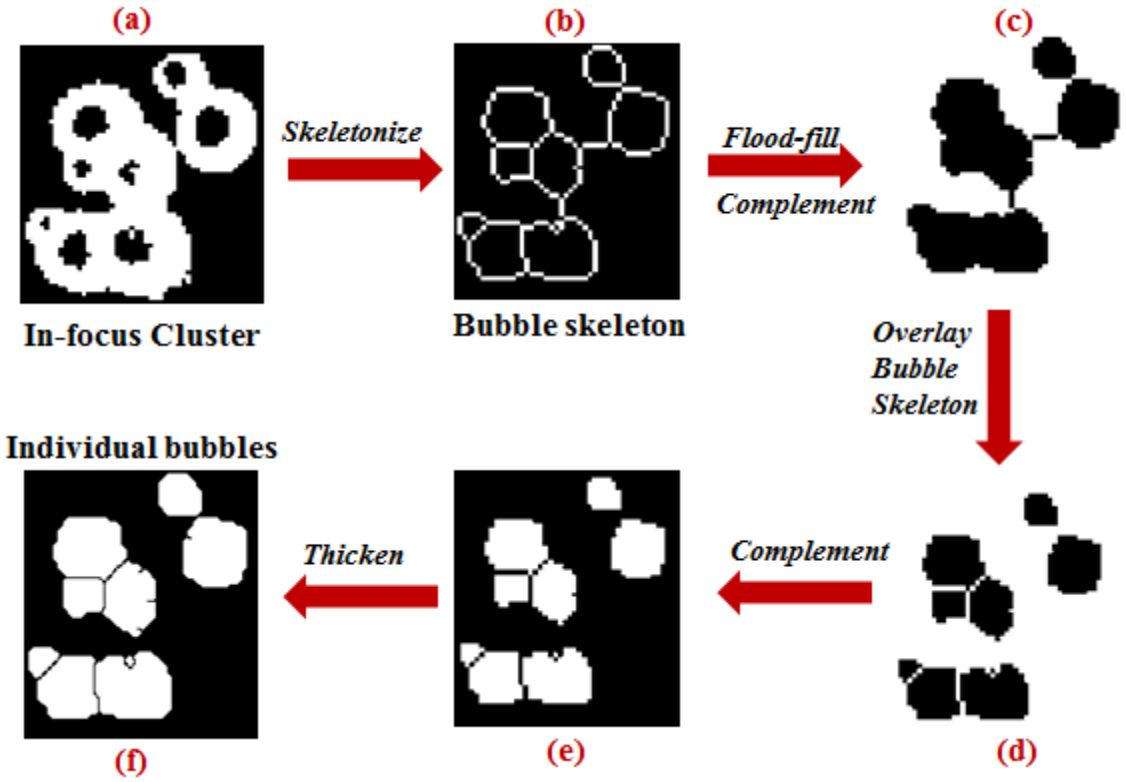

Figure 2.7: Cluster-processing technique for the in-focus bubble clusters

The proposed technique essentially depends on the intensity gradients in the bubbles and is limited in resolving the out-of-focus portions of a cluster where intensity gradients are not clearly visible. For this reason, the out-of-focus cluster is resolved into separate bubbles by employing a different technique: watershed segmentation with distance transforms (Chen et al. 2004). The watershed transform is a region-based segmentation technique originally proposed by Meyer (1994), which is based on an analogy with the flooding of a landscape or topographic relief with water (Lin et al. 2008, Zhou et al. 2010, Zhang et al. 2011). This technique requires pre-processing the images

by edge detectors and smoothing filters and can otherwise lead to over-segmentation (Bonifazi et al. 1999). Considering the different sources of variability in the image, it is difficult to use watershed segmentation to resolve all the different sized in-focus bubbles accurately without sacrificing some small size bubble information. Thus, in the current research, we leverage separate approaches for in-focus and out-of-focus bubbles to extract maximum information from our bubble images.

2.4.4. Bubble size and shape measurements

The bubble information including the centroid location, size and shape is extracted based on the projected areas of each bubble in a bubble image. The bubbles are categorized as being circular or elliptical in cross-section and finally bubble size is measured and converted from pixel to metric values using the magnification of the image.

First, all the bubble regions were grouped into three categories based on size: tiny bubbles, intermediate size bubbles and large bubbles/clusters. Based on the observations in our experiments, it is clear that very small bubbles are almost always spherical, i.e. have a circular projected area in our images. The area threshold for such tiny bubbles was set to 10 pixels. For these circular bubbles, the radius was computed directly from the area measurements (A) as $d = \sqrt{4A/\pi}$. The intermediate size individual bubbles (10-30 pixels) and the bubbles resolved after 'cluster-processing' (> 30 pixels) could have a circular or elliptical projected area. Thus, the bubble shape needs to be determined before the bubble sizes are calculated. The bubble shape is determined by the calculation of Heywood Circularity Factor, defined as $HCF = P/\sqrt{4\pi A}$, where P is the perimeter and A is the area of the region. The Heywood circularity factor is defined as the ratio of bubble

perimeter to the perimeter of a circle of the same area. For each bubble, a Heywood circularity factor was calculated. Note that spherical bubbles have a HCF of unity whereas a square region has a HCF of 1.128. Again, a conservative range of HCF for a circular bubbles was selected to be 0.9 - 1.15. For bubble regions lying within this range of HCF, the radius was determined using the assumption of a spherical bubble. For other bubbles lying outside this range of circularity factor, an ellipse fitting technique proposed by Haralock and Shapiro (1992) was used to determine minor and major axis lengths and the eccentricity of the elliptical projected area.

2.5. Results and Validation

The proposed image processing technique was validated using both synthetic bubble images and air ventilation rate measured from the experiment.

2.5.1. Validation through synthetic bubble images

To quantify the precision of bubble size and shape capture, we first implement our approach to synthetic image of a single bubble. Then, polydispersed bubble images that simulate the bubble distribution in our experiments are generated to test the effectiveness of our approach in extracting bubble information from large bubble clusters.

2.5.1.1. Synthetic bubble generation procedure

The synthetic bubble images are generated using an ensemble of randomly distributed ellipses. The size, eccentricity and orientation of the elliptic objects are also randomly selected within the range of bubble characteristics measured from the experiments. As illustrated in Figure 2.8, an intensity profile, approximated using the quadratic function below, is superimposed on each ellipse to reproduce the intensity

profile of bubbles from the experiments. The intensity at any radial position, r is defined by the quadratic:

$$I = ar^2 + b \tag{2.1}$$

where,

$$a = \frac{(I_\mathrm{m} - I_\mathrm{i})}{R^2}\,; b = I_\mathrm{i} \qquad if\ |r| < R$$

$$a = \frac{(I_\mathrm{b} - I_\mathrm{m})}{(R_2^2 - R^2)}\,; b = I_\mathrm{m} - \frac{(I_\mathrm{b} - I_\mathrm{m})R^2}{(R_2^2 - R^2)} \qquad if\ R_2 > |r| > R$$

I_m , I_i and I_b correspond to different fixed pixel intensity values in a bubble image as shown in Figure 2.8. I_m refers to the minimum intensity in the bubble cross-section, I_i is the intensity of the central bright portion of the bubble and I_b refers to the background intensity of the bubble images. The bubble radius is given by: $R_2 = R + w$, where w is bubble width. The bubble centroid is chosen as the origin of the co-ordinate system. Thus, a generic elliptical synthetic bubble image was synthesized with the prescribed intensity profile that matches that of an actual bubble.

2.5.1.2. Single bubble measurement

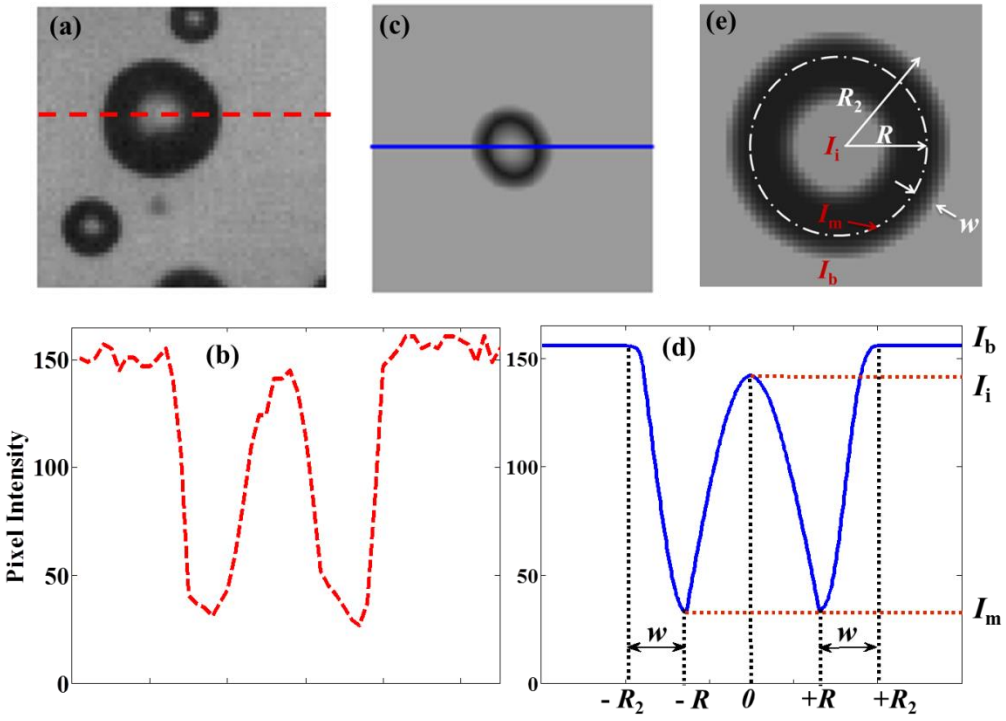

Figure 2.8: (a) An actual bubble image and (b) its corresponding intensity profile is used to replicate (c) a synthetic bubble image and (d) its intensity profile. (e) A synthetic bubble image showing different parameters involved in bubble generation.

To validate the proposed image analysis algorithm, we employ a methodology similar to that reported by Lau et al. (2013). First, we apply the image processing algorithm on single synthetic bubbles for different sizes and shapes (i.e. circular and elliptical). An elliptical shaped bubble is drawn with a specific radius in pixels and its centroid is placed in the middle of a pixel (0.5 pixel, 0.5 pixel). Subsequently, 50 new bubbles with same size and shape are generated with its centroid translated with steps of 0.01 pixel in both *x* and *y* direction. For each translation, the image analysis algorithm calculates the bubble equivalent radius and the percentage error in measurement of

bubble area-equivalent radius is calculated. The bubble area-equivalent radius is the geometric mean of the minor and major radius of a bubble. The average size and range is presented as error bar in Figure 2.9. The same process is repeated for bubbles of different radius ranging from 5 to 105 pixels and for both elliptical (eccentricity = 0.6) and circular bubble shapes. Figure 8 presents a comparison of the error in radius measurement for the circular bubbles, elliptical bubbles and the maximum possible uncertainty in the measurement estimated by Lau et al. (2013).

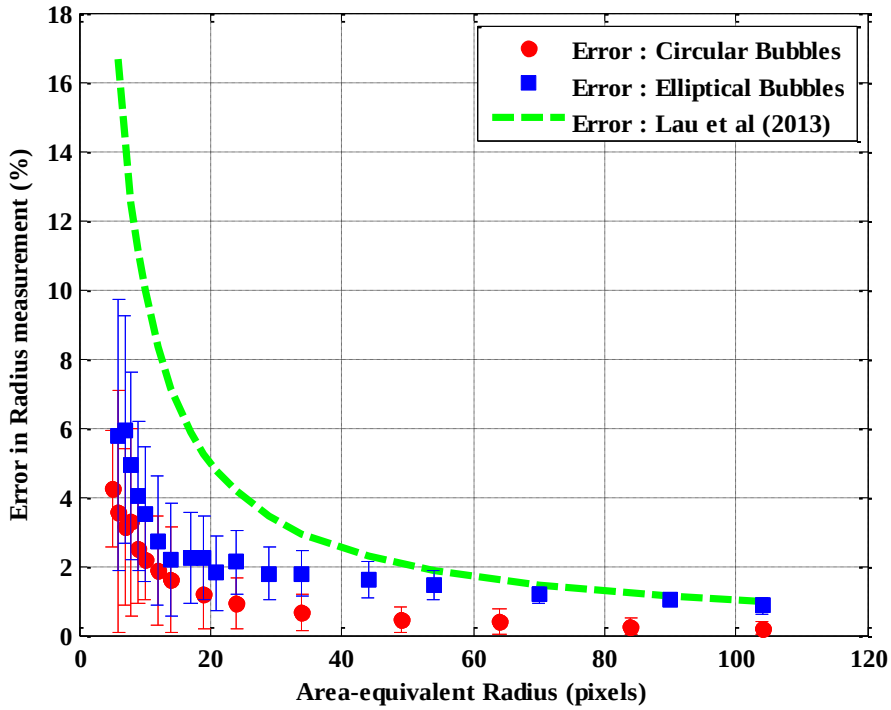

Figure 2.9: Error in radius measurement of a single bubble for both circular and elliptical bubbles (eccentricity = 0.6). Green line shows an estimate of the error which was mathematically obtained by Lau et al. (2013). The dots show the mean error whereas the error bars show the maximum and minimum errors.

For both circular and elliptical bubbles, it was observed that as the area-equivalent radius increased, both the absolute error in the measurement of the bubble size and the

uncertainty decreased. The mean error in the size measurement of a single circular bubble decreased from 4.22 % at a radius of 5 pixels to about 0.21% at a radius of 104 pixels. The errors in the measurement of an elliptical bubble were found to be slightly greater than the circle with same area-equivalent radius. The mean error in the measurement of an elliptical bubble varied from 5.77% at an area-equivalent radius of 6 pixels to 0.84% at an area-equivalent radius of 104 pixels. For the same area-equivalent radius, the larger uncertainty associated with the elliptical bubble compared to a circular bubble can be attributed to the greater uncertainty involved in the measurement of the minor radius of elliptical bubble, which is smaller than the area-equivalent radius. The uncertainty in the measurement of the bubble size can be caused by many factors such as inhomogeneous background illumination, and background fluctuations due to out-of-focus bubbles etc.

2.5.1.3. Polydisperse bubble size distribution measurement

To further validate the effectiveness of the image-processing approach to extract the individual bubbles from bubble clusters, we applied our analysis technique to synthetic bubble images resembling the bubble distributions from our experiments, with average number of bubbles exceeding 500 and void fraction ranging from 0.1 to 0.7. Figure 2.10a shows a sample of a synthetic bubble image with 900 bubbles. The bubbles were randomly placed in a 1024 × 1024 pixel grid and the bubble eccentricity was randomly chosen between 0 and 0.9, which is the range of eccentricity of bubbles observed in our experiments. The results after the image processing are illustrated in Figure 2.10b. The red and cyan ellipses denote the in-focus and out-of-focus large bubbles/clusters respectively (the bubbles segmented by the cluster-processing step), the

yellow ellipses correspond to the intermediate size bubbles and the magenta dots correspond to tiny spherical bubbles. As the figure shows, all the bubbles are well segmented and the clusters are mostly very well resolved.

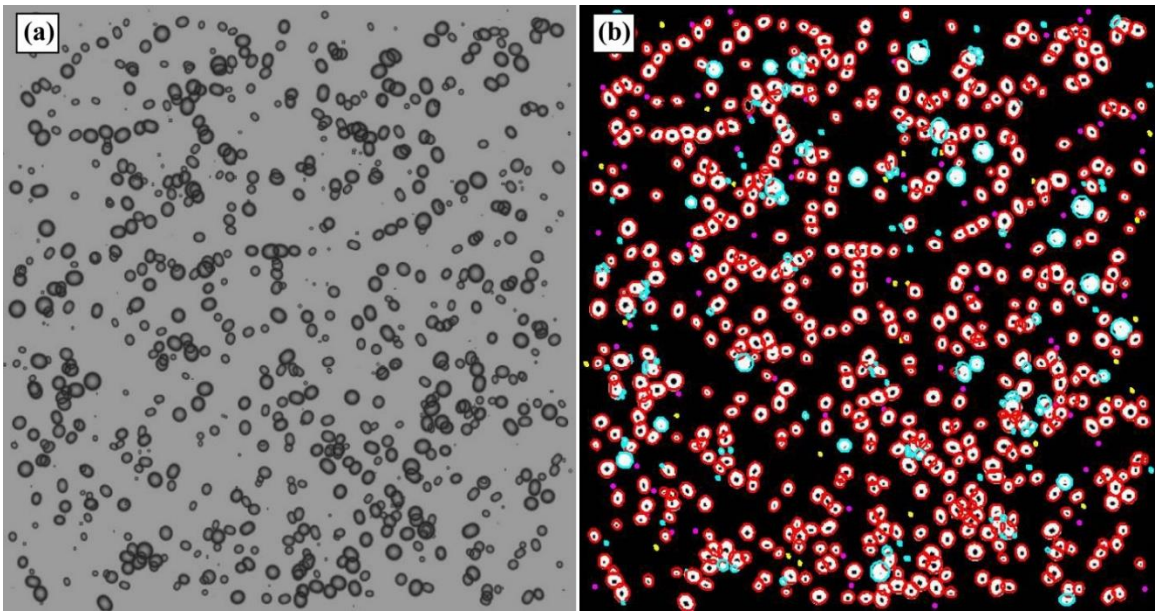

Figure 2.10: (a) A synthetic bubble image and (b) the corresponding output from the described image-processing algorithm

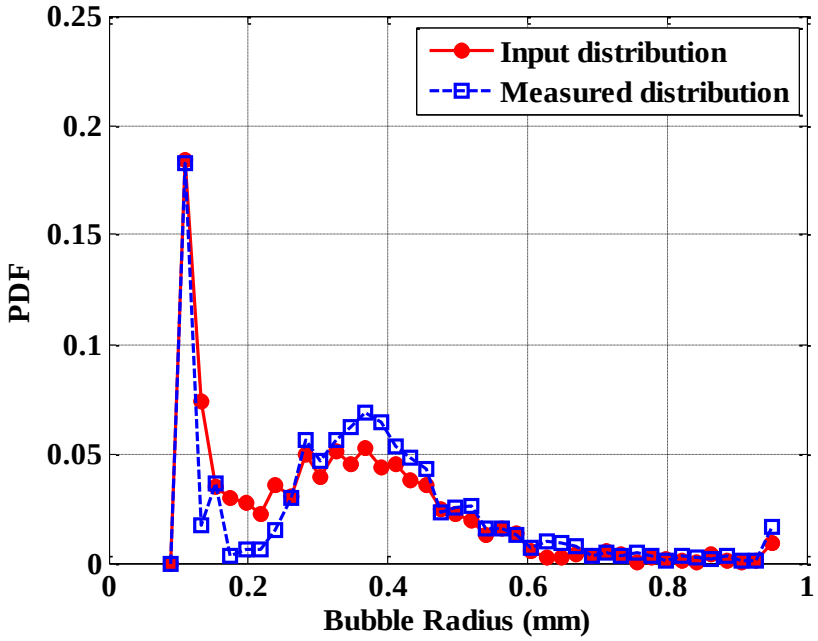

Figure 2.11: PDFs of bubble size distribution

A more quantitative assertion of the efficacy of the current approach is provided by a comparison between the probability density function (PDF) of the actual input bubble size distribution and the PDF obtained after applying the image analysis algorithm to the synthetic bubble image as shown in Figure 2.11. The input bubble size distribution was a bimodal distribution with peaks at 0.1 and 0.4 mm, which correspond to a radius of 2 pixels and 8 pixels, respectively. In general, the output PDF from our image analysis showed a good match with the input fraction of bubbles at different sizes, although a slight deviation can be observed for the intermediate bubbles in the bubble radius range of 0.15 – 0.45 mm. In addition, the image-processing algorithm captures the bimodal distribution quite well and the magnitudes in the PDFs are in good agreement.

A more comprehensive assessment of our approach is provided by implementing it on bubble images generated with different void fractions in the range of 0.02– 0.66 and comparing the Sauter mean diameters (d_{32} or SMD) obtained from our analysis with the input. According to Ferriera et al. (2012), the SMD is a significant scale for characterizing mass transfer during the interfacial processes, which is defined as

$$SMD = \frac{\sum_{i=1}^{N} n_i d_i^3}{\sum_{i=1}^{N} n_i d_i^2} \tag{2.2}$$

where,$d_i = \sqrt{a_i b_i}$, a_i and b_i are major and minor axis lengths of the bubble projected area, n_i is the number of bubbles with a particular diameter d_i and N is the total number of bubbles in an image. In general, an increase of SMD corresponds to a decrease of surface-to-volume ratio and implies an increasing portion of larger size bubbles in the image. Hence, as the number of large bubbles in the image increased leading to a change in void fraction from 0.02 to 0.66, the actual SMD increased from 0.21 to 0.71 mm. Bubble images were synthesized with different void fraction values. As the void fraction increased, there was greater overlap between bubbles. For each of these synthesized images, the actual SMD is calculated as the SMD of all the bubbles in the image. Then, the image-processing algorithm was applied and the SMD of all the detected bubbles is calculated. Then, this measured SMD is plotted against the actual SMD for all the images and is shown in Figure 2.12. As it shows, the measured SMD is in good agreement with the input results with errors staying within 6-8%. This uncertainty in the measurement can be attributed to the limitation of the image-processing algorithm to accurately resolve

highly overlapping bubbles, particularly when individual bubbles completely overlap with clusters, and also to the errors due to non-uniformity in the image background.

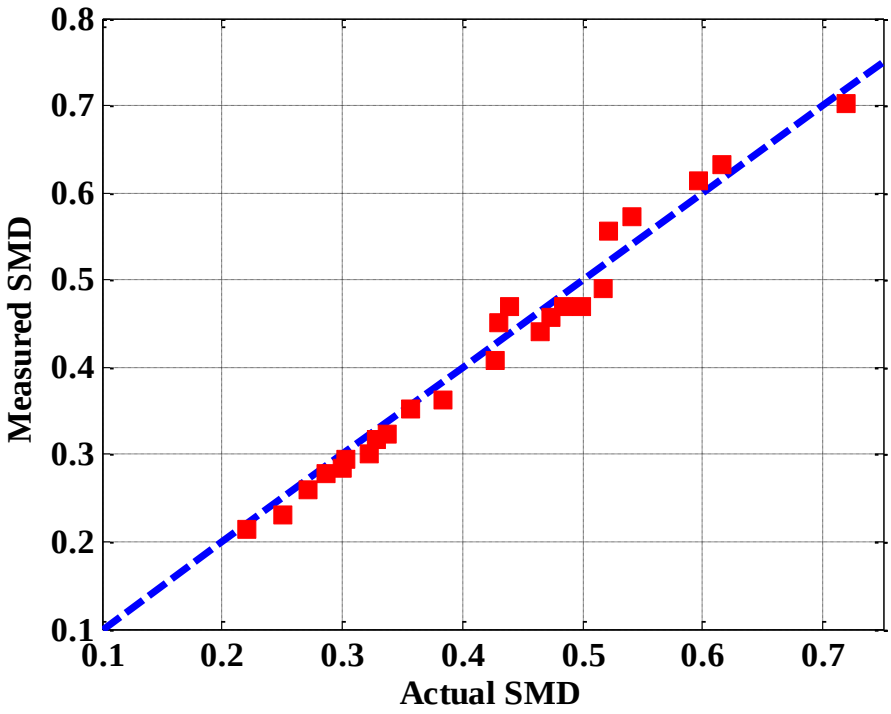

Figure 2.12: Comparison of actual and measured SMD obtained from synthetic bubble images (The line has a slope of unity)

2.5.2. Experimental validation of the image-processing approach

The bubble information extracted from our image analysis can be used to estimate the ventilation flow rate during the experiments, which can be compared with the ventilation rate measured from the mass flow controller to validate the efficacy of our image analysis technique. Note that for this comparison, air absorption in the bubbly wake is neglected considering the small time-scales (< 1s) between air injection and image capture. For such a small time-scale, gas transfer measurements in the bubbly

wake indicate a maximum possible increase in dissolved oxygen concentration to be 10^{-5} ppm. Thus, the mass flow rate of air at the two locations can be considered almost equal.

The estimation of ventilation rate from bubble images consists of three steps: (1) extract 2D bubble size information, (2) obtain the volume and velocity of individual bubbles, and (3) calculate the volume flow rate from the volume and velocity information of all the bubbles accounting for the changes in pressure and temperature.

In the first step, the extraction of 2D bubble information is accomplished by the proposed image-processing technique. In this step, the semi-major axis (a) and semi-minor axis (b) lengths of the elliptical bubbles are determined. Second, an elliptical bubble is rotated around its major axis to obtain a prolate spheroid or an ellipsoid of revolution. Then, the volume of this prolate spheroid can be mathematically determined as $(4\pi/3)b^2a$. Figure 12 presents the mean streamwise velocity of bubbles in the wake obtained using SIV technique as described in Section 2. As it is shown in Figure 2.13, the bubble velocity remains almost uniform in the wake, varying within 5% of about 5 m/s. It is noteworthy that a non-symmetric velocity field is observed with higher velocity above the centerline since the ventilated air is injected from the pressure side of the hydrofoil located below the centerline.

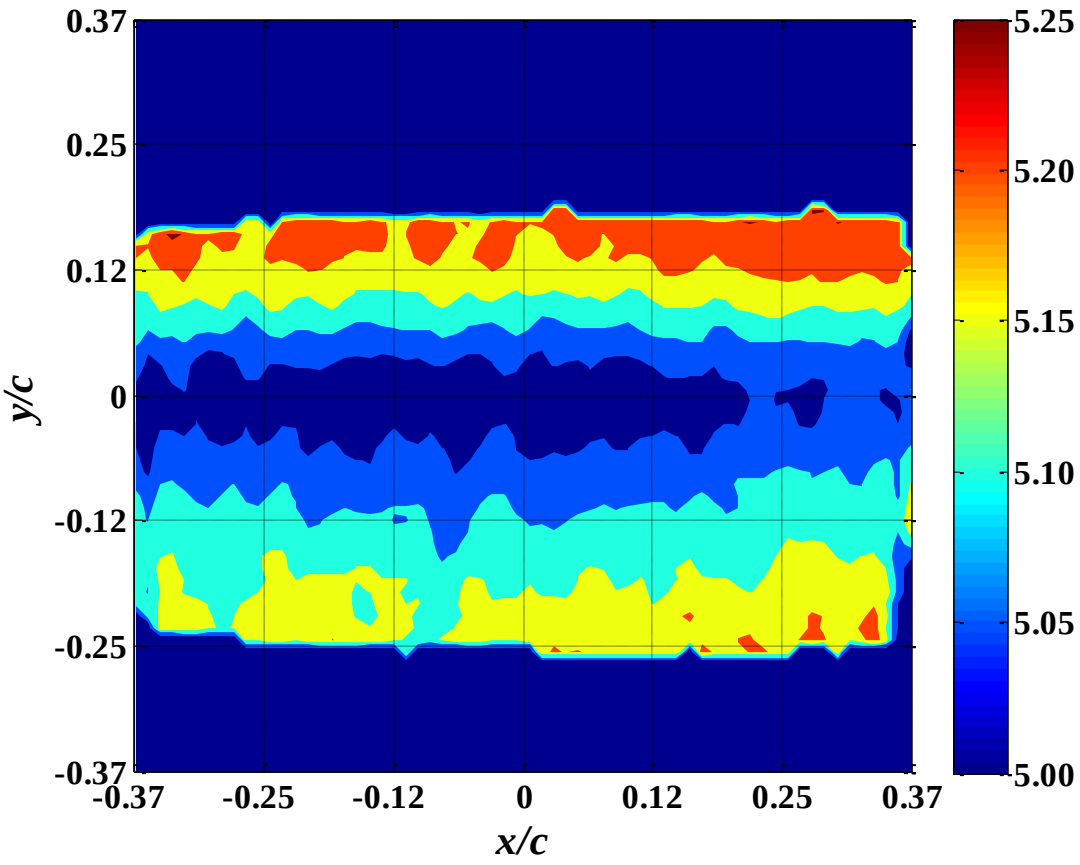

Figure 2.13: The mean horizontal velocity field obtained using SIV technique (The origin in this contour plot is located at a distance of 377mm from hydrofoil center of rotation). The units on the colorbar on the right are m/s.

Finally, in the third step, the volume and velocity information of all the bubbles are used to calculate the volume flow rate. To compare with the corresponding volumetric flow rate at standardized temperature and pressure as obtained from the mass flow controller, the volume flow rate measured from bubble images is adjusted with respect to the pressure and temperature in the test-section. It is expected that if the ventilation flow rate is measured at any downstream location in the wake based on the bubble images, the measured ventilation flow rate should match the ventilation rate actually introduced in the flow. In our experiments, the images were captured at three

different downstream locations and the ventilation flow rate was measured at all three locations. Finally, steps 1 and 2 are repeated for all the bubbles to obtain a predicted flow rate for one single image. This expression is given by

$$\dot{Q}_{total} = \frac{\beta^3}{M}\sum_{k=1}^{M}\dot{Q}_{single,k} \tag{2.3}$$

$$\dot{Q}_{single} = \sum_{i=1}^{N}\left(\frac{u_i}{w}\right)\left(v_i \times \frac{P_{TS}}{P_0} \times \frac{T_0}{T_{TS}}\right) \tag{2.4}$$

$$v_i = (4\pi/3)a_i b_i^2 \tag{2.5}$$

where M and N denote number of images over which averaging is done (M = 1000 for our experiments) and the total number of bubbles in a single image, respectively. β represents spatial resolution and *w* refers to the width of a single bubble image (1024 pixels or 60 mm). u_i and v_i signify velocity and volume of individual bubbles, respectively. Finally, P_0 and T_0 correspond to ambient temperature and pressure, and P_{TS} and T_{TS} are corresponding test-section conditions. The volume flow rate is averaged over all the 1000 images to obtain the mean ventilation rate. Figure 2.14 below shows the measured mean ventilation rate values at each of the three different downstream locations:

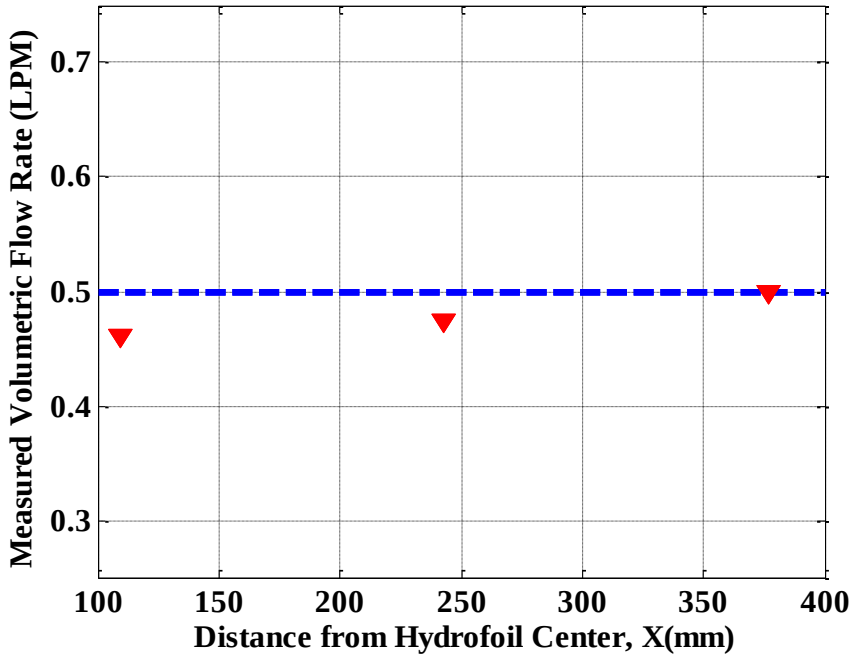

Figure 2.14: The measured volumetric flow rates as a function of downstream distance in the bubbly wake compared with the input flow rate of 0.5 SLPM

As the figure above shows, the measured mean ventilation volumetric flow rates compare well with the actual volumetric flow rate of 0.5 SLPM., with the difference within 9% of the actual value at all the three downstream locations. As the clustering phenomena reduces downstream away from the hydrofoil, the mismatch decreases to less than 1%. Larger mismatch occurring closer to the hydrofoil is likely to be associated with the higher uncertainty in extracting bubble information from very dense bubble clusters. The clustering of the bubbles underestimates the volumetric flow rate. This indicates that the accuracy of the image processing technique decreases with excessive clustering.

2.6. Conclusions

In this chapter, a robust image measurement technique is proposed to measure the bubble size distribution in dense bubbly flows. The proposed image analysis technique

divides all the bubbles into different categories including bubbles within different size range and bubble clusters based on bubble morphology and size. The bubble clusters are passed through an additional step that resolves clusters into individual bubbles. Based on the intensity gradient at the center of individual bubbles, a bubble cluster is divided into in-focus and out-of-focus portions, which are subsequently segmented using 'cluster-processing' and watershed segmentation with distance transform, respectively. We implement the proposed technique to obtain bubble information within a wide size range of 120 μm – 4 mm from the images acquired in ventilation experiments for highly turbulent bubbly flows. The image analysis technique was first validated using synthetic bubble images. A further validation was performed by comparing volumetric airflow rates derived according to the bubble size information obtained using the proposed technique with those measured from a mass flow controller.

As the result shows, the image analysis approach is able to capture the size, shape and location information of both in-focus and out-of-focus bubbles from bubble shadow images acquired using SIV technique. In our experiments, the bubble eccentricities largely varied from 0 to 0.9 and the technique was found to be robust enough to accurately resolve the overlapping bubble clusters in this range of bubble eccentricity. Further, the image analysis approach was also applied to simulated bubble images which had some overlapping elliptical bubbles with high eccentricity ($0.95 < e < 1$) and the results proved the efficacy of the image analysis approach in resolving such clusters. Although the proposed approach was found to work well at a wide range of void fractions (0.02 – 0.7), it was found that as the bubble clustering reduced, the accuracy of the

technique to resolve the bubble clusters increased. Last but not the least, the proposed image analysis technique is computationally efficient. For instance, using an Intel® Core™ i5-3320M (2.60 GHz, 4 GB Memory) processor, the average processing time per image ranged from 3 – 10 seconds. Therefore, with further development on the parallelization of the algorithm over multiple cores, the proposed technique will allow real-time monitoring of bubble distribution for a wide range of industrial applications. The proposed technique can be broadly applied to bubble characterization in different experimental facilities (e.g. inclined, vertical channels, etc.), as well as other types of two-phase flows such as sprays, drops and froth to quantify void fraction, gas hold-up and size distribution of the dispersed phases. In the next few chapters (under Part A), the developed image analysis technique is employed for the measurement of bubble size distributions.

Chapter 3. Characterization of the turbulent bubbly wake of a ventilated hydrofoil

The use of aerating hydroturbines to mitigate the problem of low dissolved oxygen in the discharge of hydroelectric power plants has recently attracted a lot of attention. The design of a ventilated hydroturbine requires a precise understanding of the dependence of the operating conditions (viz. liquid velocity, air ventilation rate, hydrofoil configuration etc.) on the bubble size distribution generated in the bubbly wake and the consequent rise in dissolved oxygen in the downstream water. In the current research, experiments are conducted in the wake of a ventilated NACA0015 hydrofoil by systematic variation of hydrodynamic conditions allowing for quantitative analysis of aeration statistics and capabilities for turbine blade hydrofoil designs. The data concerning bubble velocity distributions, bubble locations and size distribution, void fraction etc. are reported for a chosen reference case. In addition, trends in the variation

of bubbly wake are explored particularly in the light of wake physics. It is found out that an increase in Reynolds number (*Re*) led to greater breakup, while an increase in normalized air ventilation rate (C_Q) favored greater coalescence events in the wake. Further, the PDF($\tilde{d}$) of the normalized bubble size $\tilde{d} = d/d_{32}$, where d_{32} represents Sauter mean size distribution, is found to have a universally similar shape independent of either *Re*, C_Q or hydrofoil angle of attack.. Finally, a numerical formulation is proposed for the bubble sizes in the hydrofoil wake. This rich dataset will also contribute to the development of a numerical turbulence model, to investigate turbulence effects on bubble size distribution and predict the rate of air entrainment and the oxygen transfer occurring in the wake at different hydrodynamic conditions.

3.1. Relevance

Over the past few decades, environmental concerns have broadly affected the electric power industry, including the depletion of fossil fuel supplies, the potential of global climatic changes and challenges involved in long-term nuclear waste management (March et al. 1992). In response to such concerns, the electric power industry has increasingly focused attention on renewable non-polluting energy technologies such as hydroelectric power. Hydroelectric power generation is clean, inexpensive and reliable and does not significantly pollute the land, air or water. However, environmental problems resulting from the discharge of water with low dissolved oxygen (DO) levels are a concern at many hydroelectric facilities. The problem of low DO is well documented in the literature (Ruane and Hauser 1993) and a variety of methods have been suggested to provide dissolved oxygen (Bohac and Ruane 1990). The low DO water

when released to the river downstream can adversely affect the aquatic habitat and contribute to other water quality problems viz. dissolution of trace metals, formation of hydrogen sulfide and depression of pH (Wilhelms et al. 1987).

One of the most attractive techniques currently being investigated to mitigate low DO while maintaining operation efficiency, is the use of an auto-venting turbine (AVT). AVT is a self-aspirating hydroturbine designed to aerate the turbine discharge through ports located at low pressure regions which are open to the atmosphere. When air is allowed to flow through these ports, it breaks down into small bubbles by the high velocity and turbulence of the water flow through the turbine. DO transfer is augmented by the high interfacial area of these bubbles and the level of turbulence in the water (Thompson and Gulliver 1997).

To maximize the DO transfer in the flow through AVT, the knowledge of the bubble sizes of the entrained air at different locations in the bubbly wake is extremely important. The size of bubbles in the wake are a result of different bubble breakup and coalescence processes which consequently affects the gas transfer at different downstream positions. Ultimately, it is desired to have a numerical turbulence model to investigate turbulence effects on bubble size distribution and predict the rate of air entrainment and the oxygen transfer occurring in the wake at different hydrodynamic conditions. The accurate prediction of bubble sizes in the wake at a given flow field is imperative for the prediction of oxygen transfer occurring in the wake. However, both for the operation and validation of such a computational model, there is a desperate need for a high quality experimental dataset that can provide information on bubble sizes and void

fraction in the wake, pressure at the air entrainment location and the rate of oxygen transfer. To the best of our knowledge such relevant experimental reports on the bubbly wakes are scarce.

Thus, in the current chapter, a series of ventilation experiments are reported at several hydrodynamic conditions at the Saint Anthony Falls Laboratory (SAFL) water tunnel, allowing for quantitative analysis of aeration statistics and capabilities for turbine blade hydrofoil designs. SAFL has pioneered the study of bubble wakes (Kjeldsen et al. 2000, Arndt et al. 2007) and has several hydrofoil designs specifically modified for ventilation studies. In the present study, a systematic investigation into a bubbly wake is being carried out at multiple hydraulic operating conditions such as different air ventilation rates, liquid velocities, hydrofoil configuration etc. to serve as a test-bed for computational turbine aeration programs. The data concerning bubble velocity distributions, bubble locations and size distribution, void fraction etc. are obtained. In addition, some simple numerical formulations are proposed for the bubble sizes in the hydrofoil wake.

3.2. Experimental Setup and Conditions

The experimental setup used is already described in Chapter 2. The two NACA 0015 hydrofoils used in our experiments had a span and chord of 190 mm and 81 mm, respectively. As shown in Figure 3.1, the first hydrofoil tested had its air injection slot located near the leading edge (also referred to as ‘Leading Edge Ventilated Foil’ or ‘LEV Foil’ or Reference Foil), on the suction side when the angle of attack is non-zero. The second NACA 0015 aerating hydrofoil configuration had its air injection slot centered on

the trailing edge of the foil (also referred to as ‘Trailing Edge Ventilated Foil’ or ‘TEV Foil’).

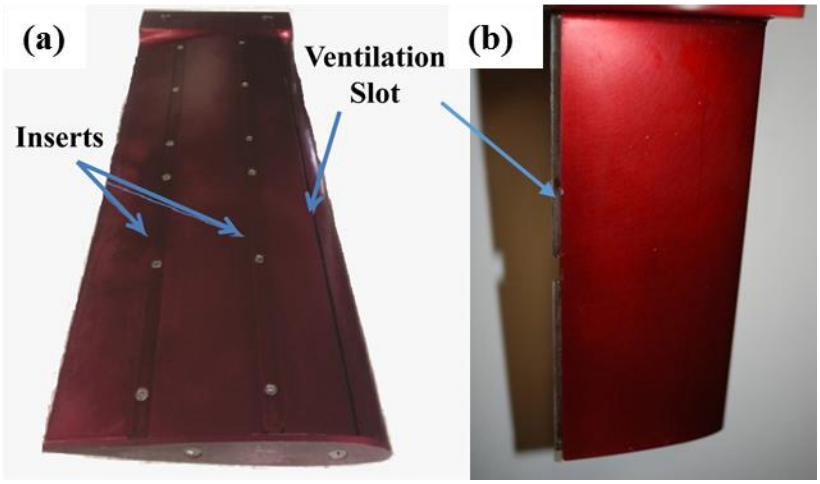

Figure 3.1: Details of the NACA0015 ventilated foils: (a) LEV Foil (b) TEV Foil.

The TEV Foil, also a 2-D NACA 0015 foil having the same dimensions as the LEV Foil but incorporating an aeration slot centered in the trailing edge, was designed and fabricated. This foil used the same mounting plug and air source that had been used previously by the LEV Foil. When assembled, the foil was air tight along all joins and contained a 1 mm wide slot that ran from the tunnel wall on the mounted side to 5 mm from the non-mounted foil end. With the use of shims of various thicknesses, a number of slot widths 1mm or less could be tested.

Since the aeration slot location and associated plenum of the TEV Foil were different than that of the LEV Foil, it was decided to rapid prototype (3-D print) an approximate version of the foil to do preliminary testing in static water. The primary intent of this testing was to assess the ability of the foil design to uniformly discharge air along the length of the slot. The prototyped foil was submerged in static water, leveled,

and ventilated using the design air flow rates that had been used in the SAFL test program. At all flows, the foil discharged the ventilation air uniformly along its length. As a result, the final foil was CNC machined in aluminum and anodized.

A narrow spanwise slot allows air to be injected into the flow near the leading edge of the hydrofoil and the full width of the injection slot is used for measurements of oxygen uptake. This setup results in a dense spanwise bubbly wake and thus, in order to make bubble measurements, ventilation is limited to a narrow 9.6 mm wide slot (5% of span) at the center of the span. This configuration ensures that bubbles remain mostly within a narrow distance away from the centerline. The findings of Silberman (1957) indicated that the bubble diameter is independent of the orifice characteristics for a gas jet coming out of an orifice into a cross flow. Also, the bottom views of the bubbly wake show a minimal lateral drift of the bubbles. Based on our observation of the bottom views of bubbly wake, the study of Silberman and the fact that slot width remained unchanged in our experiments, we posit that the bubbles obtained are a reasonable representative sample of the bubble population that exists when the full span is ventilated.

To systematically investigate the physical processes occurring in the bubbly wake, an air-entrainment coefficient is defined similar to other ventilated cavitation studies viz. Laali and Michel (1984), as $C_{\mathrm{Q}} = Q/UcS,$ where, Q, U $,S,c$ denote ventilation air flow-rate, liquid velocity, hydrofoil span and chord, respectively. Reynolds number is defined using hydrofoil chord as length scale: $Re = Uc/\nu$. To study the effect of the experimental parameters on the resulting flow physics in the bubbly wake, three different sets of experiments are performed with Reference Foil. In the first set of

experiments, C_Q and Re are fixed (C_Q = 1.6 × 10^{-4}, Re = 4.1 × 10^5) and experiments are repeated at three different angles of attack (AoA = 0, 4 and 8 degrees). The subsequent experiments are all done at a fixed zero degree angle of attack. In the second set of experiments, a fixed value of C_Q = 1.6 × 10^{-4} was chosen and *Re* spanned four different values from 2.4 × 10^5 to 8.1 × 10^5. Finally, in the third set of experiments, *Re* was kept fixed at 4.1 × 10^5 and experiments were conducted at four other values of C_Q varying between 1.1 × 10^{-4} to 3.3 × 10^{-4}. Thus, these three sets of experiments comprised of eleven different experimental conditions, which were imaged at three different downstream locations in the wake (*x/c* = 1.34, 3 and 4.65), resulting in 33 experimental datasets and a total number of 66,000 bubble images captured using a shadow imaging technique. Finally, a comparison of the bubble sizes obtained with LEV and TEV Foils are shown at different experimental conditions for a chosen downstream location. The images are processed by the technique described in chapter 2.

3.3. Results for a reference case

3.3.1. Validation of image processing approach at multiple locations

In our experiments, reference is chosen at a liquid velocity of 5 m/s, 0.5 LPM ventilation rate (or, C_Q = 1.6 × 10^{-4}, *Re* = 4.1 × 10^5) and at a location *x/c* = 4.65 from the hydrofoil center for the LEV Foil (referred to as 'reference case' from now on). Bubble images at this location shows a number of characteristics of the bubbly wake. First, there is a wide range of size distribution of bubbles. Measured bubble sizes ranged from 60 μm to a few millimeters and larger bubble clusters were observed as well. Second, these

bubbles are distributed vertically in the wake in a particular fashion. There is a meandering zig-zag pattern clearly visible. It is observed that the bubbly wake in the hydrofoil has a high-amplitude oscillation about the wake centerline, which varies depending upon the flow conditions.

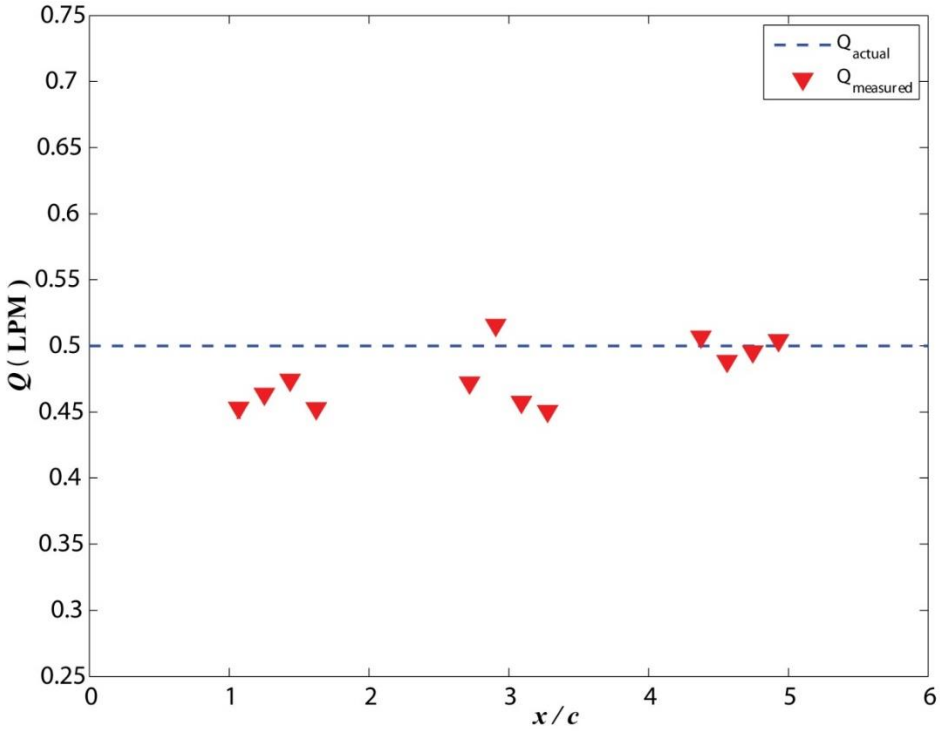

Figure 3.2: The comparison of the actual ventilation flow rate (dotted line) and the measured ventilation flow rates at twelve different streamwise locations for the reference case.

However, such a velocity field does not give any information about the size of the bubbles. Consequently, image analysis is done for all the 1000 images to obtain bubble size information. Now, the size and velocity information of all the bubbles in the wake are coupled to calculate the air flow rate in the wake. It is expected that a comparison of this calculated value with the measured volume flow rate with a mass flow controller would give an indication about the accuracy of the image analysis technique. Thus, the

volume flow rate of air is estimated based on the volume and velocity of the bubbles at twelve different locations in the wake and the comparison has been shown in Figure 3.2. As it can be seen in the figure, the measured and calculated values compared fairly well at all the locations within a 10% error. It can also be seen that the errors decreased to less than 3% at $x/c > 4.5$. The greater amount of bubble clustering close to the hydrofoil can be attributed to the deviations observed at $x/c < 4$.

The uncertainty in the volume flow rate measurements depends upon the bubble size and bubble velocity measurements and on the number of bubbles present in the flow. The uncertainty in bubble size measurements is dependent on the bubble size itself and has been described in detail by Karn et al. (2015a). Based on the simulations of bubble images, they found this uncertainty to vary from 9-10% for bubbles at size 0.2 mm to 2-3% for bubbles at size 2 mm. The uncertainty in bubble velocity measurements was found to lie between 5-6% for all bubble velocities. Finally, it is worth noting that the presence of a larger number of bubbles in the flow (viz. at high *Re*) would lead to a greater uncertainty in volume flow rate measurements.

3.3.2. Bubble size and shape distribution in the wake

Figure 3.3 above shows typical bubble size and shape distributions observed in the wake for a reference case. Bubble size (or bubble diameter) is taken to be the geometric mean of minor-axis (*b)* and major axis length (*a)* i.e. $d = 2\sqrt{ab}$. Similarly, eccentricity of bubble projected areas (called 'bubble eccentricity' from now on) is defined as: $e = \sqrt{1 - (b/a)^2}$, suggesting that a perfectly circular bubble has an

eccentricity value of zero. Figure 3.2a shows that the obtained bubble size distribution is a bimodal one, similar to the reports of Tse et al. (2003), with two modes at 0.30 mm and 0.62 mm respectively. This suggests that the bubbly wake contains an excess of small-sized bubbles at the first mode (around 25-40%) which are significantly smaller than the Sauter mean diameter. The fraction of 0.62 mm bubbles reach up to 8-16% and the fraction of larger bubbles decreases with increase in size. There are very few bubbles with bubble diameter greater than 1.5 mm. Moreover, the uncertainties in the bubble size PDF do not change significantly, when experimental conditions are varied. For this reason, the uncertainty in the PDFs has not been shown in subsequent figures.

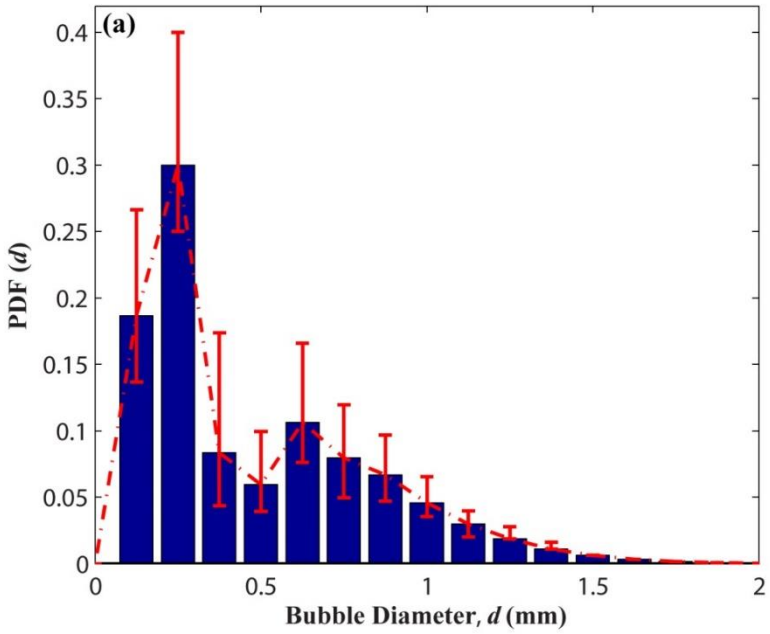

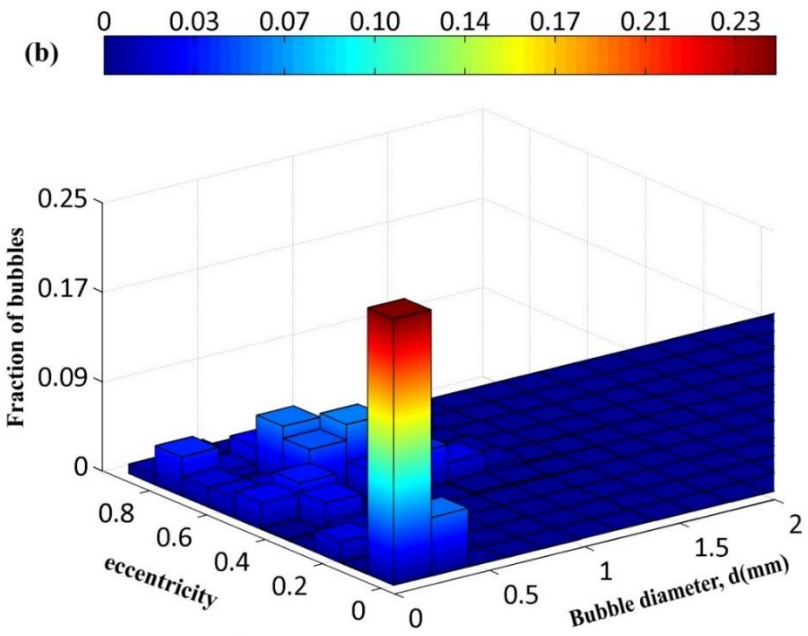

Figure 3.3: (a) Bubble size characterization for the reference case (b) Bubble shape distribution: fraction of bubbles as a function of the eccentricity and size for the reference case. The error bars represent the maximum and minimum values.

Figure 3.3b presents a three-dimensional histogram of fraction of bubbles with bubble diameter and eccentricity. As observed from the figure, about 25% of the bubbles are very small and have an eccentricity value of zero. Higher values of e can be observed only for bubbles larger than 0.5 mm. For instance, 8% of the bubbles are of size 0.6 mm with e = 0.6. It is worth mentioning here that tiny bubbles below 180 μm in size are assumed to be always spherical. For bubbles of this size, it is difficult to estimate the eccentricity accurately since the bubble is imaged onto only a few pixels. However, an imaging of these very small sized bubbles at a higher resolution confirmed our assumption regarding sphericity of these bubbles. A variety of bubble shapes are found in the bubbly wake viz. spherical, ellipsoidal, and wobbling, highly elongated bubbles etc.

The bubble and size distributions in the bubbly wake are determined by the occurrence of bubble deformation, breakup and coalescence processes in the wake. The variation in experimental parameters viz. liquid velocity, ventilation flow rate, system configuration viz. angle of attack of hydrofoil etc. govern the occurrence of these processes. It is well known that the breakup processes in turbulent dispersions are influenced by continuous phase hydrodynamics (Liao and Lucas 2009) whereas the contact and collision of bubbles determine the bubble coalescence process (Liao and Lucas 2010). The collision between bubbles is caused by their relative velocity and will be affected strongly by the bubble density in the flow.

3.3.3. Void fraction measurements.

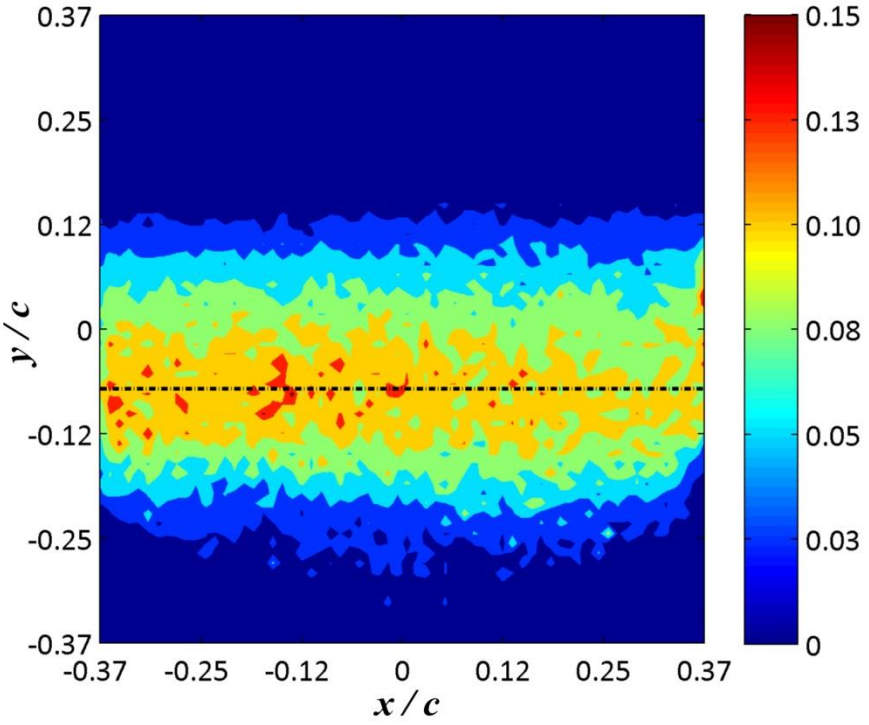

Figure 3.4: Local void fraction measurements in the bubbly wake for the reference case. Origin (0,0) of the above plot is horizontally displaced 4.65*c* from the hydrofoil center of rotation. The dotted line shows the location of the injection slot.

Figure 3.4 above shows the contour plot of the local void fraction in the bubbly wake. For the calculation of local void fraction, entire FOV is divided into a number of windows of size 0.94 mm x 0.94 mm (16 × 16 pixels). First, the projected areas of all the bubbles within each window are traced out and the volume of all the bubbles is calculated assuming a third radius equal to the semi-minor axis of the projected ellipse. The ratio of the total volume of all the bubbles and volume of each window (the depth of each window is determined by the depth of field) gives the local volume void fraction in the wake. As the figure above shows, the maximum local void fraction values are attained below the centerline (i.e. $y = 0$). The local void fraction below the centerline can reach as

high as 0.15. It should also be noted that the slot is located at 6 mm below the centerline and the void fraction distribution along transverse direction is almost symmetrical about the location of injection slot. The figure shows that the void fraction decreases gradually upon moving away from the injection slot location on either side in the vertical direction. The greater void fraction at the location of the injection slot can be attributed to both larger number of bubbles and greater size of bubbles at these locations.

3.3.4. Bubble Velocity Measurements in the wake

The turbulence in the wake flow downstream of a hydrofoil affects both bubble size and velocity in the wake. The bubble velocity fluctuations, in turn affects the local liquid velocities. The bubble velocity profiles measurements are made at three downstream locations, x/c = 1.34, 3 and 4.65 at all the three angles of attack. First, an average velocity field is obtained for entire FOV. The bubble average velocity field is obtained in a 60 mm × 60 mm window with center at x/c = 4.65. Each window is further divided into smaller windows of size 0.94 mm × 0.94 mm and a velocity vector corresponding to a bubble in each window is determined using double pulse images. Finally, this plot is generated by averaging all the 1000 bubble velocity fields obtained from 1000 image pairs. It is worth pointing out here that based on the pixel size (~60 μm) and the time between double pulse images (100 – 230 μs depending upon the liquid flow velocity), the velocity resolution in our experiments ranged from 0.26 to 0.6 m/s. The SIV analysis of the bubbly wake images show that the bubble velocity remains almost uniform in the wake, varying within 5% of about 5 m/s, with the lowest velocities at the center of the wake (Karn et al. 2015a). Later, velocities at the same vertical location are

averaged to get an averaged bubble velocity profile at the three streamwise locations. Figure 3.5 presents normalized velocity deficit profiles of bubbles at a zero angle of attack. It shows that the maximum velocity deficit occurs in the center of the wake for all the three locations. The velocity deficit peaks close to the hydrofoil, and decreases gradually as the wake continues to spread. Specifically, at x/c = 1.34, the maximum velocity deficit is 6.7%, which reduces to 3.8% and 3.4% at x/c = 3 and 4.65 is, respectively. Also, the bubble velocity profile changes significantly between x/c = 1.34 and x/c = 3 but there is a minimal evolution of the velocity profile between x/c = 3 and 4.65. Further, the maximum velocity deficit is present at the centerline; yet, the wake is not symmetrical about the centerline. This can be attributed to the preferential location of large size bubbles below the centerline. It is noteworthy that a non-symmetric velocity field is observed with higher velocity above the centerline since the ventilated air is injected from the pressure side of the hydrofoil located below the centerline. In general, it is observed that the larger bubbles had slightly lower velocities compared to the tiny bubbles, which followed the streamlines more closely.

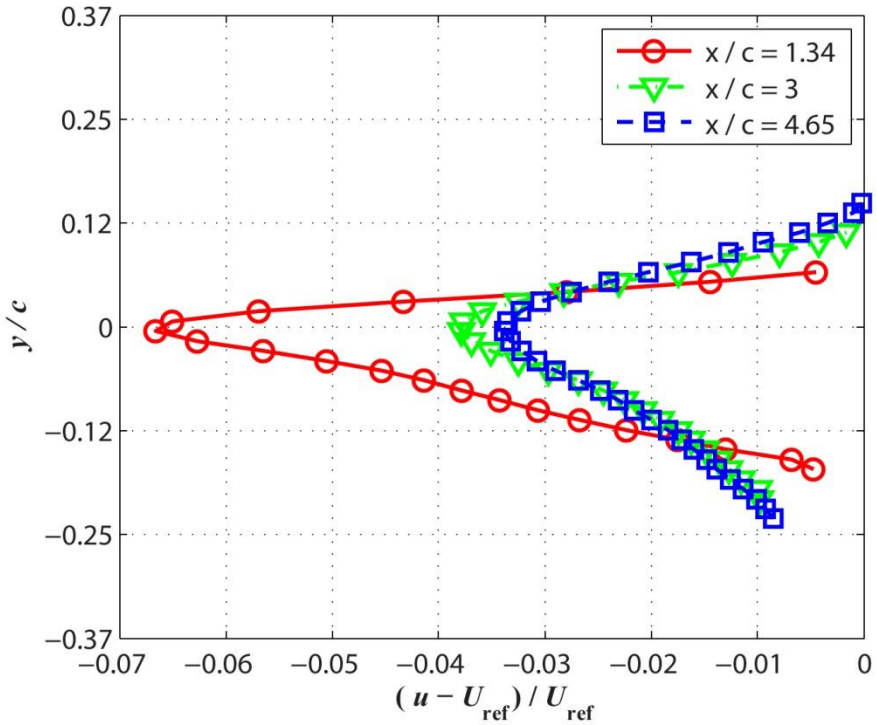

Figure 3.5: Averaged bubble velocity profile for the reference case at three different stream-wise locations. U_{ref} is the velocity at the edge of the wake at the measurement location. Uncertainty in velocity measurement at each data point is 5.2%.

3.4. Effect of variation in angle of attack of hydrofoil

The variation in the angle of attack of hydrofoil is expected to cause a drift in the bubbly wake downstream. However, it can also be conjectured that bubbles of different sizes may respond to this variation differently. To investigate the effect of variation in *AoA* upon bubble of a particular size, all the bubbles measured at a particular *AoA* are classified into six equal size bins spanning over 0 to 3 mm. It is found that the movement of the bubbles in the vertical direction is dependent upon the bubble size. Figure 3.6 shows how the bubbles are distributed across vertical direction in the wake. For all the bubbles in a particular size bin, Sauter mean diameter (referred to as *SMD* or d_{32} from

now on) is calculated and the extent of its drift in the vertical direction is measured. For a number of bubbles of same shape, *SMD* can be defined as: $d_{32} = \sum_{i=1}^{N} n_i d_i^3 / \sum_{i=1}^{N} n_i d_i^2$ (Hesketh et al. 1987, Razzaque et al. 2003) where n_i is the number of bubbles at a particular diameter d_i. It is observed that the vertical drift of the bubbles reduced as the bubble sizes increased. For the *AoA* = 0 case, it is evident that smallest sized bubbles drifted considerably from the plane of injection slot from -0.32*c* to 0.36*c*. However, the large sized bubbles remained below the injection slot within a much narrower region. This can be attributed to the greater inertia of the large-sized bubbles. The mean location of the bubbles in the size range of 2.5 – 3 mm bubbles is located approximately at a distance of 0.08*c* from the plane of injection slot. Further, as the *AoA* increases from 0 to 8 degrees, the entire bubbly wake drifted upwards.

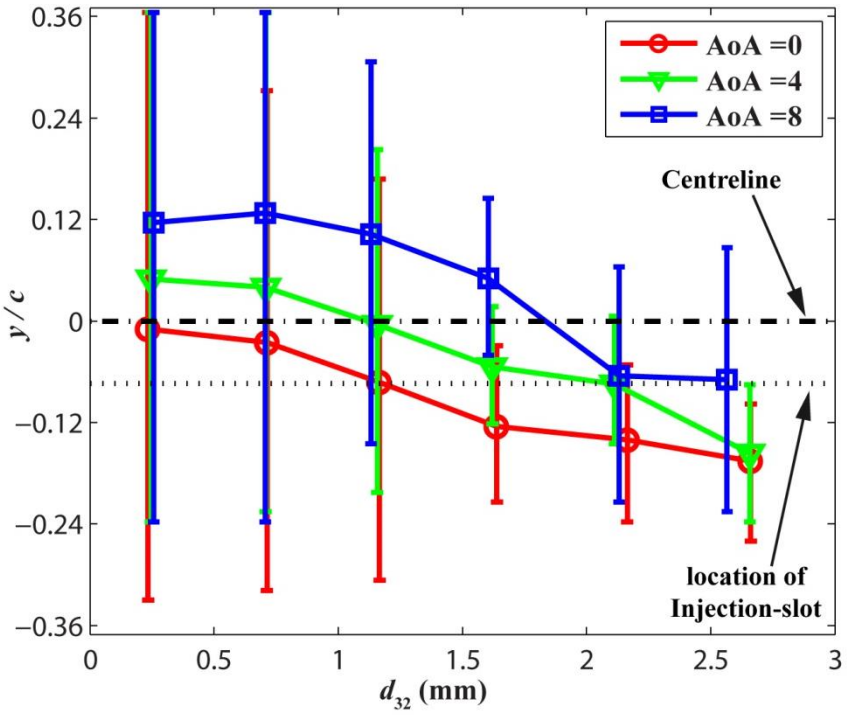

Figure 3.6: Spread of bubbles in the bubbly wake at different angles of attack. The symbols denote Sauter mean diameter and mean vertical location of all the bubbles in a size bin. The red, green and blue bars represent the y-locations over which bubbles in each size bin are observed at different *AoA*.

Apart from causing an upward drift in the bubbly wake, an increase in angle of attack also had an impact upon the total number of bubbles and bubble sizes produced. As the air is introduced through the ventilation slot, the air becomes exposed to the destabilizing effect of the turbulent velocity fluctuations in the liquid which causes the continuous air-jet to break into small bubbles. Upon increasing *AoA* from 0 to 8 degrees, there are greater levels of turbulence in the wake downstream, and thus the air bubbles are subjected to increasing values of turbulent stresses on their surface, resulting in their breakup into smaller sizes. Consequently, the value of critical bubble diameter, or the diameter of the largest stable bubble in a turbulent flow, (as defined by Tikhomirov

(1991) as) $D_c \propto (\sigma/\rho)^{3/5}\epsilon^{-2/5}$, decreases ($\sigma$, ρ and ϵ denote interfacial surface tension, density of liquid and the dissipation rate, respectively). Figure 3.7a below presents a PDF of the bubbles at different *AoA*. As the figure shows, a greater angle of attack leads to a greater fraction of bubbles in the intermediate size range (0.5 – 1 mm). The fraction of bubbles at 0.62 mm increased from 11% at an *AoA* of 0 degree to 17% at *AoA* of 8 degrees. Corresponding, there is a decrement in fraction of small size bubbles. However, in spite of the increased turbulence and greater fraction of the small sized bubbles, the shape of the PDF largely remains the same, and does not shift towards smaller sized bubbles as reported in a previous study by Martínez-Bazán et al. (2000). To represent the bubble size PDF in non-dimensional variables, a normalized bubble diameter is defined as $\tilde{d} = d/d_{32}$. The probability density function of $\tilde{d}$, PDF($\tilde{d}$) for different angles of attack are shown in figure 3.6b. It shows that all the PDFs ($\tilde{d}$) collapse on a single curve, which is an indicative of the fact that d_{32} is an effective single parameter to represent the entire bubble size distribution. This can be used to obtain PDF(*d*) for any *AoA* of hydrofoil once an estimate of d_{32} can be obtained at a particular *AoA* (for instance, using Figure 3.7b).

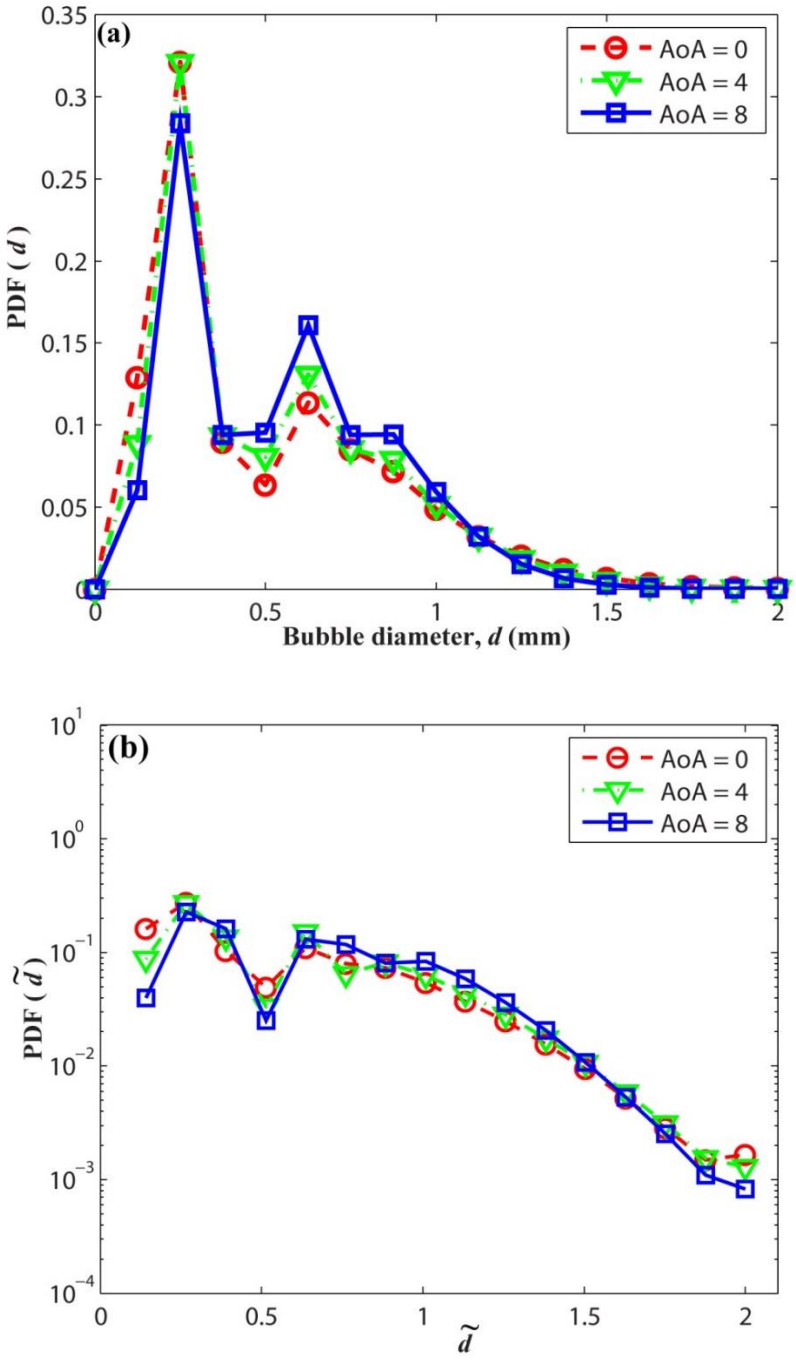

Figure 3.7: (a) Bubble size PDFs at different *AoA*. (b) Bubble size PDF of $\tilde{d}=d/d_{32}$ for different *AoA*. The data points shown correspond to the bin centers of the histograms.

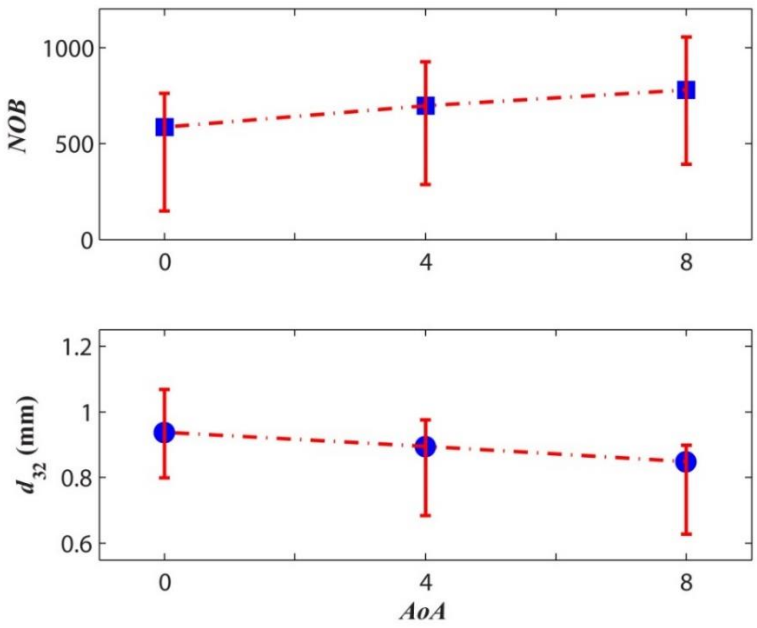

Figure 3.8: (a) NOB per image and (b) Variation of SMD with *AoA*. Error bars denote the maximum and minimum values.

Figure 3.8a presents the number of bubbles (NOB) generated and *SMD* of all the bubbles at each angle of attack, respectively. It shows that with increasing angle of attack from 0 to 8 degrees, *NOB* increased by 33% while the *SMD* decreased from 0.93 mm to 0.85 mm. Calculations based on Figure 3.7a and 3.8b reveal that the number of bubbles in the small size range does not change much since the decrease in fraction and increase in number of bubbles offset each other. Similarly, the decrement in d_{32} upon increase in *AoA* as shown in Figure 3.8b can be attributed to the significant rise in the number of bubbles in intermediate size range and a consequent decrease in number of large size bubbles.

3.5. Effect of Variation in Reynolds Number

Figure 3.9a presents a PDF of bubble sizes as *Re* is varied from 2.4×10^5 to 8.1×10^5 at $C_Q = 1.1 \times 10^{-4}$. In general, it is observed that upon increase in *Re*, there is a greater fraction of small size bubbles while the fraction of large size bubbles decreased. The fraction of small size bubbles at the first mode increased from 18% at the smallest *Re* to approximately 34% at the greatest value of *Re* tested. Conversely, in the intermediate size range (viz. 0.6-0.7mm) the fraction of bubbles decreased from 10% to below 5% for the same variation of *Re*. However, the overall shape of the PDF and the slope of the tails of the PDFs does not change significantly with the change in *Re.* Again, as shown in figure 3.9b, the normalized PDFs($\tilde{d}$) for this range of variation in *Re* collapse onto a single, self-similar curve suggesting that d_{32} is the parameter needed to describe the final state of bubble size PDF. For a given *Re*, d_{32} can be known through a power law fit (See figure 3.10c) and the PDF(*d*) can be obtained subsequently assuming the same universal shape of PDF($\tilde{d}$).

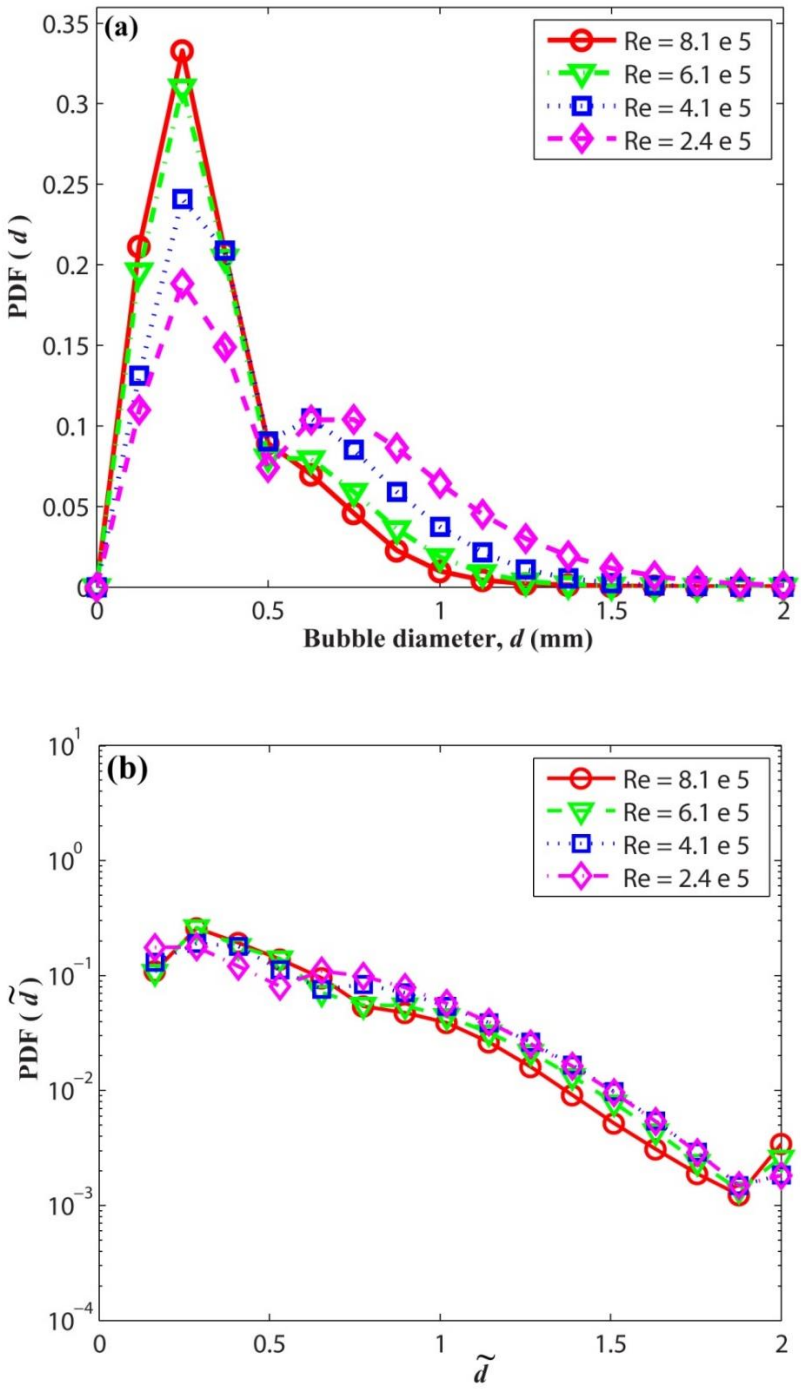

Figure 3.9: (a) Bubble size PDFs and (b) Bubble size PDF of $\tilde{d} = d/d_{32}$ for different *Re* at C_Q = 1.1 × 10-4. The data points shown correspond to the bin centers of the histograms.

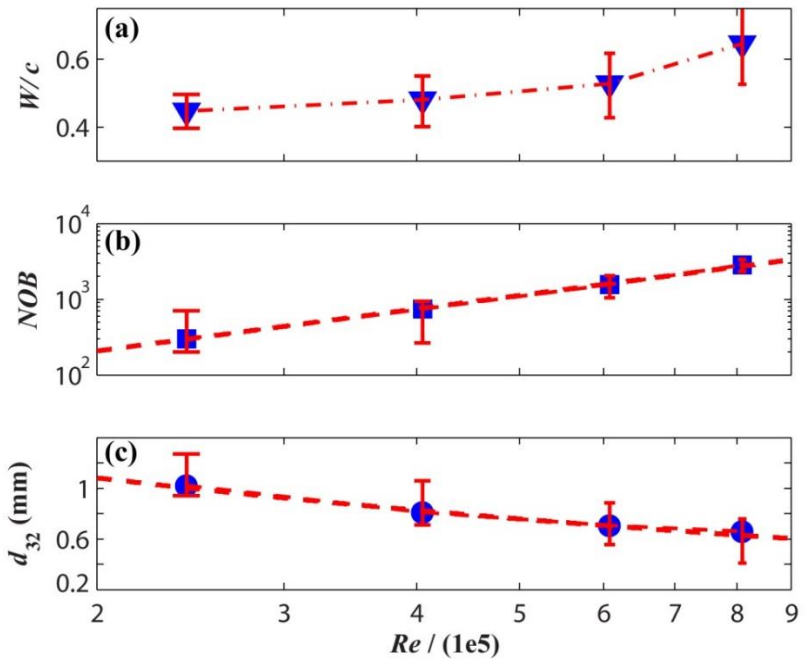

Figure 3.10: (a) Variation of normalized wake-width ($\tilde{W}$=*W/c*) in the wake (b) Number of bubbles (NOB) as a function of *Re*. (c) Sauter mean diameter of all the bubbles as a function of *Re*. Circles and squares show the data point while the dashed line shows the power

Figure 3.10a shows the variation of normalized wake-width ($\widetilde{W} = W/c$) with *Re*. Wake-width is defined as the distance between the two *y*-locations on the either side of the centerline, which had at least a minimum of 500 bubbles in the entire bubble image dataset. Figure 3.10a indicates that $\widetilde{W}$ increased from 0.45 to 0.65 as *Re* is varied from smallest to the largest value. As *Re* increases, the increase in wake-width implies a spread in the bubbly wake in the transverse direction, thus exposing a number of bubbles to the free-stream turbulence which would further break down bubbles into smaller daughter bubbles. Figure 3.10b shows the consequent increase in number of bubbles per image from 301 to 2.8×10^3 over this range of *Re*. Based on these results, it is found that at a fixed C_Q, *NOB* has a power law dependence with *Re* as: $NOB \propto Re^{1.84}$. Since a larger *Re* also leads to a larger fraction of small-size bubbles, the total number of small size

bubbles is significantly higher at a greater *Re.* This would lead to a decrement in Sauter mean diameter at a greater *Re.* Figure 3.10c shows that SMD decreases from 1 mm to 0.6 mm as *Re* is increased over the given range of *Re.* For all the conditions at a fixed C_Q, *SMD* is found to have a power law dependence with *Re,* but with a negative exponent: $d_{32} \propto Re^{-0.39}$. A further insight into the variation of *SMD* across all the y-locations reveals that in spite of the large variation in wake-width, the trend of variation of *SMD* with vertical location remains similar for all the *Re.* Figure 3.11 shows that the curve of size versus *y*/*c* shifts to the left as *Re* is increased. As explained before, the preferential presence of the large size bubbles below the centerline leads to an increase in *SMD* upon moving downwards and this trend remained unchanged with increase in *Re.* It can be seen that the *SMD* of all the bubbles reported before is approximately equal to the mean value of the *SMD* obtained over all the *y*-locations as shown below.

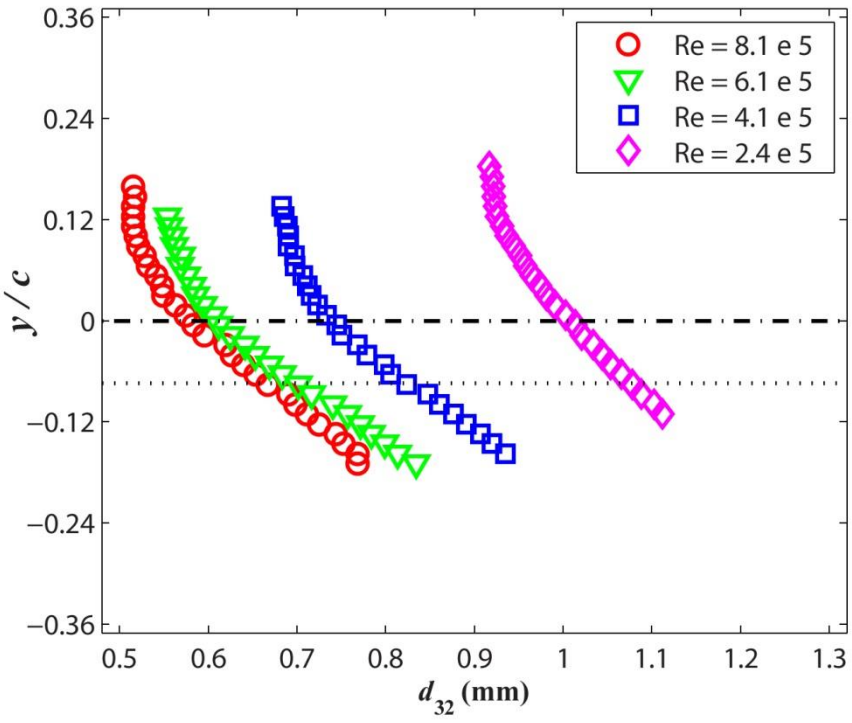

Figure 3.11: Sauter mean diameters at each vertical location for the range of *Re* tested at C_Q = 1.1 × 10-4. Note that the data points are shown only for the bubbly wake.

3.6. Effect of variation in air entrainment coefficient

Figure 3.12a below shows the effect of air entrainment on the bubble size distribution at a fixed $Re = 4.1 \times 10^5$. It suggests that at a lower C_Q, there is a greater fraction of small size bubbles while the opposite is true for the intermediate and larger size bubbles. In our experiments, C_Q is varied by a factor of three and the fraction of number of bubbles at the first mode increased by 7%. In general, it would be expected that larger value of C_Q would lead to a larger number of bubbles since the net amount of air ventilated per unit time has increased. Again, when the bubble size PDF is normalized with their corresponding d_{32}, all the PDFs collapse onto the same universal curve as

shown in Figure 3.12b. Thus, for any given C_Q, d_{32} can be known (using figure 15c) and the PDF(d) can be obtained since the PDF($\tilde{d}$) has the same universal shape.

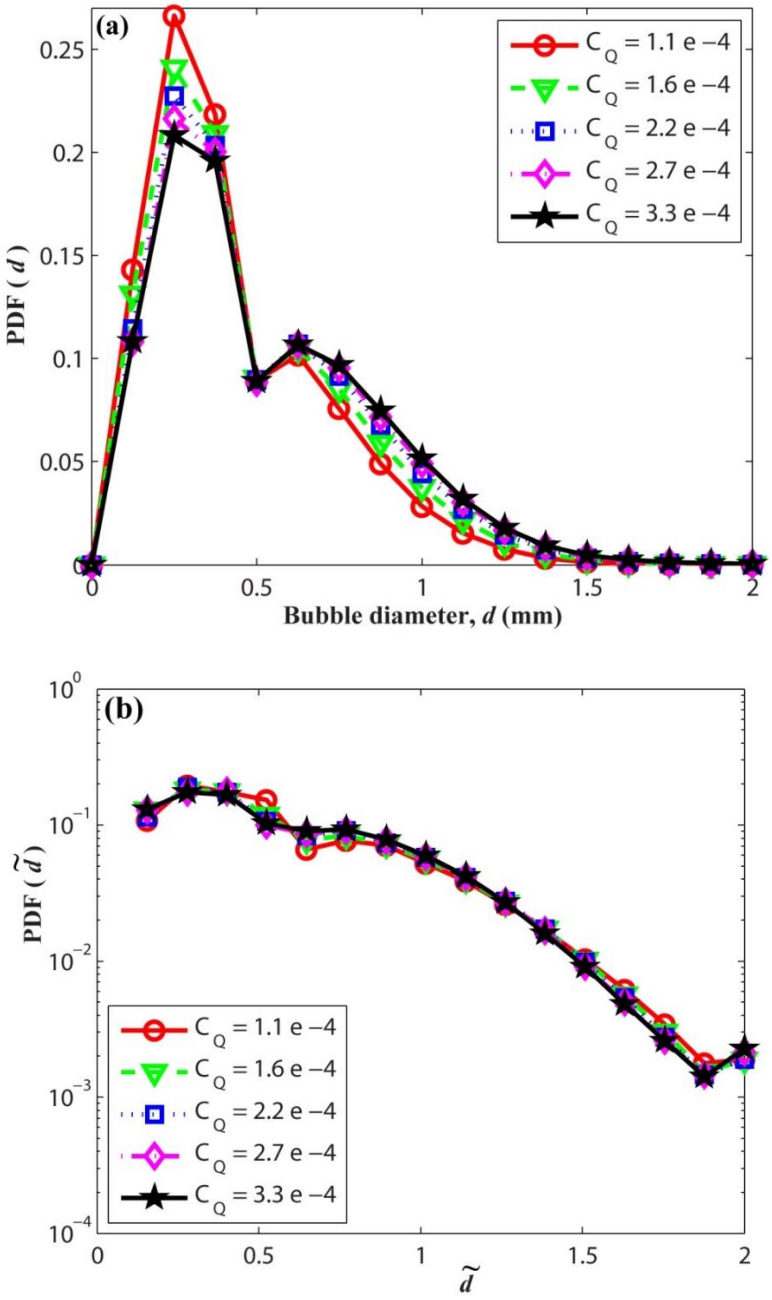

Figure 3.12: (a) Bubble size PDF with variation in C_Q, and (b) Bubble size PDF of $\tilde{d} = d/d_{32}$ for different C_Q at Re = 4.1 × 105. The data points shown correspond to the bin centers of the histograms.

Normalized wake width, $\widetilde{W}$ is found to increase from 0.4 to 0.63 as C_Q is increased by three times as shown in Figure 3.13a. Similar to the previous case, it suggests that there will be greater breakup events due to the spreading of the wake. However, it should also be noted that the larger amount of ventilation flow rate leads to formation of larger bubbles and a greater number of bubbles. Since the increase in $\widetilde{W}$ is just 57% while C_Q is increased by three times, it implies that bubbles are more closely spaced at a higher C_Q. Thus, bubbles lying in the vicinity of each other will readily undergo coalescence in the bubbly wake increasing the number of bubbles in intermediate size range as well (Tse et al. 2003). Thus, there is a net rise in total number of bubbles. Figure 3.13b shows that *NOB* increases with increase in C_Q. However, unlike the previous case, *NOB* is observed to have a linear dependence upon C_Q, with number of bubbles per image increasing from 656 at $C_Q = 1.1 \times 10^{-4}$ to 914 at $C_Q = 3.3 \times 10^{-4}$. This information when coupled with the PDF of bubbles reveals that upon an increase in C_Q, the number of bubbles increase over the entire size range of bubbles. However, the change in the number of small size bubbles is minimal while there is a significant increment in number of large size bubbles upon an incremental change in C_Q. Thus, a net increment is observed in d_{32} as C_Q increases. Figure 3.13c shows that d_{32} increases from 0.73 to 0.86 as C_Q is varied.

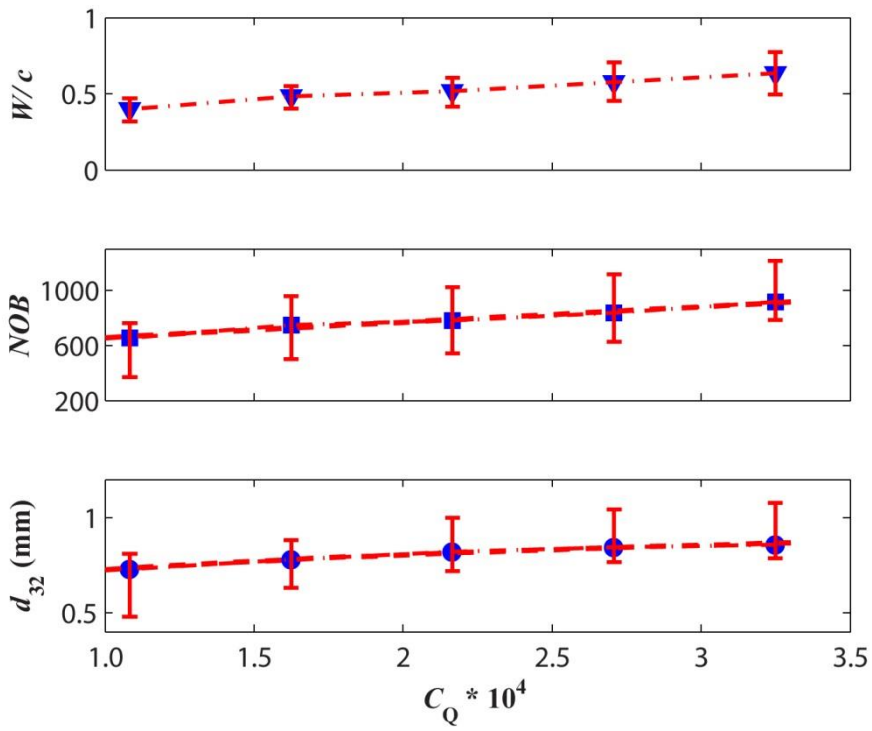

Figure 3.13: (a) Variation of $\tilde{W}$ in the wake (b) NOB (c) d_{32} of all the bubbles, as a function of C_Q at $Re = 4.1 \times 105$ Circles and squares show the data point while the dashed line shows the power law curve fit. Error bars denote the maximum and minimum values.

The variation of *SMD* in transverse direction followed similar trends (as before) at different values of C_Q. It can be conjectured that the higher void fraction in the flow leads to modification of the turbulent kinetic energy spectra, which leads to a lower value of ϵ, increasing critical bubble diameter D_c (as defined by Kolmogorov (1949)) consequently causing an increment in d_{32}. Moreover, increased coalescence of bubbles at higher C_Q also adds to an increment in d_{32}. As Figure 3.14 presents, with the increment in C_Q, the curve shifts towards the right. This suggests that at larger C_Q, there is an increase in average size of bubbles across all vertical locations. However, not much difference is seen in the profiles at large values of C_Q ($C_Q > 2.5 \times 10^{-4}$). This is because at higher values of C_Q, there is excessive clustering of bubbles leading to the formation of large

bubble clusters/cloud, a situation where the image analysis approach is limited in resolving the big clusters into individual bubbles.

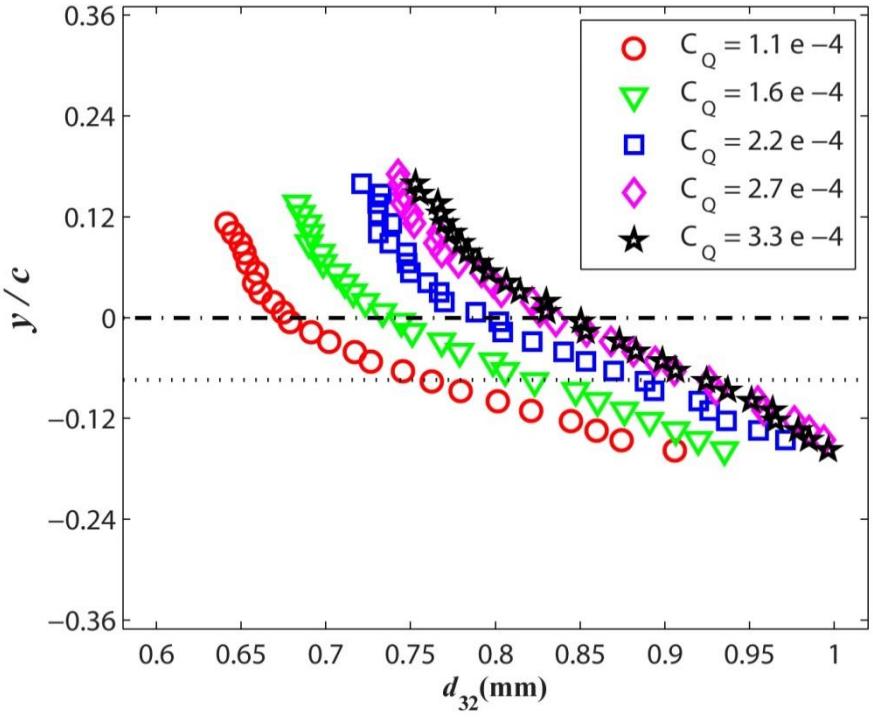

Figure 3.14: Sauter mean diameters at each vertical location for the range of C_Q tested at a fixed *Re* = 4.1 x 105. Note that data points are shown only for the bubbly wake.

3.7. Effect of air injection mechanism

To study the effect of air injection mechanism on the resulting bubble sizes, SMD was computed for both the LEV and TEV Foils for different air flow rates and water velocities. The SMD for both the foils are presented in Table 3.1. SMD increases by 11-14% (LEV Foil) and 11-31% (TEV Foil) as the ventilation airflow rate is tripled at all liquid velocities and decreases by 23-35% (LEV Foil) and 44-59% (TEV Foil) when the liquid velocity is doubled at the same airflow rate. An increase in angle of attack from 0

to 8 degrees leads to a 10-29% (LEV Foil) and 17-60% (TEV Foil) decrease in SMD, provided the liquid velocity and air ventilation rates are kept fixed.

AoA (deg)	*U* (m/s)	*Q* (SLPM)	SMD_{LEV} (mm)	SMD_{TEV} (mm)
8	5	0.5	0.79	1.20
8	5	1.5	0.89	1.53
8	7.5	1.0	0.68	0.90
8	10	0.5	0.51	0.50
8	10	1.5	0.58	0.63
4	5	0.5	0.84	1.30
4	5	1.5	0.95	1.59
4	7.5	1.0	0.75	1.05
4	10	0.5	0.58	0.67
4	10	1.5	0.66	0.85
0	5	0.5	0.88	1.61
0	5	1.5	0.98	1.79
0	7.5	1.0	0.80	1.41
0	10	0.5	0.66	0.77
0	10	1.5	0.75	1.01

Table 3.1: Bubble size for both LEV and TEV Foils at all the experimental conditions (at x = 377 mm)

The bubble size distribution was also obtained for each test condition. Initially, the data took the form of a probability density function (PDF) of bubble diameter, PDF(d), as presented in Figure 3.15 for a reference flow condition (which is chosen as AoA = 8, U = 5 m/s, Q = 0.5 SLPM, X = 377mm). However, this way of analyzing the bubble size data misrepresents the gas transfer potential of the bubble population. A better understanding of the bubble size results, one that is more closely tied to the mechanics of gas transfer, can be accomplished by scaling the bubble diameter PDF by bubble surface area as is shown in Figure 3.16. Since SMD is defined as (6*bubble

volume/bubble surface area), the number of bubbles of a certain size were scaled by, $d' = S_i/6V_{tot}$ to stay consistent with the SMD definition, where S_i represents the surface area of a single bubble and V_{tot} denotes the total volume of all the bubbles in the population. The integral (summation) of the scaled bubble size PDF (histogram) scaled in this way equals the value of 1/SMD. Since it is known that the rate of gas transfer from a bubble population to the surrounding water scales inversely with SMD, we believe scaling our bubble size data in this way most closely represents the associated gas transfer process.

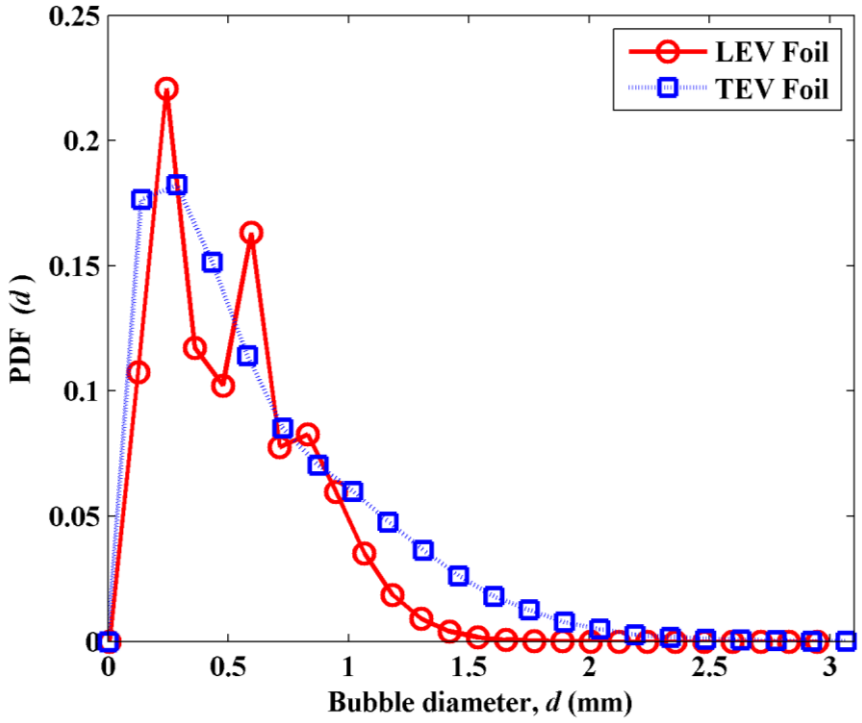

Figure 3.15: PDF of bubble diameter for both the LEV and TEV Foils at the reference flow condition.

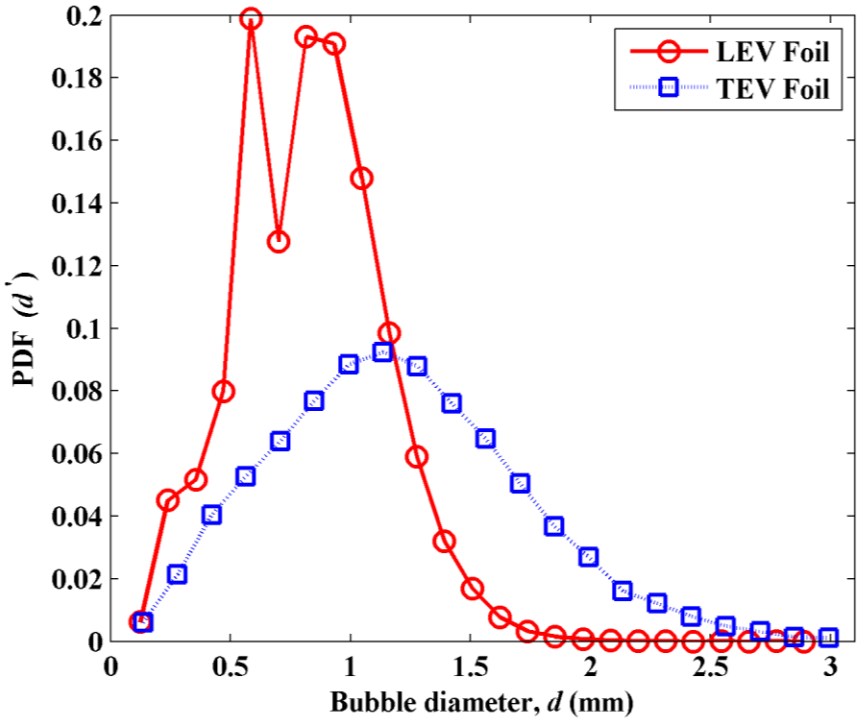

Figure 3.16: The scaled bubble diameter PDF (*d*') at the reference flow condition.

In general, the TEV Foil SMD equaled or exceeded that of the LEV Foil for the same test condition. On the basis of our data, it is conjectured that for the TEV Foil, which discharges air to the wake directly from the trailing edge, a non-zero angle of attack and higher water velocity tend to shear the bubbles down to smaller sizes. At zero degree angle of attack and water velocity of 5 m/s, the bubbles remain large because they are injected into the wake in the direction of the flow with less shear than the LEV Foil. For the LEV Foil, the bubbles experience significant shear at all velocities and angles of attack because they are injected orthogonally to the flow direction near the foil's leading edge. This results in less variation in bubble size and generally smaller bubbles for the LEV Foil compared to the TEV Foil.

3.8. Bubble size prediction

The increase of the bubble size in the wake may be caused by: bubble generation at the injection point or the numerous coalescence events in the bubbly wake. Silberman (1957) investigated the production of bubbles by the disintegration of gas jets coming out of an orifice in liquids. His study indicated that the bubble diameter is independent of orifice size as long as the gas issues as a jet from the orifice into a cross flow. He gave a simple expression for bubble diameter as, $d = \sqrt{Q/U}$, or $d/\sqrt{cS} = \sqrt{C_{\mathrm{Q}}}$. While this may be true for the bubbles generated at the injection slot, it does not capture the influence of breakup and coalescence events on the bubble size in the bubbly wake. The bubble sizes measured in our experiments are a function of the generated bubble size at the slot and breakup and coalescence processes occurring in the wake. Razzaque et al. (2003) points out that the breaking of a continuous air jet into bubbles depends upon the turbulent velocity fluctuations in the flow, which is strongly dependent upon *U* (or *Re*) as $\varepsilon \sim U^3$. According to Sevik and Park (1973), surface tension, viscous and inertial forces are three forces involved in the splitting of gas bubbles. Our experiments have proved a strong dependence of bubble size upon both *Re* and C_{Q} of the flow. An increase in *Re* decreased the *SMD*, while an increase in C_{Q} is observed to impose an opposite effect. In the literature, many studies have been reported that predict bubble size based on the theories developed by Tikhomirov (1991), Hinze (1955) and Levich (1962). These theories are based on the hypothesis that if a Weber number, *We* (defined based on a maximum bubble diameter, $d_{\max}$) exceeds a critical value We_{crit} , then the bubbles of

diameter larger than d_{max} break up due to the effect of turbulent velocity fluctuations. Many studies have suggested correlations based on these theories (P. Andreussi et al. (1999)) to predict the maximum bubble size flowing in dispersed bubble regime. However, in our study maximum bubble size is not of paramount importance and is not the most suited parameter to characterize the bubble size distribution resulting from the flow physics in the bubbly wake. In the analysis of our experiments, it is necessary to assess the effect of breakup and coalescence in the bubbly wake, since the Kolomogoroff-Hinze theory is limited to single bubble flow in turbulent liquid flow regime. According to Ferriera et al. (2012), the SMD is a significant scale for characterizing mass transfer during the interfacial processes, as also advocated previously by Hesketh et al. (1987) and Razzaque et al. (2003). Thus, in the present study, we define a Weber number (*We*) based on the Sauter mean diameter, d_{32} as: $We = (\rho U^2 d_{32}/\sigma)$. In general, *We* measures the ratio of the hydrodynamic pressure forces to surface tension forces in a bubble. Based on our experimental data across three different *AoAs* of the hydrofoil, *We* is observed to depend upon *Re* and C_Q in the following manner: $We \propto Re^{\beta} C_Q^{\gamma}$, where β and γ and the constant of proportionality are seen to depend upon the flow configuration viz. hydrofoil *AoA* as shown below in Table 3.2:

AoA	β	γ	R^2
0	1.706	0.179	0.999
4	1.543	0.140	0.999
8	1.515	0.134	0.999

Table 3.2: The parameters obtained by the experimental data to the fitting equation

Table 3.2 presents the coefficients obtained from fitting our data to the equation given above and the R^2 value which gives a measure of the fit. It can be noted that there is a decreasing trend in the values of the coefficients as *AoA* is increased. An R^2 value greater than 0.999 for all angles of attack suggests a consistent trend in the dependence of *We* upon *Re* and C_Q.

3.9. Conclusions

In this chapter, a series of ventilation experiments is conducted in the SAFL high speed water tunnel, providing aeration statistics and capabilities for the NACA 0015 hydrofoil. First, the results of a standard test-case ($Re = 4.1 \times 10^5$, $C_Q = 1.6 \times 10^{-4}$, $AoA = 0$) are discussed and then the effects of variation in experimental parameters is investigated. The image-processing approach used is experimentally validated for this reference case and is found to give excellent results. The bubble size distribution is found to be a bimodal one, with maxima at 0.30 mm and 0.62 mm. Broadly speaking, the shape distribution showed that the small size bubbles (< 0.3 mm) are mostly spherical while the large size bubbles are largely ellipsoidal. The spread of different size bubbles is studied and it is observed that because of the injection-slot being located on the pressure side of the foil, the larger bubbles stayed close to the location of the injection slot (i.e. below the centerline) due to greater inertia while the very small size bubbles (< 0.3 mm) are distributed uniformly in the wake. This preferential location of the large sized bubbles had an impact on both the bubble velocity profiles and local void fractions distribution in the wake and these profiles are symmetrical, not about the centerline, but the vertical

location of the injection slot. It is observed that upon moving downstream in the wake, the velocity deficit decreases and the wake tends to spread.

Next, the effect of variation in hydrofoil angle of attack and the flow conditions on the bubbly wake are studied. It is observed that an increase in hydrofoil angle of attack led not only to an upward drift in the wake but also increased liquid turbulence in the wake downstream, which resulted in greater splitting of large size bubbles (> 1 mm) into intermediate size bubbles (0.5 – 1 mm). Thus, the *NOB* increased while the d_{32} decreased.

An increase in *Re* (at a fixed C_Q) led to an increase in wake width and spread and greater turbulence in the wake. This promoted splitting and thus an increase in the fraction of small sized bubbles (~0.30 mm) and a reduced fraction of intermediate and larger size bubbles (> 0.5 mm). The total number of bubbles increased and d_{32} decreased. In contrast, an augmentation in C_Q (at fixed *Re*) had a contrary effect. The higher the C_Q, the smaller the fraction of small sized bubbles and the greater the fraction of intermediate to large size bubbles. An increase in C_Q resulted not only in increased number of bubbles, but also in increased bubble size due to increased coalescence events in the wake. Interestingly, the PDF($\tilde{d}$) of the normalized bubble size $\tilde{d} = d/d_{32}$, is found to have a universally similar shape independent of either *Re*, C_Q or hydrofoil *AoA*. SMD increases by 11-14% (LEV Foil) and 11-31% (TEV Foil) as the ventilation airflow rate is tripled at all liquid velocities and decreases by 23-35% (LEV Foil) and 44-59% (TEV Foil) when the liquid velocity is doubled at the same airflow rate. An increase in angle of attack from

0 to 8 degrees leads to a 10-29% (LEV Foil) and 17-60% (TEV Foil) decrease in SMD, provided the liquid velocity and air ventilation rates are kept fixed.

The position of the air injection had a significant effect on the bubble size distribution. The larger bubbles produced by the TEV Foil were generally found to occur at low angles of attack and slower water velocities. Conversely, the bubble populations produced at a high angle of attack and larger water velocities showed little measurable difference between the two foil configurations. In general, the TEV Foil SMD equaled or exceeded that of the LEV Foil for the same test condition. It is hypothesized that the smaller SMDs for the LEV Foil are due to injection close to the leading edge where the air is injected orthogonally to the flow direction, shears down to smaller bubbles immediately on exit and mixes with the outer flow more effectively. At the lower water velocities the air injected for the TEV Foil does not experience as great of a shearing force. Finally, it is proposed that *We* has a power law dependence upon *Re* and C_Q and the exact expression is derived by fitting with the experimental data. However, the current chapter does not give any information about the variation of bubble size in the wake and the underlying physical factors behind it. The next chapter explores the physical processes occurring in the wake of hydroturbine blades and the mean bubble statistics at different downstream locations in the bubbly wake.

Chapter 4. Investigations into breakup and coalescence mechanisms in the hydrofoil bubbly wake

The current design of the Auto-venting turbines (AVT) relies primarily on computational simulation. The experimental studies that focus on the physical processes occurring in turbulent bubbly wake are urgently needed to improve the performance of these simulations in predicting the bubble size distribution behind auto-venting turbines. Therefore, in the present chapter, we report the results of the detailed experimental investigations into the bubble size distributions in the wake of a ventilated hydrofoil. The mean bubble statistics is measured at different liquid velocities and air entrainment rates, and then the variation in mean bubble statistics is studied at different downstream locations in the wake. The bubble size distributions at different downstream locations have revealed the presence of distinct coalescence-dominant and breakup-dominant regimes. Analytical expressions are derived for the prediction of maximum stable

diameter and Sauter mean diameter of bubbles, in the breakup and coalescence regimes, respectively. The observations from high speed imaging provide support for the measurements of bubble statistics, and physical insights into different mechanisms of bubble breakup and coalescence in turbulent wake. It is hoped that these insights will aid in developing generic model of bubble size distribution, and will help researchers improve bubbly flow simulations for auto-venting turbines.

4.1. Relevance

In an AVT, air is drawn into the water at naturally occurring low pressure points in turbines leading to increased dissolved oxygen levels in the tailraces below hydroelectric dams. However, although the aerated hydroturbines improve the water quality, yet the increasing air ventilation in the turbine has a detrimental effect on the turbine efficiency due to subsequent hydraulic losses. Accordingly, the design and operation of such AVTs have to fulfill the twin objectives of increased DO levels, and minimal drop in turbine efficiency. Currently, much of the design of auto-venting hydroturbines is performed with computational fluid dynamics (CFD) simulations. The information available to test and verify the performance of these simulations as regards bubble size distribution is scarce. Also, these simulations are challenging since capturing the evolution of bubble size distribution in the wake accurately requires an understanding of the process of air entrainment and other physical processes occurring in the turbulent bubbly wake.

The air entrainment in such a hydroturbine can be carried out by opening a port connected to the low-pressure regions in the turbine. Evidently, when air is entrained into

the wake, it breaks into individual bubbles because of the presence of turbulent velocity fluctuations in the wake. Further, the collision of bubbles might also produce bubbles with increased size due to coalescence. In a turbulent and dispersed liquid flow, breakup and coalescence processes occur continuously and interplay between these two processes determines the bubble size distribution. Finally, bubbles attain a stable size due to the establishment of a local dynamic equilibrium between these two processes. However, the underlying mechanism in which the entrained air breaks into bubbles and the change of bubble size in the turbulent wake of a ventilated hydrofoil is not very clearly understood. Also, these processes will depend upon the liquid flow, air ventilation rate and the downstream distance from the turbine. The detailed understanding of the bubble coalescence and breakup events in the wake as a function of these parameters will aid to the development of physical models for bubble size distribution.

There have been numerous reports on the bubble breakup phenomena (Hinze 1955, Sevik and Park 1973, Hesketh et al. 1991, Liao and Lucas 2009), and similarly some studies have exclusively focused on coalescence of bubbles (Razzaque et al. 2003, Liao and Lucas 2010). Many previous studies have reported the occurrence of coalescence and breakup of bubbles or its effect on resulting bubble size distributions in different types of flow configurations such as air-sparged bubble columns (Crabtree and Bridgwater 1971, Prince and Blanch 1990, Olmos et al. 2001, Laari and Turunen 2003, Atkinson et al. 2003, Tse et al. 2003), a two-dimensional packed bed (Daeseong and revankar 2010), pipes (Hesketh et al. 1987, Andreussi et al. 1999, Frank et al. 2008), water jet (Martínez-Bazán et al. 1999) etc. However, to the best of our knowledge, there

are hardly any studies conducted in the wake of a turbine hydrofoil blade. The flow physics in the bubbly wake of a hydroturbine is markedly different as compared to these other flow configurations often reported. Specifically, there are very few reports on the prediction of bubble size in a turbulent bubbly wake flow. A detailed insight into the physical processes in the wake and its effect on the resulting bubble size has not been provided. Therefore, in the current chapter, we conducted a detailed investigation into the breakup and coalescence processes in the wake of a ventilated hydrofoil and also proposed a theory to predict the maximum stable bubble size for dilute dispersions in a turbulent bubbly wake.

4.2. Experimental Setup and Conditions

The experimental setup used is already described in Chapter 2. The NACA 0015 hydrofoil used in our experiments has a span of 190 mm and a chord length of 81 mm. As shown in Figure 4.1, a narrow spanwise slot allows air to be injected into the flow near the leading edge of the hydrofoil and the full width of the injection slot is used for measurements of oxygen uptake. This setup results in a dense spanwise bubbly wake and thus, in order to make bubble measurements, ventilation is limited to a narrow 9.6 mm wide slot (5% of span) at the center of the span. This configuration ensures that bubbles remain mostly within a narrow distance away from the centerline. The findings of Silberman (1957) indicated that the bubble diameter is independent of the orifice characteristics for a gas jet coming out of an orifice into a cross flow. Also, the bottom views of the bubbly wake show a minimal lateral drift of the bubbles. Based on our observation of the bottom views of bubbly wake, the study of Silberman and the fact that

slot width remained unchanged in our experiments, we posit that the bubbles obtained are a reasonable representative sample of the bubble population that exists when the full span is ventilated.

The water velocity in the experiments ranges from 3 to 10 m/s with the air ventilation rate in the range of 1 - 3 × 10^{-5} kg/s. The pressures inside the test-section and the air temperature under these conditions have been tabulated in Table 4.1. Under each experimental condition, two sets of bubble images are recorded at 50 and 1500 frames/s, respectively. Each data set consists of 2000 images acquired over a duration of 40 s. To examine the detailed dynamics of the bubbles in the wake, high speed imaging at 2000 frames/s is employed with an exposure time of 15 μs to prevent any blurring of bubbles in the images. The images are processed by the technique described in chapter 2.

V (m/s)	***Q*** **(**× 10^{-5} kg/s**)**	***P (kPa)***	***T*** **(K)**
10	3.00	49.8	294
10	1.00	49.5	294
7.5	2.26	72.5	294
7.5	1.00	72.7	294
5	3.00	89.5	294
5	2.50	89.8	294
5	2.00	89.6	294
5	1.50	89.6	294
5	1.00	89.8	294
3	1.00	98.0	294

Table 4.1: Pressure in the test-section and the air temperature at each experimental condition.

4.3. Results and Discussion

4.3.1. Mean bubble statistics

Experiments are performed to determine the mean bubble size statistics at ten different experimental conditions over four different water velocities (U = 10, 7.5, 5 and

3 m/s) and varying air ventilation rates (Q = 0.50, 1.00, 1.50, 2.00, 2.50, 3.00 $\times 10^{-5}$ kg/s). Table 4.2 below shows the mean bubble statistics for these different test cases at the farthest downstream location (i.e. x/c = 4.7, referred to as 'reference location' hereafter). The average void fraction is obtained by processing the bubble images. As presented in Table 4.2, this average void fraction increases with increased air ventilation at a fixed liquid velocity. A number of experiments are carried out at a liquid velocity of 5 m/s, with air ventilation rates increasing by three times from 1.0 $\times 10^{-5}$ kg/s to 3.0$\times 10^{-5}$ kg/s and the void fraction consequently increases from 0.032 to 0.065. For a fixed air ventilation rate of 1.0 $\times 10^{-5}$ kg/s, average void fraction increases from 0.028 to 0.047 as liquid velocity is increased from 3 to 10 m/s. This increment in void fraction can be explained based on the measurements of total number of bubbles in the flow and the resultant bubble size.

V (m/s)	Q ($\times 10^{-5}$ kg/s)	*Average void fraction, ϕ*	*Number of bubbles, N*/(1e6)	d_{99} (mm)	d_{32} (mm)	C_n	$d_{99.8}$ (mm)	d_{max} (mm)
10	3.00	0.091	2.382	0.88	0.54	0.61	0.95	0.95
10	1.00	0.047	1.805	0.73	0.43	0.59	0.78	0.78
7.5	2.26	0.059	1.325	0.96	0.60	0.62	1.03	1.03
7.5	1.00	0.036	1.068	0.84	0.51	0.61	0.90	0.90
5	3.00	0.065	0.782	1.27	0.81	0.64	1.38	1.38
5	2.50	0.057	0.723	1.25	0.79	0.63	1.35	1.35
5	2.00	0.050	0.677	1.22	0.77	0.63	1.31	1.31
5	1.50	0.042	0.645	1.15	0.73	0.63	1.24	1.24
5	1.00	0.032	0.573	1.08	0.68	0.63	1.16	1.16
3	1.00	0.028	0.242	1.51	0.97	0.64	1.62	1.62

Table 4.2: Bubble size characteristics obtained at different experimental conditions at the reference location. N is the total number of bubbles at each downstream location in the entire dataset of 2000 images.

In general, Table 4.2 shows that an increase in liquid velocity increases the number of bubbles and brings about a decrement in the size of the bubbles. This result

suggests a production of smaller bubbles upon the increase in liquid velocity, resulting in increased bubble surface area, and thus void fraction. Table 4.2 also presents the values of different characteristic diameters from our bubble size measurements. In our experiments, a more reliable estimate of the maximum stable bubble diameter is obtained from the cumulative size distributions. Accordingly, d_{99} or $d_{99.8}$, or the bubble diameter that is larger than 99% and 99.8% respectively, of all the bubble diameters in the population, is chosen as a representative maximum bubble size. The Sauter mean diameter, d_{32} is computed as:

$$d_{32} = \sum_{i=1}^{N} d_i^3 \Big/ \sum_{i=1}^{N} d_i^2 \tag{4.1}$$

where d_i is diameter of a single bubble and N denotes the total number of bubbles in the population. Further, to characterize the bubble size distributions in our experiments, we compute the value of another coefficient C_n which is defined as the ratio of d_{32} and d_{99}. C_n is an important design parameter and it can be used to estimate the corresponding value of d_{32} (provided d_{99} is known), which is important to determine interfacial area of dispersed phase, usually required for heat and mass transfer applications. As presented in Table 2, for the bubble populations in our experiments, C_n has an average value of 0.62 with minimal variations over all the experimental conditions. This value matches with that of 0.62 reported by Hesketh et. al (1987) for gas-liquid dispersions and 0.60 reported by Calabrese et al. (1986) for liquid-liquid dispersions.

4.3.2. Bubble size distributions at the reference location

In general, bubble populations with a minimum bubble size are expected to show a lognormal distribution, as reported in the previous studies of Hesketh et. al (1987) and Razzaque et al. (2003). Therefore, in order to further characterize the bubble populations in our study, we compare our bubble size distributions to standard log-normal distributions. It is found that generally the bubble size distributions at the reference location in our experiments indeed follow a log-normal pattern. The lognormal distribution function in number, $f(d)$ is given as

$$f(d) = \frac{1}{\sqrt{2\pi}\ln\sigma_g}\exp\left[-\frac{1}{2}\left(\frac{\ln(d/d_g)}{\ln\sigma_g}\right)^2\right] \tag{4.2}$$

where d_g and σ_g are the geometric mean size of the bubbles and geometric mean standard deviation, respectively and can be estimated from the raw data as follows:

$$d_g = \left(\prod_{i=1}^{N} d_i\right)^{1/N} \tag{4.3}$$

$$\log\sigma_g = \sqrt{\frac{\sum_{i=1}^{N}\left[\log d_i - \log d_g\right]^2}{N}} \tag{4.4}$$

Table 4.3 below presents the value of d_g and $\sigma_g$obtained by fitting bubble size data to a lognormal distribution for different experimental conditions:

U (m/s)	Q ($\times 10^{-5}$ kg/s)	d_g	σ_g	C_n'
10	3.00	0.30	1.66	2.26
10	1.00	0.25	1.57	2.20
7.5	2.26	0.32	1.70	2.28
7.5	1.00	0.28	1.64	2.25
5	3.00	0.43	1.83	2.29
5	2.50	0.42	1.82	2.29
5	2.00	0.41	1.81	2.29
5	1.50	0.39	1.79	2.29
5	1.00	0.36	1.76	2.29
3	1.00	0.49	1.95	2.24

Table 4.3: Fitting parameters used to fit bubble size distribution with a lognormal distribution at different experimental conditions. C_n' is defined in equation 5.

From the above table, it can be observed that at a fixed liquid velocity, the change in air ventilation rate does not affect the mean geometric size or the width of the distribution. However, both d_g and σ_g decrease as the average water velocity is increased, i.e. the bubble size distribution becomes wider and shifts towards left with increasing average water velocity at a fixed air ventilation rate of 1.0×10^{-5} kg/s. In the reported literature on bubble size distributions, the lognormal behavior of the bubble size distribution has been confirmed by the calculation of another parameter C_n', which is defined as $C_n' = d_{99.8}/d_{32}$. Further, based on lognormal distribution, it can be shown that C_n' is only a function of the width of distribution σ_g :

$$C_n' = \frac{d_{99.8}}{d_{32}} = \exp[-(2.5\, ln^2\sigma_g - 2.88 \ln \sigma_g)] \qquad (4.5)$$

For the obtained values of σ_g from bubble size distribution in our experiments, the value of C_n' is calculated and shown in Table 4.2. These values are close to 2.2 as reported before for lognormal bubble size distributions (Razzaque et al. 2003).

The calculation of C_n' parameter has important practical implications. Provided $d_{99.8}$ is known, it can yield an estimate of the value of Sauter mean diameter of a bubble population, which is very important for numerous practical applications concerning heat and mass transfer. As a consequence, the estimation of Sauter mean diameter essentially reduces to the determination of $d_{99.8}$. Based on Table 4.2, it can be pointed out that the values of $d_{99.8}$ and the maximum stable bubble size in the flow, d_{max} are almost equal, as evidenced in our experiments. Assuming that $d_{99.8}$ represents the maximum stable bubble size in the flow, the determination of d_{32} and d_{max} can be correlated. The estimation of d_{max} in a flow has been the subject of research for several studies beginning with that of Hinze (1955). Many authors such as Levich (1962), Sevik and Park (1973) and Hesketh (1987) have investigated the stable bubble size due to bubble breakup in low void fraction flows. In our study, we employ Hinze's theory to predict the maximum bubble size in the turbulent hydrofoil wake flow, which is presented in following section.

4.3.3. Stable bubble size in the turbulent hydrofoil wake

To estimate the maximum stable bubble size due to the bubble breakup, we choose a location in the wake closest to the hydrofoil. Compared with other measurement locations, the most breakup events associated with turbulent fluctuations are expected at this location (please refer to the following section for detailed discussions on the dominant regimes of bubble breakup and coalescence). The maximum stable bubble size in a flow-field is determined by a balance between turbulent pressure fluctuations and surface tension forces (Hinze 1955, Sevik and Park 1973, Prince and Blanch 1990, Levich 1962, Tikhomirov 1991). Turbulent fluctuations tend to deform or break the

bubble while surface tension forces resist such deformation. Considering a balance between these two forces, Hinze defined a critical Weber number as follows:

$$We_{Crit} = \frac{\tau}{\sigma/d_{max}} \tag{4.6}$$

where τ is the stress on the bubble surface due to turbulent fluctuations in the continuous phase, σ is the interfacial tension, ρ_d and ρ_c are the dispersed and continuous phase densities, respectively and d_{max} is the diameter of the largest stable bubble in the turbulent flow field. Hinze characterized the dynamic pressure force of the continuous phase as

$$\tau = \rho_c \overline{v^2} \tag{4.7}$$

where the mean-square spatial fluctuating velocity term, $\overline{v^2}$ has been estimated by Batchelor (1959) for homogeneous isotropic turbulence as

$$\overline{v^2} = 2\,(\epsilon d_{max})^{2/3} \tag{4.8}$$

where ϵ denotes the energy dissipation rate per unit mass. Hesketh (1987) approximated the local energy dissipation rate using the average energy dissipation $\bar{\epsilon}$ calculated from mean turbulent velocity profile in the flow.

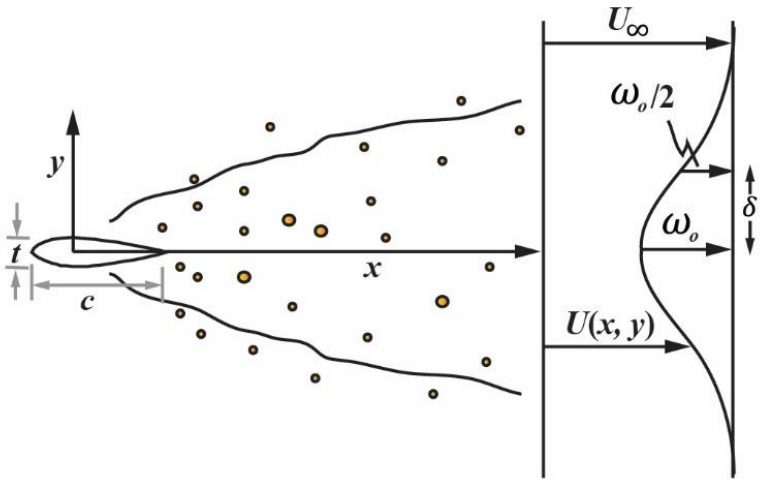

Figure 4.1: A schematic of the two dimensional bubbly wake

As shown in Figure 4.1, the liquid velocity at any location in the wake is a function of both *x* and *y* coordinates. The streamwise liquid velocity outside the wake is designated as U_∞ and the velocity at the centerline of the wake is denoted by $U_o(x)$. The difference $U_\infty - U(x,y)$ is the velocity deficit, ω, and the maximum velocity deficit at a particular location is $\omega_o\ [= U_\infty - U(x,0)]$. The distance between the wake centerline and the location where the velocity deficit is half the maximum is denoted by δ. At a sufficient downstream distance away from the hydrofoil in the wake, the mean and turbulence quantities attain self-preservation. Hence, ω/ω_o is solely a function of y/δ and the dependence upon the streamwise direction comes into play because of the streamwise variation of $\omega_o\ (x)$ and $\delta\ (x)$. According to Sreenivasan (1995), the ensemble average of the energy dissipation rate can be expressed as:

$$\langle\varepsilon\rangle = 0.035\frac{{\omega_o}^3}{\delta} \tag{4.9}$$

Combining equations (4.6) to (4.9); an expression for maximum stable bubble size can be obtained as:

$$d_{max} = \epsilon^{-\frac{2}{5}} \left(\frac{\sigma We_c}{2\rho_w} \right)^{\frac{3}{5}} \tag{4.10}$$

For the dispersions in air-water fluid pair, a critical Weber number of 1.1 is used, as reported by a number of prior studies (Prince and Blanch 1990, Broder and Sommerfeld 2002, Razzaque et al. 2003). As a result, d_{max} can be expressed as:

$$d_{max} = 2.67 \left(\frac{\delta}{\omega_o^3} \right)^{2/5} \left(\frac{\sigma}{\rho_w} \right)^{3/5} \tag{4.11}$$

Further, δ and ω_o at a particular downstream distance in the wake can be calculated from the expressions given below, which are deduced based on the velocities obtained from previous PIV measurements conducted at SAFL in the wake of a NACA0015 hydrofoil at different downstream locations:

$$\frac{\omega_o(x)}{U_\infty} = 0.12 \left(\frac{x}{c} \right)^{-\frac{1}{2}} \tag{4.12}$$

$$\frac{\delta(x)}{c} = 0.07 \left(\frac{x}{c} \right)^{\frac{1}{2}} \tag{4.13}$$

In our study, the above expressions were found to match with the velocity field derived from the bubble velocities. Note that although bubbles in a flow do not accurately trace the flow, yet the mean velocities of the bubbles are an accurate representation of the actual mean velocity field, provided that the bubbles are not accelerating.

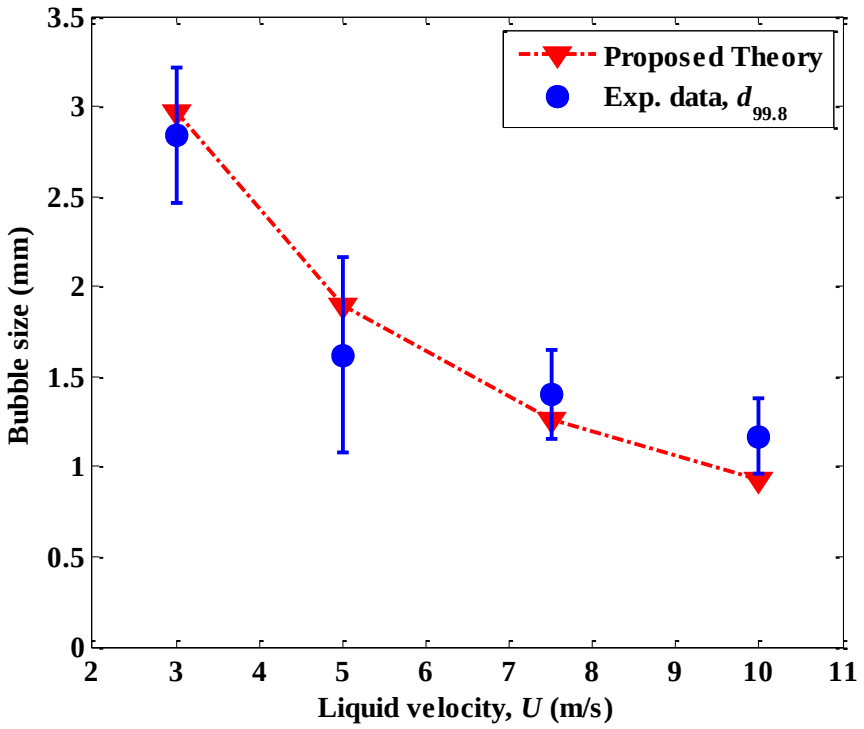

Figure 4.2: Comparison of maximum bubble size as proposed by our bubble dispersion theory and as observed at the viewing location closest to the hydrofoil. All experiments correspond to an air flow rate of 1.0×10^{-5} kg/s. The error-bars denote one standard deviation in the chosen experimental dataset at each flow condition.

Figure 4.2 above presents the comparison of the measured maximum bubble size with the largest stable bubble size, d_{max} predicted by theory. Although there is significant deviation in the experimental data, yet the mean values of the maximum bubble size closely matches the prediction from Hinze's theory. In general, the proposed theory has a slightly steeper variation in bubble size with respect to freestream velocity compared to the experimental data. It must also be pointed out that the flow conditions chosen for this comparison are the ones that correspond to a low ventilation flowrate of 1.0×10^{-5} kg/s and at a location closest to the hydrofoil. This ensures that measured

bubble sizes are a result of bubble breakup processes and are not influenced by the occurrence of coalescence in the bubbly wake.

4.3.4. Variation of mean bubble statistics in the wake

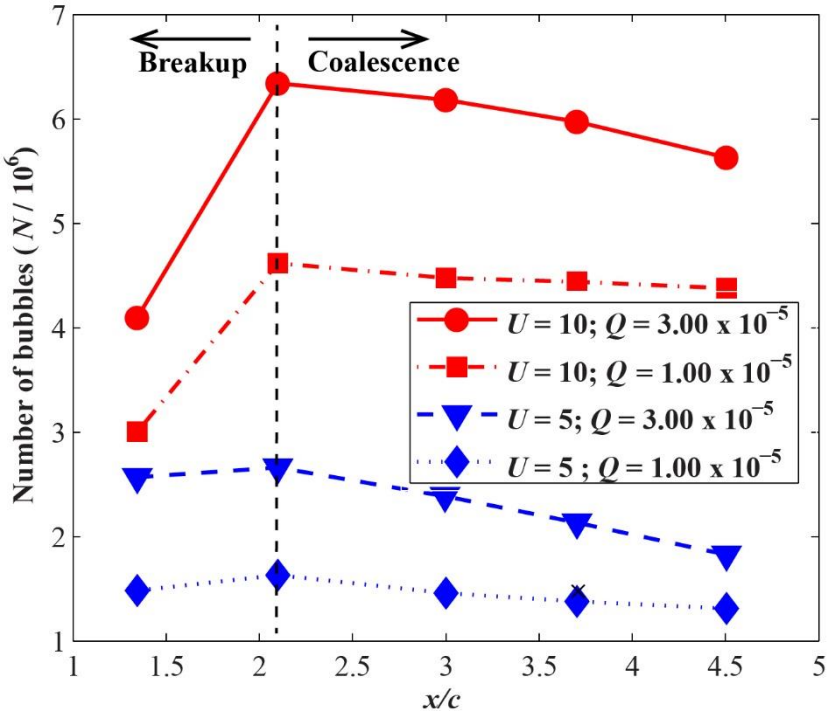

Figure 4.3: Number of bubbles passing through different downstream locations in the wake. N is the total number of bubbles at a particular downstream location in the entire dataset of 2000 images. The units of U and Q are m/s and kg/s, respectively.

The mean bubble statistics in the hydrofoil wake are investigated at different downstream locations in the bubbly wake by examining the number of bubbles passing through each viewing section for the entire dataset for each experimental condition. Figure 4.3 above shows the number of bubbles present at each viewing section at four different experimental conditions comprising two different water velocities and air ventilation rates. As the figure shows, for all the experimental cases, the number of bubbles increases from x/c = 1.3 to x/c = 2.1, and starts decreasing upon moving

downstream from x/c = 2.1. The change in the number of bubbles at different downstream locations is related to the relative significance of competing breakup and coalescence events in the wake. It is observed that the predominance of the breakup and coalescence events in the wake varied at different locations. There exists a break-up dominant regime close to the hydrofoil, whereas coalescence dominates farther in the wake. In addition, the slopes of the curves in the breakup-dominant and coalescence-dominant regimes are governed by liquid velocity and air ventilation rates, respectively. The occurrence of distinct breakup and coalescence regimes in the hydrofoil wake is further confirmed by the measurements of d_{32} at different locations as shown in Table 4.4:

$\boldsymbol{U}$ (m/s)	$\boldsymbol{Q}$ ($\times 10^{-5}$ kg/s)	$\boldsymbol{d_{32\|x/c\,=\,1.3}}$ (mm)	$\boldsymbol{d_{32\|x/c\,=\,2.1}}$ (mm)	$\boldsymbol{d_{32\|x/c\,=\,3.0}}$ (mm)	$\boldsymbol{d_{32\|x/c\,=\,4.7}}$ (mm)
5	1.00	0.85	0.63	0.67	0.68
5	3.00	0.97	0.71	0.76	0.81
10	1.00	0.82	0.42	0.42	0.43
10	3.00	1.02	0.51	0.50	0.54

Table 4.4: Variation of d_{32} at different downstream locations in the hydrofoil wake for selected test-cases

As Table 4.4 shows, for all the test cases, d_{32} decreases from x/c = 1.3 to x/c = 2.1, and increases upon moving downstream from x/c = 2.1 to x/c = 4.7, confirming the distinct occurrence of bubble breakup close to the hydrofoil and coalescence at a farther downstream location in the wake. It is noteworthy that no appreciable change in bubble size is observed between x/c = 3.7 and x/c = 4.7.

4.4. The Coalescence-dominant regime

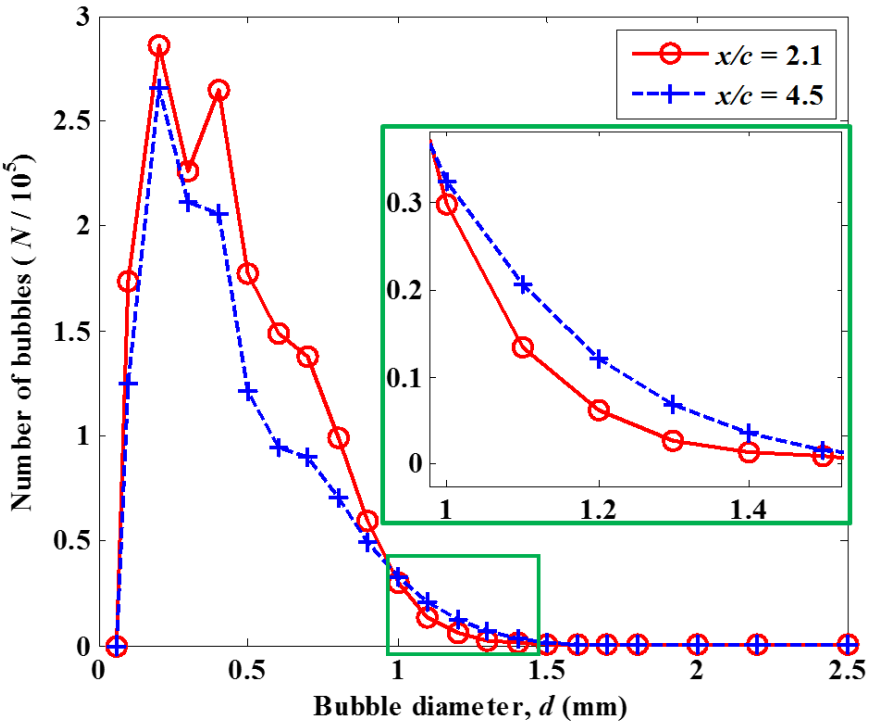

Figure 4.4: Number of bubbles distribution at two downstream locations in the wake showing the occurrence of bubble coalescence. Both the distributions are for U = 5 m/s and Q = 3.0 × 10^{-5} kg/s. Inset is a magnified view of the green rectangle shown on the plot.

Figure 4.4 presents BSDs at x/c = 2.1 and x/c = 4.7, respectively. As shown in the figure, upon moving from x/c = 2.1 to x/c = 4.7, the number of bubbles less than 1 mm, especially between 0.3 – 0.9 mm, decrease while there is an increase for bubbles of size larger than 1 mm (see inset). This result suggests that between these two downstream locations in the wake, the bubbles in 0.3 – 0.9 mm size range undergo coalescence, producing bubbles in the larger size range. The resulting larger bubbles do not further undergo coalescence because of the reduced efficiency of coalescence at larger sizes. Previous reports in the literature have shown that the coalescence efficiency between two bubbles depends strongly on the size of the bubbles involved (Liao and Lucas 2010). As

pointed out by them, coalescence process consists of three stages: (1) Collision of bubbles leading to entrapment of a liquid film between them; (2) Bubbles staying in contact with each other till the liquid film drains to a critical thickness; (3) Rupture of the liquid film resulting in coalescence. The duration of the collision is limited by the velocity fluctuations existing in the flow, and coalescence occurs only when the time of interaction of two bubbles (t_{contact}) is sufficient to allow for the intervening film to drain out to a critical rupture thickness, i.e., t_{contact} exceeds the film drainage time (t_{drainage}). According to Coulaloglou (1979), the coalescence efficiency is given by $\exp\left(-t_{\text{drainage}} / t_{\text{contact}}\right)$, and drainage time has been reported to vary as the square of the equivalent diameter of the two colliding bubbles (Davis et al. 1989, Chesters 1991, Luo 1993). Thus, the smaller the coalescing bubbles, less is the drainage time and greater the coalescence efficiency. This observation has been confirmed by our experiments in the horizontal turbulent hydrofoil wake. Figure 4.5 shows two separate cases of bubble interaction illustrating the dependence of bubble coalescence upon bubble size. As the figure shows, the smaller bubbles coalesce rapidly as they come into contact (referred to as 'immediate coalescence' by Liao and Lucas 2009), whereas the larger bubbles need to remain in contact for a much longer period for coalescence to take place. As shown in Figure 4.5b, even after the formation of a liquid film between the two bubbles, the velocity fluctuations around the bubble might separate them as the bubbles acquire sufficient energy. The dependence of coalescence efficiency on size explains the preferential coalescence of bubbles in the size range of 0.3 – 0.9 mm compared with that of larger bubbles. Further, as reported by Crabtree and Bridgwater (1971), in our

experiments coalescence of bubbles was observed to occur along the diagonals (especially when a trailing bubble is about to overtake a leading bubble) and such events were much more abundantly present than the occurrence of bubble coalescence upon head-on interaction of the bubbles.

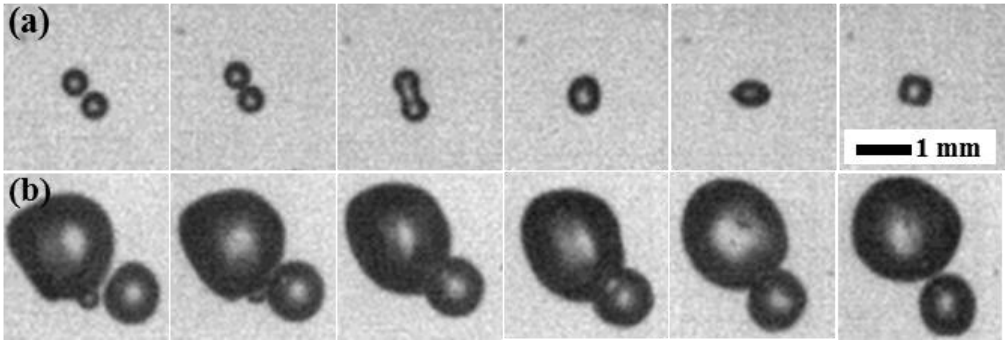

Figure 4.5: (a) Immediate coalescence of two small bubbles. (b) Contact of bubbles, film rupture and separation of bubbles. The scale bar applies to all the images.

The careful investigation of BSD in the coalescence-dominant regime also reveals the presence of extremely large individual bubbles with diameters above 4 mm. The generation of such large size individual bubbles through a successive coalescence route seemed unlikely. Hence, to explain the occurrence of these extremely large bubbles, we carried out systematic and careful investigations into the formation of such large size bubbles through high speed imaging of the bubbly wake. Our observations revealed the occurrence of a 'cluster-coalescence' mechanism, whereby more than two bubbles can approach and coalesce simultaneously. Figure 4.6 shows an example of such process. As the figure shows, in a cluster-coalescence process, many bubbles simultaneously approach together and concomitant multiple film formation and film drainage events occur, generating a large size bubble.

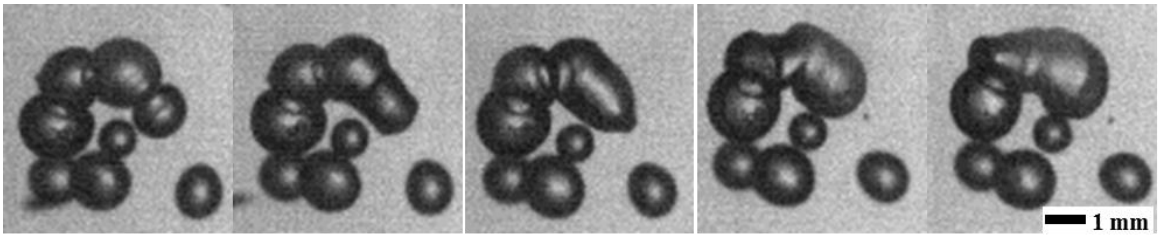

Figure 4.6: Occurrence of 'cluster coalescence'. The scale bar applies to all the images.

Finally, we focus our attention on the small size range of the BSD as presented in Figure 4.4. It can be observed that at both the downstream locations, there is a large number of small size bubbles (smaller than 0.5 mm) present in the flow. This is somewhat surprising since the small bubbles might end up coalescing by virtue of their extremely high coalescence efficiency. In the reported literature on gas-liquid systems in coalescence-dominant regime, there are only a few studies which report the presence of significant number of very small size bubbles in addition to large bubbles in the flow (Martin 1996, Machon et al. 1997). Martin (1996) proposed that such small bubbles may be generated by re-shedding from the rim of very large bubbles and may survive coalescence as a result of their small size among much larger bubbles. In our experiments, it is observed that the flow conditions favoring coalescence and a consequent increase in d_{32} also showed a simultaneous rise in the number of small size bubbles upon moving downstream in the wake. Although this appears counter-intuitive, yet it seems to suggest a strong link between the generation of large bubbles through coalescence and the number of these small bubbles. To get an insight into this, we carefully investigated the high speed videos of hundreds of binary coalescence events. In some of these events, it is observed that post-coalescence, the coalesced bubble

undergoes severe shape oscillations forming a spherical or spherical-cap bubble, and sometimes undergoing a minor pinch-off. Figure 4.7 shows such a process of coalescence-mediated breakup of small bubbles (Ohnishi et al. 1999, Tse et al. 2003). As the figure shows, rapid deformation during coalescence produces lobes at the ends of the original bubbles, and these lobes can be successively broken into microbubbles bubbles due to Rayleigh instability. Note that although the formation of these lobes are invariably observed in a coalescence event, often the pinched off microbubble is obscured by the coalescing bubble or large bubble present nearby.

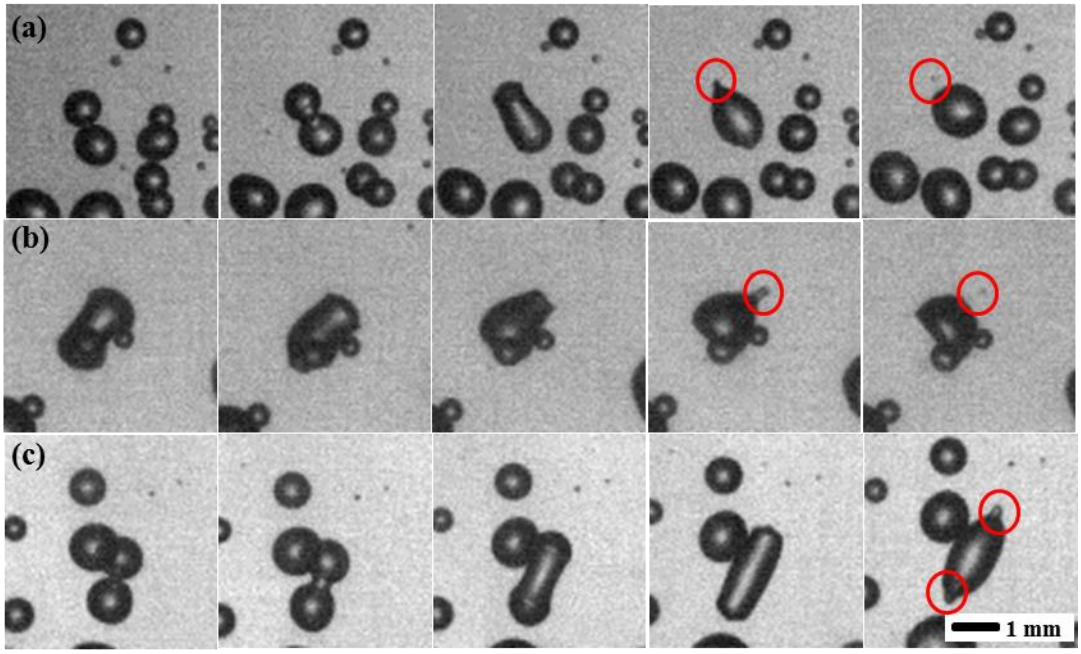

Figure 4.7: (a), (b), (c): Three different cases of occurrence of 'coalescence-mediated breakup'. The scale applies to all the images.

In summary, the contact and collision of bubbles is the very basis of coalescence process (Liao and Lucas 2010) and such collisions are augmented by the presence of increasing number of bubbles in the flow. In other words, an increase in air ventilation

rate augments the occurrence of coalescence events in the coalescence-dominant-regime of the wake, leading to an increase in Sauter mean diameter of the bubbles. Since a larger air ventilation increases the void fraction in the flow, the Sauter mean diameter shows a significant dependence on the void fraction. In our experiments, the bubble Sauter mean diameter can be characterized as function of void fraction φ at a fixed average liquid velocity as follows:

$$d_{32} \propto \sqrt{\varphi} + c \tag{4.14}$$

where c is a constant for air-water fluid pair and the system properties. Similar dependence of bubble size upon the void fraction has been reported previously for coalescence-dominant regime by other authors (Calderbank 1958, Razzaque et al. 2003).

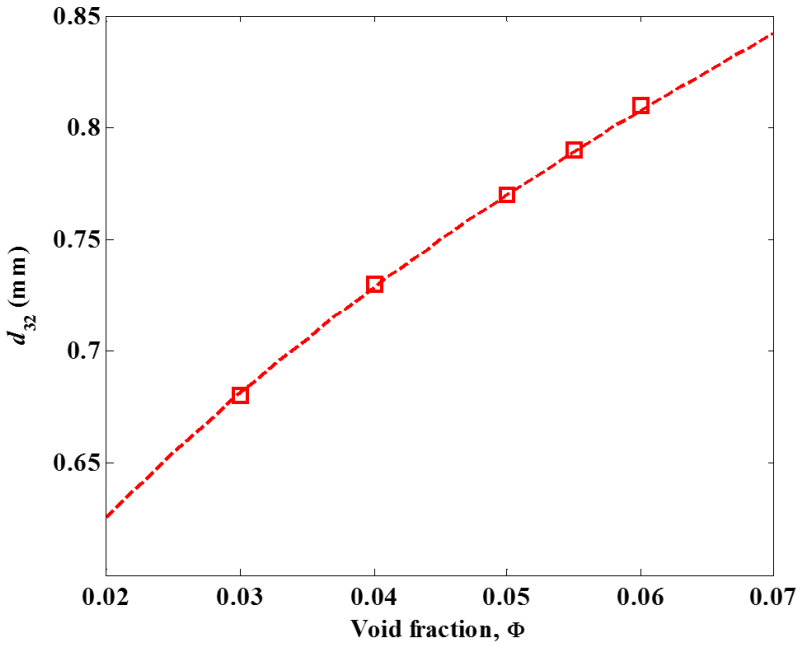

Figure 4.8: Dependence of $\boldsymbol{d_{32}}$ upon void fraction, $\boldsymbol{\varphi}$, at a fixed continuous phase velocity of 5 m/s. The squares show the values from the experiments while the dotted line shows the fit according to equation (4.14).

Figure 4.8 shows this dependence of d_{32} upon the void fraction. As the figure shows, d_{32} increased from 0.67 mm at φ = 3% to 0.81 mm at φ = 6%. Further, there is an excellent agreement between the measurements of Sauter mean diameter at different void fractions from our experiments and the fitting expression as defined in equation (4.14).

4.5. The breakup-dominant regime

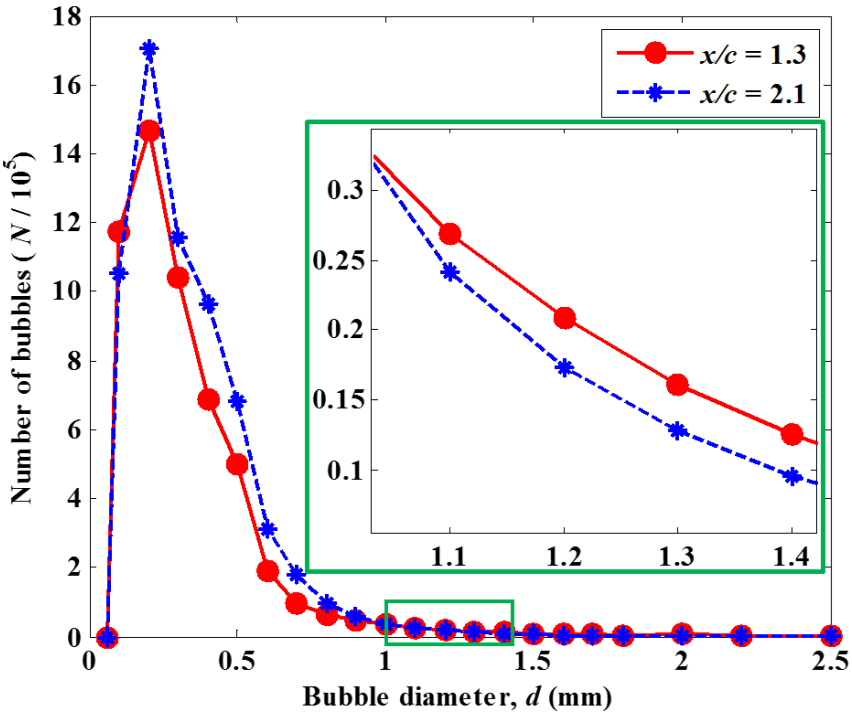

Figure 4.9: Number of bubbles distribution at two downstream locations in the wake showing the occurrence of bubble breakup. Both the distributions are for V = 10 m/s and Q = 3.0 × 10^{-5} kg/s. Inset is a magnified view of the green rectangle shown on the plot. The axis labels for the inset are the same as the original plot.

To further investigate the breakup phenomena, the number of bubbles distribution at *x/c* = 1.3 and *x/c* = 2.1 is plotted as shown in Figure 4.9. As the figure presents, the location closer to the hydrofoil is marked by a greater number of large size bubbles

(larger than 1 mm, as shown in the inset). On the other hand, at a further downstream location of x/c = 2.1, a larger number of smaller bubbles are present in the flow. This suggests that the larger bubbles present at x/c = 1.3 split to produce these smaller bubbles. Our observations indicate that large size bubbles readily undergo deformation and thus are more likely to split into small size bubbles. High speed videos of the bubbles in the breakup-dominant-regime shows that the bubble surface is in continuous irregular motion caused by the turbulent eddies interacting with its surface. These deformations are mainly observed in the large-diameter (> 1 mm) ellipsoidal bubbles, which have a lower internal pressure and thus, are easily deformed. Further, these deformations occur when the diameter of a bubble is larger than the Kolomogorov length scale, and is of the order of the size of energy-containing eddies. The eddies that are larger than the bubble size merely carry the bubbles, whereas the eddies much smaller than the bubbles do not have ample energy to break it (Laari and Turunen 2003). But, the deformation caused by the eddies of a similar size as the bubble sets up motion in the gas phase and destabilizes the bubble due to an increase in surface energy. When the amplitude of the oscillation becomes large, it makes the bubble surface unstable. Then bubble surface starts to deform and stretch in one direction, giving rise to a neck that contracts further to cause breakage. Figure 4.10 below shows three examples of such breakup events as observed in the breakup-dominant regime.

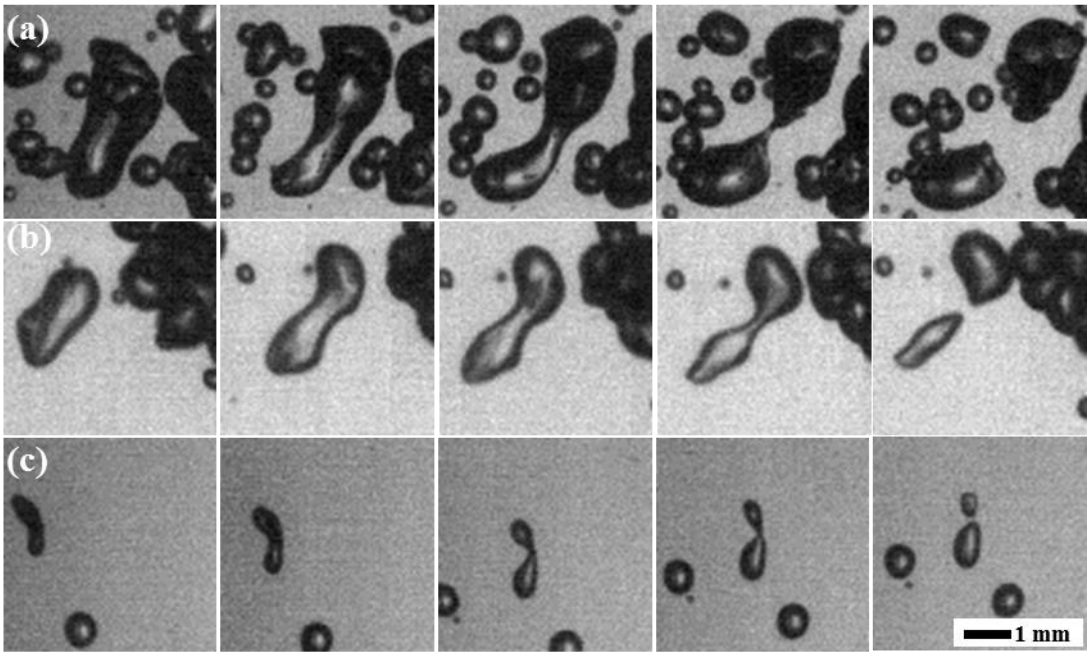

Figure 4.10: (a), (b) and (c): Three different cases of bubble breakup caused by turbulent pressure fluctuation or by bubble-eddy collision. The scale applies to all the three cases.

The above images show an initial bubble ranging from 1 – 3 mm undergoing breakup into two individual bubbles of almost equal size. There is no generation of small daughter bubbles observed in these images. This is not surprising since Hesketh et al. (1991) also experimentally found that bubble breakup is essentially always binary in horizontal pipe flow. However, our high-speed imaging observations revealed another mechanism of generation of these microbubbles through bubble collision and subsequent tearing as shown in Figure 4.11. As the figure shows, a small bubble of 0.2 mm in diameter enters into the wake region of a leading bubble that is more than 2 mm in length. In the wake of the larger bubble, the small bubble undergoes acceleration, and finally collides with the preceding bubble at a speed higher than the liquid velocity. Such acceleration of a small bubble caused in the wake of a larger bubble has been discussed

before by Bilicki and Kestin (1987). In some cases, such a collision may cause tearing of the leading bubble and the teared portion of the bubble can further get sheared to microbubbles observed in the images.

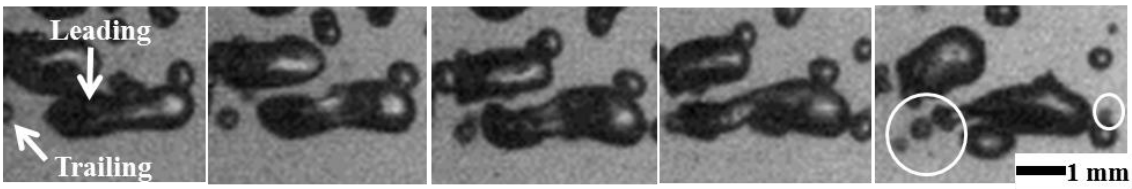

Figure 4.11: Bubble breakup caused by bubble tearing. Flow is from left to right. The image sequences are from left to right, and top to bottom row.

As the air gets entrained into the wake, it breaks down into small bubbles because of continuous phase hydrodynamics and interfacial interactions. Such breakup can be caused by turbulent velocity fluctuations, bubble collisions, viscous shear stresses, interfacial instability or other shear effects (Liao and Lucas 2009). However, in our experiments, apart from the coalescence-mediated breakup, the breakup of bubbles can be primarily attributed to turbulent velocity fluctuations, bubble-eddy collisions in the flow and bubble tearing resulting from bubble collisions. Our observations do not show a significant occurrence of coalescence events in the breakup dominant regime. Due to high turbulent pressure fluctuations in the near-wake of the hydrofoil, there is significant bubble breakup. In this breakup-dominant regime, where coalescence effects are not dominant, our proposed theory of bubble dispersion (refer to section 4.3.3) can predict maximum bubble sizes quite accurately.

4.6. Conclusions

In this chapter, some insights into the breakup and coalescence phenomena occurring in the horizontal turbulent bubbly wake of a ventilated hydrofoil are presented.

The bubble images in the bubbly wake are captured at five different downstream locations through a shadow imaging technique and the bubble images are processed through an image-analysis technique proposed in chapter 2. The experiments are carried out at ten different flow conditions with liquid velocity varying in the range of 3 – 10 m/s and air ventilation rates spanning 0.5 - 1.5 $\times 10^{-5}$ kg/s. For the bubble size data obtained at these flow conditions, a dispersion theory to predict the bubble size is presented for dilute dispersions in a turbulent wake flow. The proposed dispersion theory is in a reasonably good agreement with the bubble size measured from the experimental data in the breakup dominant regime at low ventilation rates. For the bubble population in our experiments, the parameter C_n (= d_{32}/d_{99}) obtained experimentally has a mean value of 0.62, which matches well with the value predicted by prior studies, both for gas-liquid dispersions (Prince and Blanch 1990) and liquid-liquid dispersions (Levich 1962). Further, bubble sizes from our experiments fit a lognormal distribution. This is confirmed by the good match of the value of parameter $\boldsymbol{C_n'}$, which can be expressed solely in terms of the width of the bubble size distribution. It is found that the obtained ratio of 2.2 matches perfectly with the previous reports of lognormal bubble size distributions (Razzaque et al. 2003).

Next, the number of bubbles and Sauter mean diameter is analyzed at different downstream locations to explore the occurrence of bubble breakup or coalescence. Based on the number of bubbles, it is observed that breakup dominates in the wake till a downstream distance of *x/c* = 2.1 (breakup-dominant regime) while coalescence is predominant farther down in the wake (coalescence-dominant regime). It is understood

that near the hydrofoil, the velocity fluctuations of the underlying turbulence of the jet results in deformation forces that exceed the confinement forces due to surface tension leading to more pronounced bubble breakup. The breakup continues while the bubbles are convected downstream to regions of lower dissipation rates, where breakup effects are superseded by the occurrence of coalescence.

Through high-speed imaging, we observed that coalescence process is augmented by increase in number of collisions between bubbles, which increases with number of bubbles in the flow, or the air ventilation rate. With an increase in air ventilation, the bubbles undergo successive coalescence causing an increment in Sauter mean diameter. Based on our experimental data, an expression for d_{32} is proposed in terms of the void fraction in the flow at a fixed continuous phase velocity. The BSD at two different locations in the coalescence-dominant regime show that bubbles lesser than 1 mm undergo coalescence to produce larger bubbles. Further, it is also observed that small bubbles undergo "immediate coalescence" whereas the larger bubbles need to remain in contact for a longer time to coalesce. The presence of the extremely large bubbles (above 4 mm in diameter) is attributed to a phenomenon called "cluster coalescence". The presence of a large concentration of microbubbles in coalescence-dominant regime is found to be linked with the coalescence process through a 'coalescence-mediated breakup' mechanism. As far as breakup-dominant regime is concerned, two possible mechanisms are considered most important contributors to the bubble breakup. The breakup caused by the turbulent velocity fluctuations begins with a deformation on a large size bubble, stretches in one direction, giving rise to a neck that contracts to cause

bubble breakage. In our experiments, such breakup events are always observed to be binary and no generation of microbubbles is observed, consistent with the assertion of Hesketh (1991) for a horizontal pipe flow. Instead, the generation of these microbubbles can be attributed to a bubble collision and tearing process. In the wake of a large leading bubble, a small bubble might accelerate and collide with the leading bubble tearing away a portion of it, resulting in microbubbles observed in BSD.

Overall, this study provides the bubble size distributions obtained in the turbulent bubbly wake of a ventilated hydrofoil at different downstream locations in the wake. The BSDs are supported by actual observations of breakup and coalescence obtained from high speed imaging. And finally, expressions are provided for the prediction of Sauter mean diameter at different flow conditions, both in the breakup-dominant and coalescence-dominant regimes. In sync with the gas transfer measurements at the same conditions, these bubble size measurements can serve as a test-bed for computational fluid dynamics (CFD) simulations of an auto-venting hydroturbine through the use of a ventilated hydrofoil. These results provide a rich experimental dataset that can be used by researchers to verify their CFD model against known bubble size distributions in a flow that simulates the wake of a vented hydroturbine. The next chapter discusses the gas transfer characteristics and its relationship with the bubble size in the wake of a ventilated hydrofoil.

Chapter 5. Mass transfer studies across ventilated hydrofoils: A step towards hydroturbine aeration.

Much of the design of auto-venting hydroturbines is currently performed with computational fluid dynamics (CFD) simulations. However, there is little information available to test and verify the performance of these simulations regarding gas transfer and bubble size distribution. This chapter investigates the performance of a water tunnel test-bed for CFD simulations of an auto-venting hydroturbine through the use of a ventilated hydrofoil. Bubble size distributions are measured by a shadow imaging technique and found to have a Sauter mean diameter of 0.9 mm for a reference case. Higher liquid velocities, a lower airflow rate and a higher angle of attack all resulted in a greater number of small bubbles and a lower weighted mean bubble size. Bubble-water oxygen transfer is measured by the disturbed equilibrium technique. The gas transfer model of Azbel (1981) is utilized to characterize the liquid film coefficient for oxygen

transfer, with one scaling coefficient to reflect the fact that characteristic turbulent velocity is replaced by cross-sectional mean velocity. The value of the coefficient is found to stay constant at a particular hydrofoil configuration while it varied over a narrow range of 0.52-0.60 for different hydrofoil angles of attack. This suggests that it is an appropriate coefficient for flow over a ventilated hydrofoil and possibly other flow situations. These results can be used by investigators to test and verify their CFD model against known bubble size distributions and gas transfer in a water tunnel flow that has important similarities to an auto-venting hydroturbine.

5.1. Background and literature review

Due to the depletion of fossil fuel supplies, global climatic changes and concern over nuclear waste management, the electric power industry is focusing attention on renewable energy technologies such as hydropower. Conventional hydropower has the potential to contribute a substantial portion of our energy requirements. However, the water discharged by hydropower facilities is of increasing concern due to its effect on downstream water quality (March et al. 1992, Gulliver and Arndt 1992). This decreased water quality arises from two different mechanisms: increased dissolved gases such as nitrogen over high spillways and greatly diminished oxygen content in the water discharged from hydroturbines to the downstream environment.

The impoundments necessary for creating the hydraulic head to operate conventional hydroturbines can degrade water quality. The residence time of water within these reservoirs is long and processes such as respiration by aquatic plant and animal life, biodegradation of organic materials in the sediments, oxygen-consuming chemical

reactions, etc. can decrease the DO levels, especially at greater depths (i.e. the hypolimnion) within the reservoir. Thermal stratification due to solar heating enhances conditions for low DO in the hypolimnion. Such a system, being hydrodynamically stable, inhibits mixing between layers and isolates the bottom water from atmospheric oxygen. Only surface waters are replenished with oxygen through gas transfer processes resulting from wave action (Gulliver 1998). Thus, oxygen concentration drops as water depth increases, as shown in Figure 5.1.

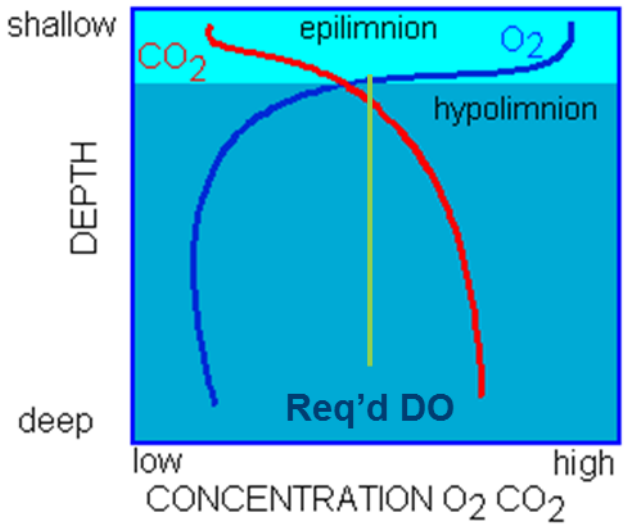

Figure 5.1: The variation in concentration of O_2 and CO_2 across different water depths (adapted from Scott et al. 2015)

Hydropower projects often have hydroturbine intakes located in the hypolimnion where DO levels may drop to anoxic conditions (Daniil and Gulliver 1991, Cong et al. 2011). Hypolimnetic anoxia in turn leads to trace metals, nutrients, and hydrogen sulfide being released from sediments and a drop in the pH of the water endangering fish and other aquatic life in downstream rivers (O'Boyle et al. 2009). Often, air injection is

suggested as a method to improve DO concentration in lakes and rivers (Weiss et al. 1996, Buscagalia et al. 2002, McGinnis et al. 2004, Alp and Melching 2011). Research on oxygen mass transfer between air and water has focused on free surface flows viz. gas transfer in spillway discharges (Hibbs and Gulliver 1997, Parkhill and Gulliver 1997, Urban et al. 2008). The auto venting turbine (AVT) has been proposed as a cost-effective and promising technology that can be employed to mitigate the problems associated with low DO concentration in the hydroelectric releases (Raney and Arnold 1973, Raney 1977). The AVT is a self-aspirating hydroturbine designed to aerate the turbine discharge through ports located at low pressure regions which are connected to the atmosphere. Air released to the water from these ports breaks up into small bubbles due to the water's high velocity and turbulence. Oxygen transfer is augmented by the high interfacial area of these bubbles (Thompson and Gulliver 1997).

In the late 1980's the Tennessee Valley Authority (TVA) started an initiative to develop physical modeling and numerical modeling tools for auto-venting turbine design and to demonstrate auto-venting turbine technology with a full-scale installation. Working together with Voith Hydro, Inc. led to the study and development of a new auto-venting runner for the Norris Dam site in Tennessee. Several venting options were evaluated using air injection including a redesigned turbine hub, or deflector; discharge edges of the turbine blades; coaxial diffuser; discharge ring; draft tube cone; and a combination of these (for e.g. central aeration, distributed aeration and peripheral aeration) as shown in Figure 5.2.

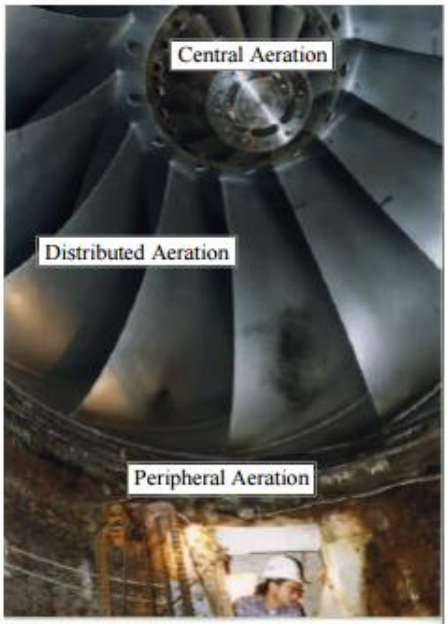

Figure 5.2: Different aeration strategies in AVTs for Norris Dam (adapted from Hopping et al. 1997; reproduced with permission from ASCE)

In the early 1990's, physical model studies, of a new runner design showed an increase in capacity of 7 percent and efficiency of 1.8 percent when not aerating. While aerating, the results showed increased efficiency while operating with the discharge edges presumable due to reduced flow separation at high head/high gate conditions. The discharge ring, draft tube cone, and combination of discharge edge and draft tube cone provided a reasonable balance between efficiency losses and aeration performance. The largest efficiency losses were observed with the coaxial diffuser (Hopping et al. 1997). Following the model studies, full scale auto-vented turbine runners were installed at Norris Dam in Tennessee. Using a variety of aeration techniques, an average DO level of 5.5 mg/L was obtained during low DO flows. This is near the target level of 6 mg/L. Auto vented turbines are an exciting technology, but require more investigation. Like

most water resource technologies, AVTs are designed uniquely for each site. This can be an expensive process of rendering physical models to test the proposed design. Numerical models can be used in the design process to avoid rendering physical models, but there are a limited number of models focused on predicting DO uptake of AVTs. Research must be done to close the gap from a numerical flow field in a turbine to predicted DO uptake to improve the design of AVTs (Monson 2013).

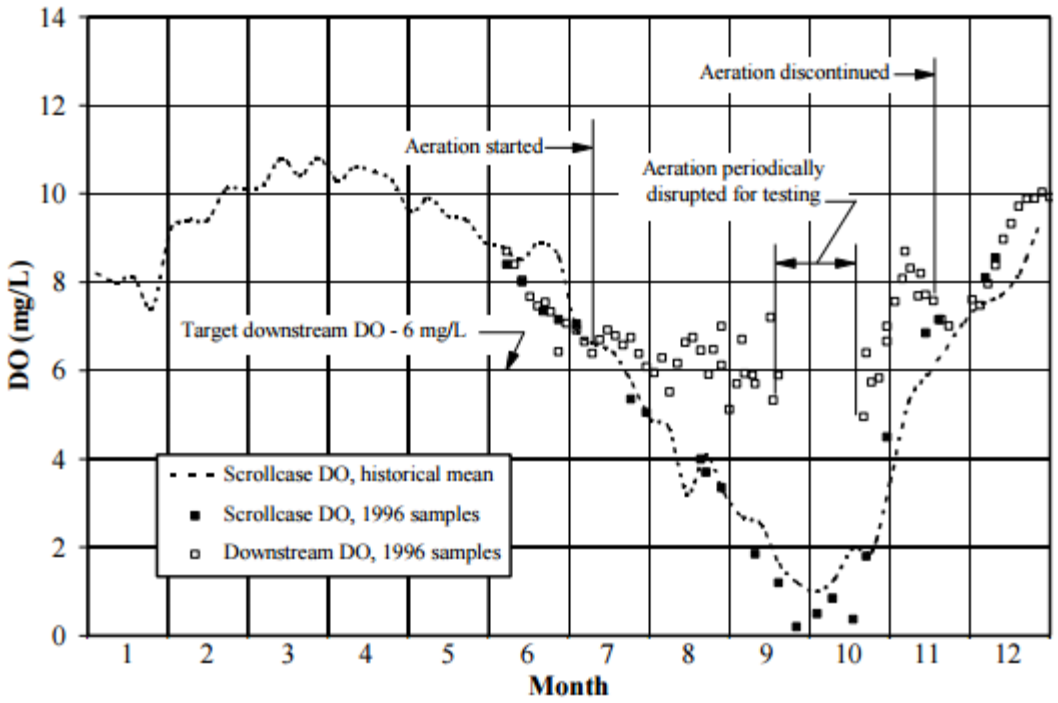

Figure 5.3: Dissolved oxygen improvement for Norris dam (adapted from Hopping et al. 1997, reproduced with permission from ASCE)

Relatively limited research has been undertaken on optimizing the performance of auto venting systems. There are three important factors influencing the performance of an AVT: the quantity of entrained air, the bubble sizes and the rate of oxygen transfer from the bubbles. Further, computational models to study the impact of entrained air on the

flow field and vice versa need to be developed. Such computational models need to quantify DO transfer as a function of flow conditions occurring in AVTs. To validate such a computational model, a dataset that allows quantitative analysis of aeration statistics for different hydroturbine blade hydrofoil designs is required. Such a dataset must provide information on bubble sizes, void fraction in the wake and the rate of oxygen transfer in the wake as a function of the different flow parameters**.** An aeration test-bed should be capable of testing these computational codes using configurations similar to an AVT. Such an aeration test-bed will advance the development and implementation of aerating hydroturbines at hydropower facilities, reduce the cost and regulatory uncertainty prior to hydropower development and enhance the aeration design capabilities.

In this study, a series of air injection experiments were conducted on a hydrofoil at several hydrodynamic conditions to investigate the effects of flow field on the size of the bubbles generated and the resulting rate of oxygen transfer. Experiments conducted to establish the methodology for creating a test bed were designed to study the impact of varying water velocities, airflow, and hydrofoil orientation (angle of attack) on the bubble sizes generated, void fraction in the wake, and oxygen transfer from the bubbles. A one-dimensional mass transfer model is developed to lend insight into the mass transfer characteristics observed in these experiments.

5.2. Experimental Setup and Conditions

Fifteen different experiments were conducted at test section water speeds of 5, 7.5 and 10 m/s, ventilation gas flow of 10, 20 and 30 SLPM per unit span and hydrofoil angle

of attack (*AoA*) of 0, 4 and 8 degrees. For the bubble size analysis experiments, only 5% of the air injection slot was left unmasked and the air flow rates were reduced to 5% of those used in the gas transfer testing. Thus, for any air flow test condition, the air flow rate per unit slot length was kept constant. The bubbly wake images were obtained at 3 streamwise distances of 109, 243, and 377 mm downstream of the hydrofoil center (or 1.3, 3.0 and 4.7 times the chord length, respectively.) The resulting bubble diameters obtained from the 377 mm location was chosen because it was believed to have the best view of the bubbles. The experimental setup and the image processing techniques for measurements of bubble size are similar to those described in Chapter 2. However, new instrumentation was required to monitor water temperature and dissolved oxygen concentration. A YSI thermistor probe was used to monitor water temperature in the water tunnel. An Omega Engineering FMA-2609A mass flow controller is used to set and measure airflow to the hydrofoil. Two Hach luminescent dissolved oxygen (LDO) probes and controller are used to measure DO concentration in both the settling chamber and the elbow vane downstream of the diffuser.

A degassing loop was developed and constructed at SAFL to strip dissolved gasses from the water in the high speed water tunnel. Water is withdrawn from the bottom of the tunnel upstream of the test section and pumped up to a degassing chamber with a diameter of 0.45 meters and a height of 4.8 meters for a chamber volume of approximately 0.76 m3. The water is discharged into the chamber through eight randomly oriented nozzles, creating a cloud of droplets falling through the chamber. Dissolved gasses are stripped from these droplets by applying a vacuum pressure as low as half an

atmosphere. This vacuum pressure is created by the free-jet water tunnel at SAFL which uses gravity fed river water through a contraction causing a venturi affect to create a vacuum pressure which is translated to the nearby degassing chamber via a pipe. When the droplets have passed through the chamber, they collect at the bottom and are conveyed by gravity through a pipe to the high speed water tunnel just upstream of the motor. The degassing loop was created to improve the degassing capabilities of the high speed water tunnel at SAFL. This system reduces the amount of time taken to degas the high speed water tunnel between aeration experiments. The dissolved oxygen (DO) concentrations could be reduced to an acceptable starting concentration of approximately 4 ppm from super saturated concentrations in excess of 8 ppm in less than 24 hours.

5.3. Mass Transfer Model

A one-dimensional model of the change in dissolved oxygen (DO) concentration in the tunnel was developed to fit the results of the physical experiments to a mass transfer theory using a single coefficient. The simplified conservation equation for the concentration of oxygen in a section of the tunnel is given by equation 5.1 as:

$$U\frac{dC}{dx^*} = k_L a\,(C_s - C) \tag{5.1}$$

where C refers to DO concentration and C_S corresponds to equilibrium DO concentration in a particular section of the tunnel, x^* refers to a moving co-ordinate system given as $x^* = x - Ut$, U is cross-sectional mean velocity, k_L is the liquid film coefficient for transfer of a volatile gas across the bubble-liquid interface, and a is specific surface area of bubbles (or the surface area of bubbles divided by volume associated with those bubbles), given

by equation 5.2 below:

$$a = \frac{A_{\mathrm{St}}}{V_{\mathrm{w}}} \tag{5.2}$$

where A_{St} is the total surface area of the bubbles and V_{w} is the volume of water in which A_{St} is determined. Bubble diameter is determined from from the shadow imaging experiments, with limited width, and surface area weighted bubble diameter is defined as:

$$d_2 = \sqrt{\frac{A_{si}}{\pi N_{si}}} \tag{5.3}$$

where A_{si} and N_{si} are the bubble surface area and the number of bubbles from the shadow imaging experiments, respectively. Next, it is assumed that the limited width of the shadow imaging experiments does not alter this ratio:

$$\frac{A_{si}}{N_{si}} = \frac{A_{st}}{N_t} \tag{5.4}$$

where N_{t} is the total number of bubbles corresponding to $A_{St.}$ Then, the combination of equation 5.3 and 5.4 gives:

$$A_{St} = \pi d_2^2 N_t \tag{5.5}$$

The void fraction of air (φ) is given as:

$$\varphi = \frac{V_b}{V_w} = \frac{N_t \pi d_3^2}{6V_w} \tag{5.6}$$

where V_b is the total volume of bubbles in control volume V_w, and d_3 is the volume weighted bubble diameter determined from the shadow imaging experiments:

$$d_3 = \left(\frac{6V_{si}}{\pi N_{si}}\right)^{1/3} \tag{5.7}$$

where V_{si} is the total volume of bubbles from the shadow imaging experiments, and

equation 5.6 may be solved for N_t :

$$N_t = {6\varphi V_w}\Big/{\pi d_3^3} \tag{5.8}$$

Equations 5.2, 5.5 and 5.8 may be combined to give:

$$a = 6\varphi \ {d_2^2}\Big/{d_3^3} = {6\varphi}\Big/{d_{32}} \tag{5.9}$$

where d_{32} is the Sauter mean diameter of the generated bubble population (Sauter 1926). The equilbrium concentration C_s is given by Henry's law and varies with temperature, pressure and solute content (Daniil and Gulliver 1988, Parkhill and Gulliver 1997) . The mass transfer coefficient k_L depends on the local air void fraction, the geometrical characteristics of the bubbles and local flow characteristics. Therefore, k_L may be approximated by predictive relations (Azbel 1981, Thompson and Gulliver 1997, Giovannettone and Gulliver 2008), but is best determined by controlled, flow-specific laboratory experiments. The theory of Azbel (1981) is employed to determine the liquid film coefficient in the model, k_L as:

$$k_L = \beta \ \frac{D^{1/2}}{4\pi} \ \frac{u^{3/4}}{\left(\nu_f l\right)^{1/4}} \ \frac{(1-\varphi)^{1/2}}{(1-\varphi^{5/3})^{1/4}} \tag{5.10}$$

where, D is the diffusion coefficient of the solute (oxygen) in water, ν_f is kinematic viscosity, l is a characteristic turbulent length scale, u is a characteristic turbulent velocity, and β is a coefficient on the order of 1 to be determined by fitting with the experimental data.

The one-dimensional mass transfer model requires certain inputs such as water

velocity, test-section pressure and temperature and the initial and steady state oxygen concentrations. The model partitions the water tunnel into six sections: test section, diffuser, right leg, bottom leg, left leg, and settling chamber. It requires inputs of test section velocity, test section pressure, average bubble diameter, airflow rate, water temperature, initial DO concentration, and DO system steady state or saturation concentration (referred to as 'saturation concentration' from now on). A section's cross-sectional mean velocity is substituted for characteristic turbulent velocity, the hydraulic radius of each section is substituted for turbulent length scale and the total bubble surface area is adjusted based on the change in bubble diameter caused by mass transfer and pressure changes using the ideal gas law. The model begins in the test section where it calculates k_L based on the inputs and tunnel geometry and an assumed value of β. A fourth-order Runge Kutta method is employed to solve for the change in DO that results from the water's transit of the test section. The model then steps to the next section of the tunnel where it executes the same procedure using the DO concentration that leaves the previous tunnel section as the section's inlet concentration. This process is repeated for all remaining tunnel sections. The bubbles then leave the tunnel via the gas collector dome above the low velocity settling chamber. The loop is then repeated with the new concentration in the settling chamber as the inlet concentration to the test section, where bubbles are injected into flow at the foil. This process is repeated until a steady state concentration is reached. The time it takes for the water to complete one loop is known based on calculated cross-section mean velocities throughout the water tunnel. This time is used to compare the calculated to measured DO concentrations where the LDO probes are

located as a function of time. A nonlinear regression was then undertaken on the coefficient β. An initial value of β was chosen, and varied by the slope-intercept method until the optimum curve-fit was achieved, as indicated by the minimum residual sum of squares.

5.4. Results and Discussion

5.4.1. Results on Bubble Size

A reference case, chosen to introduce the reader to a bubbly wake of a ventilated hydrofoil, will be presented herein. The reference case is at zero degrees *AoA*, a water velocity of 5 m/s and a ventilation mass airflow rate of 10 SLPM (standard liters per minute). Figure 5.4 shows the probability density functions (PDF) of number of bubbles, total surface area and total volume as functions of bubble diameter in the wake of the foil The PDF of bubble number illustrates the large fraction of very small size bubbles in the wake. As can be seen from the plot, more than 40% of the bubbles are around 0.3 mm in diameter. Liao and Lucas (2009) suggest that these small-sized bubbles are not generated at the air injection point but are produced as a result of breakup processes related to increased turbulence in the wake.

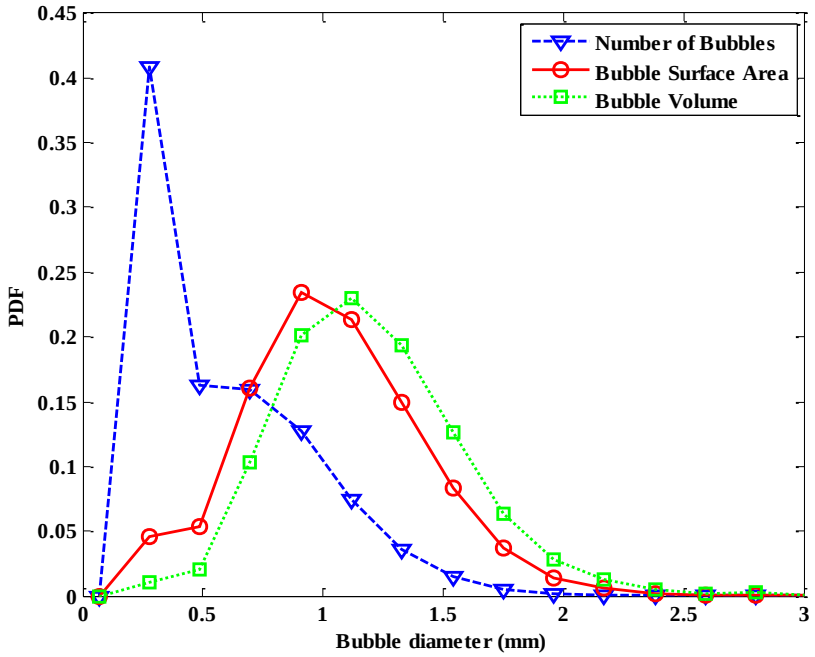

Figure 5.4: PDFs of number of bubbles, bubble surface area and volume in the bubbly wake for the reference case

The PDFs of the bubble surface area and bubble volume exhibit maxima just below and just above a bubble diameter of 1 mm, respectively. Around 24% of the entire surface area of the bubbles is contributed by bubbles with a diameter of between 0.8 mm and 1 mm. An equal amount of total bubble surface area is represented by slightly larger bubbles with diameters between 1 mm and 1.2 mm. It should be noted that the bubble size associated with the mean value of total surface area or volume denotes Sauter mean diameter (denoted interchangeably by SMD or d_{32}) or volume mean diameter (VMD or d_{43}), respectively. From the figure above, the approximate value of SMD and VMD are seen to be 0.95 mm and 1.1 mm respectively. In contrast, mean surface diameter (i.e. MSD or d_{20}) and mean volume diameter (i.e. MVD or d_{30}) represent a bubble size that if

all the bubbles were of this diameter, then the total surface area and volume of the bubbles, respectively, would be the same as in the actual bubble population.

In general, for a distribution of bubbles of similar shape, a weighted mean diameter d_{mn} is defined as:

$$d_{mn} = \left[\frac{\sum n_i d_i^m}{\sum n_i d_i^n}\right]^{1/(m-n)} \tag{5.11}$$

where the summation is carried out over the variable *i*. Table 5.1 shows the variation of these different representative diameters for the bubble size distribution for the reference case. It is evident from Table 5.1 that these representative diameters vary greatly and caution should be exercised in using the correct weighted mean diameter for the considered purpose. For instance, the value of SMD is significantly larger than MSD indicating the effect of large bubbles on SMD. However, as pointed out previously, SMD (or d_{32}) is the correct representative bubble size for mass transfer models.

Nomenclature	***m***	***n***	$\boldsymbol{d_{mn}}$ **(mm)**
Mean Length Diameter, MLD	1	0	0.48
Mean Surface Diameter, MSD	2	0	0.59
Mean Volume Diameter, MVD	3	0	0.69
Length Mean Diameter, LMD	2	1	0.73
Sauter Mean Diameter, SMD	3	2	0.88
Volume Mean Diameter, VMD	4	3	1.09

Table 5.1: The variation of different representative diameters for the reference case. d_2 and d_3 in equations 3 and 5 - 9 are equivalent to d_{20} and d_{30}, respectively in equation 5.11.

The SMD of bubbles in the wake varies with experimental conditions. Trends are observed with the variation of ventilation airflow rate (Q) and cross-sectional mean water velocity (U). Figure 5.5 shows the effect of variation of these parameters as a function of vertical location in the wake. Since the bubble images spanned a finite width in the stream-wise direction (~ 60 mm), the bubble data are averaged along the image width to get a variation along the vertical axis. Several observations can be made from this figure.

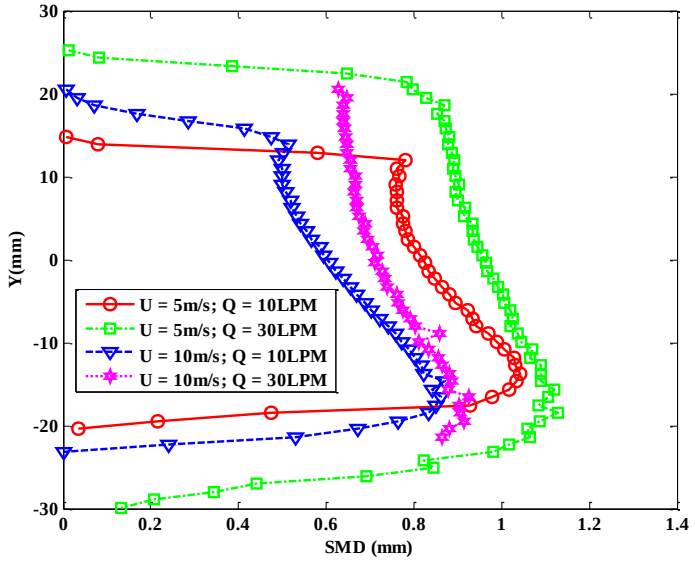

Figure 5.5: Effect of variation of liquid velocity or ventilation flow on SMD across all the vertical positions in the wake

The increase in SMD moving from outside toward the center of wake is due to the inertial effects of bubble size. Also, the largest bubbles are found below the centerline due to the ventilation slot being positioned on the suction side, which was located on the bottom of the hydrofoil in the test setup. The rise velocity of bubbles of all sizes is small compared to the liquid velocity (but the inertial effect of added or virtual mass is substantial for large bubbles. It is observed that a higher liquid velocity led to a lower

SMD (compare red circles with blue triangles). This could be due to the influence of liquid velocity on the production of bubbles (Silberman 1957) or the greater turbulence at higher liquid velocities leading to breakup of bubbles into smaller sizes (Liao and Lucas 2009). At a fixed liquid velocity, an increase in ventilation flow led to an increase in SMD (compare red circles with green squares). The increase in SMD is likely due to the influence of ventilation flow rate on bubble diameter (Silberman 1957).

AoA (deg)	*U* (m/s)	*Q* (SLPM)	C_{sat} (ppm)	t_{sat} (min)	d_{32} (mm)	$K_La * 10^4$ (s^{-1})	β
8	5	10	10.19	421.6	0.79	1.58	0.54
8	5	30	10.19	154.5	0.89	4.29	0.54
8	7.5	20	8.82	151.2	0.68	3.51	0.54
8	10	10	8.88	438.4	0.51	1.68	0.34
8	10	30	9.03	112.5	0.58	6.30	0.54
4	5	10	9.69	458.6	0.84	1.55	0.54
4	5	30	10.10	171.3	0.95	4.32	0.59
4	7.5	20	9.02	189.2	0.75	3.39	0.59
4	10	10	7.95	232.6	0.58	2.58	0.59
4	10	30	8.64	107.5	0.66	5.74	0.54
0	5	10	9.46	389.7	0.88	1.69	0.60
0	5	30	9.72	166.3	0.98	4.31	0.60
0	7.5	20	8.98	175.8	0.80	3.43	0.60
0	10	10	8.58	254.5	0.66	2.40	0.60
0	10	30	8.76	114.2	0.75	5.91	0.60

Table 5.2: Description of gas transfer experiments conducted in the present study with all the relevant experimental conditions. d_{32} is obtained from imaging experiments. The β values are determined from a fit of the model to experiments. Time to approach saturation, t_{sat} is for gas transfer experiments.

Table 5.2 shows the variation of d_{32} across all conditions. A tripling of ventilation flow rate produces an approximately 14% increase in d_{32} at both water velocities and three angles of attack. Similarly, between a 44 and 55% increase in d_{32} is observed when water velocity is halved at both airflow rates, and 4° and 8° angles of attack. The increase is somewhat smaller (31 and 33%) at zero angle of attack. It can also be seen from Table

5.2 that there is a slight decrease in d_{32} with increasing angles of attack, and a consistent trend can be observed.

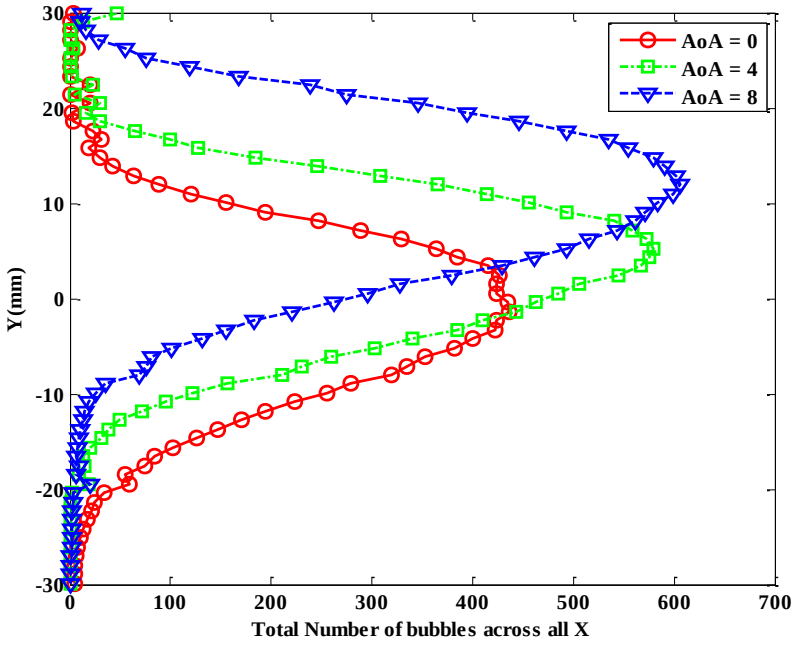

Figure 5.6: Effect of variation angle of attack (*AoA*) of hydrofoil on number of bubbles in the wake

Figure 5.6 shows the effect of variation of *AoA* at a fixed water velocity of 10 m/s and ventilation flow rate of 10 SLPM. The maximum of the curve at zero angle of attack is below the centerline. This is again because of the ventilation slot being located on the suction (bottom) side of the hydrofoil. As *AoA* is increased, this maximum shifts upwards following the shift of the entire bubbly wake. Figure 5.6 indicates that the number of bubbles increases substantially with *AoA*. The area under these curves would yield the total number of bubbles at each angle of attack. Continuity dictates that for the same ventilation flow rate, an increase in the in number of bubbles with *AoA* must occur concomitantly with smaller bubble sizes, which is seen in Table 5.2. The smaller

bubbles, in turn, may be attributed to the increased shearing of bubbles from the injection point and the greater breakdown of bubbles in a more turbulent wake.

5.4.2. Results on Dissolved Oxygen Uptake

The proposed one-dimensional mass transfer model requires certain inputs such as liquid velocity, the test-section pressure (reference pressure) and temperature and the initial and steady state oxygen concentration. $k_L a$ values for all the conditions are determined by a best fit linear regression of the experimental data as shown by Boyle (1993) and the β coefficient is adjusted to fit the curvature of the experimental data. Historically, the β coefficient has been difficult to determine, primarily due to the unavailability of data on bubble surface area and the resulting bulk coefficients needed in the analysis (Thompson and Gulliver 1997, Geldert et al. 1998, DeMoyer et al. 2003, Wilhelms and Gulliver 2005, Schierholz et al. 2006, Urban and Gulliver 2008, Giovannettone and Gulliver 2008, Witt and Gulliver 2012). Table 5.2 shows the variation of the β coefficient over the range of experimental conditions tested. It is seen that, except for the β value of 0.40 at AoA = 8^o, U = 10 m/s, Q = 10 SLPM which is considered an outlier, the value of β depends only on the hydrofoil configuration an d has close to a constant value for all the flow conditions at a particular AoA. The β coefficient increases from approximately 0.54 to 0.60 as AoA is varied from 0 to 8^o. Figure 5.7 shows percentage saturation (100 C / C_S) over time and the model fit at two air flow rates for an AoA of 0 degress and water velocity of 5 m/s. The lines represent the experimental data while the marker symbols denote the model best fit using a β value of 0.60. The fact that β is less than its expected value (on the order of one) could be due to the cross-sectional

mean velocity being substituted for the characteristic turbulent velocity in equation 10. If the characteristic turbulent velocity is approximately 0.43 (*AoA* = 8°) to 0.51 (*AoA* = 0°) times the free stream mean velocity, the value of β, as calculated from equation 10, would be 1. A value of 0.43 to 0.51 for the ratio of the characteristic turbulent velocity to mean velocity is realistic for the flow in the wake of a hydrofoil. Determining a β value in the range of 0.53-0.60 for different hydrofoil angles of attack, independent of water velocity and airflow rate, is a seen as a confirmation of Azbel's (1981) theory.

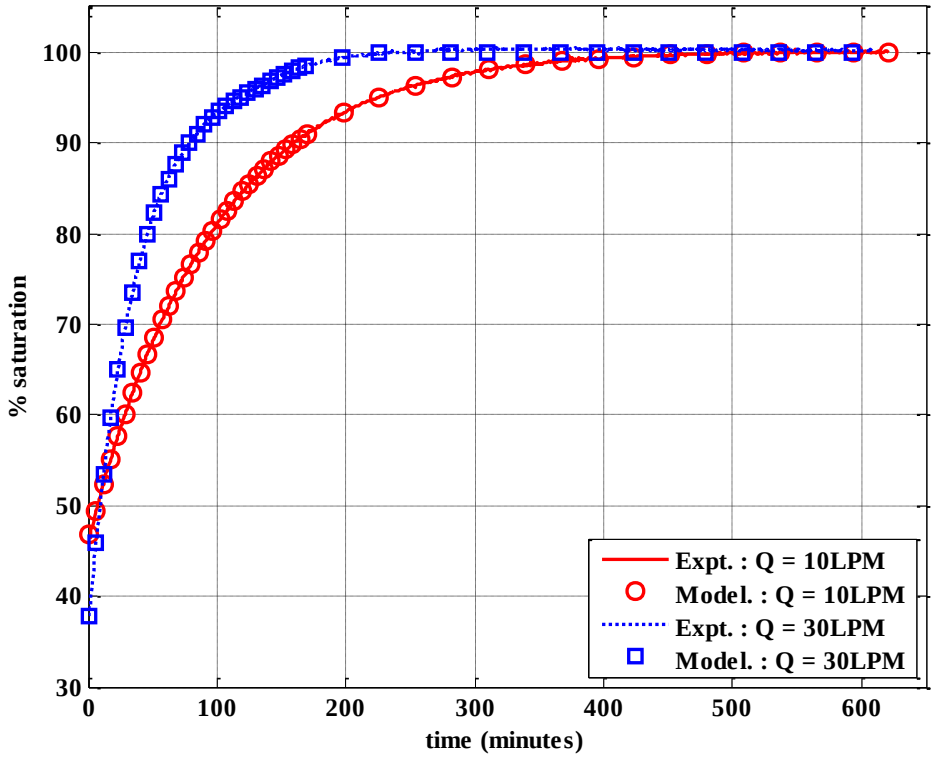

Figure 5.7: Effect of variation of ventilation rate on % saturation at zero *AoA* and superficial liquid velocity, $U = 5$ m/s

Further, it might be interesting to separately explore the effects of change in liquid velocity, air flow rate and hydrofoil angle of attack on the gas transfer. Figure 5.8 provides the DO measurements and model predictions at two different conditions with

fixed angle of attack and superficial liquid velocity while the ventilation flows are varied. The lines represent the experimental data while the marker symbols denote the model predictions at a fixed β value of 0.60. Two different line types and marker symbols represent the different airflow rates. The excellent fit between the experimental data and the model with β = 0.60 is evident. Dissolved oxygen concentration rose to 9.75 ppm with a ventilation flow of 30 SLPM. However, for the 10 SLPM case, the final concentration is 9.45 ppm. Larger number of bubbles for the 30 SLPM case also reflects in higher $k_L a$ value as shown in Table 5.2. The incremental change in Q from 10 to 30 SLPM led to a corresponding incremental change from 1.69 x10^{-4} s^{-1} to 4.31 x10^{-4} s^{-1} in $k_L a$. Thus, the greater DO uptake at a larger airflow rate is due to larger number of bubbles. For the same reason, the time required to reach saturation concentration is significantly lower for the 30 SLPM case.

Similar to the previous case, the DO uptake can be compared at a fixed angle of attack and ventilation flow while the liquid velocities can be varied. Figure 5.9 shows the comparison of DO concentrations at liquid velocities of 5 and 10 m/s. Two distinct observations can be made from this plot: First, the time required to approach saturation concentration is shorter at 10 m/s than at 5 m/s, indicating that the combination $k_L a$ is higher at 10 m/s. Table 5.2 indicates an increment from 1.69 x 10^{-4} s^{-1} to 2.40 x 10^{-4} s^{-1} as liquid velocity is increased from 5 to 10 m/s. Second, the system saturation concentration is higher (9.45 ppm) at a liquid velocity U = 5 m/s compared to 8.73 ppm at a higher velocity of U = 10 m/s.

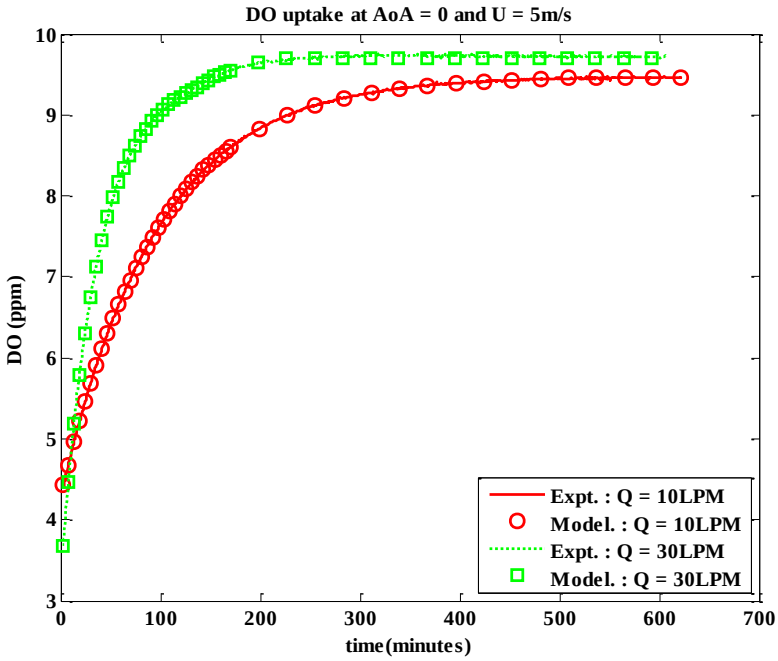

Figure 5.8: Effect of variation of ventilation rate on DO uptake at fixed *AoA* and superficial liquid velocity. 'LPM' still refers to the measurement at 'standard conditions.

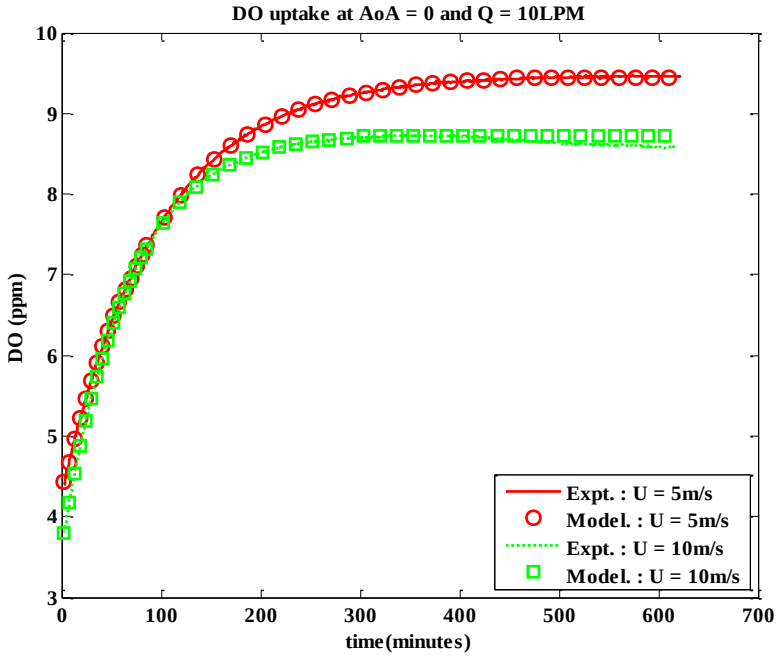

Figure 5.9: Effect of superficial liquid velocity on DO uptake at fixed *AoA* and variation of ventilation rate

A higher liquid velocity reduces the time required to reach saturation through increased levels of turbulence in the wake. In a previous section, it is also shown that a higher superficial liquid velocity leads to a greater number of small-sized bubbles and thereby a greater interfacial area, or $k_L\alpha$ value. Thus, it is expected that higher liquid velocities would lead to quicker attainment of saturation concentration. Further, the saturation concentration obtained is a function of the pressure. A greater pressure results in higher saturation concentration of gas in the liquid. Since, in the current experimental facility, the increase in the test-section velocity led to a subsequent decrease in test-section pressure, a net decrease in saturation concentration is observed with increasing liquid velocity.

Finally, DO uptake at different hydrofoil configurations can be compared. Figure 5.10 provides the effect of variation of angle of attack on the resulting DO uptake at U = 5 m/s. It has been magnified to show the difference in saturation concentration values. Figure 5.10 suggests that higher the *AoA*, the greater the DO saturation concentration. The increase in saturation DO concentration is found to be much greater upon moving from a symmetrical case to an *AoA* of 4 than an increase in *AoA* from 4 to 8. This may be explained because of the drastic increment in turbulence levels in the wake at an *AoA* of 4 compared to a symmetrical case, which leads to greater bubble breakup and a large number of small sized bubbles. As expected, the change of angle of attack did not affect the $k_L\alpha$ values. Table 5.2 gives nearly a constant value of 4.30 x 10^{-4} s^{-1} for $k_L\alpha$ at U = 5 m/s and Q = 30 LPM as *AoA* is varied from 0 to 8.

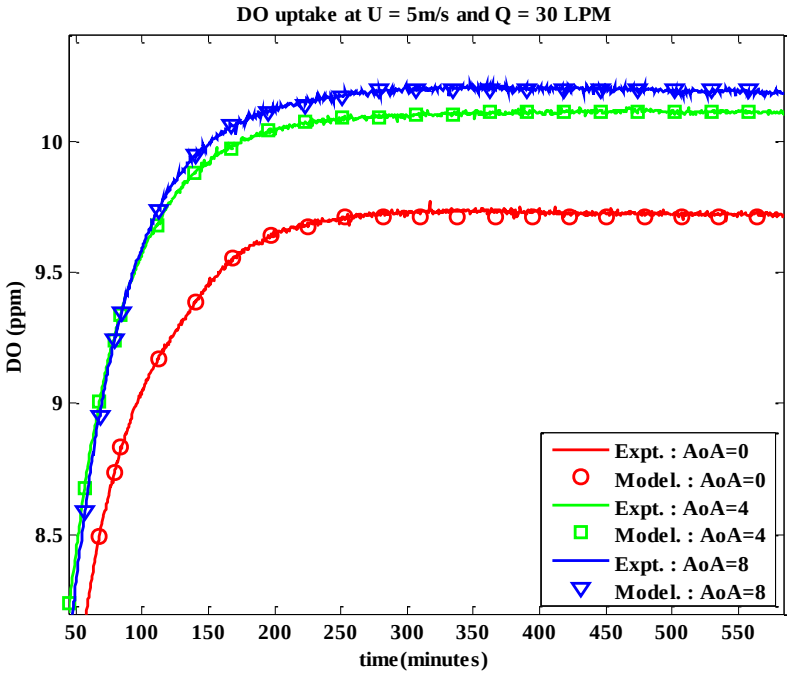

Figure 5.10: Effect of variation of *AoA* on DO uptake at fixed U = 5m/s and Q = 30 LPM.

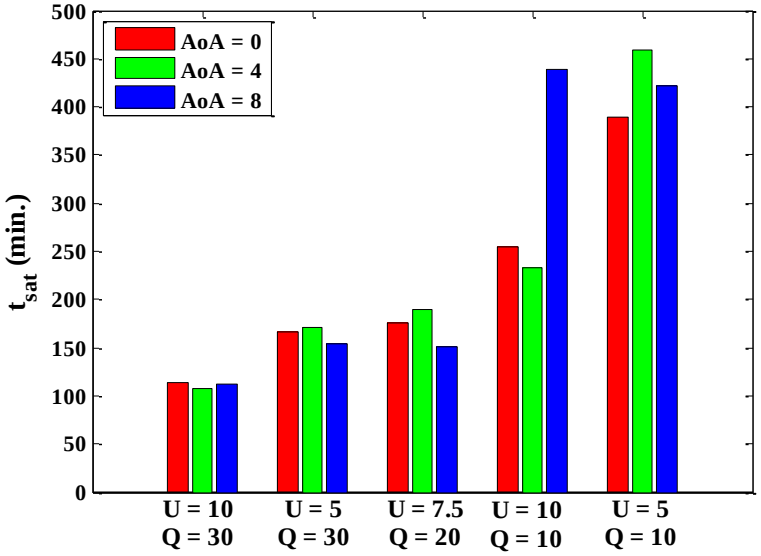

Figure 5.11: Time required to reach 99% of saturation at different cases in our experiment, t_{sat}

Finally, Figure 5.11 summarizes the time required to approach saturation (t_{sat}) for different cases in our experiment. As the airflow rates increase, t_{sat} decreases. For

identical *Q*, t_{sat} decreases as U increases. In general, the variation in *AoA* does not significantly affect $t_{sat.}$

5.5. Conclusions

Experiments on bubble-water mass transfer were performed in a closed, recirculating high-speed water tunnel using a ventilated hydrofoil by varying the free stream water velocity, ventilation air flow rate and the hydrofoil angle of attack. The goal of these experiments is to investigate the effect of these parameters on the size of the bubbles generated by air injection and the resulting rate of oxygen transfer. The shadow imaging experiments in the bubbly wake revealed that for our reference case of 0^o *AoA*, a water velocity of 5 m/s and a ventilation mass airflow rate of 10 SLPM, ~ 40% of the bubbles in the wake had diameters around 0.3 mm. It is also found that bubbles larger than 0.45 mm in diameter have a greater influence on the Sauter mean diameter of the population. Sauter mean diameter increases by approximately 14% as a result of tripling the airflow rate at all water velocities. Sauter mean diameter decreased by 44% to 55%, when the velocity is doubled without changing airflow rate at 4^o and 8^o angle of attacks and by 31% to 33 % at zero angle of attack. An increase in angle of attack from 0 to 8 degrees produced smaller bubbles.

A one-dimensional mass transfer model is developed to lend insight into the oxygen transfer characteristics observed in these experiments using a mass transfer conservation equation and a predictive relation for liquid film coefficient, $k_{L,}$ by Azbel. For ease of application, mean free stream velocity (*U*) was substituted for characteristic

turbulent velocity (u') in the predictive relation. Thus, a β coefficient was introduced to account for this difference, $\beta = (u'/U)^{3/4}$ where u'/U is the turbulence intensity. This β coefficient was determined by fitting the prediction of the numerical model with the experimental data obtained from the DO measurements in the water-tunnel. The gas transfer model required the test conditions and Sauter mean diameter of the bubbles in the wake of the hydrofoil as input to predict liquid film coefficient, k_L. Except for one outlier, the results of the model showed that β coefficient is constant for a given angle of attack. β decreases slightly as hydrofoil *AoA* increases. We believe the values of β derived in this study can be used with Azbel's k_L relationship as a predictive tool for mass transfer in bubbly flows, which are similar to those studied here. Prior attempts at this have largely been unsuccessful due to the lack of experimental measurements of bubble size distributions, forcing a reliance on empirical formulations for bubble size and surface area.

This study is part of a larger effort to develop computational tools to relate the conditions in a high-speed bubbly flow to the associated gas transfer. The study provides a rich dataset on bubble sizes and void fraction in the wake of a ventilated hydrofoil and the rate of oxygen transfer as a function of flow and foil parameters that can be used in the validation of these tools. It is hoped that such computational models will soon be integral parts of the design process in the development of effective auto-venting hydroturbines.

Part B: Supercavity Bubble Regime

Chapter 6. An experimental investigation into supercavity closure mechanisms

Substantial discrepancy in the conditions for attainment of different closure modes of a ventilated supercavity has existed widely in the published literature. In this study, supercavity closure is investigated with an objective to understand the physical mechanisms determining closure formation and transition between different closure modes and to reconcile the observations from prior studies under various flow settings. The experiments are conducted in a closed-wall recirculating water tunnel to image ventilated supercavity closure using high speed and high-resolution photography and simultaneously measure pressure inside the cavity. The flow conditions are varied systematically to cover a broad range of water velocity, ventilation flow rate and cavitator size, which correspond to different Froude numbers, air entrainment coefficients and blockage ratios, respectively. In addition to the classical closure modes reported in the

literature (e.g. re-entrant jet, twin vortex, quad vortex, etc.), the study has revealed a number of new closure modes that occur during the transition between classical modes, or under very specific flow conditions. Closure maps are constructed to depict the flow regimes, i.e. the range of Froude number and air entrainment coefficient, for various closure modes at different blockage ratios. From the closure map at each blockage ratio, a critical ventilation flow rate, below which the supercavity collapses into foamy cavity upon reduction of Froude number, is identified. The air entrainment coefficients corresponding to such critical ventilation rate are found to be independent of blockage ratio. It has been observed that in the process of generating a supercavity by increasing ventilation flow rate, the cavitation number gradually reduces to a minimum value and stays fixed upon further increments in the ventilation rate. Once a supercavity is formed, the ventilation rate can be decreased to a much lower value with no change in cavitation number while still maintaining a supercavity. This process is accompanied by a change in closure modes, which generally goes from twin vortex, to quad vortex, and then to re-entrant jet. In addition, the blockage effect is shown to play an important role in promoting the occurrence of twin-vortex closure modes. Subsequently, a physical framework governing the variation of different closure modes is proposed, and is used to explain mode transition upon the change of flow conditions, including the blockage effect. This framework is further extended to shed light on the occurrence of closure modes for ventilated supercavitation experiments across different types of flow facilities, the natural supercavity closure and the pulsating supercavity reported in the literature. Finally, in combination with a recent numerical study, our research discusses the role of

the internal flow physics on the observed features during supercavity formation and closure-mode transition, paving the way for future investigations in this direction.

6.1. Background and literature review

Supercavitation is a special case of cavitation which can be employed to create a bubble of gas inside water, large enough to encompass an object travelling through the water. It greatly reduces the skin friction drag on the object enabling achievement of high speeds under water. The creation of a supercavity is thus, of great interest for naval applications, e.g. high-speed underwater vehicles. From an initially non-cavitating flow, the conditions required for a moving object underwater to form a natural supercavity are very stringent. Therefore, ventilation is generally used to form a supercavity artificially, by blowing non-condensable gas into the low-pressure region at the rear part of the moving object. Ventilated supercaviation has been investigated by many prior researchers through analytical, experimental and numerical approaches. This process generally depends on the physical parameters such as incoming velocity (U), ventilation flow rate ($\dot{Q}_{\mathrm{A}}$), ambient pressure (P_{∞}), cavity pressure (P_{C}), cavitator diameter (d_{C}). These parameters are commonly expressed using dimensionless groups: Froude number, $Fr = U/\sqrt{g d_{\mathrm{C}}}$, air entrainment coefficient, $C_{\mathrm{Q}} = \dot{Q}_{\mathrm{A}}/U d_{\mathrm{C}}^2$, cavitation number, $\sigma_{\mathrm{C}} = (P_{\infty} - P_{\mathrm{C}})/(1/2\,\rho U^2)$ etc., where g and ρ denote gravitational acceleration and water density, respectively. The prior studies in the area of ventilated supercavitation focus on deriving empirical or semi-empirical relations of these dimensionless quantities to characterize supercavity geometry and ventilation demand, which is the amount of gas required to

form and sustain a supercavity (Logvinovich 1973; Epshtein 1973; Spurk & König 2002). It has been shown that the ventilation demand depends not only upon the flow conditions but also on specific features of flow patterns in the cavity sealing zone, commonly referred to as closure mechanism or closure mode (Logvinovich 1973). Although a variety of supercavity closure modes have been identified and studied separately, but there is no universally accepted theory on the relationship between closure mechanism and ventilation demand yet (Semenenko 2001a). To accurately estimate gas requirements for underwater applications using supercavitation, it would be profitable to systematically study the closure mechanism under different flow conditions and determine the criteria that govern the transition among different closure modes.

Up to date, many authors have studied different closure modes, and the empirical relationships governing different closure modes have been discussed (e.g., Cox and Clayden 1956; Campbell & Hilborne 1958; Kapankin and Gusev 1981; Semenenko 2001a; Kawakami & Arndt 2011). In the published literature on ventilated supercavitation, four main closure modes have been widely reported: re-entrant jet (RJ), twin vortex (TV), quad vortex (QV) and pulsating cavity (PC). The RJ closure is reported to occur when *Fr* is high, i.e. when the effect of gravity is not significant. In such a case, the hydrostatic pressure gradient is negligible as compared to the dynamic forces and thus the cavity closely resembles an axisymmetric shape. The cavity rear end fills with foam which is periodically ejected in the form of toroidal vortices (Semenenko 2001a). The TV closure is usually observed at low *Fr* and σ_c values, when the effect of gravity becomes predominant. According to Cox & Clayden (1956), for TV closure, the locus of the

centroids of the cavity section tends to rise under buoyancy forces, and the cavity is effectively cambered upwards and is no longer axisymmetric. The circulation setup around the supercavity due to hydrostatic pressure gradient produces a lift force which is equal and opposite to the buoyancy force on the bubble. This circulation about the cavity mid-plane associated with this lift force sheds downstream in the form of two counter-rotating vortices. Thus, this streamwise vorticity due to the cavity asymmetry eventually splits the supercavity lengthwise into two vortex tubes through which the ventilation air escapes out of the supercavity. Although significant number of studies have been conducted to investigate the criteria for the formation of TV and RJ closure and their transitions (e.g. Campbell & Hilborne 1958; Buyvol 1980; Spurk & König 2002), there is a lack of concurrence on the empirical formulations and physical phenomena reported from different studies (e.g. Peng *et al.* 2006; Zhang *et al.* 2007; Zhou *et al.* 2010; Kawakami & Arndt 2011; Skidmore *et al*. 2015). For instance, the first such empirical criterion for transition was given by Campbell & Hilborne (1958) based on experiments conducted in a whirling arm channel for limited range of Fr from 5 to 25. Their experiments show that a RJ cavity occurs at $\sigma_C Fr > 1$, and TV cavity forms at $\sigma_C Fr < 1$. Later, Buyvol (1980) proposed the criterion for the existence of RJ as: $\sigma_C^{1.5} Fr^2 > 1.5$. More recently, a slightly different condition for RJ cavity is provided by Spurk & König (2002) as $\sigma_C Fr^2 > 1$. However, contrary to the published reports, experiments at Saint Anthony Falls Laboratory (SAFL) show that the RJ closure occurs at low *Fr,* and is not observed even at very high values of $\sigma_C Fr$ (Kawakami & Arndt 2011). Similar to Kawakami & Arndt (2011), many other studies report only one closure mode across a

wide range of σ_C and *Fr*, and found other types of closures to be conspicuously unattainable. For example, some studies have only reported the occurrence of TV closure in their closed-wall water tunnel (e.g., Cox & Clayden 1956, Kawakami 2010, Zhou *et al.* 2010) or free surface channel (e.g., Campbell and Hilborne 1958), while others only observe RJ closure in closed-wall water tunnel facility (e.g., Gadd & Grant 1965; Skidmore 2013). The QV mode is a special case of a stable vortex closure, when each vortex of the TV further splits into two, such that one pair of vortices lies above the other. The QV was first reported by Kapankin & Gusev (1984), and more recently by Kawakami & Arndt (2011) at low *Fr* and C_Q values. However, the formation mechanism and criterion for this closure is not well ascertained. The PC closure, first observed by Silberman & Song (1959), has been reported by many other studies (e.g., Song 1961; Karlikov *et al.* 1987; Semenenko 2001a; Semenenko 2001b; Skidmore 2013), typically at high air entrainment rates. This regime is different from other closure types since the entire supercavity has a wavy surface, and the gas loss is primarily due to periodic ejections of air-water mixture at the rear of the supercavity causing great variation in its length. Akin to other closure modes, the conditions governing the occurrence of pulsating cavities are not very clear as well (Silberman & Song 1959; Woods 1966; Michel 1984; Stinebring *et al.* 2001; Paryshev 2003).

The observed discrepancies from the above-mentioned studies in predicting the supercavity closure mode can be attributed to several factors, e.g. the nature of experimental facility (e.g. towing tank, closed-wall tunnel *vs* free surface facility, etc.), blockage (defined in terms of percentage as $B = d_C/D_T$, where D_T is the tunnel

equivalent diameter) etc., but the exact bearing of the variations of these parameters on supercavitation phenomena is not understood on a fundamental physical level. Hence, in this chapter we have attempted an in-depth investigation into the phenomena of supercavity closure, in order to better understand the impact of flow conditions including the blockage and the flow facility on the dynamics of ventilated supercavities.

6.2. Experimental Methods

The experiments are conducted to image ventilated supercavity closure and obtain the corresponding pressure measurements inside the cavity under different flow conditions. The study is conducted at the Saint Anthony Falls Laboratory's high speed water tunnel, which is shown as a schematic in Figure 2.1. It is a recirculating, closed-jet facility with absolute pressure regulation. It has a horizontal test-section of 1.20 m in length, with a 0.19 m × 0.19 m square cross section (i.e. 0.21 m in hydraulic diameter). The two side walls and the bottom wall of the test-section are made of Plexiglas for optical access. The tunnel is designed for cavitation and air ventilation studies and is capable of operating at a velocity in excess of 20 m/s with the turbulence level of approximately 0.3%. As shown in Figure 2.1, the facility includes a large dome-shape settling chamber, which provides for fast removal of air bubbles generated during cavitation and ventilation experiments. This feature allows the cavitation experiments to be conducted for extended periods with little change on test-section conditions.

The ventilated supercavitation experiments are done with the backward facing cavitator model as described in Kawakami & Arndt (2011) and shown in Figure 6.1. In the backward facing model, a thin NACA0012 hydrofoil strut is placed upstream of the

cavitator to avoid the interaction between the formed cavity and the strut body leading to a free closure as reported by Logvinovich (1973). To minimize the disturbance to the flow, the thickness of the hydrofoil strut is just enough to envelope the ventilation pipe running to the cavitator. The maximum thickness and the chord length of the hydrofoil are 5 mm and 41 mm, respectively. The hydrofoil spans the test-section and is mounted near its geometric center. The angle of attack of the hydrofoil is measured between the axis of the test-section and the axis perpendicular to the flat surface of the disk cavitator. For all the results reported in this chapter, the angle of attack is kept to 0^o with a measurement uncertainty of $\pm 0.5^o$. Both the cavitators and the hydrofoil are made of brass and polished to a smooth finish. High speed videos of the supercavity under such a configuration reveal that the thin and streamlined hydrofoil strut upstream does not produce considerable disturbance, and only a slight wake signature is observed on the side of the cavity.

The images and the videos of the supercavity closure are obtained with a 1k × 1k pixel Photon APX-RS camera, which is capable of acquiring 3000 frames/s at full resolution. To ensure uniform backlighting in these videos and images, a light shaping diffuser is placed between the light source and the flow. Pressures in the test-section and the supercavity are measured using two separate Validyne AP-10 pressure transducers. A Validyne DP-10 differential pressure transducer is employed to measure the differential pressure between the settling chamber and test-section and is used to calculate test-section velocity. The pressure transducers are calibrated before each experiment and the pressure lines are purged with compressed air once before the pressure measurements are

recorded at each condition. The calibrations are performed using a mercury manometer for both transducers. The pressure transducer calibrations are linear, with R-squared values typically 0.9999 or higher for both transducers. Standard errors of the pressure calibrations are approximately 0.1 kPa for both absolute pressure transducers. These errors lead to a maximum error of 0.11 m/s in the velocity measurement, with mean error around 0.02 m/s.

The imaging of supercavity closure and pressure measurements are conducted with four sizes of cavitators: 10, 20, 30 and 40 mm in diameter (corresponding to B = 5 %, 9 %, 14 % and 19 %, respectively), across a wide range of test-section flow speed and ventilation flow rate. Test-section flow speed is controlled through the rotational velocity of the tunnel's axial flow impeller which is driven with a 75HP alternating current motor. During experiments, tunnel water temperature is monitored using a YSI thermistor, which varies between 16 ^{o}C to 22 ^{o}C over the course of the tests. In our experiments, the water surface in the settling chamber is vented to the atmosphere, and the test-section pressure is determined by the water velocity inside. Since the cross-sectional area of the settling chamber is significantly larger than that of the test-section, the water velocity in the settling chamber is negligible as compared to that in the test-section (See Figure 2.1). Thus, from conservation of energy principle, as the water velocity in the test-section increases, the test-section pressure decreases. The ventilation flow rate to the cavitator is controlled and measured by Omega Engineering FMA-2609A mass flow controller. In our experiments, air flux is reported at the standard conditions (i.e. a temperature of 273 K and a pressure of 1 bar) in terms of standard liters per minutes (SLPM). In the current

work, the corresponding air entrainment coefficient at standard conditions is defined as: $C_{Qs} = \dot{Q}_{As}/Ud_C^2$, where $\dot{Q}_{As}$ represents the air ventilation flow rate at standard conditions that is direct reading from the mass flow controller. It is worth noting that in the present study, the mass flow rate (or volume flow rate at standard conditions) is employed instead of volume flow rate used in the literature to give a sense of ventilation requirement corresponding to each specific type of closure. The rationale behind adapting this definition is that, for the operation of supercavitating vehicles, it is the mass flow rate of air determines the ventilation requirements to be carried on-board. The full scale reading of the MFC is 55 SLPM and the uncertainty in the flow measurement is ± 1% of the full scale reading. A few data points in our experiments are also collected at flow rates exceeding 55 SLPM. These large ventilation flow rates are regulated by a valve at the inlet to an Omega Engineering rotameter with a maximum mass flow rate of 100 SLPM. Factory calibrations are used for the rotameter and the uncertainty in the rotameter's scale is less than 2% of the value. Overall, in our experiments, the maximum uncertainty in the measurement of C_{Qs}, Fr and σ_C are estimated to be 2%, 2% and 2.2%, respectively.

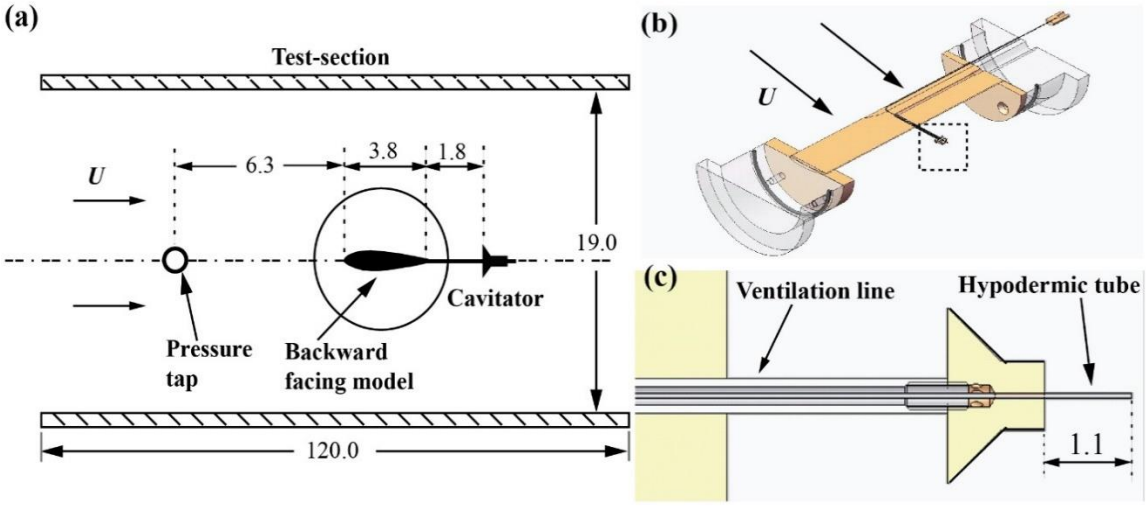

Figure 6.1: (a) A side view of the test-section and the mounting configuration of the backward facing cavitator. (b) A sectional view and (c) a close-up view of the cavitator, ventilation line and the hypodermic tube used for pressure measurement. The dimensions shown in the figure are in centimeters.

6.3. Experimental Observations

6.3.1. Observations of different closure modes

There are a variety of closure modes observed in our experiments, with the vortex-based closure mode being dominant. The acronyms and the names of different closure modes are summarized in Table 1. In general, there are four stable states of a ventilated supercavity (Figure 6.2), which include three stable closure modes (i.e. RJ, TV, QV), and foamy cavity (FC). The FC refers to the state before the clear supercavity is formed, when the cavity consists of bubbles and foam without a clear gas-water interface (Savchenko 2001). In addition, as shown in Figure 6.3, five unstable closure modes are discovered in our experiments, i.e., hybrid quad vortex and re-entrant jet closure (QVRJ), hybrid twin vortex and quad vortex closure (TVQV), hybrid twin vortex and re-entrant jet closure (TVRJ), a pulsating twin vortex closure (PTV) and an interacting vortex closure

(IV). These unstable modes are either observed at the transition of two stable closure modes or at high ventilation flow rates (>55 SLPM). For example, QVRJ closure occurs at the transition of QV and RJ closure, and is characterized by a foamy end with four vortices, exhibiting the characteristics of both QV and RJ (Figure 6.3a). TVQV closure is formed during the transition between QV and TV modes (Figure 6.3b). The number of vortices for TVQV changes intermittently at the closure, fluctuating between one and four and with the bottom two being usually more stable than the upper ones. TVRJ mode yields similar features as those of QVRJ, but only two vortices appear at the closure (Figure 6.3c). At ventilation flow rates above 55 SLPM, IV mode is observed, where the two vortices interact with each other to form one single thick vortex at the closure (Figure 6.3d). At flow conditions similar to that for IV but at lower blockage (i.e., B = 5%), PTV occurs, where both the vortices pulsate in longitudinal direction, and the cavity end intermittently breaks into elongated air pockets due to Kelvin-Helmholtz instability on the cavity surface (Kuklinski, Castano & Henoch 2001). Note that the PC reported in the literature (Silberman & Song 1959, Skidmore 2013) is not observed in our experiments, and more information including images of PC can be found in a recent paper by Skidmore *et al.* (2015).

Acronym	Name
RJ	Re-entrant jet closure
TV	Twin vortex closure
QV	Quad vortex closure
FC	Foamy cavity
QVRJ	Hybrid quad vortex and re-entrant jet closure
TVQV	Hybrid twin vortex and quad vortex closure
TVRJ	Hybrid twin vortex and re-entrant jet closure
PTV	Pulsating twin vortex closure
IV	Interacting vortex closure
PC	Pulsating cavity closure

Table 6.1: The acronyms and the names of different closure modes observed in our experiments. Note that FC listed here is considered as a state of supercavity not a closure mode.

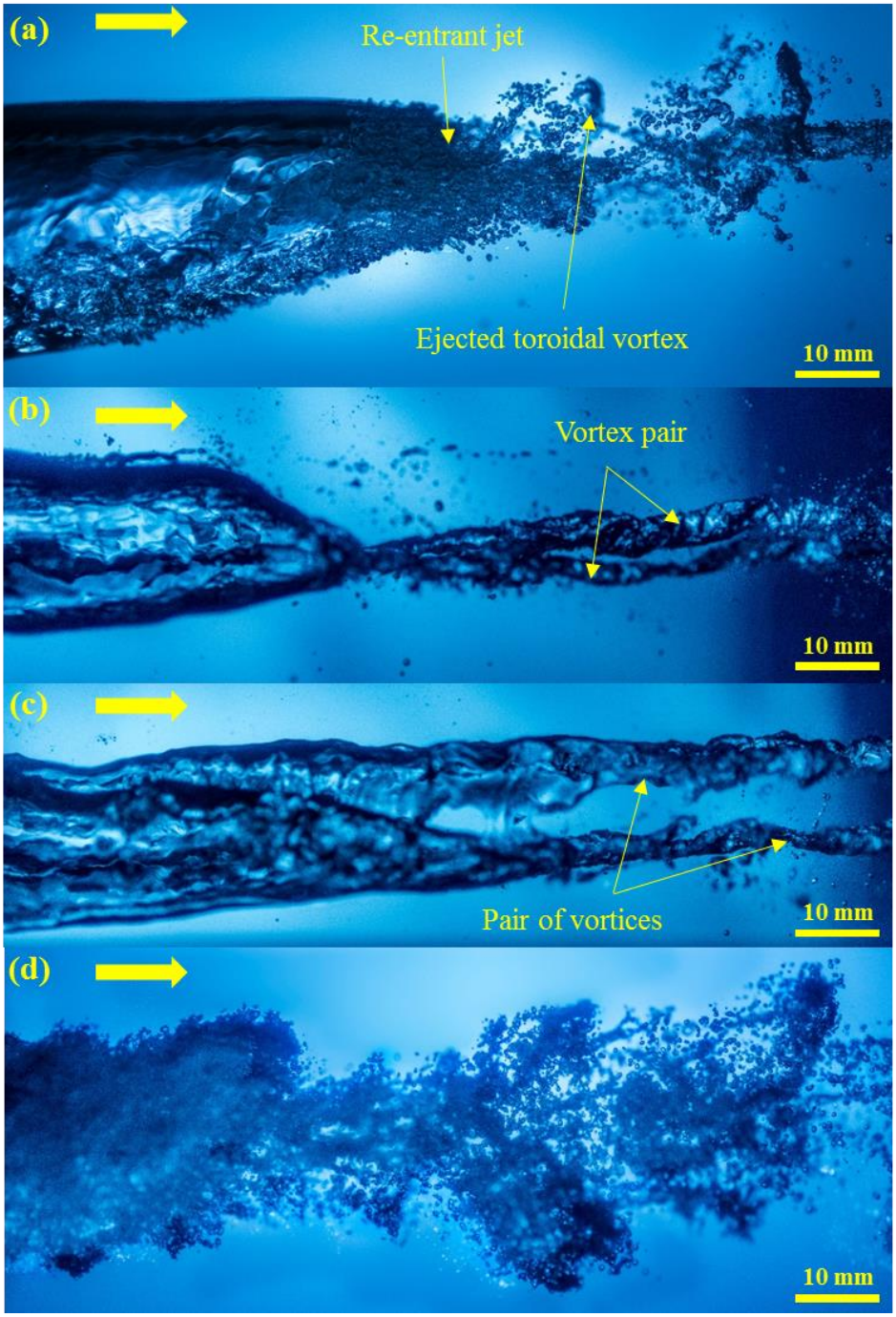

Figure 6.2: Side views of various stable states of the ventilated supercavity observed in our experiments: (a) RJ (b) TV (c) QV (d) FC. All the images are obtained for the 20 mm cavitator, corresponding to B = 9 %. Note that the vortices are filled with air, and one vortex is hidden behind the other for both TV and QV closures due to the perspective of the camera. The horizontal arrow in the figures indicates the direction of water flow.

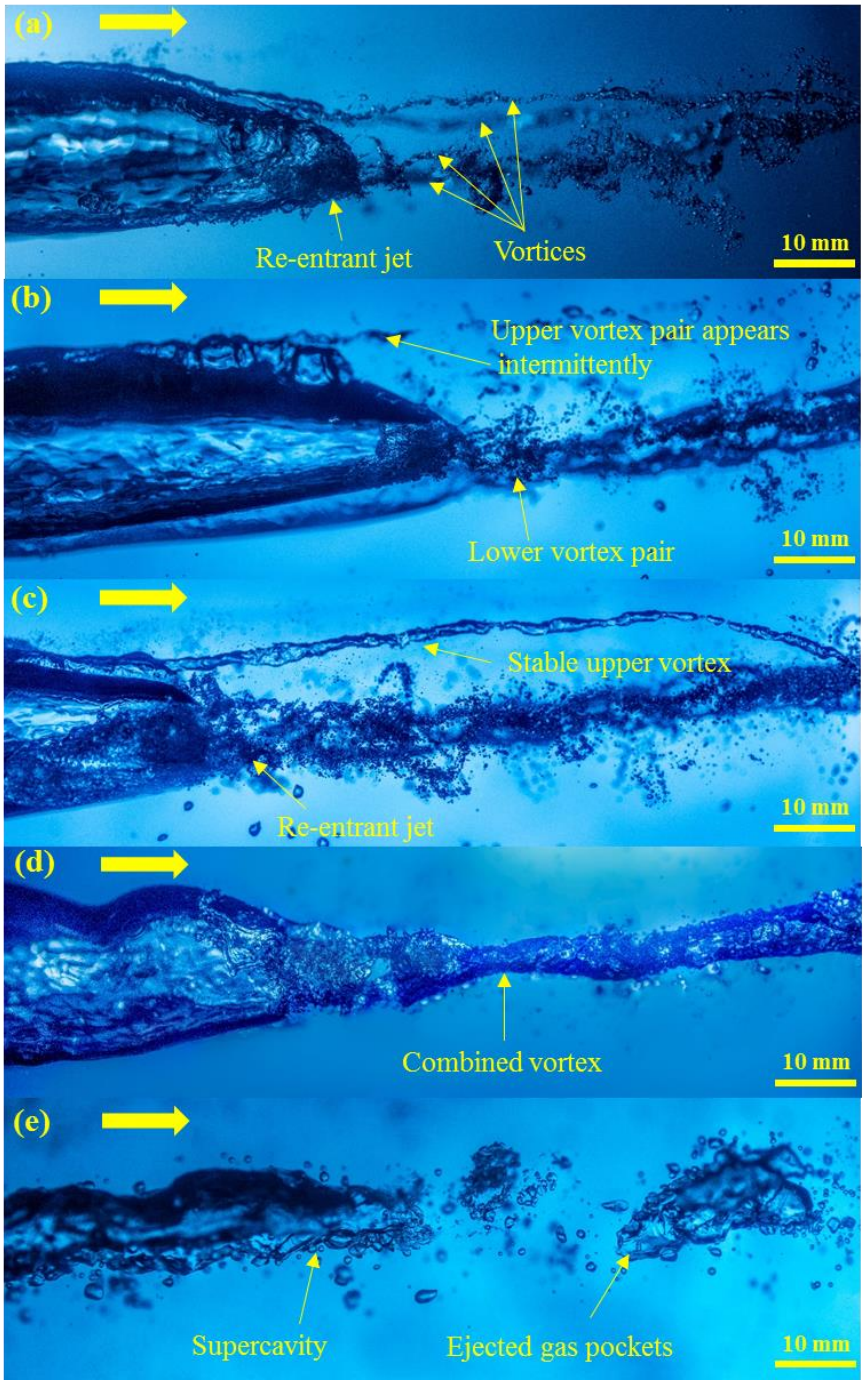

Figure 6.3: Side views of the various unstable closure modes observed in our experiments: (a) QVRJ (b) TVQV (c) TVRJ (d) IV (e) PTV. PTV mode is observed at B = 5 % while all other modes correspond to B = 9 %. Note that the vortices are filled with air, and one vortex is hidden behind the other for both TV and QV closures due to the perspective of the camera. The horizontal arrow in the figures indicates the direction of water flow.

The trends of these closure modes and the transitions between them are studied by varying the parameters Fr and C_{Qs}. A closure map is obtained (Fr *vs* C_{Qs}) by holding Fr constant and lowering C_{Qs} from 10 to 0.001. Figure 6.4 shows the closure map at a fixed blockage of B = 5 %, which corresponds to the lowest blockage in our experiments. In this closure map, a movement along the x-axis corresponds to a fixed Fr (or constant water velocity) and increasing C_{Qs}, while the slanted curves denote the lines of each fixed ventilation flow rate.

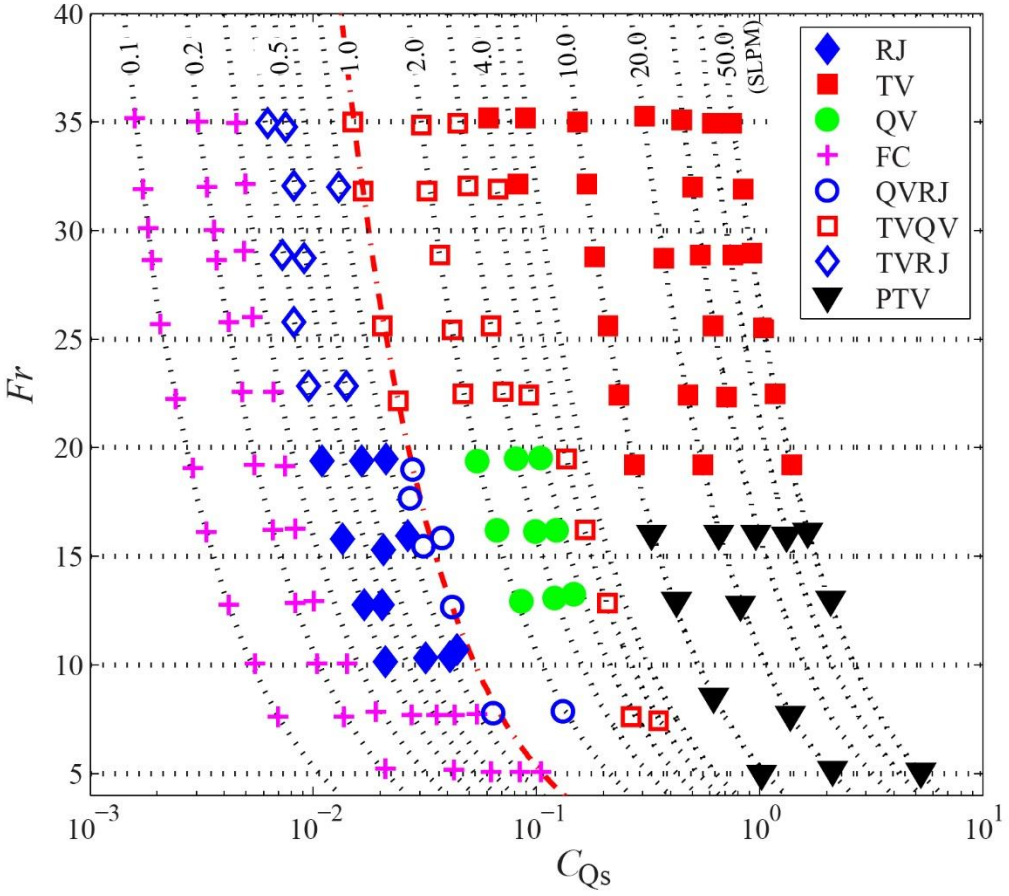

Figure 6.4: Closure map of different closure modes at B = 5 %. The slanted dotted lines denote lines of fixed ventilation flow rates. The values of the ventilation flow rate (in SLPM) are indicated on a selected number of the curves. The red dash-dotted line denotes the line of 'critical ventilation flow rate'.

The closure map identifies separate regimes for a foamy cavity state and a supercavity state where different closure modes are observed (Figure 6.4). In general, a foamy cavity state occurs at very low values of C_{Qs} (< 0.01), when the ventilation flow rate, dependent of *Fr*, is not sufficient to sustain a supercavity. Particularly, a critical ventilation flow rate, Q_{crit} (defined at standard conditions) of 1.0 SLPM for the chosen cavitator (marked as a red dash-dotted line) is identified, which governs the transition from the supercavity state to the foamy cavity state. Above this critical ventilation rate, the supercavity does not transition to a foamy cavity as *Fr is* reduced even to very low values. On the other hand, below this critical ventilation rate, the supercavity collapses into a foamy cavity as *Fr* deceases from an initial high value.

In a supercavity state, the regime for each closure mode, represented by the range of *Fr* and C_{Qs}, can be clearly identified in the closure map (Figure 6.4). For stable closure modes, the TV occurs at high values of C_{Qs} and *Fr* (C_{Qs} > 0.2, *Fr* > 20), while QV is concentrated in moderate C_{Qs} and *Fr* (C_{Qs} = 0.03 – 0.15, *Fr* = 12 – 20). In comparison, RJ closure appears at low to moderate *Fr* (*Fr* = 10 – 20) and in a narrow range of small C_{Qs} (= 0.02 – 0.04). It has been found that RJ closure is susceptible to transition upon small changes in *Fr* or C_{Qs}, and a rapid reduction in C_{Qs} (at a fixed *Fr*) leads to supercavity collapse (A further discussion on this susceptibility is provided in § 6.5.4). The unstable modes are located in the transitional regimes between different stable modes. Specifically, the regimes of TVRJ and QVRJ are adjacent to RJ regime, but situated at a higher values of *Fr*, and C_{Qs}, respectively. Upon an increase in C_{Qs} from TVRJ, the

closure mode migrates to TVQV and then to TV. Similarly, with further increment of C_Q, the supercavity transits gradually from QVRJ to QV, and TVQV. At very high C_{Qs} (> 0.5), the supercavity becomes less stable and PTV is observed. It is noteworthy that each closure mode shown in the closure map is independent of the path taken to obtain it as long as the path does not intersect with foamy cavity state. In other words, the same closure map can be depicted by changing *Fr* or C_{Qs} in many other ways provided a supercavity is maintained during the variation of flow conditions.

To elucidate the interrelationships between σ_C, C_{Qs} and different cavity states, the variation in cavity states upon a change in C_{Qs} are examined at two selected *Fr* numbers. As Figure 6.5 shows, at both *Fr* numbers, upon increment in C_{Qs}, σ_C decreases for a foamy cavity and the cavity size increases until a supercavity (i.e. the cavity with a clear interface) is formed. With further increase in $C_{Qs,}$ σ_C does not change and the supercavity yields TV closure. More interestingly, as long as a supercavity state is attained, C_{Qs} can be decreased to very low values while still maintaining the cavity and the same σ_C. This phenomenon is referred to as 'ventilation hysteresis', and has been reported by a few prior studies (e.g. Song 1961; Savchenko 2001; Kawakami & Arndt 2011). As shown by our experiments, although such decrement in C_{Qs} does not alter σ_C, the cavity closure changes from TV to RJ. Since σ_C stays fixed and the test-section pressure does not change appreciably upon the variation in ventilation flow rate, it can be inferred that the pressure inside the supercavity does not vary with $C_{Qs.}$ Therefore, the simultaneous change in closure mode indicates that the internal supercavity pressure is determined not only by a combination of *Fr* and C_{Qs}, but also the supercavity closure mechanism. This

implication can be related to Spurk & König's theory (Spurk & König 2002), which suggests that the supercavity closure is associated with a change in streamline curvature at the cavity rear portion. Specifically, the curvature of RJ mode effectively limits ventilation leakage at the closure, promoting pressure buildup inside the cavity. Thus, although the value of C_{Qs} for a RJ closure is significantly lower than that of a TV mode, the pressure inside the supercavity stays nearly the same as that of a TV mode.

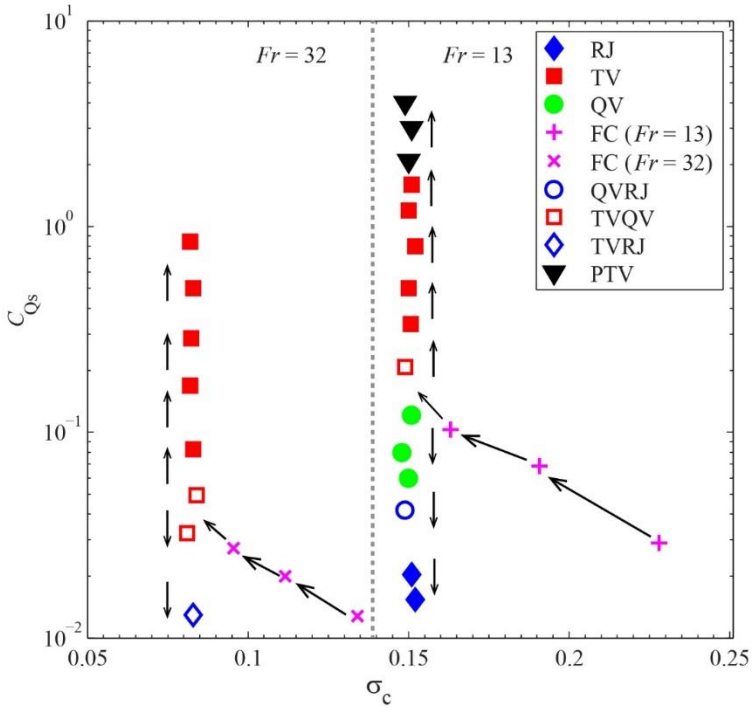

Figure 6.5: Variation of different closure modes upon the change of C_{Qs} for two selected *Fr* numbers at B = 5 %. The arrows denote gradual changes in ventilation flow rates. The dotted vertical line in the middle separates the data points corresponding to the two *Fr* numbers

6.3.2. Blockage Effects

To examine the blockage effect on closure modes, Figure 6.6 shows a closure map for B = 9 % in comparison with the one for B = 5 % presented in Figure 6.4. The

comparison shows that the trends for the distribution of closure modes are similar, except that PTV closure which appears in the bottom right of the closure map for B = 5%, is replaced by IV closure for B = 9 %. It is noteworthy that essentially, both PTV and IV closures are unstable variants of TV mode obtained at low Fr and high C_{Qs}. At higher blockages, the closure maps remain largely the same, and are not shown here for brevity.

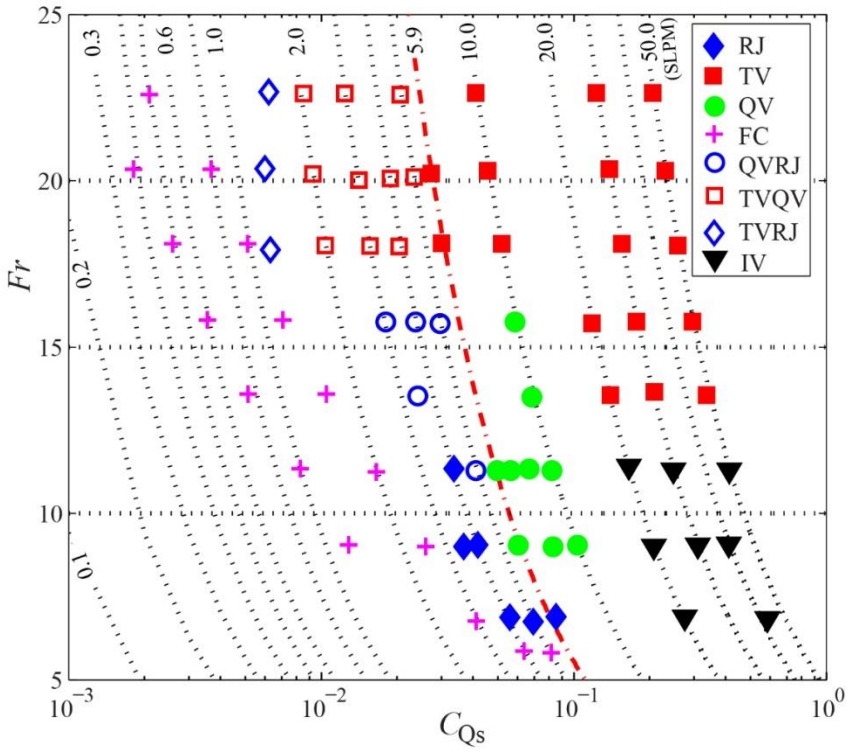

Figure 6.6: Closure map of different closure modes at B = 9 %. The slanted dotted lines denote lines of fixed ventilation flow rates. The values of the ventilation flow rate (in SLPM) are indicated on a selected number of the curves. The red dash-dotted line denotes the 'critical ventilation flow rate'.

B (%)	Q_{crit} (SLPM)
5	1.0
9	5.9
14	16.4
19	34.0

Table 6.2: Critical ventilation flow rates at different blockage ratios.

According to Figure 6.6, a critical ventilation rate has also been identified at higher blockage. This critical rate grows with increasing blockage as shown in Table 2. Moreover, an interesting aspect of the critical air entrainment becomes evident when the data are further analyzed by plotting critical air entrainment coefficient ($C_{Qs,crit}$) vs. Fr (Figure 6.7). As it shows, the curves for the critical air entrainment at different blockage ratios collapse onto a single hyperbolic curve, i.e. $Fr \times C_{Qs,crit} = 0.532$, which suggests that the characteristics of the critical air entrainment is independent of blockage effect.

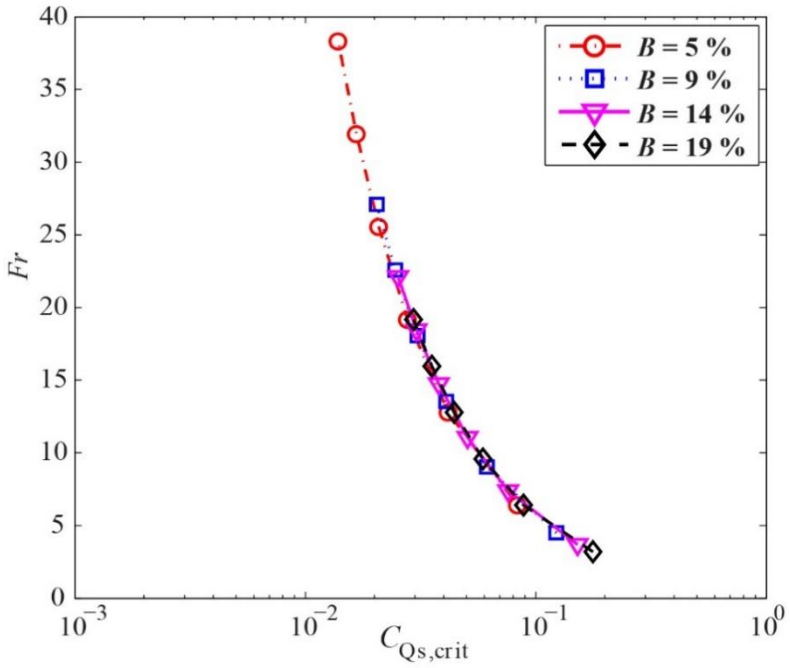

Figure 6.7: Relationship between Fr and $\boldsymbol{C_{Qs,crit}}$ for different blockage ratios

As shown in Figure 6.7, σ_C reaches to a minimum value when a supercavity state is attained and stays fixed upon further changes in C_{Qs}. Here the trend of σ_C with varying Fr is examined at different blockage ratios in Figure 6.8. For each blockage ratio, σ_C decreases in different rates as Fr increases. As high values of Fr are approached, σ_C

reaches a minimum value ($\sigma_{C,min}$), and further reduction in σ_C is limited with any further increment in *Fr*. For *B* = 5 %, 9%, 14% and 19%, the values of $\sigma_{C,min}$ are 0.08, 0.21, 0.35 and 0.51, and are obtained at *Fr* of 32, 18, 14 and 11, respectively. Such dependence of σ_C on *Fr* can be attributed to the choking phenomenon encountered in a closed-wall water tunnel due to blockage effect (Gadd & Grant 1965; Kawakami 2010).

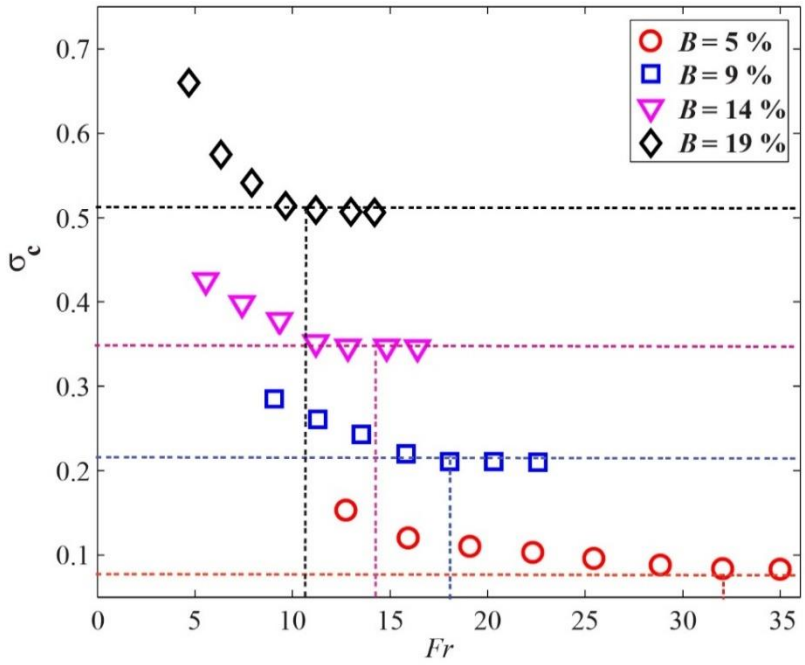

Figure 6.8: Variation of $\boldsymbol{\sigma_C}$ with *Fr* at different blockage ratios. The dotted lines indicate the minimum values of $\boldsymbol{\sigma_C}$ and the corresponding *Fr* when $\boldsymbol{\sigma_C}$ reaches minimum.

Using control volume analysis, Kawakami *et al*. (2010) showed that σ_C can be approximated by the maximum diameter of the supercavity (D_C) and hydraulic diameter of the closed-wall water tunnel as

$$\sqrt{1+\sigma_c} = \left(1 - \left(\frac{D_C}{D_T}\right)^2\right)^{-1} \tag{6.1}$$

The above expression suggests the dependence of σ_C on D_C. Since our observations show that D_C depends upon Fr for a fixed blockage and it attains a minimum with an increase in Fr, a consequent decrement in σ_C is limited with increasing Fr.

The blockage effect on the occurrence of different closure modes is further investigated under a range of flow conditions defined using 'Flow number' (F_L) according to a prior study of ventilated cavitation by Kshatriya, Patwardhan & Eaglesham (2007) and Reynolds number (Re) The F_L is a dimensionless number defined as: $F_L = \dot{Q}_{As}/\dot{Q}_{Ws}$, where $\dot{Q}_{As}$ and $\dot{Q}_{Ws}$ are the air ventilation flow rate and water flow rate at standard conditions through the test-section, respectively. The Re is constructed using incoming flow velocity, hydraulic diameter of the water tunnel and kinematic viscosity (ν) as: $Re = UD_T/\nu$. Unlike C_{Qs} and Fr, F_L and Re offer a characterization of flow conditions independent of cavitator size, facilitating the examination of blockage effect, although F_L can be expressed in terms of C_{Qs} and B, i.e. $(4/\pi)C_{Qs}B^2$.

Based on the framework above, Figure 6.9 provides a summary of distribution of different closure modes corresponding to F_L at two selected Re numbers for four blockage ratios in our experiments. The stable states of the supercavity (i.e. FC, RJ, TV and QV) are primarily considered here for comparison among different blockage ratios. The unstable closure modes shown in the figure refer to PTV for B = 5 % and IV for B = 9 %. The hybrid closure modes (i.e. QVRJ, TVRJ and TVQV) occur over a narrow range of F_L and are thus excluded from the figure.

As figures 6.9a and b show, at $Re = 6.42 \times 10^5$, the larger F_L is required to reach to a supercavity state from FC as B increases. This trend may be more related to the effect

of cavitator size rather than the blockage ratio. A possible explanation for this trend is the transition of FC into a supercavity is driven by bubble coalescence. With increasing ventilation flow rate, it is observed that both the size and number of bubbles increase at the periphery of the cavity. For a larger cavitator size, the bubbles in the foam are more sparsely situated and thus more air is required to drive this coalescence process for its transition to a supercavity. Furthermore, as the figures show, for all blockage ratios, RJ mode is always located between FC and vortex-based closures and over a narrow range of small F_L consistent with Cox and Clayden (1956). With increasing F_L, the closure transitions gradually from RJ to QV mode, then to TV and unstable modes (i.e. PTV for B = 5 %, IV for B = 9 %). It is clear that the range of F_L for QV increases significantly as B increases. Since the extent of RJ mode does not vary appreciably with the change in B, the expansion of F_L range for QV indicates the tendency to form vortex-based closures as B increases. Note that the range of F_L for QV at B = 19% may persist beyond the upper limit of F_L as displayed in the figures, which is constrained by test-section length for observation (since the cavity elongates beyond the test-section as F_L increases) in our experimental facility. The above observation on blockage effect is supported by a number of prior studies in ventilated supercavitation (e.g. Karlikov & Sholomovich 1966; Zhou *et al.* 2010; Skidmore 2013). For example, the experimental results of Skidmore showed that a large water tunnel (i.e. 1.219 m in diameter) leads to RJ closure whereas a smaller one of 0.305 m in diameter yields only TV mode. Using numerical approach and taking into account the effect of blockage on the pressure outside the supercavity, another study

by Zhou *et al.* (2010) presented a good match with the Campbell & Hilborne criterion (Campbell & Hilborne 1958) for transition to TV.

As shown in Figure 6.9c and d, when *Re* increases by a factor of three (i.e. $Re = 1.93 \times 10^6$) in comparison with the results in Figure 6.9a and b, the trend of the closure mode distribution under the influence of F_L and B changes although the trend of FC largely remains the same as before. The RJ mode almost disappears for all blockage ratios. Further, the QV mode disappears for the lower values of B of 5 % and 9 %, suggesting that an increase in *Re* promotes the occurrence of TV mode over QV. To summarize, based on the presented observations in § 6.3.1- 6.3.2, it can be concluded that the supercavity closure is not merely a function of *Fr*, C_{Qs} and σ_C as discussed by numerous prior studies. Instead, a clear understanding of the physical mechanism is needed while formulating a criterion that determines supercavity closure viz. flow conditions, blockage effect and the type of experimental facility, etc. In the following sections, we present a hypothesis on the physical mechanism determining closure, provide supporting evidences for this hypothesis, and use it further to explain experimental observations at SAFL and other facilities.

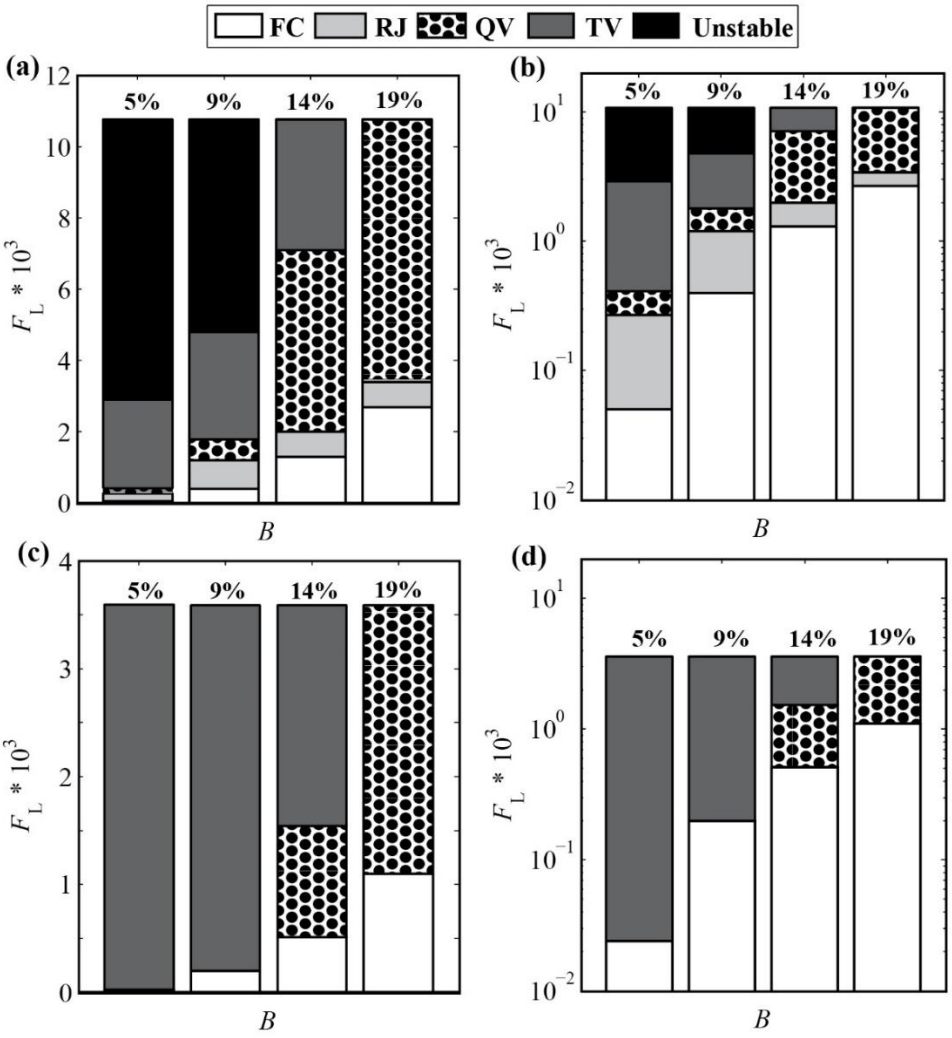

Figure 6.9: Variation of different closure modes with B and F_L at (a) $Re = 6.42 \times 10^5$, linear scale (b) $Re = 6.42 \times 10^5$, logarithmic scale (c) $Re = 1.93 \times 10^6$, linear scale (d) $Re = 1.93 \times 10^6$, logarithmic scale. The figures in percentage above the bars represent the values of B.

6.4. Hypothesis and explanation of observations

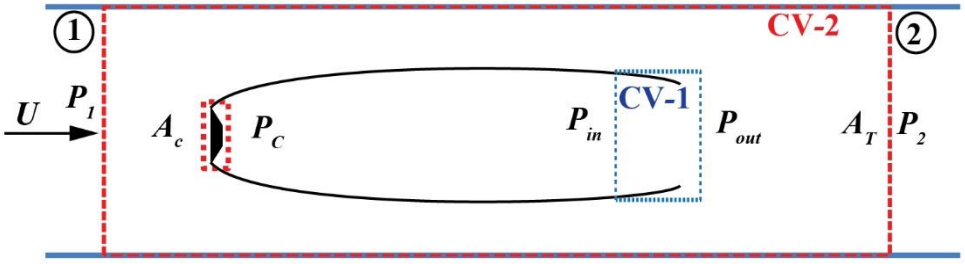

Figure 6.10: Schematic showing the two control volumes related to the supercavity. CV-1 is the control volume at the closure, and CV-2 is the one encompassing the entire cavity.

A hypothesis on the physical mechanism that determines the closure modes of a ventilated supercavity is proposed as follows, in order to explain the experimental observations. The hypothesis posits that the closure mechanism is mainly determined by the pressure difference across the gas-water interface at the cavity closure. This pressure difference is constructed in a dimensionless form as $\Delta\tilde{P} = (P_{\text{out}} - P_{\text{in}})/q = \tilde{P}_{\text{out}} - \tilde{P}_{\text{in}}$, where q $(= 1/2\rho U^2)$ is the dynamic pressure of water in the test section, $\tilde{P}_{\text{in}}$ and $\tilde{P}_{\text{out}}$ are the dimensionless static pressures inside and just outside the cavity at the closure, respectively (illustrated in Figure 6.10). Note that P_{in} may deviate from the mean cavity pressure due to the internal flows of the supercavity (Pan et al. 2010). We hypothesize that the change of Fr, C_{Qs}, B or type of experimental facility leads to the change of $\Delta\tilde{P}$, resulting in the variation of closure modes. Based on a momentum analysis of the control volume at the closure (CV-1 in Figure 6.10), $\Delta\tilde{P}$ is determined by gas/water phase momentum across the closure, and other physical factors such as surface tension. Among these factors, the net water momentum flux at the closure is dominant since the water density is much higher than that of the ventilated air. It is noteworthy that a number of

prior studies have examined cavity closure using physics-based analysis. For instance, Tulin (1965) used momentum theory to show a pressure recovery at the closure of the supercavitating propellers, although his study did not involve different closure modes. Using boundary layer analysis, Spurk & König (2002) noted that the cavity closure is determined by the change of streamline curvature at the rear portion of the cavity.

According to the conceptual framework above, for RJ mode, the $\Delta\tilde{P}$ is dominated by the momentum of re-entrant water jet, while for a vortex-based closure (e.g. TV and QV modes), such pressure difference is significantly smaller in the absence of a re-entrant jet, i.e. $\Delta\tilde{P}_{\mathrm{RJ}} \gg \Delta\tilde{P}_{\mathrm{TV}}, \Delta\tilde{P}_{\mathrm{QV}}$. Nevertheless, the distinct geometric differences between various vortex-based closures suggest that surface tension may contribute to small variation of pressure difference at the closure which causes the change of closure modes. The influence of surface tension on twin vortex closures has been admitted in the prior studies by Cox & Clayden (1956), Logvinovich (1973), Epshtein (1973) and more recently by Shi, Itoh & Takami (2000). In the case of a stable air bubble in water, the surface tension on the curved interface induces a pressure difference across a bubble film. In a similar manner, we speculate here that the variation of mean curvature at the closure among different vortex-based closure modes indicates a surface tension effect and a small variation of $\Delta\tilde{P}$. Since a QV closure results from the further splitting of each vortex of a TV closure, it is further hypothesized that the mean curvature at QV closure is smaller than that for TV mode. Consequently, the pressure difference for QV mode is smaller than that for TV, i.e. $\Delta\tilde{P}_{\mathrm{QV}} > \Delta\tilde{P}_{\mathrm{TV}}$. Summarily, the above discussion leads to a $\Delta\tilde{P}$

criterion for the occurrence of different closure modes, i.e. $\Delta\tilde{P}_{\mathrm{RJ}} >> \Delta\tilde{P}_{\mathrm{QV}} > \Delta\tilde{P}_{\mathrm{TV}}$. Specifically, this criterion implies that RJ occurs when $\tilde{P}_{\mathrm{out}}$ is significantly higher than $\tilde{P}_{\mathrm{in}}$. As $\Delta\tilde{P}$ reduces to a critical value when it is no longer sufficient to sustain a re-entrant jet, the closure region transitions from RJ to vortex-based closures, from QV to TV gradually as $\Delta\tilde{P}$ keeps decreasing.

The above framework can be further extended to include blockage effect of a closed-wall water tunnel. This extension is conducted through a momentum analysis on the control volume encompassing the entire supercavity (i.e., CV-2 as shown in Figure 6.10). The CV-2 consists of the horizontal control surfaces coinciding with the test-section walls, vertical surfaces located far upstream (with pressure P_1) and downstream (with pressure P_2) of the cavity, and the surfaces that just enclose the cavitator. Assuming that viscous shear stress on the horizontal control surfaces is negligible, the horizontal momentum equation of CV-2 can be expressed as follows:

$$P_1 A_{\mathrm{T}} = P_2 A_{\mathrm{T}} + F_{\mathrm{D}} \tag{6.2}$$

where A_{T} represents the cross-sectional area of the tunnel and F_{D} is the drag force on the cavitator. To make a connection among the above equation, σ_{C} and B, the follow relations are used:

$$F_{\mathrm{D}} = C_{\mathrm{D}} A_{\mathrm{C}} (1/2\rho U^2) = C_{\mathrm{D}} A_{\mathrm{C}} q \tag{6.3}$$

$$\sigma_{\mathrm{C}} = (P_1 - P_{\mathrm{C}})/\, q \tag{6.4}$$

$$A_{\mathrm{C}}/A_{\mathrm{T}} = B^2 \tag{6.5}$$

$$C_{\mathrm{D}} = C_{\mathrm{xD}}(1 + \sigma_{\mathrm{C}}) \tag{6.6}$$

where, A_{C} is the cross-sectional area of disk cavitator and P_{C} is the internal cavity pressure measured close to the cavitator as shown in Figure 6.11. C_{xD} is a constant equaling 0.82 for a disk cavitator (Stinebring et al. 2001). As a result,

$$(P_2 - P_{\mathrm{c}})/q = \sigma_{\mathrm{C}}(1 - C_{\mathrm{xD}}B^2) - C_{\mathrm{xD}}B^2 \tag{6.7}$$

Since a ventilated supercavity is predominantly filled with air and the air density is significantly smaller than that of water, the difference between P_{C} and P_{in} cannot be significant. According to Nesteruk (2014), a constant σ_{C} over entire cavity surface can be assumed for a ventilated cavity i.e. $P_{\mathrm{C}} \approx P_{\mathrm{in}}$. Further, assuming $P_{\mathrm{out}} \approx P_2$, we obtain:

$$\Delta\tilde{P} = \sigma_{\mathrm{C}}(1 - C_{\mathrm{xD}}B^2) - C_{\mathrm{xD}}B^2 \tag{6.8}$$

The above equation shows the direct connection between $\Delta\tilde{P}$ and the blockage ratio. In addition, based on this equation, an estimate of $\Delta\tilde{P}$ can be obtained from the current measurements, which provides experimental evidence of the proposed $\Delta\tilde{P}$ criterion. As an example, Table 6.3 presents estimated $\Delta\tilde{P}$ along with the observed closure modes for B = 9 %. The different Fr numbers are selected at C_{Qs} = 0.04 to include different cavity states in the flow map shown in Figure 6.4. As the table shows, as estimated $\Delta\tilde{P}$ reduces, supercavity transitions from a RJ to a QV, and then to a TV closure, consistent with the proposed criterion. Note that the estimated $\Delta\tilde{P}$ may yield some difference from the $\Delta\tilde{P}$ in the proposed criterion due to the assumptions made to derive equation (6.8).

Fr	σ_C	$\Delta\tilde{P}$	Cavity States
6.8	0.363	0.354	FC
9.0	0.288	0.279	RJ
15.0	0.221	0.213	QV
20.0	0.210	0.202	TV

Table 6.3: Variation of estimated $\Delta\tilde{P}$ with cavity states for B = 9 %

Furthermore, we also conducted some experiments to study the effect of relative change in pressure inside and outside of the cavity on supercavity closure, for hybrid modes. In these experiments, the test-section pressure was adjusted independently with fixed Fr and C_{Qs}. The results show that a slight change in the test-section pressure can lead to the transition of hybrid closure modes to stable modes. For instance, it is observed that for QVRJ closure, an increase in test-section pressure (i.e. larger $\tilde{P}_{\text{out}}$ and $\Delta\tilde{P}$) leads to a transition to RJ mode, whereas a decrease in the pressure (i.e. smaller $\tilde{P}_{\text{out}}$ and $\Delta\tilde{P}$) makes the closure transition to QV mode. It should be noted here that a change in test-section pressure is also coupled with a change in the value of $C_{Q,}$ which might also contribute to such closure transitions. Similarly, the recent study by Karn, Arndt & Hong (2015) suggests the effect of variation in $\Delta\tilde{P}$ on supercavity closure under unsteady flow conditions.

It is worth pointing out that it is difficult to carry out pressure measurements inside and outside of the closure because of the presence of the highly unsteady two-phase flow at the supercavity rear portion and limitations of the available experimental techniques. However, the evidences presented above provide both qualitative and quantitative support to our proposed $\Delta\tilde{P}$ criterion in determining supercavity closure.

The developed framework is now employed to further explain the experimental observations as follows.

6.4.1. Variation of Closure with Fr or C_{Qs}

Based on the above discussion, we postulate that the variation of flow conditions (i.e. the change in C_{Qs} and Fr) leads to a change in $\Delta\tilde{P}$, thus causing the transition among closure modes reported in § 6.3.1. Specifically, for a fixed B and Fr, an increase in C_{Qs} implies an increase in cavity pressure, which results in higher $\tilde{P}_{in}$. Since $\tilde{P}_{out}$ is little dependent on C_{Qs}, the $\Delta\tilde{P}$ is likely to continue decreasing with increasing C_{Qs}. According to the proposed $\Delta\tilde{P}$ criterion, this reduction of $\Delta\tilde{P}$ can lead to a gradual transition of closure modes from RJ to QV, and then to TV, consistent with the observations presented in Figure 6.5. On the other hand, for fixed B and C_{Qs}, an increase in Fr, corresponding to higher water velocity, leads to an increment in fluid dynamic pressure and a decrement in static pressure outside the closure, and thus reduces $\tilde{P}_{out}$. However, the increase in Fr also leads to a reduction in $\tilde{P}_{in}$ due to the change in cavity geometry. Therefore, its net effect on $\Delta\tilde{P}$ cannot be readily decoupled with C_{Qs}. This phenomenon causes some subtle variation in closure mode transition at different C_{Qs} values upon change in Fr as observed in Figure 6.4 and Figure 6.6.

6.4.2. Variation of supercavity closure with blockage ratios

The equation (6.8) provides a direct link between $\Delta\tilde{P}$ and blockage ratios. As it shows, higher blockage leads to smaller $\Delta\tilde{P}$, promoting the occurrence of TV modes according to the proposed $\Delta\tilde{P}$ criterion. This conclusion is consistent with the

experimental observations and prior studies reported in § 6.3.2. It worthwhile noting that at a high blockage, two additional effects have a bearing on the $\Delta\tilde{P}$. First, the growth of turbulent boundary layer at the test-section walls effectively reduces the flow area and leads to a longitudinal pressure gradient in the test-section (Wu, Whitney & Brennen 1971). Second, the wall viscous effect that is neglected in the derivation of equation (6.8) may also become substantial. Nevertheless, these effects would contribute to a greater drop in $\tilde{P}_{\text{out,}}$ as compared to $\tilde{P}_{\text{in,}}$ thus resulting in a lower $\Delta\tilde{P}$, which is in favor of the occurrence of TV mode.

As shown in Figure 6.9, the TV mode is dominant even at the lowest blockage ratio, which indicates the presence of considerable blockage effect in our experiments according to the proposed framework. This assessment is supported by a recent experiment using a large water tunnel (Skidmore 2013). In this study, a maximum blockage ratio of 1.6% is observed to yield RJ closure as the dominant mode, which is still significantly lower than the smallest *B* in our experiments (i.e. 5%). It is important to note that the effect of cavitator size may also play a role when interpreting the observations of RJ closure modes at different blockage ratios. According to a number of prior studies (Gopalan & Katz 2000; Callaneare *et al.* 2001; Kshatriya, Patwardhan & Eaglesham 2007), a slender cavity generated from a small cavitator does not yield sufficient adverse pressure gradient to create a reentrant jet and consequently TV is favored. Gadd & Grant (1965) conjectured that the observation of RJ modes in their water tunnel experiments with relatively high blockage (i.e., B = 7 - 11 %) may be related to the large size of cavitators used (i.e., 8 – 14 cm in diameter). Therefore, it is possible

that the attainment of RJ closure mode in a closed wall facility requires not only a low B but also a cavitator of sufficient size.

6.5. Summary and Discussion

A study has been conducted to investigate the physical mechanisms determining the closure formation and transition between different closure modes for ventilated supercavitation. We carried out the experiments in a closed-wall recirculating water tunnel to image ventilated supercavity closure using high-speed and high-resolution photography and to measure pressure inside the cavity over a wide range of flow conditions. Apart from the classical closure modes reported in the literature, the study has revealed a number of new closure modes occurring during the transition between classical modes or under very specific flow conditions. We construct closure maps to depict the flow regimes of each closure mode as a function of Fr and C_{Qs} for different blockage ratios. Based on the closure map, a critical ventilation flow rate is identified at each blockage ratio, and the corresponding critical air entrainment coefficient is found to be independent of blockage ratio. It has also been observed that in the process of generating a supercavity by increasing ventilation flow rate, the cavitation number gradually reduces to a minimum value and stays fixed upon a further increment in ventilation rate. Once a supercavity is formed, the ventilation rate can be decreased to a much lower value with no change in cavitation number while maintaining a supercavity. This process is accompanied by a transition in closure modes which generally goes from twin vortex, to quad vortex and then to re-entrant jet. In addition, the blockage effect is shown to play an important role in promoting the occurrence of twin vortex closure

modes. Subsequently, a physical framework governing the variation of closure modes is proposed, and is used to explain mode transition upon the change of flow conditions including the blockage effect. In the discussion below, this framework is further extended to examine the closure variation across different types of flow facilities, the natural supercavity closure and the pulsating supercavity reported in the literature, and shed light on a recent numerical study of supercavity internal flows.

6.5.1. Closure of a ventilated supercavity in a free surface facility

The fundamentals established in § 6.4 can be extended to explain the different observations of supercavity closure obtained in a free surface facility. For such facility, P_{out} is primarily controlled by the pressure at the free surface and the depth of submergence, which determines the hydrostatic pressure outside the supercavity, whereas P_{in} is largely regulated by the ventilation flow rate. Specifically, unlike the closed wall tunnel, both the pressure upstream the cavity and the pressure outside the closure in a free surface facility are dictated by the presence of the free surface, and are less dependent on *Fr*. Thus, for the same set of *Fr*, C_{Qs} and upstream cavity pressure, the pressure difference at the closure ($\Delta\tilde{P}$) in a free surface facility is generally larger than that in a closed-wall tunnel. According to our discussion in § 6.4, this difference in attainable $\Delta\tilde{P}$ between facilities implies that free surface facilities favor the occurrence of RJ over TV compared with closed wall tunnels influenced by blockage effect. Similarly, the above discussion also suggests that for same *Fr* and C_{Qs}, an increasing depth of submergence leads to a consequent decrease in C_Q, and promotes RJ over TV closure in a free surface facility. These inferences are consistent with general trends of the closures observed in closed

wall and free surface facilities (e.g., Cox & Clayden 1956; Campbell & Hilborne 1958; Epshtein 1973). Note that our reasoning does not preclude the possibility of TV occurrence in a free surface facility or the formation of RJ in a closed wall tunnel, but rather provides a qualitative comparison of the trends of occurrence of RJ or TV modes in different types of facilities.

6.5.2. On the closure of a natural supercavity

In a natural supercavity, the P_{in} is equal to the vapor pressure. Therefore, P_{out}, determined by *B* in a closed wall tunnel or hydrostatic pressure head at the cavity closure for a free surface facility, is usually much higher than P_{in}. This large difference in pressure leads to a high value of $\Delta\tilde{P}$, and the occurrence of RJ closure is favored based on our discussion in § 6.4. To verify this, natural supercavitation experiments are conducted at SAFL by systematically varying *Fr* at different values of *B*, and it is observed that the RJ closure is dominant mode for a natural supercavity (Figure 6.11). As the figure shows, the RJ closure is marked by the presence of such recurrent toroidal vortices in the wake of the cavity. According to Semenenko (2001a), the re-entrant jet at the cavity rear creates a foamy region, which moves as a toroidal vortex, experiencing tangential stresses from the cavity wall and the forces due to pressure gradient in the central part of the cavity. The growth of these vortices continues with the incoming vapor-water mixture till a time, when both these forces (i.e. tangential force and pressure force) are equal and the vortices are ejected in a recurrent fashion. This invariable occurrence of RJ closure for natural supercavitation agrees with the experiments reported from different facilities

(e.g., Logvinovich 1973; Hrubes 2001; Semenenko 2001a; Stinebring *et al.* 2001; Vlasenko 2003; Zhang *et al.* 2007; Ahn *et al.* 2013).

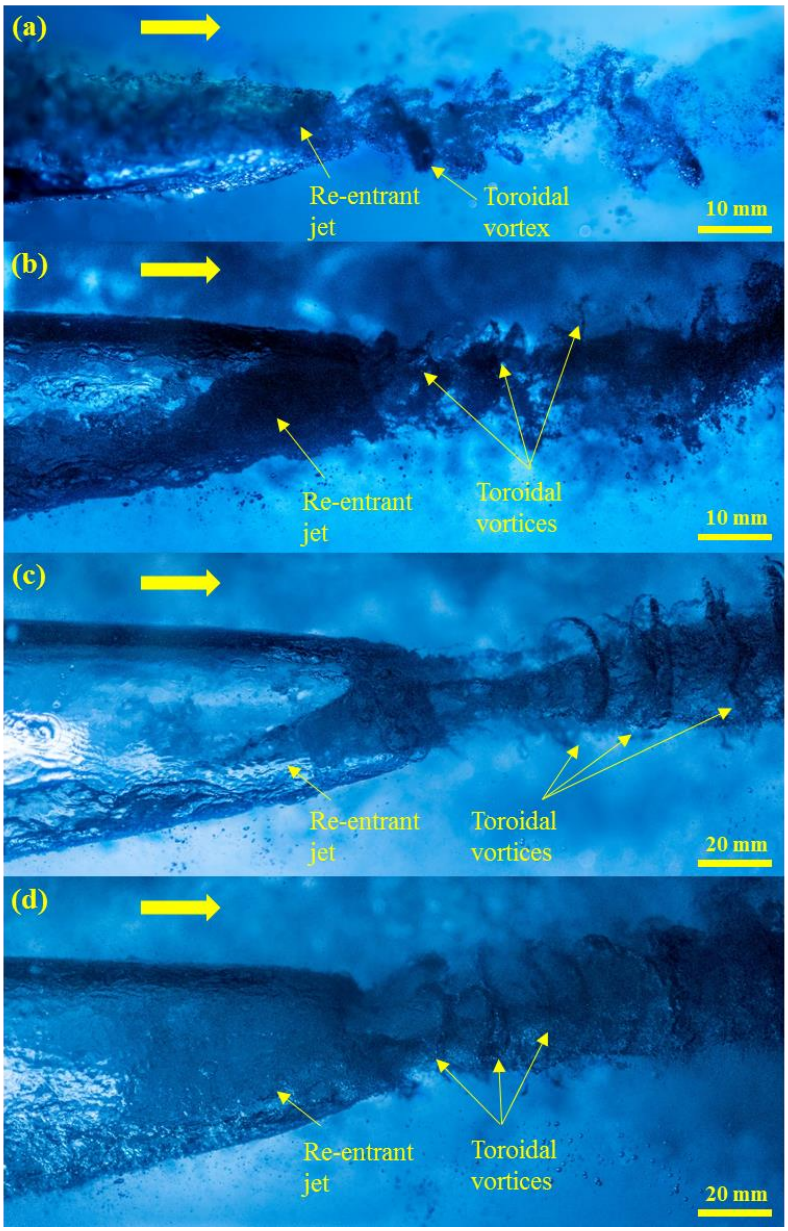

Figure 6.11: Closure images of natural supercavity at (a) B = 5 % (b) B = 9 % (c) B = 14 % (d) B = 19 %. Note that the vortices are filled with water vapor. The horizontal arrow indicates the direction of the water flow.

6.5.3. On the occurrence of pulsating cavity closure

Based on our discussion in § 6.4, we posit that the cavity pulsation may result from the periodic pressure fluctuations inside the cavity, which necessitates the presence of a free surface in the facility since the tunnel walls would restrict the radial expansion of the cavity associated with pulsation. Despite the debate regarding the mechanism of PC in literature, a careful scrutiny of the experimental facilities in all the reported studies reveals the presence of a free surface either in the test-section or in a tank connected to the test-section (e.g. Song 1961; Michel 1984; Skidmore 2013). This remark is further supported through a comparison among Silberman & Song (1959), Skidmore (2013) and our current study. Specifically, Silberman & Song observed PC across a much wider range of flow conditions in a vertical water tunnel with two free surfaces compared to Skidmore's experiments in a free surface flume. In addition, in our current experiments at SAFL closed-wall water tunnel, the pulsating cavity is not obtained even though the experiments are conducted over a wide range of water velocity and air ventilation flow rate at all blockage ratios.

6.5.4. Dependence of supercavity behavior upon internal cavity flow

The previous sections have delineated how our proposed hypothesis can be used to explain the supercavity closure under a variety of flow environments. It is noteworthy that one of the key premises of our theory is that the internal flow within a ventilated supercavity can yield a non-uniform pressure distribution, and thus affect cavity closure. However, due to the experimental challenges involved in quantifying flows across gas-water interface, very few researchers have examined the internal cavity flows. Using a

numerical approach, a recent study by Kinzel, Lindau & Kunz (2009) shows that the internal flow within the cavity core is intricately related to the ventilation flow rate. For C_{Qs} greater than a threshold value (i.e., $C_{Qs,thres}$), the mean flow velocity inside the cavity core (U_C) is in the downstream direction (i.e., $U_C > 0$) and a pressure-driven twin vortex cavity results. For C_Q close to $C_{Qs,thres}$, there is negligible flow of air inside the cavity core and the mean flow velocity is close to zero, and a RJ closure occurs. On the other hand, when C_{Qs} is less than $C_{Qs,thres,}$ there is flow recirculation inside the cavity and the mean flow velocity inside the cavity core is in the upstream direction (i.e., $U_C < 0$). Here we combine their numerical results with our proposed framework in § 6.4 to explain some interesting observations pertaining to closure transitions in our experiments, which highlights the significance of internal flow within a cavity. In particular, we will focus on the following four observations as noted in § 6.3:

(a) *Critical ventilation flow rate*: Our experiments show a critical ventilation flow rate (Q_{crit}) for each blockage ratio, below which the supercavity collapses (i.e. transition to FC) as *Fr is* decreased from a large initial value. As shown in Table 6.3, large $\Delta\tilde{P}$ values lead to a transition of a supercavity into FC state. Based on our framework in § 6.4.1, as *Fr* is decreased at a fixed *B* (or, cavitator cross-sectional area A_c), the consequent reduction in dynamic pressure and increment of test-section pressure leads to an increment in $\tilde{P}_{out}$. For the cavity to sustain, $\tilde{P}_{in}$ has to be high enough to ensure $U_C > 0$, and prevent water at the cavity rear to rush into the upstream portion of the cavity and cause cavity collapse. Since $\tilde{P}_{in}$ at different *Fr* depends upon the ventilation flow rate, there exists a critical ventilation flow rate corresponding to each cavitator, such that $\Delta\tilde{P}$ is

small enough to prevent cavity collapse in the range of *Fr* tested. This argument has been supported by examining the dependence of Q_{crit} upon cavitator size presented in Figure 6.12, which shows direct proportionality of Q_{crit} with respect to A_c.

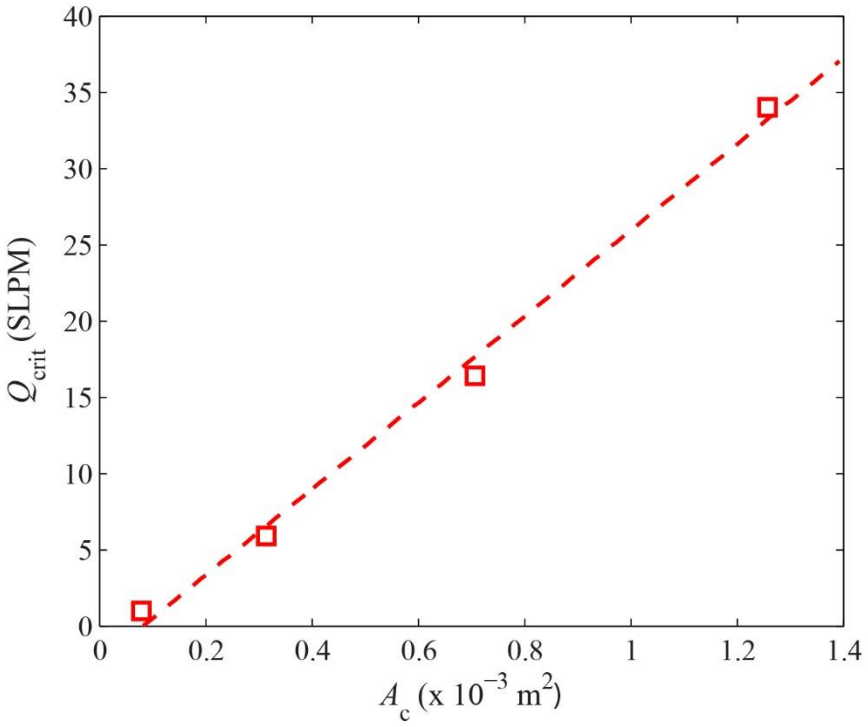

Figure 6.12: Dependence of Q_{crit} upon A_c. The square symbol denotes the Q_{crit} corresponding to each cavitator used in the experiments, and the straight line is the least square linear fit of the square symbols.

(b) *Ventilation hysteresis*: significantly higher ventilation flow rate is required to establish a supercavity than to sustain it. FC consists of a number of closely packed small individual bubbles, which increase both in number and size upon increment in ventilation flow rate due to bubble coalescence events (Wu 1972; Kshatriya, Patwardhan & Eaglesham 2007). With further increase in the ventilation flow rate, the bubbles along the periphery are subjected to high shear flow, resulting in elongation and coalescence until a

clear supercavity is formed. Thus, to drive this coalescence process into a supercavity necessitates sufficient ventilation flow to generate a pressure-driven twin vortex cavity with $U_C > 0$. However, once a supercavity is formed, it is possible to maintain the cavity by lowering C_{Qs}. Upon such reduction in ventilation flow, the internal cavity flow adapts itself (i.e., U_C reduces and becomes non-positive) with a simultaneous change in closure mechanism.

(c) *Path selectivity*: RJ closure cannot be generated from a foamy cavity by increasing ventilation flow rate. It can only be obtained by gradually decreasing ventilation flow rate from an established TV closure. This phenomenon is related to the ventilation hysteresis discussed above. According to our discussion, a minimum ventilation flow rate (i.e. $C_{Qs,thres}$) is required to drive the process of bubble coalescence for generating the supercavity. For RJ closure, U_C is close to zero which generally corresponds to a large $\Delta\tilde{P}$ and air entrainment coefficient below $C_{Qs,thres}$. Therefore, RJ closure can only be obtained by lowering C_{Qs} after the supercavity is formed.

(d) *Susceptibility*: The formation of RJ closure is sensitive to the changes in Fr and C_{Qs}. During the transition from TV to RJ closure, an abrupt reduction in Fr or C_{Qs} leads to cavity collapse. Further, RJ closure is stable only in a very narrow range of Fr and C_{Qs}. As discussed above, the attainment of RJ requires U_C to reduce to a value very close to zero. During this process, an abrupt change in water velocity or ventilation rate (corresponding to a change in Fr or C_{Qs}) could set up a strong recirculation in the upstream direction (i.e. $U_C<0$), causing cavity breakdown.

However, to substantiate above reasoning and elucidate the flow physics inside a supercavity requires some advanced imaging experiments across the water-supercavity interface, which might be considered in future investigations.

Chapter 7. Dependence of supercavity closure upon flow unsteadiness

The current chapter reports some interesting experimental results for ventilated supercavitation in an unsteady flow. Our experiments have shown that incoming flow unsteadiness does not only affect supercavity shape but also leads to a change in supercavity closure, irrespective of the presence of a body inside the supercavity. Synchronized high-speed imaging and pressure measurements have ascertained the dependence of supercavity closure on instantaneous cavitation number under unsteady flow conditions. Further, control-volume analysis at the closure shows the intricate relation among the cavitation number, pressure difference occurring at the supercavity closure and the obtained closure mechanisms.

7.1. Relevance of unsteady flows in the study of supercavitation

The supercavitation phenomenon is of great practical interest due to its advantages in the drag and noise reduction for high-speed underwater vehicles (Brennen 1995, Franc and Michel 2004, Nesteruk 2012). Such high-speed supercavitating vehicles travel inside cavities which may be naturally or artificially generated (Dzielski 2011). A supercavity can be formed at lower speeds by injecting non-condensable gas, viz. air at the downstream of the cavitator, commonly referred to as artificial or ventilated supercavitation (Cameron et al. 2011). The study of supercavity closure, i.e. how a supercavity closes in the rear portion, is significant, since a majority of ventilated gas leaks from the closure region, and the ventilation demand to form and sustain a supercavity is dependent upon the closure mode of a supercavity under different flow conditions (Stinebring et al. 2001, Lindau and Kinzel 2013, Skidmore 2013).

Twin-vortex (TV) and re-entrant jet (RJ) are two major supercavity closure mechanisms reported in the published literature (Cox and Clayden 1956, Campbell and Hilborne 1958, Buyvol 1980, Spurk 2002, Kawakami and Arndt 2011). These studies have investigated the flow conditions that govern the formation and transition of different closure modes based on empirical formulations using dimensionless parameters. In most cases, different types of closure modes have been studied separately, and no universal physics-based model of supercavity closure and gas entrainment has been yet proposed (Semenenko 2001a). Thus, the conditions of formation of a particular closure mode reported by different authors are not in agreement with each other (Campbell and Hilborne 1958, Buyvol 1980, Spurk 2002, Kawakami and Arndt 2011).

Moreover, the behavior of supercavity closure is intricately related to the unsteadiness of the external flow conditions. In reality, for a supercavitating vehicle operating under the sea, the supercavity might encounter varying external flow conditions and unsteadiness particularly when the underwater vehicle moves close to the sea surface and encounters the effect of sea waves. The unsteady flow induced by the movement below a wave train might result in fluctuations in the angle of attack and can affect the supercavity. Until now, there have been very few studies on supercavitation in unsteady flows. The computational study by Semenenko on dynamic processes of supercavitation entailed an investigation into the change in supercavity shape upon introducing an unsteady oncoming flow with a sinusoidal disturbance (Semenenko 2001b). The recent study of Lee *et al.* (2013) provided further insight by examining the change in shape of a ventilated supercavity upon duplication of different sea-states. Qi-tao et al. (2008) investigated the case of a supercavitating vehicle pitching up and down in a ventilated supercavity to examine the effect of impact of vehicle body and supercavity on the evolution of pressure inside the cavity. Recent study by Nouri et al. (2015) explored the dynamic characteristics of the cavity with the fluctuations caused by a change in supercavity parameters. However, the effect of flow unsteadiness on supercavity closure has not yet been explored and investigated in detail.

7.2. Setup and Conditions for unsteady state experiments

The experiments are conducted at the Saint Anthony Falls Laboratory high-speed water tunnel. The unsteadiness in the flow is introduced by means of a gust generator as in previous studies (Kopriva et al. 2008). Figure 7.1a below shows a schematic of the

experimental setup. The gust generator consists of two slender oscillating hydrofoils, which are placed upstream of the cavitator at a distance 180 mm. These two hydrofoils oscillate in phase by the system's pivot arm to generate uniform gusts. The pivot arm is linked to a flywheel through a connecting arm, which extracts the periodic motion from the motor. The eccentricity flywheel allows for gusts of varying amplitudes. Time-varying velocity amplitudes of periodic gust flows are measured with Laser Doppler Velocimetry (LDV) as described by Lee et al. (2013). The LDV measurements show that the frequency of the periodic gust flow in the test-section is equal to the oscillation frequency of the gust generator at each flow condition.

A cavitator with back surface facing the incoming flow, referred to as the backward facing model, is employed in the experiment following the previous experiments by Kawakami and Arndt (2011). Figure 7.1b illustrates the general placement of backward-facing model within the test section. As it shows, a hydrofoil strut is placed upstream of the cavitator to avoid the interaction between the formed cavity and the strut body leading to a free closure as reported by Logvinovich (1973). High speed videos of the supercavity are taken to ensure that the slender streamlined hydrofoil upstream does not produce significant disturbance on the cavity and only a faint wake signature could be observed. The model has special ventilation ports at the rear of the cavitator to create a supercavity. The air flow rate is controlled by a mass flow controller and is kept steady during the experiments.

The hypodermic tube used for pressure measurement runs axially inside the ventilation line as shown in Figure 7.1c. Pressures in the test section and the supercavity

are measured using two separate Validyne AP-10 pressure transducers. The pressure transducers are calibrated before each experiment and the pressure lines are purged with compressed air once before the pressure measurements are recorded at each condition. Uncertainty in the upstream pressure obtained using a pressure transducer is found to be less than 3%. The Fast Fourier Transform and the subsequent plot of power spectral density of pressure data show that the dominant frequency matches the oscillation frequency of the gust generator exactly (not shown). The images and the videos of the supercavity closure are obtained with a 1K × 1K pixel Photron APX-RS camera, which is capable of acquiring 3000 frames/s at full resolution. To ensure uniform backlighting in these videos and images, a light shaping diffuser is placed between the light source and the flow. The high speed imaging and the pressure measurements inside the cavity and test-section are synchronized using LABVIEW software. The experiments are conducted at a fixed Fr = 20 and C_Q = 0.03 with a cavitator diameter of 10 mm, which corresponds to a minimal blockage of about 4.7%. At the steady state, the closure observed is re-entrant jet, with a disturbance propagating in upstream direction as also observed in previous studies (Stutz and Reboud 1997, Wu and Chahine 2007, Rashidi et al. 2014). The gust amplitude is kept fixed at 10 degrees for all the experiments and the gust frequencies are varied between 1 – 10 Hz. The pressure measurements and high speed videos are captured at a sampling rate of 1500 Hz.

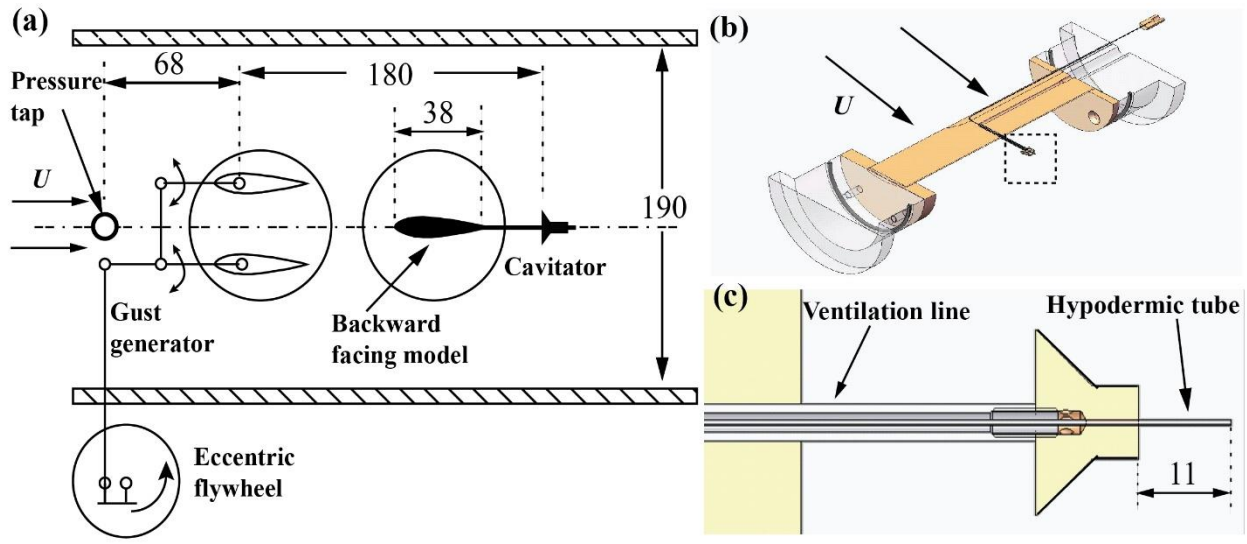

Figure 7.1: (a) The experimental setup for studying unsteady ventilated supercavitation. (b) The schematic of the backward-facing cavitator model. (c) The close-up side view of the cavitator. All dimensions are in mm

7.3. Closure transitions under unsteady flows

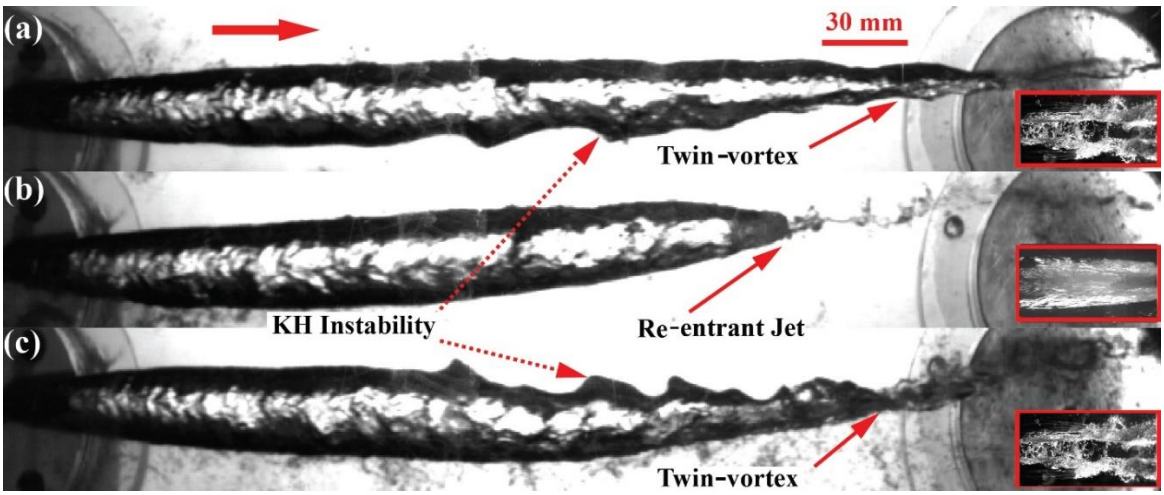

Figure 7.2: The closure variations during a gust cycle with the backward-facing cavitator. The insets show the corresponding bottom views of these closure mechanisms. The arrow on the top left indicates the direction of the liquid flow. The scale bar applies to all three images.

Figure 7.2 shows the supercavity geometry at different time stamps during a gust cycle with the backward-facing cavitator. As the figure shows, the closure mode

alternates between TV and RJ closure in one gust cycle. In the TV closure, the supercavity closes in two counter-rotating hollow vortex tubes with opposite circulation whereas in the RJ closure, the cavity end is filled with foam which is periodically rejected by portions in the form of toroidal vortices. Although the side views of the closure cannot ascertain the presence of a TV closure, it is substantiated by the bottom views of the closures as shown in the insets of Figure 7.2a and Figure 7.2b. Careful observations of high speed videos indicate that TV is formed around the mean location of the oscillating hydrofoil (at the point of minimum blockage in the tunnel) whereas RJ occurs when the oscillating hydrofoils reach their extrema. Further, it is interesting to note the presence of Kelvin-Helmholtz (KH) instability on the supercavity surface for a TV closure, while there is no such instability observed when RJ mode is present. The presence of this instability can be attributed to the unsteadiness in the incoming flow and the instantaneous rise in relative velocity between water and air (Kuklinski et al. 2001). This velocity rise is caused by the large tunnel blockage that is momentarily created at the amplitudes of the oscillating hydrofoils. Note that such closure transitions under unsteady flow conditions are not only limited to free closures, but they can also be observed when there is a body present inside the cavity as shown in Figure 7.3. In addition, for supercavities obtained with both backward and forward-facing cavitators, the expansion of each cross-section of the cavity is relative to the path of supercavity center, consistent with the principle of independent expansion given by Logvinovich (1973). Logvinovich's principle, which is considered to be an efficient tool for calculating the shape of long

three-dimensional supercavities, further states that the supercavity shape also depends on velocity and pressure difference upstream and inside the cavity (Nesteruk 2014).

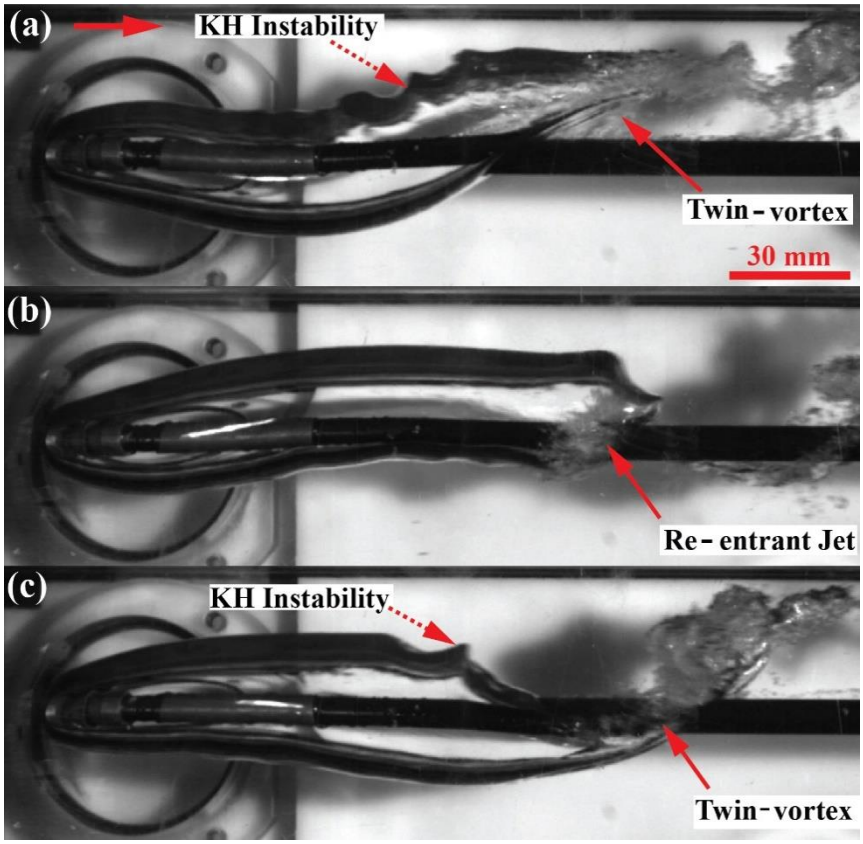

Figure 7.3: The closure variations during a gust cycle with the forward-facing model. The arrow on the top left indicates the direction of the liquid flow. The scale bar applies to all three images

To get an insight into the physical mechanisms that cause the change in cavity shape and closure, we conducted simultaneous pressure measurements both inside and outside the cavity in sync with the high-speed imaging of cavity behavior under different gust frequencies. To quantify the effect of unsteadiness, the pressure data are recorded at steady state (Fr = 20, C_Q = 0.03), under which RJ closure is present. The acquired values yield a non-dimensional test-section pressure ($\widetilde{P_o} = 2P_O/\rho_w U^2$) of 1.92 and non-dimensional cavity pressure ($\widetilde{P_c} = 2P_C/\rho_w U^2$) of 1.66, respectively, corresponding to a

cavitation number ($\sigma = \widetilde{P_o} - \widetilde{P_c}$) of 0.26. When unsteadiness is introduced at a low gust frequency of 0.71 Hz (Figure 7.4a), compared to the steady state values, $\widetilde{P_o}$ drops a little while $\widetilde{P_c}$ increases slightly, thus causing a decrement in σ. The flapping of the gust generator causes fluctuation of test-section pressure which in turn leads to an oscillation in cavity pressure. However, as noted by Kuklinski et al. (2001), pressure information in the liquid may propagate at different speeds than in the gas cavity, resulting in the variation of $\widetilde{P_c}$ that lags half cycle behind that of $\widetilde{P_o}$ in our experiments. This difference in phase of the test-section pressure and cavity pressure leads to the oscillating nature of σ. As the figure shows, σ peaks at the maxima of $\widetilde{P_o}$ and minima of $\widetilde{P_c}$, varying between 0.12 and 0.22. In the time series of σ, the RJ closure occurs at the crests ($\sigma = 0.22$) and TV mode coincides with the troughs ($\sigma = 0.12$). Compared to the steady state, the occurrence of TV closure effectively leads to a lower cavitation for the entire gust cycle. This observation is in agreement with the published reports of Semenenko (2001a) where the RJ closure is reported to have a higher value of $\sigma * Fr$ as compared to TV closure. In our experiments, the parameter $\sigma * Fr$ varies between 2.4 and 4.4 in one gust cycle as the closure modes alternate between TV and RJ respectively. In actuality, if the local increment in Fr due to the blockage caused by gust generator is considered, the actual value of $\sigma * Fr$ are slightly greater. Thus, in all cases it is observed that both TV and RJ closure modes are present at $\sigma * Fr > 2.4$. However, this observed value of $\sigma * Fr$ is in contradiction to the observations of Campbell and Hilborne (1958) and many other

researchers (Buyvol 1980, Semenenko 2001a) who proposed a critical value of unity for $\sigma * Fr$ for TV-RJ closure transition.

This disagreement persists even when the experiments are carried out at a higher gust frequency of 7.10 Hz. The value of $\sigma * Fr$ varies in a narrower range of 3.2 – 3.9 over the entire gust cycle, and the observed closure exhibit the characteristics of both twin vortex and re-entrant jet modes (referred to as TVRJ) as reported in Skidmore (2013). In addition, as shown in Figure 7.4b, both $\widetilde{P_o}$ and $\widetilde{P_c}$ move further away from their steady-state values. Although the trends in variation of $\widetilde{P_o}$ and σ largely remain the same, the peak-to-peak variation of both $\widetilde{P_o}$ and σ decreases considerably while the cavity pressure almost stays constant since it cannot match the high rate oscillations of unsteady ambient flow conditions.

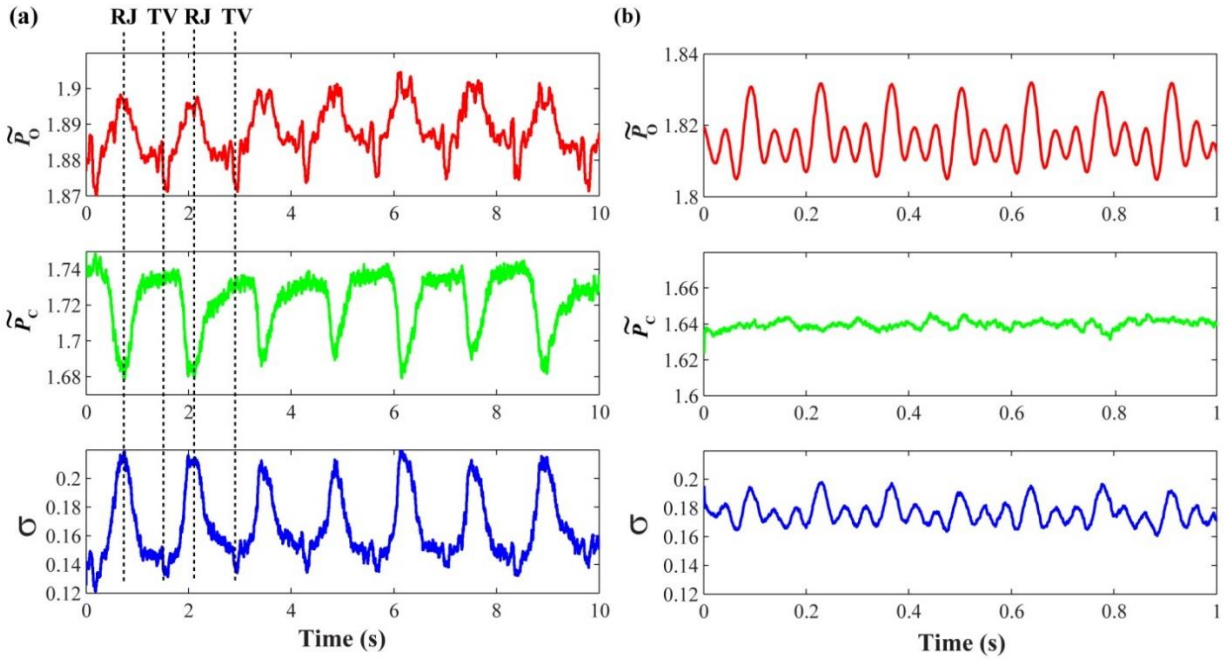

Figure 7.4: The periodic variation of test section pressure, cavity pressure, and the cavitation number defined by their difference for the gust frequency at (a) 0.71 Hz and (b) 7.10 Hz.

Finally, control volume (CV) analysis has been conducted at the RJ closure (CV-1) to provide some insight into the comparison between the pressure difference at the closure and the measurements of σ from our experiments. As shown in Figure 7.5, U indicates upcoming liquid velocity, U_{RJ} is the velocity of liquid rushing into the cavity, U_{Cg} and U_{Og} refer to the velocity of gas entering and exiting the CV-1, respectively, A_C is the cross-sectional area of the CV-1 on the cavity side whereas A_{RJ} refers to the effective area through which liquid enters into the cavity. P_{in} denotes the pressures on the cavity side of CV-1 and P_{out} represents the pressure outside CV-1.

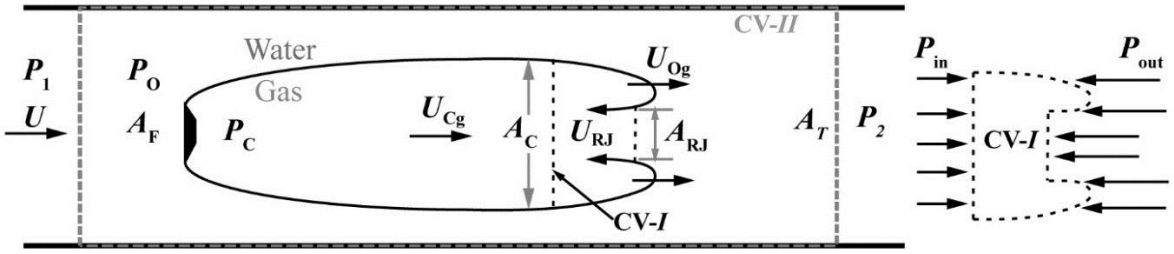

Figure 7.5: Schematic showing the two control volumes: CV-1 is the control volume encompassing the cavity while CV-2 is a control volume at the RJ closure. The horizontal boundaries of CV-2 coincide with the test-section walls

Based on the above definitions, the momentum equation for CV-1 in the x-direction can be written as:

$$A_C P_{in} - A_C P_{out} = -A_C \rho_g {U_{Cg}}^2 + \dot{M}_{in} - \dot{M}_{out}$$

$$(P_{out} - P_{in}) A_C = (A_C \rho_g {U_{Cg}}^2 + A_{RJ} \rho_w {U_{RJ}}^2) - A_C \rho_g {U_{Og}}^2 \quad (7.1)$$

An estimate of P_{out} can be derived through momentum analysis of the control volume that completely encompasses the supercavity (CV-2). For CV-2, the pressure acting on the left and the right surfaces are denoted by P_1 and P_2, respectively, F_D is the

drag force on the cavitator, A_F and A_T are the frontal area of the cavitator and the cross-sectional area of the test-section, respectively. Then the relation between the pressures and drag force on the cavitator can be expressed as:

$$P_2 A_T = P_1 A_T - F_D \tag{7.2}$$

Further, $P_1 \approx P_O$ and $P_2 \approx P_{out}$

$$P_{out} = P_O - F_D / A_T = P_O - \frac{1}{2} * C_D * A_F * \rho_w * U^2 / A_T \tag{7.3}$$

Considering that the momentum carried out by gas in comparison to liquid is negligible, and assuming $P_{in} \approx P_C$ and negligible pressure drop across the cavity, i.e., $P_{out} = P_O$, we can derive:

$$(P_O - P_C) - \frac{1}{2} * C_D * A_F * \rho_w * U^2 / A_T \approx \rho_w (A_{RJ}/A_C) U_{RJ}^2$$

$$2(P_O - P_C)/\rho_w U^2 \approx 2(A_{RJ}/A_C)(U_{RJ}/U)^2 + C_D * A_F / A_T \tag{7.4}$$

Moreover, since the blockage in the test-section due to the cavitator is fairly minimal, the formation of the cavity does not lead to an appreciable increase in liquid velocity outside the cavity. Therefore,

$$\sigma_{RJ} \approx 2(A_{RJ}/A_C)(U_{RJ}/U)^2 + C_D * A_F / A_T \tag{7.5}$$

Using high-speed videos of the RJ closure under the same Fr and C_Q, (A_{RJ}/A_C) and (U_{RJ}/U) is estimated to be about 0.5, and a value of $C_D = 1.17$ is chosen for a disk in a turbulent flow (Fox, Pritchard and McDonald 1998). Substituting these values in the above expression, we obtain: $\sigma_{RJ} \approx 0.25$. Although the CV analysis is conducted for steady state, the calculated value of σ_{RJ} compares well with the maximal cavitation number (corresponding to RJ closure) for the unsteady state, particularly, at low gust

frequency. This remarkable agreement indicates the connection between the fluctuation of cavitation number and the variation of flow patterns and pressure difference across the rear end of a supercavity. Specifically, we have shown that the variations in measured instantaneous cavitation number are coupled with the change in supercavity closure modes during a gust cycle. Thus, the transition among different supercavity closures are actually governed by the physical processes that induce the pressure variation at the closure and flow pattern change inside supercavity, which cannot simply be demarcated by the value of $\sigma * Fr$ as reported in previous studies. However, to substantiate this hypothesis would require systematic experimental investigations of closure modes under a wide range of flow conditions with a quantification of flow and pressure distributions within a supercavity.

7.4. Conclusions

In this chapter, some interesting insights into the transition of supercavity closure mechanisms in an unsteady flow are presented. Our experiments have shown that the incoming flow unsteadiness simulated by periodic gusts, does not only affect supercavity shape but also leads to a change in supercavity closure. At a low gust frequency, it has been observed that under unsteady flow conditions, the supercavity closure alternates between TV and RJ modes at different instants for both backward and forward facing cavitators. Measurements at a higher frequency indicate a similar trend in the variation of pressures and the cavitation number, but the cyclical variation of closure modes becomes less distinct. As shown by simultaneous pressure measurements inside and outside the cavity and the synchronized high-speed imaging, the supercavity closure is a function of

instantaneous cavitation number under unsteady flow conditions. Specifically, the presence of unsteadiness in the flow generates temporal fluctuations in the cavitation number, resulting in distinct closure modes. Further, control-volume analysis at the closure suggests that the cavitation number measurements in our experiments are intricately related to the pressure difference occurring at the closure, which could be the factual cause of occurrence of a variety of closure modes in ventilated supercavitation. These findings point out the significance of looking into the fundamental physics of ventilation supercavitation, which is beyond what the empirical relations (e.g. $\sigma * Fr$ criterion) can offer. The next chapter explores the fundamental relationships between supercavity closures, ventilation hysteresis and ventilation demand.

Chapter 8. Exploring the interrelationship between supercavity closure, ventilation hysteresis and demand

The present work reports some interesting gas entrainment behaviors in the formation and collapse of a ventilated supercavity under steady and unsteady flow conditions. Our experiments show that the gas entrainment required to establish a supercavity are much greater than the minimum gas entrainment required to sustain it, and these gas entrainment values depend on Froude (*Fr*) number, cavitator size and the flow unsteadiness. Specifically, the measurements of the formation gas entrainment coefficients under different *Fr* numbers indicate that it does not monotonically increase with *Fr* but displays increasing and decreasing trends in different regimes of *Fr*. On the other hand, the collapse air entrainment coefficient initially decreases with *Fr* and then approaches to a constant. Similar trends of formation and collapse gas entrainment coefficient are observed for different cavitator sizes. Moreover, the introduction of unsteady gusts causes a slight monotonic increase in the formation and collapse gas

entrainment requirements. Our study points out the crucial factors to be considered in the estimation of gas storage requirements for a ventilated supercavitating vehicle.

8.1. Critical gas entrainment rates during ventilation hysteresis

A supercavity is attained at small σ ($\sigma < 0.1$) and this can be accomplished naturally or artificially. A natural supercavity refers to a large attached vapor cavity which is generated by a body travelling at very high speeds (> 90 knots at a depth of 1 m in open waters) or at low ambient pressure (Kawakami and Arndt 2011). On the other hand, an artificial or ventilated supercavity is generated by blowing non-condensable gas into the low pressure region near the nose of the vehicle. The non-condensable gas increases the cavity pressure, allowing for low σ to be attained at much lower speeds. Ventilated supercavitation has numerous advantages over natural supercavitation viz. greater adaptability for vehicle maneuvering and control. Also, some of the typical negative effects encountered in natural cavitation viz. surface damage, buffeting and vibrations etc. are absent in ventilated supercavitation (Kinzel et al. 2009). A vehicle can be optimally ventilated in case of maneuvering etc. to circumvent the possibility of cavity collapse at different stages of vehicle operation.

A typical design strategy of a supercavitating vehicle entails accelerating the vehicle to a high speed at which a natural supercavity can be sustained. The drastic drag reduction required to attain high speeds at the initial launch of the vehicle is achieved by ventilated supercavitation. Further, the operation of a ventilated supercavitating vehicle depends on its ability to supply sufficient gas to fill the cavity at different flow conditions and at different stages of vehicle motion. The ventilation requirements for a

ventilated supercavity is characterized by the gas entrainment coefficient $C_{\mathrm{Q}} = \dot{Q}/Ud^2$, where $\dot{Q}$ denotes the gas ventilation rate. The determination of the gas storage requirements for a ventilated supercavitating vehicle requires information on gas supply rate to form and sustain a steady supercavity at different flow conditions. Thus, it is important to understand the gas entrainment behaviors relating to supercavity formation and collapse.

A number of prior studies have investigated the gas entrainment behavior of ventilated supercavity under a wide range of conditions (Semenenko 2001a, Savchenko 2001, Kawakami 2010). Ventilation hysteresis is intricately related to the formation and collapse gas entrainments and previous studies on ventilation hysteresis have been reported before by Semenenko (2001) and Kawakami (2010). Ventilation hysteresis refers to a phenomenon whereby the supercavity can be sustained at much lower values of gas entrainment than required to form it, as shown in Figure 8.1.

As the figure below shows, a foamy cavity shows a decrement in σ (or an increase in length) when C_{Q} is increased. This process continues till a point C_{Q} equals C_{Qf} (formation gas entrainment coefficient) and a supercavity is established, after which no further reduction in σ is possible upon change in C_{Q}. Moreover, the supercavity is maintained even as C_{Q} drops down to very low values. Eventually, when C_{Q} drops below C_{Qc} (collapse gas entrainment coefficient), the supercavity transitions back into a foamy cavity. Recently, Karn et al. (2016b) discussed the phenomenon of ventilation hysteresis, particularly focusing on the transition of closure modes of a supercavity and relating

ventilation hysteresis to the internal flows in a supercavity. However, the gas entrainment rate at the formation and collapse of a supercavity have not yet been examined in detail. In this chapter, these entrainment behaviors have been examined in detail.

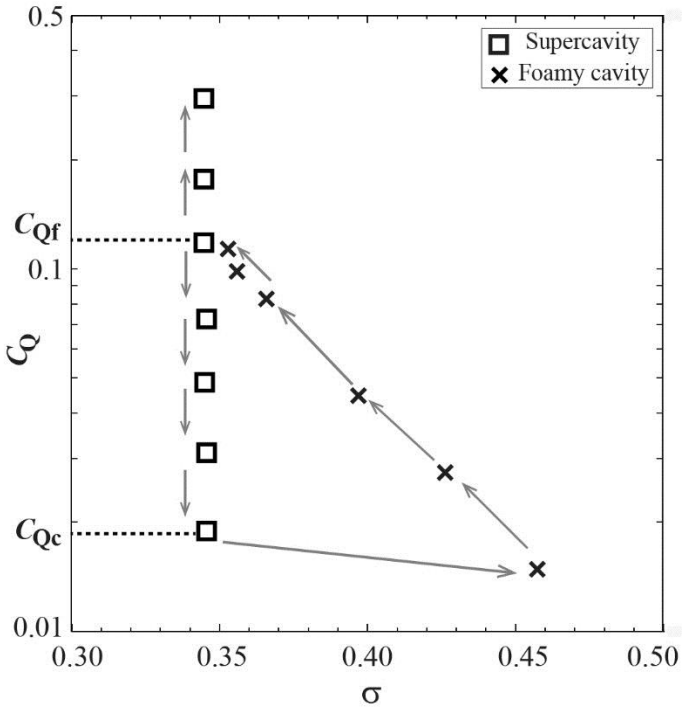

Figure 8.1: A typical ventilation hysteresis curve observed in our experiments for a cavitator of 30 mm in diameter

8.2. Experimental setup and procedure

Experiments are conducted to measure ventilation flow rates and formation and collapse processes of a ventilated supercavity under different flow conditions. The experiments are carried out in the high-speed water tunnel at the Saint Anthony Falls Laboratory. Flow unsteadiness is introduced in the test-section by means of a gust generator as described in chapter 8 and reported in previous studies (Kopriva et al. 2008,

Karn et al. 2015e, Lee et al. 2013). Experimental setup is similar to as described in chapter 2, except for the fact that multiple cavitators of different sizes are used.

A disk cavitator with its back surface facing the incoming flow and mounted downstream of a hydrofoil-shaped strut (referred to as 'backward facing model' earlier, is employed in the current experiments as described in chapter 6. The model has special ventilation ports at the rear of the cavitator to create a supercavity. The gas flow rate is controlled by a mass flow controller and is kept steady during the experiments.

The hypodermic tube used for pressure measurement runs axially inside the ventilation line. Pressures in the test section and the supercavity are measured using a Rosemount absolute pressure sensor and a Validyne DP 15-38 differential pressure transducer, respectively. The Validyne pressure transducer is calibrated before each experiment and the pressure lines are purged with compressed gas once before the pressure measurements are recorded at each condition. Uncertainty in the measurements of test-section pressure and supercavity pressure are less than 1% and 3%, respectively. During the experiments, the ventilation flow rates for the process of supercavity formation and collapse are measured, and the corresponding high speed videos of this process are recorded to obtain physical insights into the phenomena. The measurements of C_{Qf} and C_{Qc} are repeated for different cavitator sizes and flow conditions. A cavitator of 30 mm in diameter is used as the reference (also referred to as the 'reference cavitator' hereafter), and later experiments are repeated with 20 and 40 mm cavitators to study the effect of change in cavitator size. For steady-state experiments, C_{Qf} and C_{Qc} are measured at a fixed Fr, while for the unsteady state experiments, wave-height

and gust frequency are fixed as well. The experiments are carried out at gust frequencies (*f*) of 1, 3 and 5 Hz for each of the gust amplitudes (α) of 2, 4 and 6 degrees.

8.3. Gas entrainment dependencies under steady states

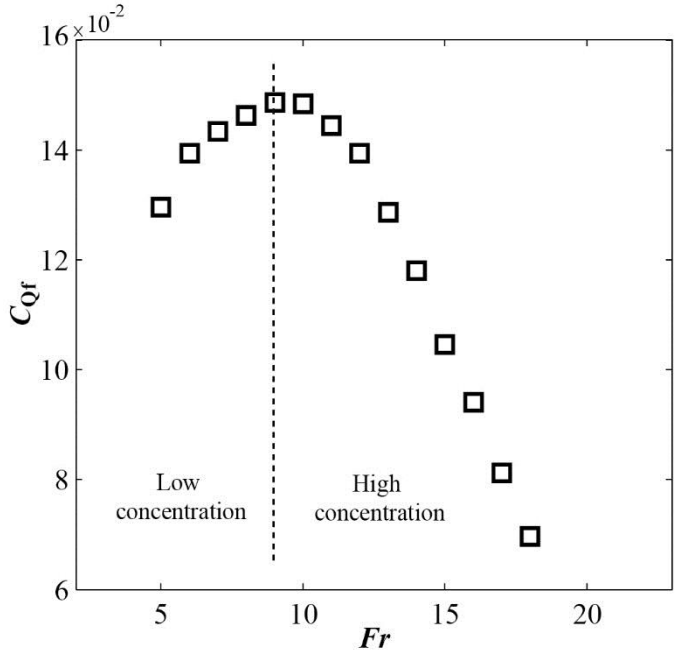

Figure 8.2: Dependence of C_{Qf} upon *Fr* for the reference cavitator

The gas entrainment behaviors at steady state are studied first for the reference cavitator by varying *Fr* in the range of 5 – 25. Figure 8.2 shows a typical variation of C_{Qf} with *Fr*. As the figure shows, with increase in *Fr*, C_{Qf} initially increases, attains a maximum and subsequently decreases. Two separate regimes can be identified around the maximum obtained in this curve, related to the concentration of individual bubbles as will be discussed later. Low *Fr* (*Fr* < 9) corresponds to a low bubble concentration regime, whereas high *Fr* (*Fr* > 9) characterizes a high bubble concentration zone. This trend can be explained based on the assertion that the supercavity formation process is

driven by bubble coalescence, as suggested in chapter 6. In general, for a fixed cavitator size, an increase in *Fr* implies an increase in flow velocity or turbulence. This increased turbulence generally breaks up the individual bubbles of smaller sizes as discussed in previous chapters on wake studies. High speed videos have shown that there are lesser number of bubbles at low *Fr* and an increase in *Fr* results in smaller individual bubbles, with a consequent increase in the number of bubbles. With increasing *Fr,* the formation of a supercavity in this regime essentially requires the coalescence of these resulting smaller individual bubbles. Thus, there is a greater ventilation requirement to increase the size and number of bubbles to form a coalesced supercavity. Previous chapters have shown that an increase in C_{Q} results in an increment in both number and size of bubbles. However, in the high concentration regime, this effect of increased number of bubbles offsets the reduction in the size of individual bubbles. In this regime, the bubble concentration becomes so high that bubbles are closely packed together in the bubble cloud. Due to the restricted free space for bubble movement and the concomitant increase in bubble collision frequency, the coalescence process is favored, resulting in decreased gas entrainment requirement for supercavity formation with increasing *Fr*.

The dependence of C_{Qc} upon *Fr* is presented in Figure 8.4a. As the figure shows, C_{Qc} initially decreases sharply with *Fr* and then becomes constant. This trend of supercavity collapse can be explained using the postulated framework of supercavity closure presented in chapter 6. As presented in chapter 6, the supercavity closure is determined by a balance of pressure inside (P_{in}) and outside (P_{out}) at the supercavity rear portion. The non-dimensional pressure difference defined as, $\Delta\tilde{P} =$

$2\,(P_{\text{out}} - P_{\text{in}})/\rho U^2$, characterizes different supercavity closure modes (e.g. twin-vortex, re-entrant jet) as well as the foamy state of a cavity (the supercavity is yet to form). Their data suggested that $\Delta\tilde{P}$ for a foamy cavity is significantly larger than for a supercavity. In other words, when P_{out} far exceeds P_{in}, the high pressure difference forces water jet to gush inside the supercavity, causing its collapse. Thus, at a high $\Delta\tilde{P}$, larger gas entrainment is required to inhibit the growth of re-entrant jet and maintain a stable supercavity. Further, based on their results, $\Delta\tilde{P}$ can be estimated from the momentum balance for the supercavity as (neglecting the pressure drop due to viscosity) $\Delta\tilde{P}_{\text{est}} = \sigma - C_D(d/D_T)^2$, where D_T represents the diameter of the water tunnel. As shown in Figure 8.3b, $\Delta\tilde{P}_{\text{est}}$ exhibits a similar trend with respect to Fr as that of C_{Qc}.Thus, larger the $\Delta\tilde{P}_{\text{est}}$, the more the supercavity is susceptible to collapse and consequently a greater gas entrainment is required to prevent such a collapse. It is noteworthy that similar to formation gas entrainment curve, the collapse gas entrainment curve can also be divided into two separate regimes. Our experiments have shown that the regime in which $\Delta\tilde{P}_{\text{est}}$ does not change significantly with Fr corresponds to supercavities with stable twin-vortex closure at C_{Qc}. On the other hand, the region in which $\Delta\tilde{P}$ decreases sharply with Fr are characterized by other closure modes at C_{Qc}, including re-entrant jet, quad-vortex or unstable closure modes as discussed in chapter 6.

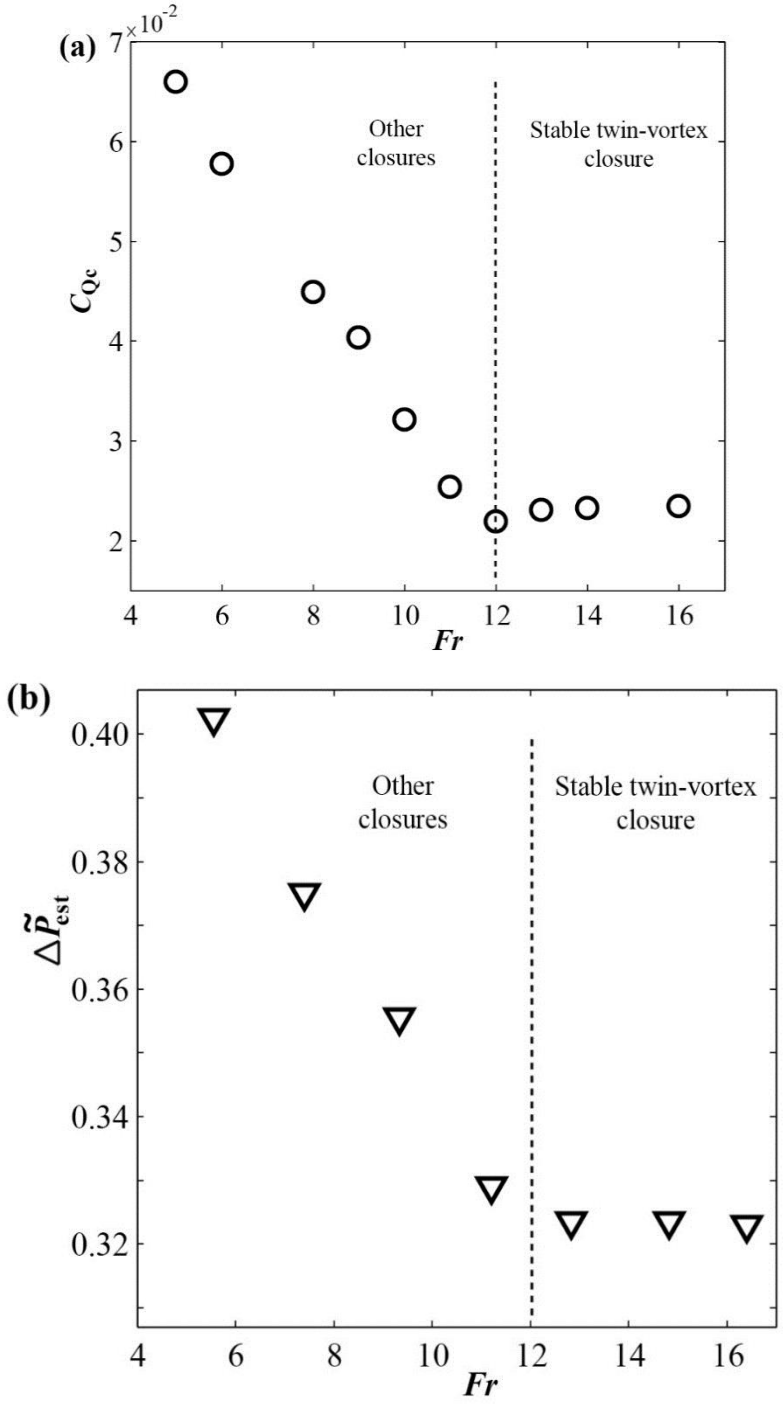

Figure 8.3: (a) Dependence of $\boldsymbol{C_{Qc}}$ upon *Fr* and (b) Dependence of $\boldsymbol{\Delta\widetilde{P}_{est}}$ upon *Fr* for the reference cavitator

Next, the effect of cavitator size on C_{Qf} and C_{Qc} are examined. Figs. 8.4 and 8.5 show the comparison of formation and collapse gas entrainment behavior for three different cavitators, respectively. The figures clearly indicate that a similar trend is observed at a cavitator size of 20 mm and 40 mm. Further, the curves shift upwards and towards left with an increase in the cavitator size. As pointed out before, for the formation gas entrainment curve, the maximum in this curve represents a transition between low and high bubble concentration regimes. The leftward displacement of the maxima in this curve suggests that the critical *Fr* for such transition decreases with increasing cavitator size. This observation can be ascribed to an increasing wake turbulence (characterized by Reynolds number defined based on the cavitator size) which promotes bubble breakup and consequently results in increased concentration of individual bubbles (Karn et al. 2016a). The upward movement of the curve can then be attributed to the larger C_{Qf} required to drive the bubble coalescence process into a wider and longer supercavity with increasing cavitator size. On the other hand, for the collapse gas entrainment behavior, the shift in the curves can be attributed to a similar variation of $\Delta\tilde{P}$ with *Fr* as shown in Figs. 8.3a and 8.3b. The upward movement of these curves with the increasing cavitator size is related to the greater gas entrainment values required to maintain a larger $\Delta\tilde{P}$ with increasing cavitator size. This observation is related to the fact that a larger size cavitator results in a supercavity with increase both in cross-sectional area and length, which the gas entrainment coefficient only accounts for the increase in cross- sectional area. As pointed out in Figure 8.3b, the flat portion of the $\Delta\tilde{P}$ vs *Fr* curve corresponds to a stable twin vortex cavity. Thus, the leftward shift in the

collapse gas entrainment curve indicates that for a larger cavitator the transition from other supercavity closure modes to a twin vortex cavity mode is established at a low *Fr* which persists upon further increase in *Fr*. This indicates that twin vortex is predominantly observed over a larger range of *Fr* for a larger cavitator, which has been previously reported and explained by (Karn et al. 2016b).

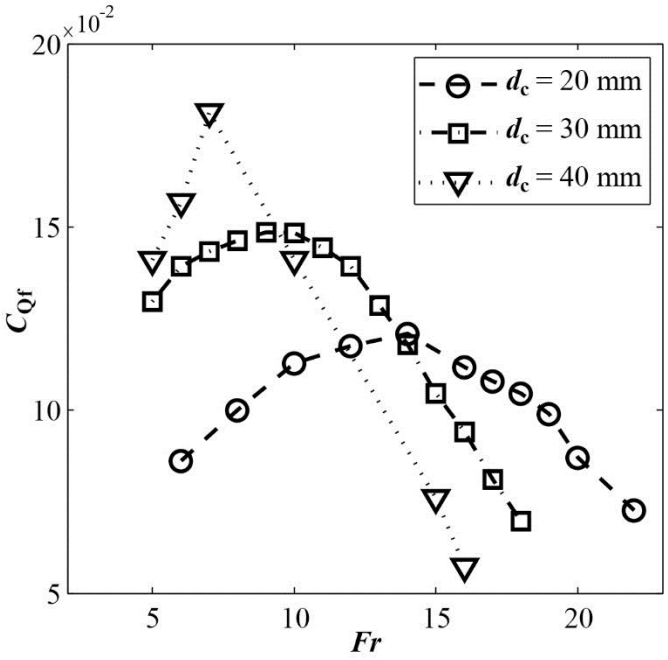

Figure 8.4: Comparison of C_{Qf} vs *Fr* curve for three cavitator sizes

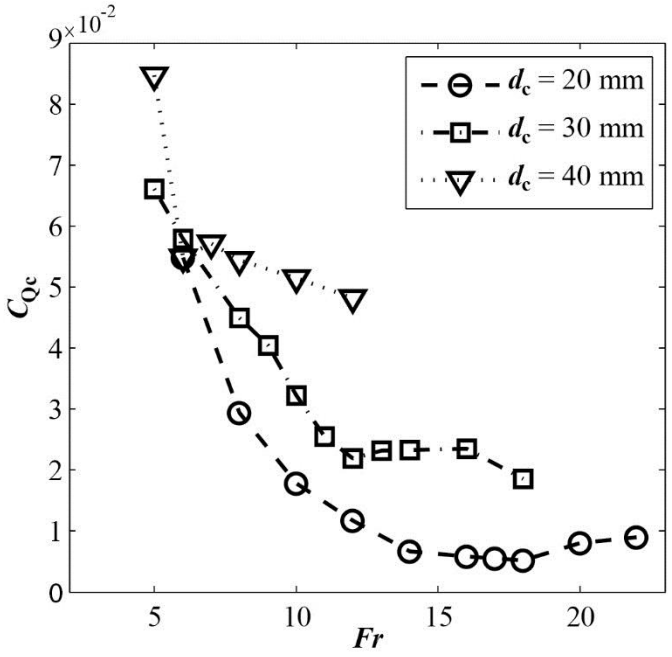

Figure 8.5: Comparison of C_{Qc} vs *Fr* curve for three cavitator sizes

8.4. Unsteady state gas entrainment characteristics

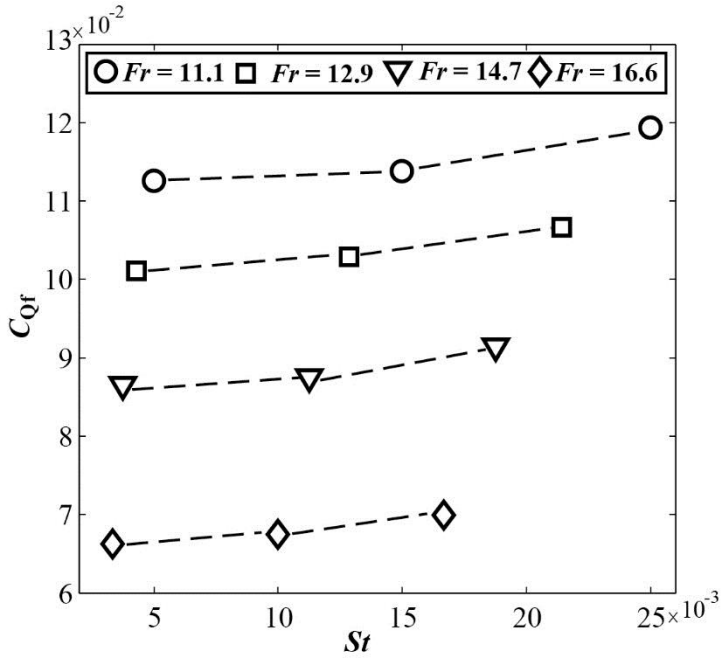

Figure 8.6: Variation of C_{Qf} with *St* at different *Fr* for the reference cavitator

The gas entrainment behaviors under unsteady conditions are studied by first holding Fr and gust amplitude (α) constant and then varying the St $(= fd/U)$ by changing the gust frequencies (f). Figure 8.6 shows the formation gas entrainment behavior under different St values for the reference cavitator at four different Fr numbers. As it shows, at a fixed Fr, C_{Qf} increases monotonically with increase in St. This trend in C_{Qf} with St indicates that the introduction of unsteady gusts in the flow impacts the bubble coalescence process by imposing a lateral velocity on the bubbles. This imposed lateral motion on bubbles makes it more difficult for the coalescence of individual bubbles into a supercavity, thus increasing the C_{Qf} requirement with an increase in St. It is noteworthy that unlike coalescence events in the flow, breakup events is much less affected by the introduction of unsteadiness since the timescales associated with bubbles breakup are substantially smaller than those of the unsteady gusts.

Figure 8.7 shows the effect of the variation of gust amplitudes upon C_{Qf} at a fixed Fr and St. As the figure shows, C_{Qf} increases monotonically with increase in α. High speed videos of the supercavity indicates that an increase in gust amplitude results in the bubbles being spread across a larger lateral cross-section (reducing the local void fraction), which decreases the collision frequency of bubbles and consequently reduces coalescence efficiency. Thus, a greater gas entrainment is required to drive the coalescence of individual bubbles into a supercavity.

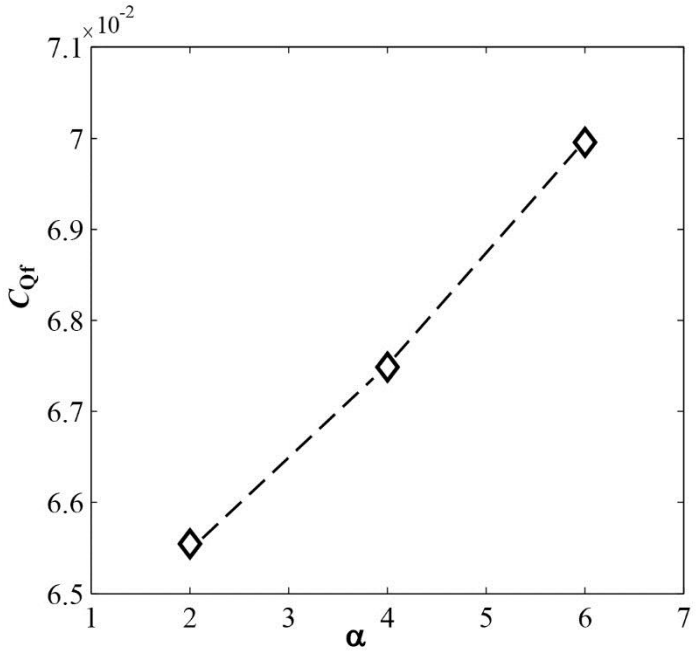

Figure 8.7: Variation of $\boldsymbol{C_{Qf}}$ with α at different *Fr* for the reference cavitator

Next, experiments are conducted to study the behavior of collapse gas entrainment under unsteady states for the reference cavitator. Figure 8.8 shows the variation of C_{Qc} with *St* at three different *Fr* numbers. As the figure shows, at a fixed *Fr*, C_{Qc} increases monotonically with increase in *St*. This monotonic increase in C_{Qc} with *St* can be explained as follows. As pointed out before, the process of supercavity collapse is preceded by a transition to a re-entrant jet closure, which makes the supercavity very unstable, particularly in an unsteady flow. A previous study (Karn et al. 2015e) has shown that the introduction of unsteady gusts in the flow lead to pressure fluctuations at the closure, intermittently causing a re-entrant jet closure. As *St* increases, a larger C_{Qc} is required to counteract the rapid pressure fluctuations occurring at re-entrant jet closure and sustain the supercavity. A similar explanation can also be given for a larger C_{Qc}

obtained at a higher *Fr*, but nearly same *St.* Previous studies (For instance, (18)) have shown that**,** the re-entrant jet velocity is approximately equal to the incoming liquid velocity. Thus, an increase in *Fr* for the same cavitator size implies an increase in re-entrant jet velocity and thus a larger C_{Qc} is needed to inhibit the re-entrant jet from reaching the cavity upstream and causing cavity collapse.

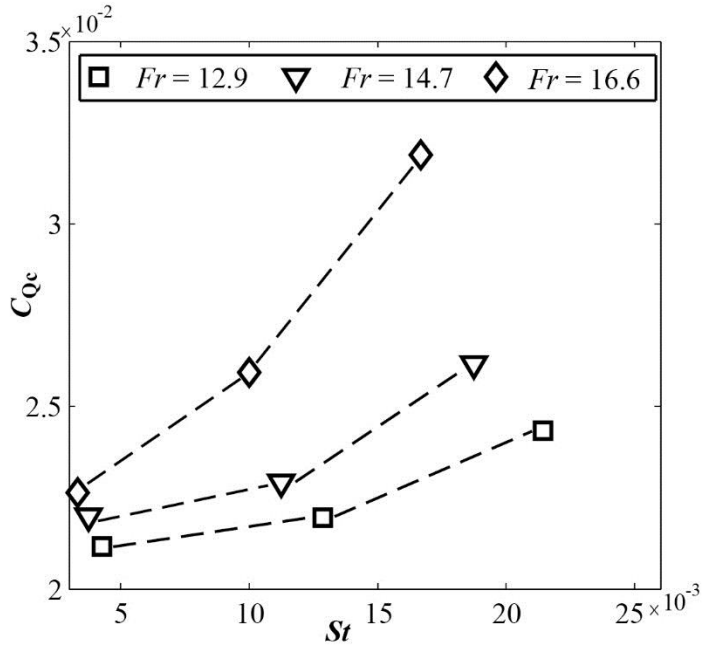

Figure 8.8: Variation of $\boldsymbol{C_{\mathrm{Qc}}}$ with *St* at different *Fr* numbers for the reference cavitator

The effect of the variation of gust amplitudes upon C_{Qc} is found to be similar to $C_{\mathrm{Qf.}}$ Figure 8.9 shows the effect of the variation of gust amplitudes upon C_{Qc} at a fixed *Fr* and *St*. From Figure 8.9, it can be seen that C_{Qc} increases monotonically with increase in α. Again, this observation can be related to the increase in the extent of pressure fluctuations at the supercavity rear with the increase in α. Thus, a larger C_{Qc} is required

to counteract the rapid pressure fluctuations occurring at the supercavity rear portion and sustain the supercavity.

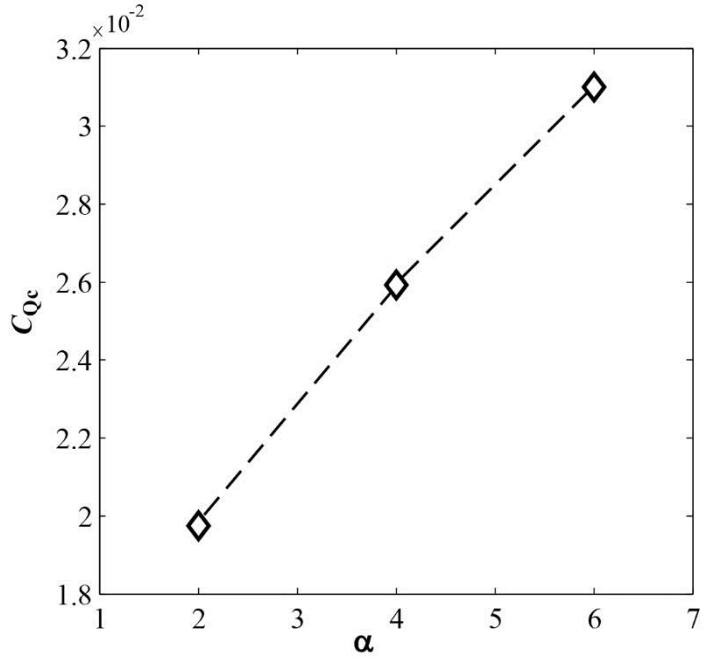

Figure 8.9: Variation of C_{Qc} with α at different *Fr* for the reference cavitator

8.5. Conclusions

In the current study, some interesting insights into the gas entrainment behaviors in the formation and collapse of a ventilated supercavity are presented for steady and unsteady flow conditions. Our experiments have shown that the gas entrainment required to establish a supercavity are much greater than the minimum gas entrainment required to sustain it. Further, these gas entrainment values depend on *Fr*, cavitator size and the flow unsteadiness. Specifically, the measurements of the formation gas entrainment coefficients under different *Fr* numbers indicate that it does not monotonically increase with *Fr* but displays increasing and decreasing trends in different

regimes of *Fr*. As shown by the high speed video observations, these trends are caused by the variation in coalescence efficiency with bubble concentration at different flow conditions. On the other hand, the collapse air entrainment coefficient initially decreases with *Fr* and then approaches to a constant. This trend has been shown to be related to the change in the non-dimensional pressure inside and outside the cavity at the supercavity rear portion. Similar trends of formation and collapse gas entrainment coefficient have been observed for different cavitator sizes.

Our unsteady state experiments have shown that both the introduction of unsteadiness and the increase in gust amplitudes cause a slight monotonic increase in the formation and collapse gas entrainment requirements. For the supercavity formation, the observed trends are related to lateral motion and expansion of the bubbles induced by the unsteadiness, which reduces the coalescent efficiency of bubbles. For the collapse case, the trends are determined by the pressure fluctuations occurring at the supercavity closure. These findings have far-reaching implications in the operation of underwater supercavitating vehicles. Specifically, knowledge of the occurrence of ventilation hysteresis and its dependence upon flow conditions can drastically reduce the ventilation demand for extended underwater missions. Our study points out the crucial factors to be considered in the estimation of gas storage requirements for such a ventilated supercavitating vehicle. However, to sufficiently understand the underlying factors behind the close interrelationships between supercavity closures, ventilation demand (i.e. different gas entrainment rates) and its dependence on other parameters requires that

experimental studies exploring fundamental physics be carried out. The next chapter discusses some attempts at such investigations.

Chapter 9. Ongoing and future work

In the prior chapters under Part B, supercavity closure mechanisms, its dependence on flow unsteadiness and its relationship with ventilation hysteresis and demand have been discussed in detail. Some novel supercavity closure modes were reported and a theory was proposed to explain the cause behind the variation of supercavity closures. It was also hypothesized and argued based on the prior literature that the supercavity closure is dependent upon the internal cavity flow (see section 6.5.4). However, to substantiate these hypotheses requires fundamental physical studies into supercavity internal flows. The ongoing and future work entails such experimental studies into supercavity internal flows. This investigation is crucial to the development of physical understanding needed for the operation and control of underwater vehicles. Finally, some future directions of the current research are suggested, which can be taken up in future investigations.

9.1. Relevance of ongoing work in control and operation of underwater vehicles

The underwater vehicle encounters unsteadiness at various phases of operation and under variable environments. Such unsteady phenomena can increase the ventilation demand and cause wetting of the body, resulting in increased drag and even cavity breakup which need to be avoided through a series of control strategies. For specific operation phase and flow environment, an optimal control strategy for a supercavitating vehicle is governed by distinct factors such as its energy efficiency, maneuverability and noise reduction which might especially be interesting from a military standpoint. To achieve this goal, a step-up understanding of supercavitation physics is needed to enhance the predictability of supercavity behaviors, which will allow designing innovative control strategies to manipulate ventilated supercavitation including cavity shape and closure mechanism for various flow settings. The control strategies relevant to the proposed research include optimizing the ventilation mechanism including ventilation flow rate and optimizing number of ventilation sites and distribution, controlling cavitator angle of the attack as well as operational speed and sea state of underwater vehicle. The following sections delineate some ideas for implementing the expected outcome from the proposed research to furnish the control strategies for supercavitating vehicles.

Different stages of vehicle operation: A supercavitating vehicle goes through different phases in the course of vehicle operation, viz. initial acceleration at start-up, steering during navigation, acceleration and deceleration during cruising operation, sudden

change in direction of motion of the vehicle and finally deceleration to rest. During the launch, a high-speed underwater vehicle starts from rest (i.e. low *Fr*), an effective control strategy should aim at establishing a stable supercavity quickly with minimal perturbation and noise generation. Although it is evident that reducing the launching depth of the vehicle will facilitate the formation of a supercavity, substantially high ventilation rate is generally required to accommodate different naval application needs. Nevertheless, a conservative choice of high ventilation supply is not necessarily the most advantageous since the high ventilation rate can trigger an unsteady pulsating cavity as reported by several prior studies (Silberman and Song 1959, Song 1961). According to Song (1961), in a pulsating supercavity, the travelling surface wave on the cavity walls causes the cavity volume and thus cavity pressure to change periodically. The pulsating cavity pressure can set the bounding liquid into radial motion, creating new disturbances at the body and new surface waves (Song 1961), which is clearly unfavorable for developing a supercavity at launching phase even for short durations. Innovative ventilation mechanisms involving ventilation through multiple 'critical' sites along the vehicle may provide an optimal solution to avoid cavity pulsation while quickly establishing a stable supercavity. To design such ventilation scheme, it is imperative to investigate the fundamental physical mechanism of pulsating cavity through advanced imaging of flow phenomena inside a supercavity, particularly in the vicinity of gas-liquid interface where significant instability may be initiated.

During the normal course of navigation, when the vehicle is enveloped inside a supercavity, the drag reduction is of prime interest for designing a control strategy. In

some occasions when swift change in vehicle direction is required, the maneuverability of a supercavitating vehicle is also important, and an effective control strategy should prevent the cavity break-up due to the cavity-vehicle interaction during sudden changes in direction. At this phase, a hybrid control strategy involving control of ventilation mechanism, cavitator angle of attack, and vehicle depth etc. is needed. Compared to the launching phase, the ventilation rate can be reduced to a minimum value by leveraging the 'ventilation hysteresis' phenomenon. The low ventilation rates add to the agility of the system and allow rapid response to changes in maneuvering a supercavitating vehicle. While exploring the agility of a supercavitating vehicle to such changes, total ventilation demand is not the only parameter of interest, but it might be of great significance to understand how the ventilation gas distributes itself inside the cavity. This knowledge can enable us to further reduce the ventilation demand for maintaining a supercavity, provided that the ventilation gas is entrained at some 'strategic' sites of the vehicle. This ventilation strategy may be of special interest for the situations where sharp maneuvering of the vehicle is required. In such situations, the chances of cavity breakup are high if a radially uniform ventilation flow is introduced. Instead, if varying ventilation flows are distributed amongst selective sites within the cavity, then the vehicle can be better equipped to carry out sharp maneuvering without breaking up the cavity. To locate such 'selective' ventilation sites requires an in-depth understanding of the flow and pressure distribution within a cavity under various unsteady conditions, which the proposed research is expected to contribute.

Vehicle operation under unsteady states: For supercavitating vehicle operating under varying sea states, the unsteady behavior of a supercavity may be contributed by the change in operational depth of a vehicle or the pressure variation induced by the overlaying ocean waves when the vehicle operates near a free surface. The change in sea states, a typical case when the vehicle rises or dips in ocean, can be initiated by changing local ambient pressure outside the supercavity. For a vehicle initially close to the sea-surface, a significant dip can result in the decrease in cavity length (i.e. vehicle not fully covered) or cavity break-up unless the ventilation demand is adjusted to cater to the variation of cavitation number and closure mechanism caused by the change of local pressure. Chapter 6 suggested the influence of local pressure on the supercavity closure. However, the physical process on how the varying local pressure affects the flow structures and pressure distribution inside the cavity and initiates a change in closure mechanism is not well understood. The proposed research envisages a study of the flow inside a cavity in sync with the unsteady cavity pressure measurements to fully characterize such processes.

For a vehicle traveling near a free surface under waves, the unsteady behavior of a supercavity can be associated with the fluctuations of angle of attack and local pressure induced by the change in frequency, amplitude or speed of the approaching sea waves. A recent study by Lee *et al* (2013) employed a gust generator to simulate such unsteady flow experienced by a supercavitating vehicle. The study revealed that the presence of a gust affects not only the supercavity shape and the ventilation demand but also the closure mechanism. To cope up with such unsteady flows, it may not be operationally practical to

adjust constantly the cavitator angle of attack and ventilation rate for maintaining a stable supercavity considering the frequent variation and unpredictability of the approaching waves. The proposed research directly quantifies the instantaneous change of flow structures and pressure distribution inside the supercavity, which may shed light on the designing of innovative ways of manipulating ventilation input (e.g. multi-site ventilation) to achieve a steady supercavity at the lowest operational cost under such varying environment.

9.2. Prior Literature

Section 6.1 presents a thorough literature review on the experimental and computational studies of supercavitation in general, and supercavity closures in particular. It was concluded there that there is a significant lack of concurrence on the empirical formulations and physical phenomena reported from many experimental studies. Although the discordant findings among these studies can be attributed to several factors such as the different nature of flow facilities (free surface tunnel vs close tunnel) and blockage etc., the exact bearing of the variations of supercavitation phenomena is not understood at a fundamental physical level. Moreover, such disagreements cannot be resolved always by resorting to analytical or numerical techniques, which have their own limitations. The analytical studies oversimplify the problem and ignore some significant details in supercavitation such as non-uniform pressure distribution inside a supercavity and ventilation hysteresis, etc. (Semenenko 2001, Kawakami and Arndt 2011). In the numerical domain, to minimize the computational load, researchers often resort to using empirical results to model the continuous cavity shape and gas leakage, etc., and neglect

physical processes such as bubble coalescence dynamics involved in supercavity formation and the internal gas flow recirculation for cavity sustenance (Xiang et al 2011). In conclusion, there are very few studies pertaining to the imaging of such internal flows.

Spurk's (2003) study underscored the significance of using physics-based approach for examining supercavitation. This work introduced a model based on the assumption that gas loss in a ventilated supercavity is caused by entrainment into the boundary layer at gas-liquid interface, and obtained results showing good agreement with the experimental data for both laminar and turbulent flows. Although Spurk's framework only applies in limited flow regimes, it highlights the significance of the flow physics at the liquid-gas interface and shows a promise to tackle ventilation supercavitation problems with a fundamental physical understanding.

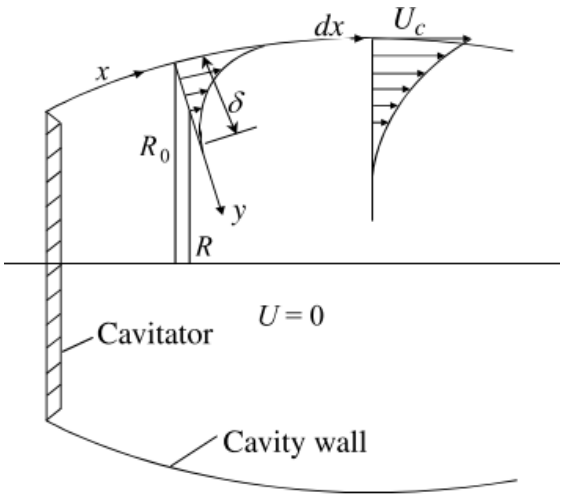

Figure 9.1: Spurk's hypothesis on gas loss from a ventilated supercavity (adapted from Spurk 2002, reproduced with permission from Springer-Verlag)

The only other study which discusses the flow imaging inside a supercavity is a brief report by Nesteruk (2012). According to Nesteruk, for the steady motion, the required ventilation demand is limited only by the gas entrainment rate at the cavity rear portion. Further, Nesteruk (2012) showed that on free axisymmetric supercavities for disk cavitators, the steady flow inside the cavity can be divide into two regions: a through flow region and a circulation flow region (denoted by F_P and F_R respectively, in Figure 9.2). The internal flow visualization experiments were carried out by adding aluminum powder in the ventilated gas and a pressure difference of about 10% of the hydrostatic pressure between leading and trailing part of supercavity was observed. However, Nesteruk (2012) does not discuss the implications of this pressure gradient upon supercavity closures.

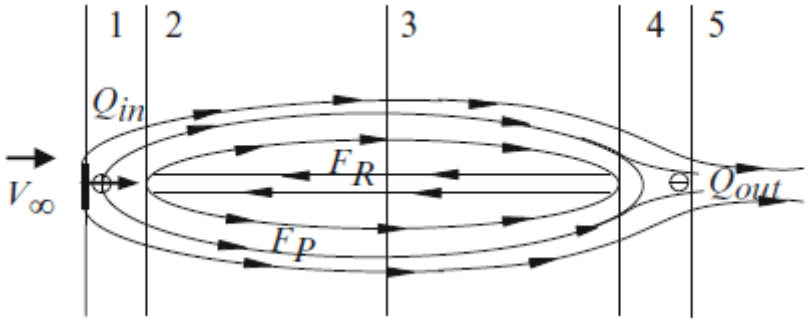

Figure 9.2: Scheme of gas flow inside the cavity (adapted from Nesteruk 2012, reproduced with permission from Springer-verlag Berlin Heidelberg)

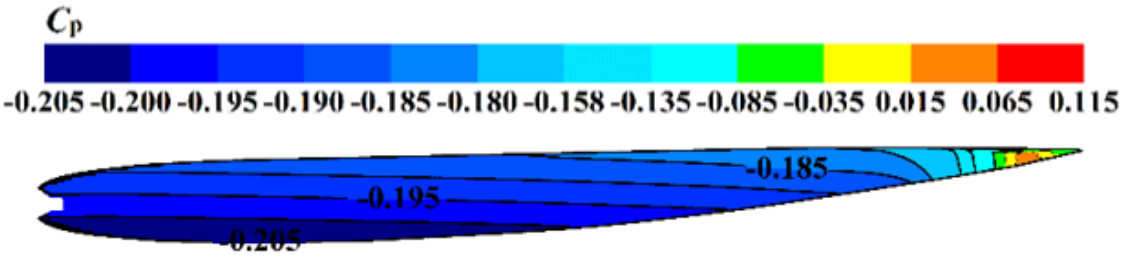

Figure 9.3: The pressure distribution (represented by pressure coefficient C_p) inside the supercavity (adapted from Cao et al. 2016)

A recent numerical study by Cao et al. (2016) has reported the internal pressure distribution of a ventilated supercavity generated from a backward-facing cavitator under different flow conditions. The simulation was performed in 3D using Eulerian multiphase model with Free Surface Model. The internal pressure in the major portion of the supercavity is primarily governed by the hydrostatic pressure of water, while steep adverse pressure gradient occurs at the closure region as shown in Figure 9.3. This study shows that the assumption of uniform pressure distribution in ventilated supercavitation is not always valid. The characterization of this pressure variation and its effect on supercavitation necessitates development of advanced experimental techniques to image across a liquid-gas interface. The following sections discuss the proposed research approach and the preliminary work done to meet these objectives.

9.3. Proposed Research Approach

The flows inside a dispersed phase (e.g., flow inside a liquid droplet in air, and flow inside a gas cavity in liquid, etc.) has significant influence on internal pressure distribution and the dynamics of gas-liquid interface. Therefore, the knowledge of such internal flow is critical for controlling and optimizing ventilation in supercavitation and many other ventilation-related applications. However, it is very challenging to perform diagnostics of the internal flow field across gas-liquid interface in a nonintrusive way. The implementation of optical diagnostic methods for internal flow measurements suffer from strong light reflection and image distortion due to large discrepancy in the optical properties across the interface. To enable such measurements, the key step is to

characterize and correct the optical distortion of particle images induced by curved gas-liquid interface (Elsinga *et al* 2005). Recently, Murphy and Adrian (2011) developed 1D refraction model for rectifying the optical distortion when implementing PIV across shocks, and this technique has been used by Liu *et al* (2013) for PIV imaging through the cylindrical wall of a test chamber.

To obtain quantitative information of internal flows, an innovative method to apply particle tracking velocimetry (PTV) across liquid-gas interface has to be developed. The method employs fluorescent particles as tracers seeded into the dispersed phase, and uses a digital camera and an optical band-pass filter to collect the fluorescent tracer images obtained through a laser illumination. An image distortion correction technique is needed to correct image distortion due to interface curvature.

9.3.1. Qualitative flow information inside a supercavity

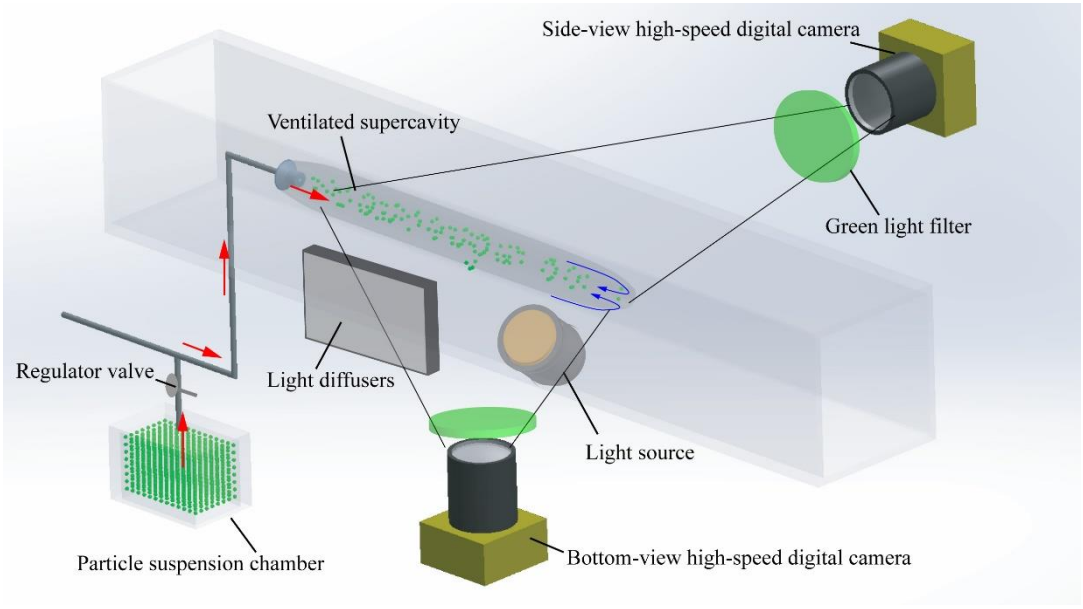

Figure 9.4: The experimental setup for two-view flow imaging inside a supercavity

To obtain the qualitative flow information, preliminary flow visualization can be conducted by injecting fog particles into the supercavity. The intensity variations of fog patterns induced by the flow structures inside the supercavity can be imaged using two high-speed cameras from two orthogonal views (from the side and bottom of the test section) as illustrated in Figure 9.4. A detailed discussion of the methods for particle injection, light illumination and two-view imaging is presented below.

The simplest way to inject smoke particles is through the ventilation gas line. Fog particles can be generated using a fog machine and retained as suspension in a chamber connected to the ventilation line through a bypass (Figure 9.4). The fog particle suspension will be delivered through the ventilation line at desired seeding rate by controlling pressure difference between the ventilation line and the suspension chamber using a regulator valve. An alternative is to test the option of seeding injection through the hypodermic tube that is used for pressure measurement. Based on these test results, we can potentially modify current ventilation lines or design new particle injection mechanisms in the cavitator models to enhance seeding quality (e.g. uniformity and proper seeding concentration) inside a supercavity.

The smoke tracers inside the supercavity can be illuminated first using a continuous high-power halogen light source. Two Photron high-speed cameras (1K×1K pixel CMOS at maximum 2000 fps) can be used to record high speed movies of fog patterns inside the supercavity at sufficiently-fast shutter speed to eliminate the image blurring. To ensure uniform background lighting, a light diffuser can be placed on one side of the test section opposite to the side-view camera.

9.3.2. Quantitative flow information inside a supercavity

Using the developed particle seeding mechanism in the previous section, airborne fluorescent particles can be injected as flow tracers for quantitative flow measurements. These particles can be manufactured by coating fluorescent dye on silica spheres with diameter < 2 μm. Based on the approach discussed in §9.2.1, 3D particle tracking using an orthogonal camera setup can be conducted, except that light sources need to be replaced by a pulsed red LED light in order to stimulate the particle fluorescence at wavelength around 532 nm (green). Moreover, green light filters can be used in front cameras to filter out the red ambient light. The tracking algorithm will follow the method reported in Adamczyk and Rimai (1988) and Guezennec *et al* (1994). Compared to the most popular 3D particle tracking velocimetry (PTV) with three-camera configuration (e.g. Maas *et al* 1993, Pereira *et al* 2006), the two-orthogonal-view tracking is more limited on spatial resolution but yields less optical distortion when imaging through gas-liquid interface. Through the orthogonal camera recording, the supercavity geometry can also be obtained, providing information for generating the ray transfer matrices.

The pressure behind the cavitator (inside the supercavity) can be measured through a hypodermic tube inserted inside the cavity (This pressure was used to obtain σ_c for different flow settings). This local pressure can be combined with time-resolved instantaneous velocity fields from PTV to estimate the pressure distribution inside a supercavity using an approach reported by Liu and Katz (2013). Relying on inviscid assumption, this approach involves integration of Euler equation (unsteady Bernoulli equation) to obtain the pressure variation from a reference point. The inviscid assumption

is expected to hold adequately for the bulk region inside the supercavity (away from the internal boundary layer) where the velocity field can be obtained with the proposed PTV techniques.

9.4. Development of an image distortion-correction approach

As mentioned before, an image distortion-correction approach is needed to correct the distortions in the captured images caused due to the interface to obtain corrected particle images for standard PIV processing. To correct image distortion due to the interface curvature, the images of the interface under laser illumination are simultaneously recorded and used to reconstruct the instantaneous geometry of the interface. Due to the convenience in characterizing the geometry of a small drop and ease in carrying out experiments, a proof-of-concept experiment for the abovementioned approach was conducted using a liquid droplet of 3 mm in diameter seeded with fluorescent particle tracers (De et al. 2016). As shown in Figure 9.5a, the fluorescent tracers inside a liquid droplet impacting surface are clearly observable. The deformed liquid-gas interface is captured and is used to correct the distorted image (Figure 9.5b).

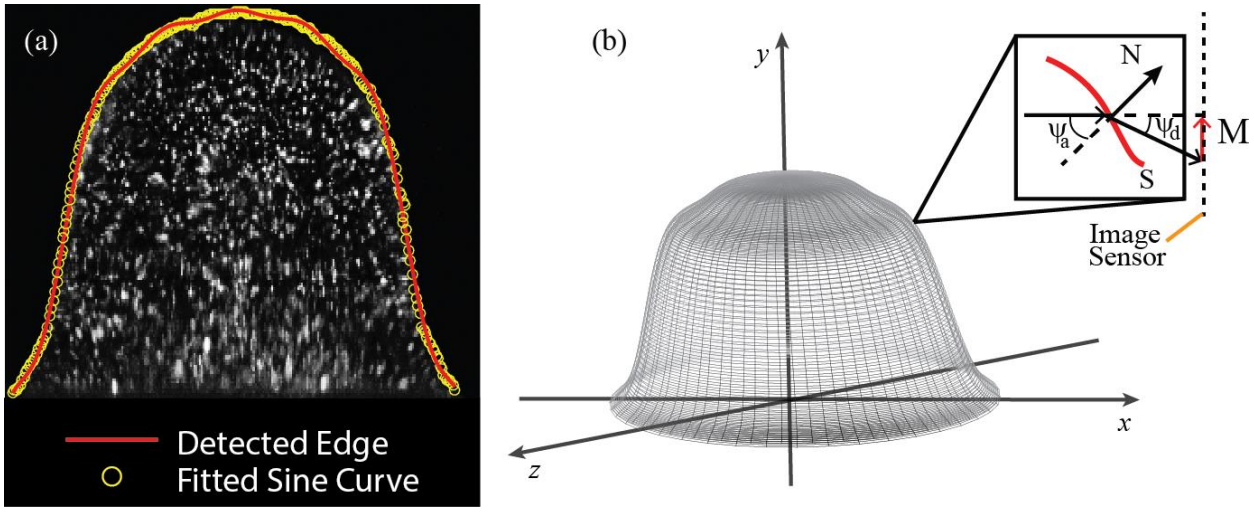

Figure 9.5: (a) Approximating the drop boundary as a sum of sine curves (b) Three dimensional (3D) reconstruction of the drop's surface for optical distortion correction (adapted from De et al. 2016)

The quantitative visualization and velocity field measurements within the drop as it impacts the solid surface is hindered by geometrical optical distortion caused by refraction of light at the drop boundary. To correct this distortion, an algorithm based on Minor et al. (2007) has been developed. The algorithm employs the principles of optical ray tracing to derive a mapping function between the image plane and the object plane. As a light ray traverses from the object plane to the image sensor, it is refracted by the drop surface. The angle of incidence,ψ_a, and the angle of refraction, ψ_d, are related by Snell's Law of refraction as

$$n_d \sin \psi_d = n_a \sin \psi_a \tag{9.1}$$

where n_a and n_d are the refractive indices of air and the drop. To correct the geometrical optical distortion, every pixel within the image must be shifted by a mapping function, $\boldsymbol{M}$. In this regard, obtaining the normal vector, $\boldsymbol{N}$, at every point on the drop surface and then

applying Snell's Law solves this problem. In obtaining the normal vector, the drop is assumed to be axisymmetric. The two-dimensional boundary of the drop is then fitted with the following sum of sines curve

$$f(x) = \sum_{i=1}^{5} a_i \sin(b_i x + c_i) \tag{9.2}$$

This yields a good fit for a wide range of drop shapes that result from the drop impacts (see Fig. 9.5a). As shown in Fig. 9.5b, revolving this curve through 360° yields a 3D reconstruction of the drop surface, S, formulated as:

$$r(x,\theta) = < x\cos\theta\,, f(x), x\sin\theta > \qquad \text{for } \theta \in [0,2\pi] \tag{9.3}$$

The normal vector to the surface is then obtained as follows:

$$\boldsymbol{N} = {}^{\nabla r}/_{|\nabla r|} \tag{9.4}$$

The subsequent mapping function, $\boldsymbol{M} = \left(M_x, M_y, M_z\right)$, can be calculated as:

$$\boldsymbol{M} = -\widehat{\boldsymbol{k}} - \tan(\psi_a - \psi_d)\,\frac{\widehat{\boldsymbol{k}}\times(\boldsymbol{N}\times\widehat{\boldsymbol{k}})}{\left|\widehat{\boldsymbol{k}}\times\left(\boldsymbol{N}\times(\widehat{\boldsymbol{k}})\right)\right|} \tag{9.5}$$

where $\widehat{\boldsymbol{k}}$ is the unit vector in the *z* direction. Thus, given (x_s, y_s) as the location of a pixel on the distorted image, the undistorted pixel's location (x_0, y_0) can be expressed as:

$$x_0 = x_s - \frac{z_s M_x}{M_z} \tag{9.6}$$

$$y_0 = y_s - \frac{z_s M_y}{M_z} \tag{9.7}$$

Note that z_s is the corresponding z-coordinate of (x_s, y_s) on the 3D reconstruction of the drop surface. This algorithm is employed over the entire recoil phase to correct the

distortion before proceeding to PIV measurements. It is noteworthy that a similar vector correction algorithm can be derived according to Minor et al. (2007), which yields the same results with significant reduction in computational time.

9.5. Preliminary work done and ongoing research

In the current research, a variety of strategies were employed to visualize the internal flows of a supercavity including fog particles, using a mixing tank to directly entrain solid particles, atomization of a particle solution, atomization of a fluorescing Rhodamine dye and finally employing a rhodamine dye solution in a humidifer.

The initial attempts were made using fog particles from a commercial fog machine. There were multiple challenges associated with the use of a fog machine. The first problem related to the uncontrolled rate of fog generation and entrainment inside the cavity. The generated fog also condensed on the ventilation tubing and particularly inside the narrow passages of the cavitator. This resulted in only a small fraction of the fog actually entering the cavity. However, we were able to entrain the fog particles through the cavity and visualize it through the high speed camera by momentarily increasing the fog concentration. However, such visualizations of fog did not show any flow structures inside the supercavity although the bulk streamwise motion of the fog could be seen. It was conjectured that this might be because of the small size of the fog particles and simultaneously less light intensity inside the cavity because of the reflections occurring at the interface.

The next attempt employed a mixing tank. 13 μm tracer particles were put in the mixing tank and a compressed air was blown into the tank to thoroughly suspend the

particles in the air. The suspension then passed through the outlet to the supercavity. However using such an approach, we could not visualize the motion of these solid particles inside the cavity. The reason behind this was that a majority of the particles were found to settle in the ventilation line and tubing, even before it entered the supercavity.

Another approach involved atomizing a liquid solution of these particles. We hoped that these small droplets of the solution could be used as tracers inside the supercavity. This concept proved fruitful, since it showed that the atomization could potentially work in generating particles small enough to be used for visualization. However, a major problem was the low concentration of these atomized drops that could actually get entrained inside the supercavity. This was also attributed in part, to the poor cavitator design. In the disk-type cavitators used in the current study, the ventilation holes point radially. Thus, the incoming atomized particles, immediately upon entrainment, got mixed with the liquid flow or followed the streamlines close to the aupercavity boundary. Because the backward facing model was being used in the current study (to ensure that there is no solid body present inside the supercavity that can interfere with the internal flow), the upstream strut produced a wake disturbance which made the region close to the supercavity boundary opaque. This made it difficult to visualize the flow inside a supercavity. Finally, we decided to carry out the flow visualization using the fluorescence produced by the Rhodamine dye solution. Currently, we are exploring the atomization of Rhodamine dye droplets for visualization of internal supercavity flows. Simultaneously, we are also improving our optics set up (for instance using a beam extender for getting higher magnification etc.), manufacturing inexpensive fluorescent particles in our lab

(based on an approach presented by Mueller et al. 2013) and exploring other techniques to produce droplets that can act follow the flow and simultaneously be visualized inside the supercavity. The next section discusses some other possible approaches that can be taken to accomplish this objective, as well as presents possible directions for future work in this area.

9.6. Scope for future work

The present dissertation provides some nice insights into the phenomenon of bubbly flows, and many possible recommendations for future work can be given based on the current research particularly in the area of supercavitation.

A number of options can be explored to visualize the flows inside a supercavity. This might include a cavitator redesign, using a fiber optic cable to directly illuminate the cavity interior, using inexpensive fluorescent particles etc. It is hoped that the smaller atomized droplets can be captured, provided laser light is normally incident on the supercavity and reflections are minimized.

Another possible area of exploration involves the characterization of axisymmetric wake of a supercavity to get an estimate of the air entrainment using the image analysis technique described in chapter 2. Using this technique, the air exiting out of the wake can be estimated, and its comparison with the ventilation demand can give some indication of the ventilation gas being entrained out of the boundary layers. This can also provide experimental proof of the Spurk's proposed hypothesis.

The current study (chapter 6) presents a systematic study of the ventilated supercavity closures as a function of different experimental parameters, and it was

suggested that the closure mechanism of a natural supercavity is predominantly a re-entrant jet. While it is definitely true that re-entrant jet is the most predominant closure mode, recent systematic experiments at SAFL have shown the occurrence of other closure modes in natural supercavitation. A natural extension of this work then, is to study the occurrence of such a closure map for a natural supercavity and its comparison with its counterpart for a ventilated supercavity. Such comparisons might shed more light on the assertion of the previous researchers who hold that the artificial and natural supercavities at same cavitation number are identical in all respects. This would also shed some light on the differences in the flow physics between a natural and artificial supercavity. A similar study can also be carried out studying the acoustic characteristics of different supercavity closure modes for natural and ventilated cases, to investigate if supercavity closures can be clearly distinguished based on their acoustic signatures.

A study should also be conducted to study the gas entrainment behaviors for a ventilated supercavity with a forward facing model. The comparison of the gas entrainment behaviors for the forward and backward facing models will indicate its dependence upon the presence of a body inside the cavity, or in other words, the internal flows. Other areas of exploration in supercavitation might also include techniques to measure and characterize the pressure distribution inside the supercavity (as asserted in chapter 6), simulations of different supercavity closures as indicated by the closure map etc.

It might also be interesting to study the effect of changing cavitator angle of attack and its resultant effect on cavitation number and flow physics. This is of

paramount interest when designing a supercavitating vehicle. Changing the cavitator angle of attack affects the supercavity shape, and the rate at which the surface pitches up, something of interest in avoiding planning effects (i.e. cavity fluid interaction).

Finally, as far as the ventilated hydrofoil wake studies are concerned, PIV measurements may be carried out in the hydrofoil wake, both for single phase and two-phase. A comparison of these two studied can lend more insights into the wake turbulence and its difference under the two cases.

References

Adamczyk, A. A., & Rimai, L. (1988). Reconstruction of a 3-dimensional flow field from orthogonal views of seed track video images. *Experiments in Fluids*, *6*(6), 380-386.

Adrian, R. J. (1991). Particle-imaging techniques for experimental fluid mechanics. *Annual review of fluid mechanics*, *23*(1), 261-304.

Alp, E., & Melching, C. S. (2011). Allocation of supplementary aeration stations in the Chicago waterway system for dissolved oxygen improvement.*Journal of environmental management*, *92*(6), 1577-1583.

Andreussi, P., Paglianti, A., & Silva, F. S. (1999). Dispersed bubble flow in horizontal pipes. *Chemical engineering science*, *54*(8), 1101-1107.

Arndt, R. E. A., Arakeri, V. H., & Higuchi, H. (1991). Some observations of tip-vortex cavitation. *Journal of fluid mechanics*, *229*, 269-289.

Arndt, R. E. A., Kawakami, D., & Wosnik, M. (2007). Measurements in cavitating flows (Handbook of Fluid Mechanics Measurements)[M].

Atkinson, B. W., Jameson, G. J., Nguyen, A. V., Evans, G. M., & Machniewski, P. M. (2003). Bubble breakup and coalescence in a plunging liquid jet bubble column. *The Canadian Journal of Chemical Engineering*,*81*(3-4), 519-527.

Azbel, D. (1981). *Two-phase flows in chemical engineering*. Cambridge University Press.

Bailey, M., Gomez, C. O., & Finch, J. A. (2005). Development and application of an image analysis method for wide bubble size distributions. *Minerals engineering*, *18*(12), 1214-1221.

Batchelor, G. K. (1953). *The theory of homogeneous turbulence*. Cambridge university press.

Bilicki, Z., & Kestin, J. (1987). Transition criteria for two-phase flow patterns in vertical upward flow. *International journal of multiphase flow*,*13*(3), 283-294.

Birkhoff, G. (2012). *Jets, wakes, and cavities*. Elsevier.

Bohac, C. E., & Ruane, R. J. (1990). Solving the dissolved oxygen problem.*Hydro Review*, *9*(1), 62-73.

Bonifazi, G., Serranti, S., Volpe, F., & Zuco, R. (1999, July). A combined morphological and color based approach to characterize flotation froth bubbles. In *Intelligent Processing and Manufacturing of Materials, 1999. IPMM'99. Proceedings of the Second International Conference on* (Vol. 1, pp. 465-470). IEEE.

Born, M., & Wolf, E. (2000). *Principles of optics: electromagnetic theory of propagation, interference and diffraction of light*. CUP Archive.

Boyle, W. C. (1993). Measurement of Oxygen Transfer in Clean Water. ASCE.

Brennen, C. (1969). A numerical solution of axisymmetric cavity flows.*Journal of Fluid Mechanics*, *37*(04), 671-688.

Brennen, C. E. (2005). *Fundamentals of multiphase flow*. Cambridge University Press.

Brennen, C. E. (2013). *Cavitation and bubble dynamics*. Cambridge University Press.

Bröder, D., & Sommerfeld, M. (2007). Planar shadow image velocimetry for the analysis of the hydrodynamics in bubbly flows. *Measurement Science and Technology*, *18*(8), 2513.

Buscaglia, G. C., Bombardelli, F. A., & García, M. H. (2002). Numerical modeling of large-scale bubble plumes accounting for mass transfer effects.*International journal of multiphase flow*, *28*(11), 1763-1785.

Buyvol, V. N. (1980). Slender cavities in flows with perturbations. *Naukova dumka*.

Calabrese, R. V., Chang, T. P. K., & Dang, P. T. (1986). Drop breakup in turbulent stirred-tank contactors. Part I: Effect of dispersed-phase viscosity. *AIChE Journal*, *32*(4), 657-666.

Calderbank, P. H. (1958). Physical rate processes in industrial fermentation. Part I: The interfacial area in gas-liquid contacting with mechanical agitation. *Trans. Inst. Chem. Eng*, *36*(5), 433-440.

Callenaere, M., Franc, J. P., Michel, J., & Riondet, M. (2001). The cavitation instability induced by the development of a re-entrant jet. *Journal of Fluid Mechanics*, *444*, 223-256.

Cameron, P. J., Rogers, P. H., Doane, J. W., & Gifford, D. H. (2011). An experiment for the study of free-flying supercavitating projectiles. *Journal of Fluids Engineering*, *133*(2), 021303.

Campbell, I. J., & Hilborne, D. V. (1958, August). Air entrainment behind artificially inflated cavities. In *Proceedings of the Second Symposium on Naval Hydrodynamics*.

Cao, L., Karn, A., Arndt, R. & Hong, J. (2016). Numerical investigations into the pressure distribution within a ventilated supercavity. *Journal of Fluids Engineering* (Under Review)

Chen, Q., Yang, X., & Petriu, E. M. (2004, October). Watershed segmentation for binary images with different distance transforms. In *Haptic, Audio and Visual Environments and*

Their Applications, 2004. HAVE 2004. Proceedings. The 3rd IEEE International Workshop (pp. 111-116).

Chesters, A. (1991). The modelling of coalescence processes in fluid-liquid dispersions: a review of current understanding. *Chemical engineering research & design*, *69*(A4), 259-270.

Clift, R., Grace, J. R., & Weber, M. E. (2005). *Bubbles, drops, and particles*. Courier Corporation.

Cong, H. B., Huang, T. L., & Chai, B. B. (2010). Water-circulating aerator: optimizing structure and predicting water flow rate and oxygen transfer.*Journal of Hydraulic Engineering*, *137*(6), 659-667.

Coulaloglou, C. A. (1979). Dispersed phase interactions in an agitated flow vessel, *Doctoral dissertation*, Illinois Institute of Technology, Chicago.

Cox, R. N., & Clayden, W. A. (1955, September). Air entrainment at the rear of a steady cavity. In *Proceedings of the Symposium on Cavitation in Hydrodynamics*.

Crabtree, J. R., & Bridgwater, J. (1971). Bubble coalescence in viscous liquids. *Chemical Engineering Science*, *26*(6), 839-851.

Daniil, E. I., & Gulliver, J. S. (1988). Temperature dependence of liquid film coefficient for gas transfer. *Journal of environmental engineering*, *114*(5), 1224-1229.

Daniil, E. I., Gulliver, J., & Thene, J. R. (1991). Water-quality impact assessment for hydropower. *Journal of environmental engineering*, *117*(2), 179-193.

Davis, R. H., Schonberg, J. A., & Rallison, J. M. (1989). The lubrication force between two viscous drops. *Physics of Fluids A: Fluid Dynamics (1989-1993)*, *1*(1), 77-81.

De, R., Karn, A., Arndt, R. E. A & Hong, J. (2016). PIV/LIF Measurements of the internal flows of a drop impacting a solid surface. (Under review in Experiments in Fluids)

DeMoyer, C. D., Schierholz, E. L., Gulliver, J. S., & Wilhelms, S. C. (2003). Impact of bubble and free surface oxygen transfer on diffused aeration systems. *Water research*, *37*(8), 1890-1904.

Do Amaral, C. E. F., Alves, R. F., Da Silva, M. J., Arruda, L. V. R., Dorini, L., Morales, R. E. M., & Pipa, D. R. (2013). Image processing techniques for high-speed videometry in horizontal two-phase slug flows. *Flow Measurement and Instrumentation*, *33*, 257-264.

Dzielski, J. E. (2011). Longitudinal stability of a supercavitating vehicle.*Oceanic Engineering, IEEE Journal of*, *36*(4), 562-570.

Elsinga, G. E., Van Oudheusden, B. W., & Scarano, F. (2005). Evaluation of aero-optical distortion effects in PIV. *Experiments in fluids*, *39*(2), 246-256.

Epshtein, L. (1973). Characteristics of ventilated cavities and some scale effects. Paper presented at the *Unsteady Water Flow with High Velocities, Proc. of Int. Symposium IUTAM,* Nauka publishing house, Moscow. 173-185.

Epshtein, L.A. *Developed cavitation flows.* Reprinted with translation from: *additions by L.A. Epshtein in book J.S. Pearsall. "Cavitation" translated into Russian,* publishing house MIR, Moscow, Russia, 1975. pp. 73-03. (Russ.)

Ferreira, A., Pereira, G., Teixeira, J. A., & Rocha, F. (2012). Statistical tool combined with image analysis to characterize hydrodynamics and mass transfer in a bubble column. *Chemical engineering journal*, *180*, 216-228.

Fox, R. W., McDonald, A. T., & Pritchard, P. J. (1985). *Introduction to fluid mechanics* (Vol. 7). New York: John Wiley & Sons.

Franc, J. P., & Michel, J. M. (Eds.). (2006). *Fundamentals of cavitation* (Vol. 76). Springer Science & Business Media.

Frank, T., Zwart, P. J., Krepper, E., Prasser, H. M., & Lucas, D. (2008). Validation of CFD models for mono-and polydisperse air–water two-phase flows in pipes. *Nuclear Engineering and Design*, *238*(3), 647-659.

Gadd, G. E., & Grant, S. (1965). Some experiments on cavities behind disks. *Journal of Fluid Mechanics*, *23*(04), 645-656.

Geary, N. W., & Rice, R. G. (1991). Bubble size prediction for rigid and flexible spargers. *AIChE journal*, *37*(2), 161-168.

Geldert, D. A., Gulliver, J. S., & Wilhelms, S. C. (1998). Modeling dissolved gas supersaturation below spillway plunge pools. *Journal of Hydraulic Engineering*, *124*(5), 513-521.

Giovannettone, J. P., & Gulliver, J. S. (2008). Gas transfer and liquid dispersion inside a deep airlift reactor. *AIChE journal*, *54*(4), 850-861.

Glover, A. R., Skippon, S. M., & Boyle, R. D. (1995). Interferometric laser imaging for droplet sizing: a method for droplet-size measurement in sparse spray systems. *Applied Optics*, *34*(36), 8409-8421.

Gonzalez, R. C., Woods, R. E., & Eddins, S. L. (2004). *Digital image processing using MATLAB*. Pearson Education India.

Gopalan, S., & Katz, J. (2000). Flow structure and modeling issues in the closure region of attached cavitation. *Physics of Fluids*,*12*(4), 895-911.

Goss, L. P., Estevadeordal, J., & Crafton, J. W. (2007, June). Velocity measurements near walls, cavities, and model surfaces using particle shadow velocimetry (PSV). In *Instrumentation in Aerospace Simulation Facilities, 2007. ICIASF 2007. 22nd International Congress on* (pp. 1-8). IEEE.

Grant, I. (1997). Particle image velocimetry: a review. *Proceedings of the Institution of Mechanical Engineers, Part C: Journal of Mechanical Engineering Science*, *211*(1), 55-76.

Guezennec, Y. G., Brodkey, R. S., Trigui, N., & Kent, J. C. (1994). Algorithms for fully automated three-dimensional particle tracking velocimetry. *Experiments in fluids*, *17*(4), 209-219.

Gulliver, J. S. (1998). Mass transfer in aerated flows. In *Second Symposium on Aeration Technology of the American Society of Mechanical Engineers, Washington, D.C., USA.*

Gulliver, J. S., & Arndt, R. E. (1992). Interfacial transport in river-reservoir systems. In *Winter Annual Meeting of the American Society of Mechanical Engineers, Anaheim, CA, USA, 11/08-13/92* (pp. 77-86).

Guoying, Z., Hong, Z., & Ning, X. (2011). Flotation bubble image segmentation based on seed region boundary growing. *Mining Science and Technology (China)*, *21*(2), 239-242.

Haberman, W. L., & Morton, R. K. (1953). *An experimental investigation of the drag and shape of air bubbles rising in various liquids* (No. DTMB-802). David Taylor Model Basin Washington DC.

Haralock, R. M., & Shapiro, L. G. (1991). *Computer and robot vision*. Addison-Wesley Longman Publishing Co., Inc.

Hesketh, R. P., Fraser Russell, T. W., & Etchells, A. W. (1987). Bubble size in horizontal pipelines. *AIChE journal*, *33*(4), 663-667.

Hibbs, D. E., & Gulliver, J. S. (1997). Prediction of effective saturation concentration at spillway plunge pools. *Journal of hydraulic engineering*,*123*(11), 940-949.

Hinze, J. O. (1955). Fundamentals of the hydrodynamic mechanism of splitting in dispersion processes. *AIChE Journal*, *1*(3), 289-295.

Honkanen, M., Eloranta, H., & Saarenrinne, P. (2010). Digital imaging measurement of dense multiphase flows in industrial processes. *Flow Measurement and Instrumentation*, *21*(1), 25-32.

Honkanen, M., Saarenrinne, P., Stoor, T., & Niinimäki, J. (2005). Recognition of highly overlapping ellipse-like bubble images. *Measurement Science and Technology*, *16*(9), 1760.

Hopping, P., March, P., Brice, T., & Cybularz, J. (1997). Update on the Development of Auto-Venting Turbine Technology. In *WATERPOWER* (Vol. 3, pp. 2020-2027). American society civil engineers.

Hrubes, J. D. (2001). High-speed imaging of supercavitating underwater projectiles. *Experiments in Fluids*, *30*(1), 57-64.

http://www.wired.com/2014/08/how-we-can-get-submarines-to-travel-at-supersonic-speed/

Ishii, M., & Hibiki, T. (2010). *Thermo-fluid dynamics of two-phase flow*. Springer Science & Business Media.

Jo, D., & Revankar, S. T. (2010). Effect of coalescence and breakup on bubble size distributions in a two-dimensional packed bed. *Chemical Engineering Science*, *65*(14), 4231-4238.

Junker, B. (2006). Measurement of bubble and pellet size distributions: past and current image analysis technology. *Bioprocess and biosystems engineering*, *29*(3), 185-206.

Kamp, A. M., Chesters, A. K., Colin, C., & Fabre, J. (2001). Bubble coalescence in turbulent flows: a mechanistic model for turbulence-induced coalescence applied to microgravity bubbly pipe flow. *International Journal of Multiphase Flow*, *27*(8), 1363-1396.

Kapankin, Y. N., & Gusev, A. V. (1984). Experimental Research of Joint Influence of Fluid and Lift Power of Cavitator on Character of Flow in Cavity Rear Part and Gas Departure from it. *Proceedings of CAHI*, (2244), 19-28.

Karlikov, V. P., Reznichenko, N. T., Khomyakov, A. N., & Sholomovich, G. I. (1987). A possible mechanism for the emergence of auto-oscillations in developed artificial cavitation flows and immersed gas jets. *Fluid Dynamics*,*22*(3), 392-398.

Karn, A., Ellis, C., Arndt, R., & Hong, J. (2015a). An integrative image measurement technique for dense bubbly flows with a wide size distribution.*Chemical Engineering Science*, *122*, 240-249.

Karn, A., Ellis, C., Hong, J., & Arndt, R. E. (2015b). Investigations into the turbulent bubbly wake of a ventilated hydrofoil: Moving toward improved turbine aeration techniques. *Experimental Thermal and Fluid Science, 64*, 186-195.

Karn, A., Monson, G. M., Ellis, C. R., Hong, J., Arndt, R. E., & Gulliver, J. S. (2015c). Mass transfer studies across ventilated hydrofoils: A step towards hydroturbine aeration. *International Journal of Heat and Mass Transfer, 87*, 512-520.

Karn, A., Ellis, C. R., Milliren, C., Hong, J., Scott, D., Arndt, R. E., & Gulliver, J. S. (2015d). Bubble size characteristics in the wake of ventilated hydrofoils with two aeration configurations. *International Journal of Fluid Machinery and Systems, 8*(2), 73-83.

Karn, A., Arndt, R. E., & Hong, J. (2015e). Dependence of supercavity closure upon flow unsteadiness. *Experimental Thermal and Fluid Science,68*, 493-498.

Karn, A., Shao, S., Arndt, R. E., & Hong, J. (2016a). Bubble coalescence and breakup in turbulent bubbly wake of a ventilated hydrofoil. *Experimental Thermal and Fluid Science, 70*, 397-407.

Karn, A., Arndt, R. E., & Hong, J. (2016b) An experimental investigation into supercavity closure mechanisms. *Journal of Fluid Mechanics, 789,* 259-284.

Karn, A., Arndt, R. E., & Hong, J. (2016c) Air entrainment behaviors in the formation and collapse of a ventilated supercavity. *Experimental Thermal and Fluid Science* (Under Review)

Kawakami, E. (2010). Investigation of the behavior of ventilated supercavities. *MS Thesis,* University of Minnesota Twin cities.

Kawakami, E., & Arndt, R. E. (2011). Investigation of the behavior of ventilated supercavities. *Journal of Fluids Engineering, 133*(9), 091305.

Kinzel, M., Lindau, J., & Kunz, R. (2009). Air entrainment mechanisms from artificial supercavities: insight based on numerical simulations. *Proceedings of the 7th International Symposium on Cavitation,* CAV 2009, 136, Ann Arbor, Michigan, USA.

Kinzel, M., Lindau, J., & Kunz, R. (2009). Air entrainment mechanisms from artificial supercavities: insight based on numerical simulations. *Proceedings of the 7th International Symposium on Cavitation*, CAV 2009 (2009), 136, Ann Arbor, Michigan, USA.

Kirschner, I. N., Fine, N. E., Uhlman, J. S., & Kring, D. C. (2001). *Numerical modeling of supercavitating flows*. Anteon/Engineering Technology Center Mystic CT. DTIC Document.

Kjeldsen, M., Arndt, R. E., & Effertz, M. (2000). Spectral characteristics of sheet/cloud cavitation. *Journal of Fluids Engineering*, *122*(3), 481-487.

Kjeldsen, M., Arndt, R. E., & Effertz, M. (2000). Spectral characteristics of sheet/cloud cavitation. *Journal of Fluids Engineering*, *122*(3), 481-487.

Kleinstreuer, Cl. *Two-phase flow: theory and applications*. CRC Press, 2003.

Kopriva, J., Arndt, R. E., & Amromin, E. L. (2008). Improvement of hydrofoil performance by partial ventilated cavitation in steady flow and periodic gusts. *Journal of Fluids Engineering*, *130*(3), 031301.

Kracht, W., Emery, X., & Paredes, C. (2013). A stochastic approach for measuring bubble size distribution via image analysis. *International Journal of Mineral Processing*, *121*, 6-11.

Kshatriya, S. S., Patwardhan, A. W., & Eaglesham, A. (2007). Experimental studies of ventilated cavities in a channel. *Chemical engineering science*,*62*(4), 979-989.

Kuklinski, R., Castano, J., & Henoch, C. (2001). Experimental study of ventilated cavities on dynamic test model. *CAV 2001: Fourth International Symposium on Cavitation.* Naval Undersa Weapons Center, Newport, RI.

Laakkonen, M., Moilanen, P., Miettinen, T., Saari, K., Honkanen, M., Saarenrinne, P., & Aittamaa, J. (2005). Local bubble size distributions in agitated vessel: comparison of three experimental techniques. *Chemical Engineering Research and Design*, *83*(1), 50-58.

Laali, A. R., & Michel, J. M. (1984). Air entrainment in ventilated cavities: case of the fully developed "half-cavity". *Journal of fluids engineering*, *106*(3), 327-335.

Laari, A., & Turunen, I. (2003). Experimental Determination of Bubble Coalescence and Break-up Rates in a Bubble Column Reactor. *The Canadian Journal of Chemical Engineering*, *81*(3-4), 395-401.

Lau, Y. M., Deen, N. G., & Kuipers, J. A. M. (2013). Development of an image measurement technique for size distribution in dense bubbly flows.*Chemical Engineering Science*, *94*, 20-29.

Lee, Q. T., Xue, L. P., & He, Y. S. (2008). Experimental study of ventilated supercavities with a dynamic pitching model. *Journal of Hydrodynamics, Ser. B*, *20*(4), 456-460.

Lee, S. J., Kawakami, E., & Arndt, R. E. (2013). Investigation of the Behavior of Ventilated Supercavities in a Periodic Gust Flow. *Journal of Fluids Engineering*, *135*(8), 081301.

Levich, V. G., & Technica, S. (1962). *Physicochemical hydrodynamics* (Vol. 689). Englewood Cliffs, NJ: Prentice-hall.

Levich, V. G., & Technica, S. (1962). *Physicochemical hydrodynamics*(Vol. 689). Englewood Cliffs, NJ: Prentice-hall.

Liao, Y., & Lucas, D. (2009). A literature review of theoretical models for drop and bubble breakup in turbulent dispersions. *Chemical Engineering Science*, *64*(15), 3389-3406.

Liao, Y., & Lucas, D. (2010). A literature review on mechanisms and models for the coalescence process of fluid particles. *Chemical Engineering Science*, *65*(10), 2851-2864.

Lin, B., Recke, B., Knudsen, J. K., & Jørgensen, S. B. (2008). Bubble size estimation for flotation processes. *Minerals Engineering*, *21*(7), 539-548.

Liu, T. J., & Bankoff, S. G. (1993). Structure of air-water bubbly flow in a vertical pipe—II. Void fraction, bubble velocity and bubble size distribution.*International Journal of Heat and Mass Transfer*, *36*(4), 1061-1072.

Liu, X., & Katz, J. (2013). Vortex-corner interactions in a cavity shear layer elucidated by time-resolved measurements of the pressure field. *Journal of Fluid Mechanics*, *728*, 417-457.

Liu, Y. H., Tseng, L. W., Huang, C. Y., Lin, K. L., & Chen, C. C. (2013). Particle image velocimetry measurement of jet impingement in a cylindrical chamber with a heated rotating disk. *International Journal of Heat and Mass Transfer*, *65*, 339-347.

Logvinovich, G. V. (1973). Hydrodynamics of free-boundary flows. Halsted Press.

Luo, H. (1993). *Coalescence, break-up and liquid circulation in bubble column reactors. Dr. ing* (Doctoral dissertation, thesis, Department of Chemical Engineering, the Norwegian Institute of Technology, Trondheim, Norway).

Maas, H. G., Gruen, A., & Papantoniou, D. (1993). Particle tracking velocimetry in three-dimensional flows. *Experiments in Fluids*, *15*(2), 133-146.

Machon, V., Pacek, A. W., & Nienow, A. W. (1997). Bubble sizes in electrolyte and alcohol solutions in a turbulent stirred vessel. *Chemical Engineering Research and Design*, *75*(3), 339-348.

March, P. A., Brice, T. A., Mobley, M. H., & Cybularz, J. M. (1992). Turbines for solving the DO dilemma. *Hydro Review*, *11*(1), 30-36.

Martin, T. (1996). *Gas dispersion with radial and hydrofoil impellers in fluids with different coalescence characteristics*. Herbert Utz Verlag.

Martínez Bazán, C., Montañés García, J. L., & Lasheras, J. C. (2000). Bubble size distribution resulting from the breakup of an air cavity injected into a turbulent water jet. *Physics of Fluids*, *12*(1), 145-148.

Martínez-Bazán, C., Montanes, J. L., & Lasheras, J. C. (1999). On the breakup of an air bubble injected into a fully developed turbulent flow. Part 2. Size PDF of the resulting daughter bubbles. *Journal of Fluid Mechanics*, *401*, 183-207.

McGinnis, D. F., Lorke, A., Wüest, A., Stöckli, A., & Little, J. C. (2004). Interaction between a bubble plume and the near field in a stratified lake.*Water Resources Research*, *40*(10).

Mena, P. C., Pons, M. N., Teixeira, J. A., & Rocha, F. A. (2005). Using image analysis in the study of multiphase gas absorption. *Chemical engineering science*, *60*(18), 5144-5150.

Meyer, F. (1994). Topographic distance and watershed lines. *Signal processing*, *38*(1), 113-125.

Michel, J. M. (1984). Some features of water flows with ventilated cavities.*Journal of fluids engineering*, *106*(3), 319-326.

Minor, G., Oshkai, P., & Djilali, N. (2007). Optical distortion correction for liquid droplet visualization using the ray tracing method: further considerations. *Measurement Science and Technology*, *18*(11), L23.

Monson, G. M. (2013). Study of mass transfer across hydrofoils for use in aerating turbines. *Masters dissertation*, University of Minnesota Twin Cities.

Mudde, R. F., Groen, J. S., & Van Den Akker, H. E. A. (1998). Application of LDA to bubbly flows. *Nuclear Engineering and Design*, *184*(2), 329-338.

Müller, A., Dreyer, M., Andreini, N., & Avellan, F. (2013). Draft tube discharge fluctuation during self-sustained pressure surge: fluorescent particle image velocimetry in two-phase flow. *Experiments in fluids*, *54*(4), 1-11.

Murphy, M. J., & Adrian, R. J. (2011). PIV through moving shocks with refracting curvature. *Experiments in fluids*, *50*(4), 847-862.

Nesteruk, I. (2012). *Supercavitation*, Springer-Verlag, Berlin Heidelberg.

Nesteruk, I. (2014). Shape of Slender Axisymmetric Ventilated Supercavities. *Journal of Computational Engineering*, *2014*.

Nouri, N. M., Madoliat, R., Jahangardy, Y., & Abdolahi, M. (2015). A study on the effects of fluctuations of the supercavity parameters. *Experimental Thermal and Fluid Science*, *60*, 188-200.

O'Boyle, S., McDermott, G., & Wilkes, R. (2009). Dissolved oxygen levels in estuarine and coastal waters around Ireland. *Marine pollution bulletin*, *58*(11), 1657-1663.

Ohnishi, M., Azuma, H., & Straub, J. (1999). Study on secondary bubble creation induced by bubble coalescence. *Advances in Space Research*,*24*(10), 1331-1336.

Olmos, E., Gentric, C., Vial, C., Wild, G., & Midoux, N. (2001). Numerical simulation of multiphase flow in bubble column reactors. Influence of bubble coalescence and break-up. *Chemical Engineering Science*, *56*(21), 6359-6365.

Otsu, N. (1975). A threshold selection method from gray-level histograms.*Automatica*, *11*(285-296), 23-27.

Pan, Z. C., Lu, C. J., Chen, Y., & Hu, S. L. (2010). Numerical study of periodically forced-pitching of a supercavitating vehicle. *Journal of Hydrodynamics, Ser. B*, *22*(5), 899-904.

Parkhill, K. L., & Gulliver, J. S. (1997). Indirect measurement of oxygen solubility. *Water Research*, *31*(10), 2564-2572.

Paryshev, E. V. (2003, November). Mathematical modeling of unsteady cavity flows. In *Fifth International Symposium on Cavitation (CAV 2003), Osaka, Japan* (pp. 1-18).

Peng, X., Wang, Z., Pan, S., & Yan, K. (2006, September). Generation mechanism of ventilated supercavitation in an axisymmetric body with cavitator. In *proceedings of Sixth International Symposium on Cavitation, CAV2006, Wageningen, The Netherlands*.

Pereira, F., Stüer, H., Graff, E. C., & Gharib, M. (2006). Two-frame 3D particle tracking. *Measurement science and technology*, *17*(7), 1680.

Pla, F. (1996). Recognition of partial circular shapes from segmented contours. *Computer Vision and Image Understanding*, *63*(2), 334-343.

Prasser, H. M. (2008). Novel experimental measuring techniques required to provide data for CFD validation. *Nuclear Engineering and Design*, *238*(3), 744-770.

Prince, M. J., & Blanch, H. W. (1990). Bubble coalescence and break-up in air-sparged bubble columns. *AIChE Journal*, *36*(10), 1485-1499.

Raney, D. C. (1977). Turbine aspiration for oxygen supplementation. *Journal of the Environmental Engineering Division*, *103*(2), 341-352.

Raney, D. C., & Arnold, T. G. (1973). Dissolved oxygen improvement by hydroelectric turbine aspiration. *Journal of the Power Division*, *99*(1), 139-153.

Rashidi, I., Pasandideh-Fard, M., Passandideh-Fard, M., & Nouri, N. M. (2014). Numerical and Experimental Study of a Ventilated Supercavitating Vehicle. *Journal of Fluids Engineering*, *136*(10), 101301.

Razzaque, M. M., Afacan, A., Liu, S., Nandakumar, K., Masliyah, J. H., & Sanders, R. S. (2003). Bubble size in coalescence dominant regime of turbulent air–water flow through horizontal pipes. *International journal of multiphase flow*, *29*(9), 1451-1471.

Roesler, T. C., & Lefebvre, A. H. (1989). Studies on aerated-liquid atomization. *International Journal of Turbo and Jet Engines*, *6*(3-4), 221-230.

Ruane, R. J., & Hauser, G. E. (1991). Factors affecting dissolved oxygen in hydropower reservoirs. In *Waterpower'91*.

Saberi, S., Shakourzadeh, K., Bastoul, D., & Militzer, J. (1995). Bubble size and velocity measurement in gas—liquid systems: Application of fiber optic technique to pilot plant scale. *The Canadian Journal of Chemical Engineering*, *73*(2), 253-257.

Sadr-Kazemi, N., & Cilliers, J. J. (1997). An image processing algorithm for measurement of flotation froth bubble size and shape distributions. *Minerals Engineering*, *10*(10), 1075-1083.

Sahoo, P. K., & Arora, G. (2004). A thresholding method based on two-dimensional Renyi's entropy. *Pattern Recognition*, *37*(6), 1149-1161.

Sahoo, P., Wilkins, C., & Yeager, J. (1997). Threshold selection using Renyi's entropy. *Pattern recognition*, *30*(1), 71-84.

Sauter, J. (1926). Determining size of drops in fuel mixture of internal combustion engines. *National Advisory Committee for Aeronautics.*

Savchenko, Y. (2001). Supercavitation-problems and perspectives. In *Fourth International Symposium on Cavitation. California Institute of Technology Pasadena, California*. 2001.

Schiebe, F. R., & Wetzel, J. M. (1964). *Further studies of ventilated cavities on submerged bodies* (No. 72). University of Minnesota Minneapolis, St. anthony falls hydraulic lab.

Schierholz, E. L., Gulliver, J. S., Wilhelms, S. C., & Henneman, H. E. (2006). Gas transfer from air diffusers. *Water research*, *40*(5), 1018-1026.

Scott, D., Sabourin, M., Beaulieu, S., Ellis, C. & Karn, A. (2015). Optimizing Dissolved Oxygen Transfer in Auto-Venting Turbines. In *Hydrovision International, Portland, OR, USA*. 07/14-17/2015.

Semenenko, V. N. (2001a). Artificial supercavitation: physics and calculation. *Ukrainian Academy of Sciences*, Kiev Inst of Hydromechanics.

Semenenko, V. N. (2001b). Dynamic processes of supercavitation and computer simulation. *Ukrainian Academy of Sciences*, Kiev Inst of Hydromechanics.

Sevik, M., & Park, S. H. (1973). The splitting of drops and bubbles by turbulent fluid flow. *Journal of Fluids Engineering*, *95*(1), 53-60.

Shi, H. H., Itoh, M., & Takami, T. (2000). Optical observation of the supercavitation induced by high-speed water entry. *Journal of fluids engineering*, *122*(4), 806-810.

Silberman, E. (1957). Production of bubbles by the disintegration of gas jets in liquid. *Proc. 5th Midwestern conference on fluid mechanics, University of Michigan, USA.*

Silberman, E. & Song, C. S. (1961). Instability of ventilated cavities. *Journal of Ship Research* 5 (1), 13-33.

Skidmore, G. (2013). The pulsation of ventilated cavities. *Masters Thesis,* Department of Aerospace Engineering, Pennsylvania State University.

Skidmore, G. M., Brungart, T. A., Lindau, J. W., & Moeny, M. J. (2015). Noise generated by ventilated supercavities. *Noise Control Engineering Journal*, *63*(1), 94-101.

Smith, J. S., Burns, L. F., Valsaraj, K. T., & Thibodeaux, L. J. (1996). Bubble column reactors for wastewater treatment. 2. The effect of sparger design on sublation column hydrodynamics in the homogeneous flow regime.*Industrial & engineering chemistry research*, *35*(5), 1700-1710.

Soille, P. (2013). *Morphological image analysis: principles and applications*. Springer Science & Business Media.

Song, C. S. (1961). Pulsation of ventilated cavities. St. Anthony Falls Laboratory, University of Minnesota.

Spurk, J. H. (2002). On the gas loss from ventilated supercavities. *Acta mechanica*, *155*(3-4), 125-135.

Sreenivasan, K. R. (1995). The energy dissipation in turbulent shear flows. *Fluid Dyn. Aerospace Eng. Banglore*, 159-190.

Stinebring, D. R., Billet, M. L., Lindau, J. W., & Kunz, R. F. (2001). Developed cavitation-cavity dynamics. Pennsylvania State Univ University Park Applied Research Lab.

Stutz, B., & Reboud, J. L. (1997). Experiments on unsteady cavitation.*Experiments in fluids*, *22*(3), 191-198.

Tayali, N. E., & Bates, C. J. (1990). Particle sizing techniques in multiphase flows: A review. *Flow Measurement and Instrumentation*, *1*(2), 77-105.

Thompson, E. J., & Gulliver, J. S. (1997). Oxygen transfer similitude for vented hydroturbine. *Journal of hydraulic engineering*, *123*(6), 529-538.

Tikhomirov, V. M. (1991). On the breakage of drops in a turbulent flow. In *Selected Works of AN Kolmogorov* (pp. 339-343). Springer Netherlands.

Tse, K. L., Martin, T., McFarlane, C. M., & Nienow, A. W. (2003). Small bubble formation via a coalescence dependent break-up mechanism. *Chemical Engineering Science*, *58*(2), 275-286.

Tulin, M. P. (1964). *Supercavitating Propellers, Momentum Theory* (No. TR-121-4). Hydronautics Inc. Laurel, MD.

Urban, A. L., Gulliver, J. S., & Johnson, D. W. (2008). Modeling total dissolved gas concentration downstream of spillways. *Journal of hydraulic engineering*, *134*(5), 550-561.

Vlasenko, Y. D. (2003). Experimental investigation of supercavitation flow regimes at subsonic and transonic speeds. In *Fifth International Symposium on Cavitation, Osaka, Japan*.

Weiss, P. T., Gulliver, J. S., & Semmens, M. J. (1996). Hypolimnetic aeration with hollow fiber membranes. *Lake and Reservoir Management*,*12*(4), 468-476.

Wilhelms, S. C., Gulliver, J. S., Ling, J. T., & Ling, R. S. (2005). Gas transfer, cavitation, and bulking in self-aerated spillway flow. *Journal of Hydraulic Research*, *43*(5), 532-539.

Wilhelms, S. C., Schneider, M. L., & Howington, S. E. (1987). Improvement of hydropower release dissolved oxygen with turbine venting. *Available from the National Technical Information Service, Springfield Virginia. 22161. Technical Report E-87-3, March 1987. Final Report. 106 p, 19 fig, 4 tab, 39 ref, 4 append.*

Witt, A. M., & Gulliver, J. S. (2012). Predicting oxygen transfer efficiency at low-head gated sill structures. *Journal of Hydraulic Research*, *50*(5), 521-531.

Wosnik, M., Schauer, T. J., & Arndt, R. E. (2003). Experimental study of a ventilated supercavitating vehicle. In *Fifth International Symposium on Cavitation, Osaka, Japan* (pp. 1-4).

Wu, T. (1972). Cavity and wake flows. *Annual Review of Fluid Mechanics,4*, 243-284.

Wu, T., Whitney, A. K., & Brennen, C. (1971). Cavity-flow wall effects and correction rules. *Journal of Fluid Mechanics*, *49*(02), 223-256.

Wu, X., & Chahine, G. L. (2007). Characterization of the content of the cavity behind a high-speed supercavitating body. *Journal of Fluids Engineering*, *129*(2), 136-145.

Xiang, M., Cheung, S. C. P., Tu, J. Y., & Zhang, W. H. (2011). Numerical research on drag reduction by ventilated partial cavity based on two-fluid model. *Ocean Engineering*, *38*(17), 2023-2032.

Zaidi, S. H. (1998). Difficulties in measuring liquid droplet size distributions using laser diffraction technique. *Atomization and Sprays*, *8*(4).

Zhang, X. W., Wei, Y. J., Zhang, J. Z., Cong, W., A. N. G., & Yu, K. P. (2007). Experimental research on the shape characters of natural and ventilated supercavitation. *Journal of Hydrodynamics, Ser. B*, *19*(5), 564-571.

Zhou, J. J., Yu, K. P., Min, J. X., & Ming, Y. (2010). The comparative study of ventilated super cavity shape in water tunnel and infinite flow field. *Journal of Hydrodynamics, Ser. B*, *22*(5), 689-696.

Zhou, K. J., Yang, C. H., Gui, W. H., & Xu, C. H. (2010). Clustering-driven watershed adaptive segmentation of bubble image. *Journal of Central South University of Technology*, *17*, 1049-1057.

Zou, W., Yu, K. P., Arndt, R. E., Zhang, G., & Li, Z. W. (2013). On the shedding of the ventilated supercavity with velocity disturbance. *Ocean Engineering*, *57*, 223-229.